Adjoint shape optimization of blood flow applications under uncertainties

Dissertation (monograph) approved by the Doctoral Degree Committee of
Hamburg University of Technology

in pursuit of the academic degree of

Doktor-Ingenieur (Dr.-Ing.)

written by
Georgios Bletsos

from
Athens, Greece

2025

Chair of the Board of Examiners:
Prof. Dr.-Ing. Jürgen Grabe

Reviewers:
1. Prof. Dr.-Ing. Thomas Rung
2. Prof. Dr. Michael Hinze
3. Prof. Dr. Kyriakos Giannakoglou
4. Prof. Dr.-Ing. Alexander Düster

Day of the oral examination:
January 23, 2025

Digital Object Identifier (DOI): 10.15480/882.15270
Open Researcher & Contributor ID (ORCID): 0000-0001-8033-9861

Abstract

This thesis aims to advance traditional gradient-based shape optimization techniques by incorporating blood-specific features. The work can be broadly classified into four main categories, (a) computational blood flow modeling, (b) parameter-free shape optimization, (c) the continuous adjoint method and (d) robust shape optimization.

As regards (a), this work presents key aspects related to the computational fluid dynamics (CFD) or fluid-structure interaction (FSI) simulations employed for the solution of the blood flow problem (primal problem). The underlying primal problem is enhanced to account for blood damage (hemolysis) by the numerical solution of an additional partial differential equation (PDE). The minimization of hemolysis is one of the main objectives of interest in this work. In order to account for the shear-thinning behavior of blood, several non-Newtonian viscosity models are also employed. The numerical solution of the primal problem is verified against analytical solutions and literature-reported results when deemed necessary.

The shape optimization problem is formulated based on a parameter-free approach. To this end, the identification of the shape gradient or at least, a suitable descent direction, based on the shape sensitivity is addressed. Several methods that compute the descent direction based on the solution of one (or two) additional PDE(s) are presented. Auxiliary aspects related to the optimization problem are also discussed in the context of (b).

The thesis presents the novel derivation of continuous adjoint equation systems dual to the blood-specific problems. Specifically, contributions to (c) relate to the development of the continuous adjoint to the steady-state Navier-Stokes equations for an incompressible fluid with hemolysis modeling and with non-Newtonian viscosity properties. The accuracy of the novel systems in estimating the shape sensitivity is assessed against second-order accurate finite difference (FD) studies.

On the topic of (d), this work focuses on the necessary uncertainty quantification techniques able to drive a robust shape optimization procedure. The problem is considered uncertain by means of the employed parameters or the boundary conditions thus rendering the objective functional a statistical quantity. The optimization targets the minimization of the statistical moments of the objective functional through the use of methods based on sampling or the method of moments.

The biomedical applications studied in this thesis refer to an idealized medical device and an idealized bypass-graft.

Acknowledgements

First and foremost, I would like to express my deepest gratitude to my supervisor, Prof. Dr.-Ing. Thomas Rung. It is rare in life to encounter individuals who become true sources of inspiration, but I can say with absolute confidence that Prof. Rung has been such a figure for me. His genuine passion for research, profound expertise in fluid dynamics, and eagerness to share his knowledge made him the ideal academic mentor throughout my doctoral journey. The path to a doctoral degree is often marked by academic challenges and moments of uncertainty. I am especially grateful for Prof. Rung's unwavering support in helping me overcome these obstacles, and for instilling in me the perspective that each challenge is not a setback, but an opportunity for growth and discovery.

I would also like to express my sincere gratitude to the other reviewers of my dissertation. I am especially thankful to Prof. Dr. Giannakoglou, who first introduced me to the field of adjoint-based shape optimization during my student years in the National Technical University of Athens, and whose consistently constructive feedback greatly enriched various aspects of my work. My discussions with Prof. Dr. Hinze, along with his influential contributions to the optimization community, have significantly deepened my mathematical understanding of the complex subject of shape optimization—an impact for which I am truly grateful. I also extend my thanks to Prof. Dr.-Ing. Düster for generously providing access to several of the computational tools developed by his team; these tools were instrumental in enabling the Fluid-structure interaction simulations carried out in this dissertation. In addition, I would like to thank Prof. Dr.-Ing. Jürgen Grabe for chairing the examination committee.

I am also deeply grateful to my colleagues at the Institute for Fluid Dynamics and Ship Theory (FDS) at Hamburg University of Technology. Beginning a doctoral journey abroad—especially during the difficult period of the COVID-19 pandemic—was made significantly easier thanks to the supportive and welcoming environment created by everyone at FDS. I would like to extend special thanks to Dr.-Ing. Lars Radtke, Dr.-Ing. Niklas Kühl, and Dr.-Ing. Peter Marvin Müller, who have been far more than colleagues—they have become true friends. I am also thankful to all members of the SENSUS Research Training Group for the many stimulating and enlightening discussions we shared throughout the course of the project.

My heartfelt thanks also go to my family and friends for their unwavering support and constant encouragement, regardless of how far—or how cold—the places I choose to call home may be. Their belief in me has been a steady source of strength.

Finally, my deepest gratitude goes to my partner, Sofia. Thank you for your patience through countless conversations about adjoint, for your understanding during the most demanding times, and above all, for choosing to share this journey with me. I am endlessly thankful for your love and support.

"Keep Ithaka always in your mind. Arriving there is what you're destined for. But don't hurry the journey at all. Better if it lasts for years, so you're old by the time you reach the island, wealthy with all you've gained on the way, not expecting Ithaka to make you rich.

Ithaka gave you the marvelous journey. Without her you wouldn't have set out. She has nothing left to give you now."

– C. P. Cavafy, "Ithaka"

Contents

List of Tables

List of Figures

List of Abbreviations

If a lower-case Latin “s” follows the abbreviation, then the plural of the abbreviated phrase is implied.

2D and 3D	Two- and Three-Dimensional
AIAA	American Institute of Aeronautics and Astronautics
ALE	Arbitrary Lagrangian-Eulerian
ATC	Adjoint Transpose Convection
BC	Boundary Condition
C	Carreau
CAD	Computer-Aided Design
CDS	Central Differencing Scheme
CFD	Computational Fluid Dynamics
CM	Control Mass
CSM	Computational Structural Mechanics
CV	Control Volume
CVD	Cardiovascular Disease
DS	Direct Sensitivity
FD	Finite Difference
FDA	United States Food and Drug Administration
FE	Finite Elements
FFD	Free-Form Deformation
FOSM	First-Order Second-Moment
FSI	Fluid-Structure Interaction
FV	Finite Volume
ITTL	Implicit Three Time Level
LB	Laplace-Beltrami
LHS	Left-Hand Side
MC	Modified-Casson (in the context of non-Newtonian viscosity models)
MC	Monte Carlo (in the context of robust optimization)
MoM	Method of Moments
MPI	Message Passing Interface
N	Newtonian
NS	Navier-Stokes
ODE	Ordinary Differential Equation
OSI	Oscillatory Shear Index
PBiCG	Preconditioned Bi-Conjugate Gradient

PCG	Preconditioned Conjugate Gradient
PDE	Partial Differential Equation
PDF	Probability Density Function
PL	Power-Law
QNLS	Quasi-Newton Least Squares
QoI	Quantity of Interest / Quantities of Interest
QUICK	Quadratic Upwind Interpolation of Convective Kinematics
RBC	Red Blood Cell
RHS	Right-Hand Side
RTT	Reynolds' Transport Theorem
SCL	Space Conservation Law
SEDF	Strain Energy Density Function
SGD(M)	Stochastic Gradient Descent (Method)
SGD-B	Stochastic Gradient Descent Method - Binning Variant
SIMPLE	Semi-Implicit Method for Pressure-Linked Equations
SOSM	Second-Order Second-Moment
SP	Steklov-Poincaré
TAHI	Time-Averaged Hemolysis Index
TVD	Total Variation Diminishing
UQ	Uncertainty Quantification
WSS	Wall Shear Stresses

1 Introduction

1.1 Background and Motivation

Numerical simulations are well-established as an indispensable tool for a variety of industries and research institutions dealing with fluid and structural mechanics. On the one hand, they provide an affordable, commonly available alternative to often costly experiments and on the other hand, they allow for investigations on conditions that would be impossible to achieve in experimental settings. The advances in computational science have not only enhanced our fundamental understanding of the investigated phenomena but have also allowed us to study the optimization of related conditions which we can control.

In fact, the interest of the engineering community is nowadays devoted mostly to the latter. Engineering sciences have already provided suitable solutions to many of the macro-scale questions of humankind, such as *"How to achieve a certain task?"*, and have now allowed the engineers to shift their attention to questions like *"How to better achieve the same task?"*. As a result, the field of shape optimization has found suitable grounds for application. The designs produced today in automotive, maritime and aeronautics industries have, in their majority, undergone a certain level of computational optimization, based on either *computational fluid dynamics* (CFD) or *computational structural mechanics* (CSM). This industrial interest on the field is naturally accompanied by a significant research effort, see e.g., Katsapoxaki et al. [2023], Kühl et al. [2022], Upadhyay et al. [2021], Papoutsis-Kiachagias et al. [2019] for some recent publications.

While computational shape optimization methods have enjoyed great appeal in the aforementioned fields, their application lags behind in the field of biomedical engineering dealing with blood flows. Even though the computational tools, i.e., CFD and CSM, are often virtually identical to those used by other industries, there are certain aspects that currently hinder the straightforward implementation of, in other fields established, shape optimization methods. The present thesis is motivated by those aspects. The main focus is on enhancing existing methods to seamlessly integrate blood-specific features. Attention is also given to the nature of the investigated applications, i.e., the interdependence between the blood flow and the surrounding structure as well as the uncertainty that experimentally assessed simulation parameters might involve when being used in silico.

This introduction includes a brief overview of the current state-of-the-art on relevant topics studied in this thesis. Additional background information and references are included in each chapter to establish the necessary links with the present thesis.

Computational Blood Flow Modeling

Numerical simulations based on continuum mechanics can sufficiently describe the flow of blood in an extensive range of applications, see e.g., Quarteroni et al. [2000] for a review on computational vascular fluid dynamics. The goal of simulating such flows, that within this thesis will be referred to as *the primal problem*, is to predict hemodynamic quantities of interest (QoI). Depending on the application at hand, the QoI can significantly vary. This thesis primarily focuses on *mechanical hemolysis*[1]. Hemolysis refers to the mechanical damage of red blood cells (RBCs) and the release of their contents, predominantly hemoglobin, in the blood plasma due to excessively high stress induced by peculiarities of the blood flow. It can lead to hemoglobinemia, which plays a significant role in the pathogenesis of sepsis, and to increased risk of infection due to its inhibitory effects on the innate immune system (Effenberger-Neidnicht and Hartmann [2018]). Hemolysis induction is encountered in many biomedical devices, where large velocity gradients are found (Thamsen et al. [2015], Yu et al. [2016]), as well as *in vivo*, i.e., in a living person, when vessels delivering blood are kinked or stenosed (Goubergrits et al. [2018]). This thesis is partially motivated by the goal of reducing hemolysis in biomedical applications through shape optimization. To this end, the main tool for the solution of the primal problem is CFD. An overview on hemolysis models coupled with CFD solvers can be found in Yu et al. [2017].

Generally, in CFD simulations of hemodynamics, blood is treated as a continuous fluid medium instead of being treated as a dispersed multiphase model. This reduces the complexity and computational cost of the problem and instead attempts to approximate the microscopic deformation and concentration variation of the suspended RBCs through appropriate viscosity models (Kishimoto et al. [2020], Yeleswarapu [1996]). A Newtonian fluid assumption is often employed to capture the rheology of blood. While this assumption has been shown to sufficiently describe blood in flows exposed to high shear rates, it falls short in flows of low shear rates due to the shear-thinning behavior of blood (Fung [1993]). Several non-Newtonian models have been proposed to deal with this inadequacy and account for pseudo-plastic behavior. Some of such models, that are also investigated in this thesis, are the Power-law (Shibeshi and Collins [2005]), Casson's law (Fan et al. [2009], Perktold et al. [1991]), as well as modified versions of it (González and Moraga [2005]), and Carreau's law (Johnston et al. [2004]). Even though these models cannot account for viscoelastic properties, they are frequently used in many computational studies due to their straightforward description as well as implementation into a CFD framework.

Furthermore, in a multitude of applications, blood interacts with a solid surface, which exhibits an increased elasticity. In such cases, the forces generated by the blood flow are sufficient to deform the surrounding structure. To this extent, the rigid wall assumption of a classical CFD simulation has in many cases proven to be inadequate, see e.g., Hsu et al. [2014], Bazilevs et al. [2010], Torii et al. [2007]. To resolve this shortcoming, extensive focus has recently been given to *fluid-structure interaction* (FSI) simulations that consider the fluid flow and the displacement of the vessel wall in a coupled manner. From a numerical point of view, FSI simulations can generally be classified as either *monolithic*, where the coupled problem is solved as a whole by one numerical method in one domain or *partitioned*, in which the fluid and structure subproblems are treated separately in their respective domains. This thesis employs the latter to study the influence of the rigid wall assumption on hemolysis, as well as other QoI, in a biomedical application of interest. In addition, FSI is used, when deemed biomedically relevant, as a post-processing tool to evaluate the

---

[1] For the sake of brevity, the word *mechanical* might be omitted throughout this thesis. In all instances, reference to hemolysis stands for mechanical hemolysis.

CFD-based optimized geometries. A general overview on cardiovascular FSI can be found in Bazilevs et al. [2013].

Shape Optimization Methods

In shape optimization, one searches for the optimal configuration of a given domain so that a *cost* or *objective functional* is minimized[2]. Certain distinctions could be made as regards the shape optimization problems.

In the context of the shape description, the solution methods could be loosely divided into *parametric* and *parameter-free*. On the one hand, parametric methods refer to a description of the geometry through a finite number of parameters. The prescribed parameterization is decided before the optimization begins and is included in the derivation process of suitable shape updates, see e.g., Papoutsis-Kiachagias and Giannakoglou [2016], Abraham et al. [2005a]. On the other hand, parameter-free methods are derived on a continuous level independently of a parameterization. This thesis considers exclusively parameter-free shape descriptions which are further discussed in Chapter 3. Nevertheless, both strategies have found suitable grounds for application depending on the needs of the design, see e.g., Trompoukis et al. [2023], Dick et al. [2022], Xu et al. [2014] for parametric and Kröger and Rung [2015], Bletzinger [2014], Stück and Rung [2013], Bletzinger et al. [2010] for parameter-free applications. A crucial aspect on deciding upon the shape description refers to the underlying optimization method.

A wide variety of optimization methods, ranging from stochastic (or global) (Bäck [1996]) to deterministic (or local) (Nocedal and Wright [2006]) exists. There is no simple answer to which optimization strategy is the best choice. Instead, the decision upon the employment of a method depends on the design task and state.

Global techniques, such as evolutionary algorithms (Jahangirian and Shahrokhi [2011], Giannakoglou et al. [2006]), are able to provide the global optimum, as the name suggests, given that a large number of candidate solutions are evaluated. This option is attractive for non-convex problems and cheap evaluation methods, but becomes computationally unfeasible for a large number of unknowns and/or expensive evaluation methods. This is due to the fact that the necessary candidate evaluations scale with the amount of design variables. In fact, in certain cases the computational time complexity of an evolutionary algorithm, which measures how the computational time of an algorithm scales with the size of the input, is polynomial or even exponential (He and Yao [2001]). Although a parameterization of the shape may drastically reduce the number of design variables, the problem of performing many costly simulations remains. This drawback can be counteracted if a reliable surrogate model, able to estimate the objective functional given the design parameters, exists (Jin [2011]). However, suppose that a parameterization of the shape doesn't exist or it is rather not desired. Then, the most conceivable design space would correspond to a subset of the discretized computational domain. In this case, the design space would be too large for a global optimization method to handle.

Deterministic strategies are generally driven by the gradient of the objective functional with respect to (w.r.t.) the control, i.e., in this case the shape. These approaches, frequently referred to as gradient-based methods, require support from a tool able to compute

---

[2] Note that a maximization problem is equivalent to a minimization, if the reciprocal of the objective functional (when defined) or the negative objective functional is considered instead.

the desired gradient. The computation of the gradient is a crucial point that in the context of parameter-free approaches can be considered as a two-step process. As a first step, one needs to compute the derivative of the objective functional, i.e., the *sensitivity derivative* (R. R. A. Martins and T. Hwang [2013]), which corresponds to a scalar field over the design sections of the geometry. On a second step, the sensitivity derivative needs to be associated to the gradient. This can be done, for instance, when a Hilbert space, i.e., a vector space equipped with an inner product, setting is considered. The sought gradient is then identified as the Riesz representative of the sensitivity derivative. This second step is usually realized by the numerical solution of a partial differential equation (PDE) that relates the gradient (or more generally speaking, an admissible descent direction) to the sensitivity derivative (Radtke et al. [2023], Allaire et al. [2021]). Generally, the first step corresponds to the costly part of the two-step process. Depending on the approach for obtaining the sensitivity derivative, the computational cost can significantly vary. For example, in the *finite difference* (FD) method, the cost of the derivative computation scales linearly with the number of design variables. On the other hand, the *adjoint method* is able to provide the sought derivative at the cost of approximately one additional simulation, independently of the number of design variables.

Adjoint Shape Optimization

The concept of the adjoint method in applications of fluid mechanics was first introduced by Pironneau in his pioneering works Pironneau [1974], Pirronneau [1984] and then popularized in applications of aerodynamics by Jameson (Jameson [1988]) who formulated the method in the context of control theory. Since then the method has enjoyed great appeal in many fields of application due to its superior efficiency in computing sensitivity derivatives in comparison to other methods.

The adjoint is based on the method of Lagrange multipliers to convert a constrained optimization problem to an unconstrained one. The essence of the method is in identifying the multipliers so that the sensitivity derivative depends exclusively on the variation of the design variables. This process is realized by solving a dual to the primal problem, the so called *adjoint problem*, after the solution of the primal. In this context, the Lagrange multipliers correspond to the adjoint variables. The computational effort for the solution of the adjoint problem is usually comparable to that of the primal, independently of the number of design variables. Upon the solution of the adjoint problem, the sought derivative can be directly computed with no additional cost, thus making the total cost for the computation of the sensitivity derivative equal to approximately two flow solutions.

The adjoint method for CFD-based applications can be basically subdivided into continuous and discrete approaches. The former follows a *derive-then-discretize* strategy while the latter a *discretize-then-derive*. In short, discrete adjoint methods guarantee exact duality to the discretized primal problem in the expense of additional required computational storage capacity while continuous adjoint offers a unique understanding to the contribution of the physics in the optimization problem and can follow a similar to the primal algorithmic strategy in the expense of compromising the duality. For a comprehensive discussion on the two approaches see Peter and Dwight [2010] or Giles and Pierce [2000]. Because this thesis focuses on studying how blood-specific characteristics affect the optimization of pertinent geometries, the continuous adjoint method is employed in this work.

The derivation of the continuous adjoint problem is exclusively based on two factors, the primal problem and the objective functional. In the context of blood flows, the primal problem, i.e. the Navier-Stokes (NS) equations, needs to take into account the non-Newtonian properties of blood. Furthermore, interest is given into minimizing hemolysis. Therefore, a suitable objective functional able to describe the blood-damaging effect needs to be mathematically formulated and implemented in an adjoint framework. In the context of adjoint shape optimization, this thesis is mainly concerned with these two aspects.

Robust Shape Optimization

Typically, strategies for shape optimization assume precise knowledge of the conditions under which a flow phenomenon occurs. This is, however, rarely the case. It is frequently observed that the initial assumption of accurate knowledge is actually a coarse approximation, with the actual value fluctuating around what was initially assumed to be precise. To this end, a shape that is considered to be optimal for one application is sometimes proven below par in reality due to the uncertain nature of the conditions under which the application occurs. This led to the emergence of the field of *robust shape optimization* or *shape optimization under uncertainties* which aims to identify an optimal solution out of a range of probable conditions. This field is of particular interest in biomedical applications due to the, frequently inherent, uncertain nature of a multitude of input parameters (Marsden [2014]).

The uncertain variables can be aleatoric or epistemic (Der Kiureghian and Ditlevsen [2009]). Aleatoric uncertainties refer to the inherent stochastic nature of a system and we can therefore not intervene for their alleviation. For instance, a normal human heart rate shows complex, unpredictable fluctuations in time, which stochastic models try to capture (Kuusela et al. [2003], Amaral et al. [1999]). Epistemic uncertainties, on the other hand, are those that could essentially be reduced by more accurate computational or experimental procedures. However, resolving these uncertainties can often be impractical or even impossible. For example, the parameters involved in non-Newtonian blood models or hemolysis prediction models have been proposed from *in vitro*, i.e., under experimental conditions, studies and can hardly be acquired *in vivo*. This thesis is concerned with both aleatoric and epistemic uncertainties, with emphasis on the latter.

In order to include the uncertainties in the optimization problem, one has to first quantify them and mathematically describe them. Generally, the uncertain variables are considered to follow known statistical distributions and are described based on the mean and standard deviation, instead of a precise value. To this extent, the QoI, that in traditional shape optimization refers to a deterministic quantity, is now affected by the randomness of the uncertain variables and also acts as a statistical quantity, characterized by its statistical moments. The optimization is then usually formulated as the minimization of functionals combining these moments. The identification of the statistical moments of the QoI is referred to as Uncertainty Quantification (UQ).

The most straightforward strategies for UQ refer to Monte Carlo (MC) (Janssen [2013]) or MC-based methods (Chatterjee et al. [2019], Morokoff and Caflisch [1995]), where the simulation of an excessive number of realizations, i.e., specific outcomes of the random process, is required. When these simulations refer to costly CFD solutions, the application of such methods during a complete shape optimization procedure often becomes unfeasible, since the rate of convergence follows the inverse square root law which states that the standard error of the MC estimator decreases with the reciprocal of the square root of the sample size. Instead, MC is frequently used as a pre-/post-processing tool to evaluate the accuracy of other UQ methods that sacrifice the accuracy of their predictions for a reduction of computational cost. Such methods are based on Polynomial Chaos Expansion (PCE) (Xiu and Karniadakis [2003]) or the Method of Moments (MoM) (Putko et al. [2001]). While the cost of the former scales with the number of the uncertain variables, the computational cost of the latter depends on the efficiency of derivative computations. A comprehensive review of UQ methods in applications of fluid mechanics can be found in Walters and Huyse [2002].

The MoM is based on a Taylor series expansion of the QoI around the mean values of the uncertain variables. The expansion is truncated after the first-order term to give rise to the First-Order Second-Moment (FOSM) method or after the second-order term for the Second-Order Second-Moment (SOSM) method. The choice between FOSM or SOSM depends on the relation between the mean of the uncertain variables (input) and the QoI (output). When the relation is linear, or approximately linear, FOSM is sufficient to describe the statistical moments while falls short when the relation becomes quadratic, or higher. Regardless of first or second-order, however, both methods require the estimation of derivatives of the QoI w.r.t. the uncertain variables. Similar to the gradient-based shape optimization method involving many design variables, the adjoint method can efficiently determine the required derivatives for many uncertain variables (Kranz et al. [2023], Papadimitriou and Giannakoglou [2013]).

Another method that has recently seen appeal in shape optimization, see e.g., Geiersbach et al. [2023], due to its success in machine learning, is the stochastic gradient descent (SGD) method. The principle of the method is to replace the true gradient by an estimate, calculated from a randomly selected sample of the stochastic space. Once the stochastic gradient is estimated, the optimization process can follow similar steps to that of a deterministic gradient descent method. In this thesis, focus is given on how existing and novel SGD algorithms can be applied in the context of uncertain fluid properties during a parameter-free shape optimization.

1.2 Contributions of the Thesis

Most of the topics addressed above, have been extensively studied in the context of marine, automotive or aeronautical engineering CFD. However, a literature survey reveals that the application of these methodologies lags behind in the field of biomedical engineering, thus creating a research gap. This thesis attempts to fill this gap by advancing the methods and studying problems that can be of potential biomedical interest in applications of blood flow. Based on this, the contributions of this thesis can be broadly classified into four categories. These are:

1. adjoint hemodynamic modeling,
2. primal FSI,
3. shape update strategies and
4. robust shape optimization.

The specific contributions to each category are summarized below.

A – Adjoint hemodynamic modeling

As outlined before, a principal contribution of this thesis is the extension of the continuous adjoint method to include aspects of interest in hemodynamics. This is done by specific, elementary contributions, relating to shape optimization for the minimization of (I) hemolysis and (II) non-Newtonian blood properties, that are summarized as follows:

(I-1) In most applications presented in this thesis, hemolysis is identified as the QoI. To this extent, a suitable, prominent model able to predict hemolysis induction based on the flow field solution is identified.

(I-2) The model which is one-way coupled to the NS equations, is implemented within a finite volume flow solver. Based on the solution of the coupled system, a scalar quantity quantifying the hemolysis potential of the flow is computed and acts as an objective functional.

(I-3) Based on the hemolysis model and the devised objective functional, a continuous adjoint system is derived and implemented in a finite volume solver.

(I-4) Analytical solutions to the adjoint system are presented for a fully-developed pipe flow. Verification and validation studies are conducted to assess the accuracy of the derived sensitivity. The method is then applied to a configuration suggested by the US American Food and Drug Administration (FDA) to investigate hemolysis.

(II-1) In order to account for the non-Newtonian behavior of blood, several viscosity models are identified and implemented on the primal side of a finite volume solver.

(II-2) While adjoint shape optimization studies considering non-Newtonian blood properties already exist, see e.g., Abraham et al. [2005a,b], viscosity is considered as ‘frozen’ on the adjoint. To this end, this thesis presents the derivation of an adjoint framework, in which the consistent differentiation of the viscosity is considered. The derivation is generalized, so that different viscosity models and objective functionals can be considered.

(II-3) A novel sensitivity expression, including non-Newtonian viscosity contributions, is proposed and its accuracy is assessed against verification cases. The model is then applied on a 3D geometry of biomedical interest for the minimization of hemolysis.

Aspects relating to the contributions of (I) and (II) are also published in Bletsos et al. [2021] and Bletsos et al. [2023], respectively.

B – Primal FSI

In addition to the primary contribution of the thesis, which is the shape optimization of blood-related geometries, an investigation of the flow conditions is also of interest. To this end, this thesis contributes to the understanding of the hemodynamics in arterial bypass-graft anastomoses (the specific application is thoroughly discussed in Chapter 6) by means of FSI simulations. Related contributions to this topic are summarized as follows:

1. An efficient coupling between a finite volume fluid solver and a high-order finite element structure solver is established so that to enable the simulation of partitioned FSI simulations. The coupling is verified against literature-reported results. The procedure is implemented in a massively parallel high-performance compute system, allowing for reasonable wall-clock time of the inherently expensive FSI simulations.
2. The framework is then employed to study the hemodynamics in 3D idealized bypass-graft anastomoses. In specific, the impact of a) different upstream flow paths, b) anastomosis sizes, c) rest or exercise conditions and d) the assumption of a rigid wall on four hemodynamic QoI, is investigated.
3. The CFD-based hemolysis model is formulated in an *Arbitrary Lagrangian-Eulerian* (ALE) framework, suitable to describe the coupling between fluid and structure.
4. FSI is used as a pre/post-evaluation tool to assess the biomedical relevance of CFD-based optimized shapes.

Aspects relating to the above contributions, in particular to point (2), are also published in Bletsos et al. [2024].

C – Shape update strategies

As already mentioned in this introduction, a crucial aspect of parameter-free shape optimization approaches is the identification, or rather computation, of an appropriate descent direction. The contributions of the thesis to this topic are summarized as follows:

1. A concise presentation of various methods that identify the adjoint-based sensitivity derivative to an applicable descent direction and thus shape deformation, is given.
2. The methods are further discussed w.r.t. their application in a finite volume CFD solver. A 2D illustrative application is studied to investigate the influence of each method on the convergence history of the algorithm.
3. A strategy to address issues arising from the identification problem formulation on geometries with design and non-design boundaries is presented.

Aspects relating to the present contributions on shape update strategies can also be found in the recently published works Müller et al. [2023] and Radtke et al. [2023].

D – Robust shape optimization

Blood flow simulations and related designs encounter uncertainties stemming from various origins, either inherent to the nature of the application or related to our lack of exact modeling. Therefore, when shape optimization is of interest, robustness should be taken into account. To this end, this dissertation provides the following contributions:

1. Various algorithms, based on both the MoM and the SGD method are devised and implemented in the context of parameter-free CFD-based shape optimization.
2. A CFD-based 2D example is presented to illustrate the differences in accuracy and computational cost of the different strategies.

3. Uncertainty on the hemolysis modeling parameters as well as the non-Newtonian viscosity model parameters is assumed and the respective robust optimization problems are formulated.

4. A FOSM-based method is employed for the robust shape optimization of an idealized bypass-graft for the minimization of hemolysis against uncertain modeling parameters.

Aspects relating to the above contributions, in particular to point (4), can also be found in Bletsos et al. [2025].

1.3 Thesis Outline

This thesis is structured into seven chapters. Following this introduction, Chapter 2 outlines the necessary mathematical and numerical background for the simulation of the primal problem(s). This refers to both CFD and FSI simulations. Special focus is given on the hemolysis modeling problem as well as the non-Newtonian properties of blood. Numerical aspects related to hemolysis and non-Newtonian elements on CFD simulations are also included. Chapter 3 is devoted to the discussion of shape update strategies. Therein, a sensitivity derivative is considered as known and focus is given exclusively on the identification of an appropriate descent direction. An illustrative CFD-based example is included to enable a comparison of the available approaches w.r.t. computational efforts, mesh-quality preservation and convergence history. In Chapter 4, the adjoint method is presented. There, the extension of the classic continuous adjoint NS equations to incorporate blood-related aspects is presented. The derived expressions are assessed by means of verification studies. Chapter 5 is devoted to the topic of robust shape optimization. The optimization problem is formally stated and three methods are investigated for its solution. Therein, suitable algorithms for each method in the context of parameter-free shape optimization are presented. The methodologies described in the previous chapters are put to the test in Chapter 6. The chapter is split into two main sections, namely Section 6.1 and Section 6.2. In the former, an adjoint-based steady-state CFD shape optimization of an FDA concept geometry targeting the minimization of its hemolysis potential is realized. In the latter, the focus is given on an idealized bypass-graft. Transient FSI simulations are conducted before its shape optimization and the results are compared w.r.t. equivalent CFD simulations. The geometry is then optimized based on a steady-state robust shape optimization strategy and the produced shape is subsequently assessed through FSI simulations to address its physiological relevance. The thesis closes in Chapter 7 with a summary and conclusions as well as suggestions for future studies.

Parts of select derivations are confined to the appendix to keep the presentation of the methods concise. Throughout the dissertation, Einstein's summation convention applies for repeated lower-case Latin subscripts. Vectors and higher-order tensors are defined with reference to Cartesian coordinates.

2 Computational Modeling

This chapter introduces the basic mathematical background and numerical tools with which this thesis targets to model and simulate the primal blood flows, respectively. In all cases, the flows are considered to be internal, i.e., the fluid is completely confined by inner surfaces of a solid material except for an inlet and an outlet plane. An initial distinction made between the employed modeling approaches depends on the assumption of whether the confining material is considered as rigid or not.

When a rigid assumption is employed, the primal problem reduces, in its simplest form, to the flow of a viscous fluid governed by conservation of mass and momentum. To introduce the basic infrastructure for the solution of these conservation equations, blood is initially considered as an incompressible, Newtonian fluid and the flow as laminar. To this end, Section 2.1 is dedicated to a concise presentation of the mathematical aspects related to the aforementioned problem as well as key features of the algorithmic strategy leading to its numerical solution. Section 2.2 expands the initially posed problem to introduce hemolysis and the numerical modeling strategy followed for its prediction. In Section 2.3 the non-Newtonian rheological behaviour of blood is considered and the conservation of momentum is further enhanced with suitable viscosity models.

Section 2.4 expands the discussion by considering the surrounding material to be elastic. To this end, one assumes that the forces produced by the blood flow are sufficient to deform the structure. Therefore, the conservation laws of mass and momentum of the structure need to be considered and subsequently coupled with the conservation laws of the fluid. This constitutes the FSI problem.

2.1 Computational Fluid Dynamics

A crucial aspect of the modeling of a physical phenomenon is our viewpoint towards it. A fluid in motion can generally be described based on two points of view. On the one hand, one can observe the fluid by following an individual fluid parcel as it moves through space and time. This refers to the *Lagrangian* or material-based description. On the other hand, the *Eulerian* description focuses on fixed locations in space through which the fluid flows as time passes. It should be noted that a third viewpoint in studying the kinematics of a continuum refers to the ALE description that attempts to combine the advantages of the other two classical descriptions. This is predominately favored in the context of fluids in moving domains and will be further discussed in Section 2.4.

In fluid flows, following a parcel of matter is often rather difficult and therefore the Eulerian description is favoured. To this end, the flow is studied within a spatial region, i.e., a *control volume* (CV). However, conservation laws are generally derived by considering a given quantity of matter or *control mass* (CM), which is more suitable in the Lagrangian description. The Reynolds' Transport Theorem (RTT) provides a way to transfer the conservation laws from the Lagrangian viewpoint to the Eulerian. A detailed derivation of the equations presented in this section can be found in Bird et al. [2006]. A concise presentation of key features of this analysis in the context of CFD can also be found in Ferziger et al. [2020].

2.1.1 Conservation of Mass

Consider a fluid flow in which mass is neither created nor destroyed. This statement can be mathematically expressed as

$$\frac{\mathrm{d}}{\mathrm{d}t} \int\limits_{V_{\mathrm{CM}}} \rho \, \mathrm{d}V = 0, \tag{2.1}$$

where V_{CM} stands for the volume occupied by the CM and ρ denotes the fluid's density. Relation (2.1) implies a Lagrangian viewpoint, since the integration occurs over a volume occupied by a given quantity of matter. Applying the RTT, an Eulerian description of the conservation of mass becomes available, viz.

$$\frac{\mathrm{d}}{\mathrm{d}t} \int\limits_{V_{\mathrm{CM}}} \rho \, \mathrm{d}V = \int\limits_{\mathrm{CV}} \frac{\partial \rho}{\partial t} \, \mathrm{d}V + \int\limits_{O(\mathrm{CV})} \rho \, v_i n_i \mathrm{d}S = 0, \tag{2.2}$$

where v_i and n_i denote the fluid velocity vector and the normal to the boundary of the CV vector, respectively. Equation (2.2) assumes the CV to be fixed. The last term is called *convective term.* Since blood is modeled as incompressible, density variations in time and space are neglected. Therefore, the first term of Eq. (2.2) disappears and by applying Gauss divergence theorem on the second term, the conservation of mass can be written as

$$\int\limits_{\mathrm{CV}} \frac{\partial v_i}{\partial x_i} \, \mathrm{d}V = 0. \tag{2.3}$$

Equation (2.3) represents the conservation of mass or *continuity equation* for an incompressible fluid in an Eulerian frame of reference for a fixed CV. Allowing the control volume to become infinitesimally small leads to the strong/differential form

$$\frac{\partial v_i}{\partial x_i} = 0. \tag{2.4}$$

2.1.2 Conservation of Momentum

Newton's law of motion states that momentum changes through the action of forces and is therefore conserved over a quantity of matter. This can be stated as

$$\frac{\mathrm{d}}{\mathrm{d}t} \int\limits_{V_{\mathrm{CM}}} \rho \, v_i \, \mathrm{d}V = F_i \quad \text{for} \quad i = 1, 2, (3), \tag{2.5}$$

where F_i denotes the sum of all forces acting on the fluid parcel in the i^{th} direction. The free index i represents that momentum is conserved in each spatial direction. The range of indices is going to be omitted in what follows and it is assumed that it always corresponds to the spatial dimensionality of the investigated problem, unless stated otherwise. Similar to Section 2.1.1, applying the RTT to convert Eq. (2.5) into a relation suitable for the Eulerian frame of reference[1],

$$\int\limits_{\mathrm{CV}} \rho \frac{\partial v_i}{\partial t}\,\mathrm{d}V + \int\limits_{\mathrm{CV}} \rho\,\frac{\partial (v_i v_k)}{\partial x_k}\mathrm{d}V = F_i. \tag{2.6}$$

If the strong form of the continuity equation (2.4) is taken into account then the conservation of momentum simplifies to

$$\int\limits_{\mathrm{CV}} \rho \frac{\partial v_i}{\partial t}\,\mathrm{d}V + \int\limits_{\mathrm{CV}} \rho\, v_k \frac{\partial v_i}{\partial x_k}\mathrm{d}V = F_i. \tag{2.7}$$

In the absence of body forces, the fluid forces can be generally described by the momentum fluxes across a surface due to pressure and stresses, viz.

$$F_i = \int\limits_{O(\mathrm{CV})} (\tau_{ki} - p\delta_{ki})\, n_k\, \mathrm{d}S = \int\limits_{\mathrm{CV}} \frac{\partial}{\partial x_k}(\tau_{ki} - p\delta_{ki})\,\mathrm{d}V, \tag{2.8}$$

where τ_{ki} is the shear stress tensor and p is the static pressure. For a Newtonian fluid under the assumption of Stokes hypothesis, the shear stress tensor can be written as

$$\tau_{ki} = \mu\left(\frac{\partial v_i}{\partial x_k} + \frac{\partial v_k}{\partial x_i}\right) - \frac{2}{3}\mu\frac{\partial v_m}{\partial x_m}\delta_{ki}, \tag{2.9}$$

where μ refers to the molecular viscosity of a fluid, which is assumed to be constant in Newtonian fluids. For an incompressible fluid, the second term of Eq. (2.9) vanishes due to the continuity equation and by substituting to Eq. (2.6), the conservation of momentum for a Newtonian, incompressible fluid in laminar flows reads

$$\int\limits_{\mathrm{CV}} \left(\rho\frac{\partial v_i}{\partial t} + \rho\, v_k\frac{\partial v_i}{\partial x_k} - \frac{\partial}{\partial x_k}(2\mu S_{ik} - p\delta_{ki})\right)\mathrm{d}V = 0, \tag{2.10}$$

where $S_{ik} = 0.5\,(\partial v_i/\partial x_k + \partial v_k/\partial x_i)$ is used to denote the strain rate tensor. Within this thesis *Navier-Stokes* equations collectively refer to the momentum and continuity equations (2.3), (2.10) for an incompressible fluid. The strong/differential form of the momentum equations thus reads

$$\rho\frac{\partial v_i}{\partial t} + \rho\, v_k\frac{\partial v_i}{\partial x_k} - \frac{\partial}{\partial x_k}(2\mu S_{ik} - p\delta_{ki}) = 0. \tag{2.11}$$

2.1.3 Numerical Solution

The physical state of blood flows is given by the solution of the integro-differential equations system (2.3, 2.10). This system of equations is (in)famous for its lack of analytical solutions except for special cases or when simplifying assumptions are made. To this end, one

---

[1] This equation assumes a fixed CV, an incompressible fluid and Gauss divergence theorem applied on the convective term.

searches for a solution using numerical, iterative methods. The field of CFD has for many years flourished on its study of appropriate numerical tools for the solution of fluid dynamics problems. The target of this section is not to present a summary of the vast range of CFD methods but rather to present key features of the solution algorithm that enable a more fruitful discussion on implementation aspects of this thesis' contributions. Nevertheless, a detailed description of CFD-related numerics can be found in Ferziger et al. [2020] or Stück [2012].

Finite volume discretization

A key aspect for the numerical solution of the equations system (2.3, 2.10) is the discretization method followed. In CFD the most common strategies are the *finite element* (FE) method, see e.g., Löhner [2008] and the *finite volume* (FV) method, see e.g., Jasak [1996]. This thesis employs exclusively the latter. All applications employ meshes formed by hexahedral or quadrilateral elements or CVs to spatially discretize the fluid domain Ω. The methods presented below are general and refer to unstructured meshes. All transport quantities are stored at the control volume centers (*cell centers*) in a collocated storage arrangement. A FV method aiming at second-order spatial accuracy is considered.

Key aspects of the FV method are outlined below for the discretization of a scalar transport equation of an incompressible fluid. The analysis considers a steady-state flow, viz.

$$\int\limits_{\mathrm{CV}} \left(\rho \, v_k \frac{\partial \phi}{\partial x_k} - \frac{\partial}{\partial x_k} \left[\gamma \frac{\partial \phi}{\partial x_k} \right] - S \right) \mathrm{d}V = 0, \tag{2.12}$$

where ϕ denotes the scalar transported quantity, γ refers to the diffusion coefficient and S represents the source. Note that Eq. (2.12) consists of three distinct terms, namely the convective (first term), diffusive (second term) and source term (last term). The general goal of the discretization method is to convert the system of integro-differential equations, into a more suitable for numerical solution algebraic equation system referring to the complete fluid domain Ω as well as its boundaries $\partial\Omega \equiv \Gamma$, viz.

$$A_{ij} \tilde{\phi}_j = B_i \quad \text{for} \quad i, j = 1, 2, ..., \mathrm{N(CVs)}, \tag{2.13}$$

where $\tilde{\phi}_j$ is used to denote the discretized vector of unknowns and A_{ij}, B_i denote the coefficient matrix and the right-hand side (RHS) vector, respectively. N(CVs) refers to the total number of CVs used to discretize Ω.

To assist the notation on a discrete level, consider a CV with a center denoted as P and a neighbour with its center N, cf. Fig. 2.1. The volume occupied by each CV is denoted as V^{P} or V^{N}, respectively. The discretized transport quantities referring to the cell center are denoted by ϕ^{P} or ϕ^{N}. Equation (2.12) can be written as

$$\int\limits_{\mathrm{CV}} \rho \, v_k \frac{\partial \phi}{\partial x_k} \, \mathrm{d}V - \int\limits_{\mathrm{CV}} \frac{\partial}{\partial x_k} \left[\gamma \frac{\partial \phi}{\partial x_k} \right] \mathrm{d}V - \int\limits_{\mathrm{CV}} S \, \mathrm{d}V = 0 \tag{2.14}$$

and the discretization of each term is considered separately for the P-centered CV.

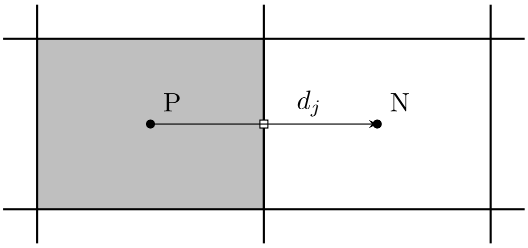

Figure 2.1: Cells with centers P and N. Distance between them denoted as d_j.

Source term

If the source term is constant, e.g., gravitational contribution, then the straightforward discretization of the source term is

$$\int\limits_{V^{\mathrm{P}}} S \,\mathrm{d}V = S^{\mathrm{P}} V^{\mathrm{P}} \tag{2.15}$$

and the above contribution can be added to the i^{th} component of the RHS vector B_i (cf. 2.13) corresponding to the CV with center P.

However, consider a source term that linearly scales with ϕ, e.g., $S = k\phi$ where k is constant. By assuming that ϕ varies linearly across the CV,

$$\int\limits_{V^{\mathrm{P}}} S \,\mathrm{d}V = k \int\limits_{V^{\mathrm{P}}} \phi \mathrm{d}V \approx k\phi^{\mathrm{P}} \int\limits_{V^{\mathrm{P}}} \mathrm{d}V + \left.\frac{\partial \phi}{\partial x_j}\right|^{\mathrm{P}} \underline{\int\limits_{V^{\mathrm{P}}} (x_j - x_j^{\mathrm{P}}) \,\mathrm{d}V} = k\phi^{\mathrm{P}} V^{\mathrm{P}}. \tag{2.16}$$

The underlined term is identically equal to zero by definition of the centroid P. The contribution $k\phi^{\mathrm{P}} V^{\mathrm{P}}$ can be added on the linear algebraic equation system (2.13) either *implicitly*, i.e., on the left-hand side (LHS) or *explicitly*, i.e., on the RHS. The decision upon implicit or explicit treatment depends on whether this contribution increases or not the diagonal dominance (this concept is further discussed on the algebraic equation system section) of A_{ij}. This decision can be made on the fly during a CFD simulation.

For higher-order source terms, e.g. $S = k\phi^2$, one can linearize the term by using the solution of a previous iteration. Then an implicit or explicit treatment can be decided upon, depending on the diagonal dominance of the coefficient matrix A_{ij}.

Convective term

The development of proper convection discretization schemes has been of great interest to the CFD community for many decades (Lien and Leschziner [1994], Harten [1983], van Leer [1974]). The treatment of the convective term begins by the application of Gauss divergence theorem, viz.

$$\int\limits_{V^{\mathrm{P}}} \rho\, v_k \frac{\partial \phi}{\partial x_k} \,\mathrm{d}V = \int\limits_{O(V^{\mathrm{P}})} \rho\, v_k n_k \phi \,\mathrm{d}S = \sum_{\mathrm{N(P)}} \int\limits_{\Delta\Gamma} \rho v_k n_k \phi \,\mathrm{d}\Gamma, \tag{2.17}$$

where the surface integral is written as the sum of all individual face integrals defining the CV. The number of terms in this sum depends on the total number of neighbouring cells to P, i.e., N(P). The area of a face is denoted as $\Delta\Gamma$. Without loss of generality, one can consider only one face and write based on the midpoint rule

$$\int\limits_{\Delta\Gamma} \rho v_k n_k \phi \, \mathrm{d}\Gamma \approx [\rho v_k n_k \Delta\Gamma]^{\mathrm{F}} \phi^{\mathrm{F}} = \dot{m}^{\mathrm{F}} \, \phi^{\mathrm{F}}, \tag{2.18}$$

where $\dot{m}^{\mathrm{F}}$ and ϕ^{F} represent the mass flow rate and sought variable computed at the face center, respectively. However, since the values are only known on the cell centers, an interpolation is needed in order to approximate the face value ϕ^{F} and the face value v_k^{F}, required for the estimation of the mass flow rate. In specific, the latter always follows from a linear interpolation of the cell-centered values of the adjacent cells. Several choices exist for the reconstruction of ϕ^{F}, e.g., the upwind scheme, the central differencing scheme, QUICK, etc. As an example, the second-order accurate central differencing scheme (CDS) is considered herein.

In a fully orthogonal mesh, the CDS approximates the face value at the face between cells P and N through a linear interpolation of the, adjacent to the face, cell center values as

$$\phi^{\mathrm{F}} \approx (1-\lambda)\phi^{\mathrm{P}} + \lambda\phi^{\mathrm{N}}, \tag{2.19}$$

with the interpolation factor

$$\lambda = \frac{(x_j^{\mathrm{F}} - x_j^{\mathrm{P}}) d_j}{d_k \, d_k}, \tag{2.20}$$

where $d_j = x_j^{\mathrm{N}} - x_j^{\mathrm{P}}$ denotes the distance between the face-adjacent CVs P and N. If the mesh is locally orthogonal and the two cell centers are equidistant to the face center connecting them then $\lambda = 0.5$. However, suppose that the cells P and N are not orthogonal to each other, i.e., the angle between d_j and n_j is not zero, as shown in Fig. 2.2 . Then a correction needs to be considered for Eq. (2.19) which reads

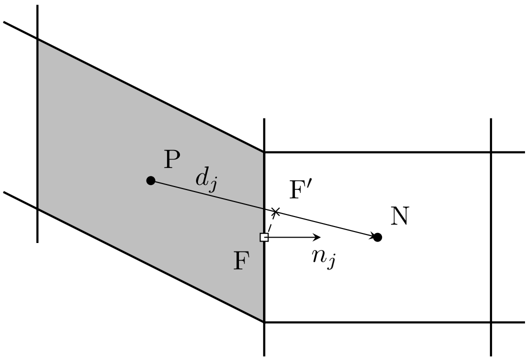

Figure 2.2: Non-orthogonal cells with centers P and N. Face center denoted by F. Face unit normal n_j.

$$\phi^{\mathrm{F}} \approx (1-\lambda)\phi^{\mathrm{P}} + \lambda\phi^{\mathrm{N}} + (x_j^{\mathrm{F}} - x_j^{\mathrm{F'}}) \frac{\partial \phi}{\partial x_j}\bigg|^{\mathrm{F'}}, \tag{2.21}$$

where the auxiliary point F′ is located at

$$x_j^{\mathrm{F}'} = x_j^{\mathrm{P}} + \lambda d_j. \tag{2.22}$$

The correction added in Eq. (2.21) is treated explicitly. The gradient at point F′ is computed based on the linear interpolation

$$\left.\frac{\partial \phi}{\partial x_j}\right|^{\mathrm{F}'} \approx (1-\lambda)\left.\frac{\partial \phi}{\partial x_j}\right|^{\mathrm{P}} + \lambda\left.\frac{\partial \phi}{\partial x_j}\right|^{\mathrm{N}}, \tag{2.23}$$

where the gradients at the cell centers are computed either based on a Gauss approach or a (weighted) Least-Squares approach. The former follows from the application of the Gauss divergence theorem on the gradient field[2] and reads

$$\int\limits_{V^{\mathrm{P}}} \frac{\partial \phi}{\partial x_j}\,\mathrm{d}V = \int\limits_{O(V^{\mathrm{P}})} \phi n_j\,\mathrm{d}S = \sum_{\mathrm{N(P)}} \int\limits_{\Delta\Gamma} \phi n_j\,\mathrm{d}\Gamma. \tag{2.24}$$

By using the midpoint rule for both the LHS and RHS of Eq. (2.24) one gets, for the discrete cell P,

$$\left.\frac{\partial \phi}{\partial x_j}\right|^{\mathrm{P}} \approx \frac{1}{V^{\mathrm{P}}} \sum_{\mathrm{N(P)}} [\phi n_j \Delta\Gamma]^{\mathrm{F}}. \tag{2.25}$$

However, Eq. (2.25) requires face values that are computed based on Eq. (2.21) that in return requires gradient information. In general, this is not a problem due to the explicit treatment of the non-orthogonality correction but for the first iteration. To counteract this problem, the Least-Squares approach can be used to approximate the gradient at the cell centers, either to complement the first iteration when Gauss approach is used or throughout the simulation. The computation of the gradient based on the Least-Squares approach is not based on face values and is instead based on a first-order Taylor series expansion that reads

$$\phi^{\mathrm{N}} \approx \phi^{\mathrm{P}} + d_j \left.\frac{\partial \phi}{\partial x_j}\right|^{\mathrm{P}} \rightarrow d_j \left.\frac{\partial \phi}{\partial x_j}\right|^{\mathrm{P}} \approx \phi^{\mathrm{N}} - \phi^{\mathrm{P}}. \tag{2.26}$$

Equation (2.26) is not only true for the neighbouring cell N but also for any neighbouring cell to P. In this sense, one can construct a linear system in the form of Eq. (2.13) where the coefficient matrix A_{ij} corresponds to the distance vector d_j for each neighbouring cell i, the unknown variable vector is $\left.\frac{\partial \phi}{\partial x_j}\right|^{\mathrm{P}}$ and the RHS is the cell center value difference between each neighbouring cell, i.e., $[\phi^{\mathrm{N}} - \phi^{\mathrm{P}}]_i$. However, A_{ij} is not necessarily square since the number of adjacent cells might exceed the spatial dimension and thus the linear system is overdetermined. The solution of the system is thus approximated and each i entry is inflicted by a numerical error. The concept of the Least-Squares approach is to minimize the sum of the errors squared. The solution of this minimization problem results

---

[2] The proof of this can be found on Appendix A.1

in

$$\left.\frac{\partial \phi}{\partial x_j}\right|^{\mathrm{P}} \approx G_{jk}^{-1} A_{ki} [\phi^{\mathrm{N}} - \phi^{\mathrm{P}}]_i \quad \text{with} \quad G_{jk} = (A_{ij})^T A_{ik} = A_{ji} A_{ik}$$
$$\text{and} \quad j,k = x,y,z \quad \text{and} \quad i = 1, \ldots, \mathrm{N(P)}. \tag{2.27}$$

However even this approach can become problematic for sub-optimal configuration of control volumes. To counteract this issue the initial problem constructed by Eq. (2.26) is weighted on both sides by the reciprocal of the magnitude of the distance of each adjacent cell. The initial problem reads

$$\frac{d_j}{\sqrt{d_k^2}} \left.\frac{\partial \phi}{\partial x_j}\right|^{\mathrm{P}} \approx \frac{1}{\sqrt{d_k^2}} \left(\phi^{\mathrm{N}} - \phi^{\mathrm{P}}\right) \tag{2.28}$$

and the same procedure as described above is followed. Note that in this case the resulting G_{jk} matrix is modified accordingly. This approach is favored when the numerical mesh includes highly skewed cells.

Diffusive term

The diffusive term is discretized by applying Gauss divergence theorem as

$$\int\limits_{V^{\mathrm{P}}} \frac{\partial}{\partial x_k} \left[\gamma \frac{\partial \phi}{\partial x_k}\right] \mathrm{d}V = \int\limits_{O(V^{\mathrm{P}})} \gamma \frac{\partial \phi}{\partial x_k} n_k \, \mathrm{d}S = \sum_{\mathrm{N(P)}} \int\limits_{\Delta\Gamma} \gamma \frac{\partial \phi}{\partial x_k} n_k \, \mathrm{d}\Gamma. \tag{2.29}$$

By consideration of one face of P and based on the midpoint rule

$$\int\limits_{\Delta\Gamma} \gamma \frac{\partial \phi}{\partial x_k} n_k \mathrm{d}\Gamma \approx \left[\gamma \frac{\partial \phi}{\partial x_k} n_k \Delta\Gamma\right]^{\mathrm{F}}. \tag{2.30}$$

The diffusivity coefficient at the face center can be linearly interpolated as in Eq. (2.19) from the adjacent to the face cell center values. For the remaining terms, the decomposition (2.31) is initially considered,

$$n_k = \xi_k + \eta_k \quad \text{with} \quad \xi_k = R \frac{d_k}{\sqrt{d_i^2}}, \tag{2.31}$$

where R is the length of the vector ξ_k which points in the direction of d_k. This decomposition is visualized for the face connecting P and N cells in Fig. 2.3.

Using the decomposed normal vector, one can write

$$\left.\frac{\partial \phi}{\partial n}\right|^{\mathrm{F}} = \left[\frac{\partial \phi}{\partial x_k} n_k\right]^{\mathrm{F}} = \left[\frac{\partial \phi}{\partial x_k} (\xi_k + \eta_k)\right]^{\mathrm{F}} = \left[\underbrace{\frac{\partial \phi}{\partial x_k} \xi_k}_{\text{implicit}} + \underbrace{\frac{\partial \phi}{\partial x_k} \eta_k}_{\text{explicit}}\right]^{\mathrm{F}}, \tag{2.32}$$

where the first and second term is handled implicitly and explicitly, respectively. The explicit face-based gradient can be computed from Eq. (2.23) based on the values of the

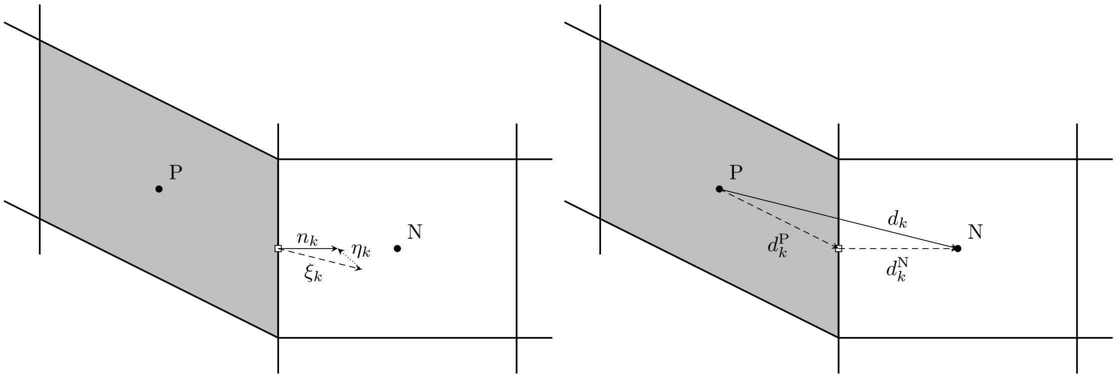

Figure 2.3: Left: Decomposition of normal vector n_k on face connecting CVs P and N. Right: Decomposition of distance vector of the two cell centers.

previous iteration while the implicit contribution can be approximated as

$$\frac{\partial \phi}{\partial x_k}\bigg|^{\mathrm{F}} \xi_k = \frac{\partial \phi}{\partial x_k}\bigg|^{\mathrm{F}} d_k R \frac{1}{\sqrt{d_i^2}} = \frac{\partial \phi}{\partial x_k}\bigg|^{\mathrm{F}} (d_k^{\mathrm{P}} + d_k^{\mathrm{N}}) R \frac{1}{\sqrt{d_i^2}}, \tag{2.33}$$

when a decomposition of vector d_k is considered as in Fig. 2.3. Then,

$$\phi^{\mathrm{N}} = \phi(x_k^{\mathrm{F}} + d_k^{\mathrm{N}}) \approx \phi(x_k^{\mathrm{F}}) + \frac{\partial \phi}{\partial x_k}\bigg|^{\mathrm{F}} d_k^{\mathrm{N}}, \tag{2.34}$$

$$\phi^{\mathrm{P}} = \phi(x_k^{\mathrm{F}} - d_k^{\mathrm{P}}) \approx \phi(x_k^{\mathrm{F}}) - \frac{\partial \phi}{\partial x_k}\bigg|^{\mathrm{F}} d_k^{\mathrm{P}} \tag{2.35}$$

and by subtracting Eq. (2.35) from (2.34),

$$\frac{\partial \phi}{\partial x_k}\bigg|^{\mathrm{F}} (d_k^{\mathrm{N}} + d_k^{\mathrm{P}}) \approx \phi^{\mathrm{N}} - \phi^{\mathrm{P}} \xrightarrow{\text{Eq. (2.33)}} \frac{\partial \phi}{\partial x_k}\bigg|^{\mathrm{F}} \xi_k \approx (\phi^{\mathrm{N}} - \phi^{\mathrm{P}}) R \frac{1}{\sqrt{d_i^2}}. \tag{2.36}$$

By substitution of Eq. (2.36) in Eq. (2.32) and by expansion of η_k based on Eq. (2.31) one gets

$$\begin{aligned} \frac{\partial \phi}{\partial n}\bigg|^{\mathrm{F}} &\approx \left[(\phi^{\mathrm{N}} - \phi^{\mathrm{P}}) R \frac{1}{\sqrt{d_i^2}} + \frac{\partial \phi}{\partial x_k} (n_k - \xi_k) \right] \\ &= \Bigg[\underbrace{(\phi^{\mathrm{N}} - \phi^{\mathrm{P}}) R \frac{1}{\sqrt{d_i^2}}}_{\text{implicit}} + \underbrace{\frac{\partial \phi}{\partial x_k}\bigg|^{\mathrm{F}} \left(n_k - R \frac{d_k}{\sqrt{d_i^2}} \right)}_{\text{explicit}} \Bigg]. \end{aligned} \tag{2.37}$$

The choice of R depends on the orientation of the normal vectors throughout the mesh. Usual choices are $R = 1$ and $R = \sqrt{d_i^2}/(d_k n_k)$, which refer to an orthogonal and an over-relaxation method, respectively. The former is predominately used, while the latter is favoured for the pressure correction equation. Note that Eq. (2.36) is only first-order accurate if d_k^{N} is not equal to d_k^{P}. Therefore, in general, this discretization approach is also first-order accurate in space.

Temporal discretization

Even though steady-state simulations are primarily considered in this work, the discussion on temporal discretization is deemed useful for the following two reasons. Firstly, it is common practice to use pseudo-unsteady simulations to converge the primal problem to a steady-state solution. This is because a time discretization increases the diagonal dominance of the assembled system. Secondly, FSI simulations, which are unsteady by construction, are considered in this thesis. To this extent, time-stepping is necessary.

Temporal discretization is relevant for applications in which the time derivative term does not vanish. This term is discretized by a first-order (in time) backward Euler method which reads

$$\int\limits_{V^{\mathrm{P}}} \frac{\partial \phi}{\partial t}\,\mathrm{d}V \approx \left.\frac{\partial \phi}{\partial t}\right|^{\mathrm{P}} V^{\mathrm{P}} = \left(\frac{\phi^{\mathrm{P},t} - \phi^{\mathrm{P},t-1}}{\Delta t} + \mathcal{O}(\Delta t)\right) V^{\mathrm{P}}, \tag{2.38}$$

where the superscripts t and $t-1$ denote that the quantities are computed on the current and previous time step, respectively. In this sense, all the remaining terms of the general transport equation are assumed to be computed in t and thus, the main diagonal of the assembled system is reinforced by the term $V^{\mathrm{P}}/\Delta t$ and an additional RHS contribution in the form of $\phi^{\mathrm{P},t-1}V^{\mathrm{P}}/\Delta t$ enters the system. In all unsteady or pseudo-unsteady applications considered in this work the time step is constant throughout the simulation. However, it must be noted that a general approach on selecting the time step refers to an adaptive strategy based on the Courant number distribution.

An additional scheme for temporal discretization is the second-order accurate in time implicit three time level (ITTL) method which reads

$$\int\limits_{V^{\mathrm{P}}} \frac{\partial \phi}{\partial t}\,\mathrm{d}V \approx \left.\frac{\partial \phi}{\partial t}\right|^{\mathrm{P}} V^{\mathrm{P}} = \left(\frac{3\phi^{\mathrm{P},t} - 4\phi^{\mathrm{P},t-1} + \phi^{\mathrm{P},t-2}}{2\Delta t} + \mathcal{O}(\Delta t^2)\right) V^{\mathrm{P}}. \tag{2.39}$$

This discretization approach is not considered in this work, and temporal accuracy is sustained by a sufficiently small time step choice.

Boundary conditions

In what concerns the applications studied in this work, the flow boundary Γ consists of three parts, namely the inlet (Γ_{in}), outlet (Γ_{out}) and wall (Γ_{w}). It also holds that $\Gamma = \Gamma_{\mathrm{in}} \cup \Gamma_{\mathrm{out}} \cup \Gamma_{\mathrm{w}}$.

Transport equations provide the physical state of the system within a domain of interest. This state, however, does not only depend on the inherent characteristics of the equations describing its physics, but most importantly, on the conditions applied to the boundaries of the investigated domain. In a sense, the physics of the numerical experiments are primarily dependant on the *boundary conditions* (BCs) which one prescribes. This being said, blood flow applications often refer to complex systems, in which a multitude of biological factors might affect the conditions which we wish to emulate. For example, the blood flow rate through a blood vessel might significantly differ when a person is exercising or resting (Wilson et al. [2005]). To this end, simulation efforts oftentimes try to approximate the physical complexity of the system by applying suitable BCs for the given problem. This is further discussed in Chapter 6.

The number of equations appearing in Eq. (2.13) are equal to the number of CVs used to discretize the domain. Therefore, BCs should not increase the number of unknowns and instead refer to the transport quantity values on faces coinciding with the boundary of the domain, i.e., ϕ^{B}. However, as shown above the discretization of the control volumes comprising the domain requires the computation of boundary fluxes in certain instances. This necessitates the appropriate handling of BCs in terms of the numerical process. Typically, BCs are of Dirichlet or Neumann type or a combination of the two, i.e. Robin conditions. Dirichlet conditions prescribe a fixed boundary value, i.e., $\phi^{\mathrm{B}} = \text{const.}$ while Neumann a fixed normal-pointing gradient, i.e. $\frac{\partial \phi}{\partial n}\Big|^{\mathrm{B}} = \text{const.}$

If one assumes that at least one of the faces of the P cell-centered CV is a boundary face, the boundary contributions to its discretized equation can generally be summarized as

$$\sum_{\mathrm{B}(V^{\mathrm{P}})} \left[\max(\dot{m}^{\mathrm{B}}, 0)\phi^{\mathrm{P}} - \max(-\dot{m}^{\mathrm{B}}, 0)\phi^{\mathrm{B}}\right] + \left[(\Delta\Gamma\gamma)^{\mathrm{B}} \frac{(\phi^{\mathrm{P}} - \phi^{\mathrm{B}})}{\sqrt{[d_j^2]^{\mathrm{B}}}}\right], \tag{2.40}$$

where $\mathrm{B}(V^{\mathrm{P}})$ is used to denote the number of boundary faces of P, and $[d_j]^{\mathrm{B}}$ refers to the distance from the cell center P to the boundary face center B. The treatment of each contribution is considered for each boundary respectively.

Inlet: On the inlet and based on the convention that the normal to a face points always outwards of a domain, $\dot{m}^{\mathrm{B}} < 0$ which means that the convective contribution reduces to

$$-\max(-\dot{m}^{\mathrm{B}}, 0)\phi^{\mathrm{B}}. \tag{2.41}$$

A Dirichlet conditions is usually applied on the inlet and therefore the convective term contributes to the RHS of the discretized P CV while the diffusive term inheres both LHS and RHS contributions.

Outlet: On the outlet, the mass flux is $\dot{m}^{\mathrm{B}} > 0$ and therefore the convective term only inheres LHS contributions. When a zero Neumann condition is applied, then one can approximate $\phi^{\mathrm{B}} = \phi^{\mathrm{P}}$ which results in a vanishing diffusive contribution.

Wall: The convective flux disappears on a wall boundary due to $\dot{m}^{\mathrm{B}} = 0$. The treatment of the diffusive term depends on the BC imposed for ϕ on the wall. Note that the treatment of no-slip walls becomes significantly more involved for turbulent flows.

Finally note that in terms of the NS equation system, setting for one boundary plane Dirichlet conditions for both velocity and pressure is not possible.

Algebraic equation system

Once the proper discretization of each term has been realized, a form of Eq. (2.13) is reached, where the free index i implies that this form corresponds to an equation system of size equal to the total number of CVs used for the spatial discretization. The equation system is always sparse and its structure differs between structured or unstructured grids. In a discrete sense, without loss of generality, the corresponding equation for the P CV can be written as

$$A^{\mathrm{P}}\phi^{\mathrm{P}} + \sum_{\mathrm{N(P)}} A^{\mathrm{N}}\phi^{\mathrm{N}} = B^{\mathrm{P}}. \tag{2.42}$$

The system of equations created by consideration of each cell is solved by an iterative method due to the (frequent) non-linearity of the non-discretized equations and also its sparsity. To this extent, certain properties need to be satisfied in order to guarantee, boundedness of the solution and convergence of the method. Boundedness of the solution implies that the computed value must lie between neighbouring values and is required to avoid oscillating unphysical solutions. This is guaranteed by demanding that for each cell $A^{\mathrm{P}} > 0$ and $A^{\mathrm{N}} < 0$ as well[3]. To guarantee convergence of a linear system, the diagonal dominance of the matrix, i.e., $|A^{\mathrm{P}}| \geq \sum\limits_{\mathrm{N(P)}} |A^{\mathrm{N}}|$, is required for each row of the assembled system. At least for one row, it should hold that the diagonal element is exclusively greater than the sum of the non-diagonal. As discussed for the discretization of each term, several methods exist, especially for the convective term, to increase the diagonal dominance of the system, usually in expense to the accuracy of the scheme. An additional strategy that helps the diagonal dominance of Eq. (2.13) is the under-relaxation of the system. In the context of an iterative process, consider $\phi^{\mathrm{P},n}$, $\phi^{\mathrm{P},o}$ and $\phi^{\mathrm{P},ur}$ which refer to the new (as computed from the assembled system (2.42)), old and under-relaxed solution and set

$$\phi^{\mathrm{P},ur} = \omega^{\phi}\phi^{\mathrm{P},n} + (1-\omega^{\phi})\phi^{\mathrm{P},o} \rightarrow \phi^{\mathrm{P},n} = \frac{1}{\omega^{\phi}}\phi^{\mathrm{P},ur} - \frac{1-\omega^{\phi}}{\omega^{\phi}}\phi^{\mathrm{P},o}, \tag{2.43}$$

where $0 < \omega^{\phi} \leq 1$ is a limiting factor. If $\phi^{\mathrm{P},n}$ from (2.43) is inserted to (2.42) one gets an implicit under-relaxed discretized system

$$\frac{A^{\mathrm{P}}}{\omega^{\phi}}\phi^{\mathrm{P},ur} + \sum_{\mathrm{N(P)}} A^{\mathrm{N}}\phi^{\mathrm{N}} = B^{\mathrm{P}} + \frac{1-\omega^{\phi}}{\omega^{\phi}}A^{\mathrm{P}}\phi^{\mathrm{P},o}. \tag{2.44}$$

The larger the value of ω^{ϕ} the faster the convergence but also the less stable the system. The solution of algebraic systems in this thesis is mostly realized with the preconditioned (bi-)conjugate gradient method (PCG/PBiCG).

Momentum discretization

Recall the conservation of the momentum equation(s) for an incompressible fluid in a steady-state flow

$$\int\limits_{\mathrm{CV}} \left(\rho\, v_k \frac{\partial v_i}{\partial x_k} - \frac{\partial}{\partial x_k}(2\mu S_{ik} - p\delta_{ki})\right) \mathrm{d}V = 0. \tag{2.45}$$

If Eq. (2.45) is further expanded, viz.

$$\underbrace{\int\limits_{\mathrm{CV}} \rho\, v_k \frac{\partial v_i}{\partial x_k}\,\mathrm{d}V}_{\text{convective term}} - \underbrace{\int\limits_{\mathrm{CV}} \frac{\partial}{\partial x_k}\left(\mu\left(\frac{\partial v_i}{\partial x_k} + \frac{\partial v_k}{\partial x_i}\right)\right)\mathrm{d}V}_{\text{diffusive term}} + \underbrace{\int\limits_{\mathrm{CV}} \frac{\partial p}{\partial x_i}\,\mathrm{d}V}_{\text{pressure term}} = 0, \tag{2.46}$$

it becomes evident that the discretization methods discussed above are suitable for application in Eq. (2.46). However, certain details regarding the momentum equation(s) need

---

[3] This applies for the convention that the algebraic equation is written as in Eq. (2.42). If a minus is considered on the LHS of the equation, then it is required that $A^{\mathrm{P}}, A^{\mathrm{N}} > 0$.

to be addressed.

The convective term is non-linear in the velocity. A Picard linearization can be used so that the mass fluxes $\dot{m}$ appearing in Eq. (2.18) are explicitly evaluated, based on Eq. (2.21), using the cell-centered values of the previous iteration. The rest can follow same strategies as the ones employed for the discretization of the convective term of the general scalar transport equation.

The diffusive term can be written as

$$\int\limits_{\mathrm{CV}} \frac{\partial}{\partial x_k}\left(\mu\left(\frac{\partial v_i}{\partial x_k}+\frac{\partial v_k}{\partial x_i}\right)\right)\mathrm{d}V=\int\limits_{\mathrm{CV}} \frac{\partial}{\partial x_k}\left(\mu\frac{\partial v_i}{\partial x_k}\right)\mathrm{d}V+\int\limits_{\mathrm{CV}} \frac{\partial}{\partial x_k}\left(\mu\frac{\partial v_k}{\partial x_i}\right)\mathrm{d}V. \tag{2.47}$$

The first term on the RHS of Eq. (2.47) can be discretized as described for the diffusive term of the scalar transport equation. The second term disappears for an incompressible, Newtonian fluid (on the converged solution), due to the continuity equation. However, instead of neglecting it, it can be treated explicitly. The Gauss divergence theorem is applied and the face-centered gradient is calculated based on an interpolation (2.23) using the cell-centered gradient values of the previous iteration.

The pressure term is treated conservatively as a face flux, viz.

$$\int\limits_{V^{\mathrm{P}}} \frac{\partial p}{\partial x_i}\,\mathrm{d}V=\int\limits_{O(V^{\mathrm{P}})} p n_i\,\mathrm{d}S=\sum_{\mathrm{N(P)}}\int\limits_{\Delta\Gamma} p n_i\,\mathrm{d}\Gamma. \tag{2.48}$$

The integral is approximated based on the midpoint rule and the face value of pressure is linearly interpolated between the neighbouring cell based on Eq. (2.21). While the discretization of the pressure term is rather obvious, its computation is not.

Pressure correction scheme

The discretized version of Eq(s). (2.45) leads to a determination of the velocity components. However, pressure is still unknown and its computation unclear. The remaining continuity equation (2.3) does not contain the pressure. Therefore, a method to determine the pressure is required. The solution to this problem is devised by a pressure correction scheme in the SIMPLE algorithm first proposed in Caretto et al. [1973], Patankar and Spalding [1972]. In all applications presented in this thesis, pressure correction is based on the SIMPLE algorithm, which is briefly outlined below.

In the context of an iterative process, consider quantities with the superscript $(.)^{\mathrm{P},n}$ and $(.)^{\mathrm{P},o}$ to refer to computed values at the current and previous iteration at the cell center P, respectively. A Picard-linearized semi-discrete form of the momentum equations reads

$$A^{\mathrm{P}} v_i^{*\mathrm{P},n}+\sum_{\mathrm{N(P)}} A^{\mathrm{N}} v_i^{*\mathrm{N},n}=-V^{\mathrm{P}}\left(\frac{\partial p}{\partial x_i}\right)^{\mathrm{P},o}+B_i^{\mathrm{P}}, \tag{2.49}$$

where v_i^* is a velocity prediction. It is assumed that B_i^{P} is independent of pressure and velocity, e.g., if it relates to gravitational contributions, and therefore a superscript denoting the iteration can be omitted. Equation (2.49) refers only to a (semi-) discretized form of the momentum equations and at this point the continuity equation is yet to be accounted for. This means that the resulting v_i^* field is not necessarily solenoidal.

Consider $v_i^{\mathrm{P},n}$ and $p^{\mathrm{P},n}$ to be the discrete values of velocity and pressure at P, so that continuity is satisfied. In this case, one can think of corrections $v_i'^{\mathrm{P},n}$ and $p'^{\mathrm{P},n}$, which if added to the computed values, one gets

$$v_i^{\mathrm{P},n} = v_i^{*\mathrm{P},n} + v_i'^{\mathrm{P},n} \quad \text{and} \quad p^{\mathrm{P},n} = p^{\mathrm{P},o} + p'^{\mathrm{P},n}. \tag{2.50}$$

Based on this, if Eq. (2.49) is subtracted from a semi-discrete form of the momentum equation for the corrected values, i.e.

$$A^{\mathrm{P}} v_i^{\mathrm{P},n} + \sum_{\mathrm{N(P)}} A^{\mathrm{N}} v_i^{\mathrm{N},n} = -V^{\mathrm{P}} \left(\frac{\partial p}{\partial x_i}\right)^{\mathrm{P},n} + B_i^{\mathrm{P}}. \tag{2.51}$$

an equation for the correction appears

$$A^{\mathrm{P}} v_i'^{\mathrm{P},n} = -\sum_{\mathrm{N(P)}} A^{\mathrm{N}} v_i'^{\mathrm{N},n} - V^{\mathrm{P}} \left(\frac{\partial p'}{\partial x_i}\right)^{\mathrm{P},n}. \tag{2.52}$$

An assumption made by SIMPLE is that the first term of the RHS of Eq. (2.52) is negligible in comparison to the gradient of the pressure correction and so

$$v_i'^{\mathrm{P},n} = -\frac{V^{\mathrm{P}}}{A^{\mathrm{P}}} \left(\frac{\partial p'}{\partial x_i}\right)^{\mathrm{P},n}. \tag{2.53}$$

Considering the continuity equation for the solenoidal field $v_i^{\mathrm{P},n}$ and expanding based on Eq. (2.50) as

$$\begin{aligned}
&\int_{V^{\mathrm{P}}} \frac{\partial v_i^{\mathrm{P},n}}{\partial x_i}\,\mathrm{d}V = \int_{V^{\mathrm{P}}} \frac{\partial v_i^{*\mathrm{P},n}}{\partial x_i}\,\mathrm{d}V + \int_{V^{\mathrm{P}}} \frac{\partial v_i'^{\mathrm{P},n}}{\partial x_i}\,\mathrm{d}V = 0.\\
\xrightarrow[\text{divergence}]{\text{Gauss}}\quad & -\sum_{\mathrm{N(P)}} \int_{\Delta\Gamma} v_i'^{\mathrm{F},n} n_i\,\mathrm{d}\Gamma = \sum_{\mathrm{N(P)}} \int_{\Delta\Gamma} v_i^{*\mathrm{F},n} n_i\,\mathrm{d}\Gamma\\
\xrightarrow{\text{Eq (2.53)}}\quad & \sum_{\mathrm{N(P)}} \int_{\Delta\Gamma} \frac{V^{\mathrm{F}}}{A^{\mathrm{F}}} \left(\frac{\partial p'}{\partial x_i}\right)^{\mathrm{F},n} n_i\,\mathrm{d}\Gamma = \sum_{\mathrm{N(P)}} \int_{\Delta\Gamma} v_i^{*\mathrm{F},n} n_i\,\mathrm{d}\Gamma.
\end{aligned} \tag{2.54}$$

Equation (2.54) can be used to assemble an algebraic equation for the pressure correction. The discretization of the pressure term can follow a similar strategy to that of the diffusive term of the scalar transport equation while the RHS term can be used as a source term based on the already computed from the momentum equations face-based volume fluxes. Note that the notation V^{F} and A^{F} implies that the values V^{P} and A^{P} need to be formulated for the faces. The latter can be interpolated based on (2.19) and the volume as

$$V^{\mathrm{F}} \approx d_j n_j \Delta\Gamma. \tag{2.55}$$

The SIMPLE algorithm can be summarized by the following steps:

1. Obtain a velocity prediction $v_i^{*\mathrm{P},n}$ based on Eq. (2.49).

2. Update the volume (and mass) fluxes based on $v_i^{*\mathrm{P},n}$ and compute a pressure correction, $p'^{\mathrm{P},n}$ based on Eq. (2.54).

3. Update the pressure based on
$$p^{\mathrm{P},n} = p^{\mathrm{P},o} + \omega^p p'^{\mathrm{P},n}, \tag{2.56}$$
where $0 < \omega^p \leq 1$ is a relaxation factor. As a golden rule, $\omega^p + \omega^v = 1$ has been shown to oftentimes be a good combination for convergence (Raithby and Schneider [1979]). Note that, in contrast to the assembled algebraic equation system for the momentum, in the case of the pressure equation, no under-relaxation is performed implicitly as described in (Eq 2.44) since this would introduce artificial compressibility to the system because the assembled equation for the pressure correction does not depend on the computed pressure correction of a previous iteration.

4. Update the velocity and fluxes based on Eq. (2.53) and (2.50). The fluxes can then be used on the next step 1 of the algorithm for the Picard-linearized discretized momentum equations for the convective term.

5. Solve any additional transport equation that depends on velocity or pressure.

6. Repeat until sufficient convergence is obtained.

Steps (1)-(5) are commonly denoted as an *outer iteration*. The iterations performed for the solution of the algebraic equation system refer to the *inner iterations*. Convergence of the outer iterations is tracked by means of residuals and the convergence criterion to be satisfied is
$$\max(r_i^v, r^p) \leq e^{\mathrm{tol}}, \tag{2.57}$$
where r_i^v and r^p refer to a normalized norm, usually the L1-norm, of the individual residuals of each CV for the momentum and pressure algebraic equations, respectively. The tolerance e^{tol} is determined by the user and for the applications studied in this thesis is usually set to the order of $\mathcal{O}(10^{-8})$.

For the CFD simulations performed in this thesis, all algebraic equation systems are preconditioned using the Jacobi preconditioner. The pressure correction equation is mainly solved using the PCG method, due to the symmetry of the coefficient matrix, while the PBiCG is used for the discretized momentum equations. The complete process is parallelizable by means of a domain decomposition approach (Yakubov et al. [2015, 2013]) where the MPI protocol is employed for data communications. All the above mentioned methodologies are encapsulated into the CFD solver FreSCo$^+$ (Rung et al. [2009]) which is used for the numerical solution of primal (and adjoint) flows in this thesis.

2.2 Hemolysis Modeling

The development of blood damage models dates back to the 60s (Blackshear et al. [1965], Rand and Burton [1963]). However, a numerical model that can sufficiently predict hemolysis in a variety of flows is yet to be established (Yu et al. [2017], Goubergrits et al. [2018]). This is due to several factors that hinder efforts towards a consensus on a general hemolysis model.

Some limitations are due to inherent experimental difficulties in studying blood in vitro conditions. On the one hand, there are several ethical limitations that restrict experiments on human blood. This results in investigations using animal blood, see e.g., Zhang et al. [2011], Heuser and Opitz [1980]. While in many cases, this approach is sufficient for the purposes of the studies, the difference in the blood rheology between different animals may change the observed phenomena. On the other hand, even for human blood, challenges on experimental setups might occur. Drawing of blood, contact with foreign surfaces, handling of blood during test preparation, can be some of these challenges since they might induce blood damage irrespective of the flow conditions which are meant to be studied (Goubergrits and Affeld [2004]).

The computational challenges in modeling of blood damage usually refer to the extensive computational resources required for an accurate resolution of the phenomena. When the RBCs are explicitly considered within the simulation, the computational cost significantly increases since all possible interactions need to be resolved. This can be done by using particle dynamics, see e.g. Yamaguchi et al. [2010], for a comprehensive review on the topic. However, such approaches are only computationally feasible on the micro-scale and can hardly describe meso- or macro-scale configurations. To this end, most frequently employed hemolysis models are typically restricted to a one-way coupling approach with a usual CFD solver, dedicated to the description of the blood flow. In such approaches, the hemolysis model receives information from the numerical solution of the NS equations with no retro-action on the employed fluid properties. These models are usually categorized as *Lagrangian* or *Eulerian* and *strain-* or *stress*-based.

Similarly to the introductory discussion of Section 2.1, a distinction between Lagrangian or Eulerian model refers to our viewpoint towards the phenomenon. In a Lagrangian model, hemolysis is studied along a pathline, or identically for a steady-state simulation along a streamline. In this case a finite number of pathlines are employed, the starting points of which are usually selected at the inlet of the domain. Due to the one-way coupling assumed for most frequently employed models, this approach can be applied as a post-processing step. Even though this is an appealing feature for most computational studies, these methods can result in highly arbitrary predictions depending on the user-defined choice of pathline starting points. Furthermore, recirculation areas, boundary layers and similar flow structures, often appearing in blood flows, are associated with high blood damage potential and may remain invisible if a pathline does not pass through them. On the other hand, Eulerian models describe the phenomenon through the use of transport equations within the same reference frame as the one employed for the CFD simulation. This is advantageous since the same methodologies described in Section 2.1 can be employed for hemolysis and the transport equation can be solved in parallel with the iterative solution of continuity and momentum equations. Due to this as well as its suitability in the formulation of a continuous adjoint model, as illustrated in Chapter 4, this thesis considers exclusively Eulerian hemolysis models. For a comparison between Eulerian and Lagrangian models see Taskin et al. [2012].

The distinction between stress- or strain-based hemolysis models is used to denote strategies in which the shear stress is modeled as the direct cause of hemolysis, i.e., a stress-based model or strategies in which hemolysis is modeled based on parameters involving, e.g., the deformation of the RBC. However, many of the strain-based models are in their essence equivalent to the stress-based ones. The difference lies in the description of an equivalent shear stress, which can then be used on a scalar transport equation. Generally, a power-law formulation relating hemolysis with a scalar representantive quantity of the shear stress, encompasses many of the available CFD-based hemolysis models. It is worth noting here that the damage of other blood components, e.g., platelet lysis, frequently follows similar power-law descriptions with different parameters. While there is no consensus on this, it highlights the benefits of a general optimization formulation based on the power-law formulation.

The target of this thesis is not to advocate a specific model over another but rather to build a generalized dual problem that can describe a variety of frequently employed hemolysis prediction models. To this extent, all hemolysis related results presented in this work should be qualitatively evaluated rather than quantitatively.

2.2.1 Power-law Model

The hemolysis prediction model considered in this thesis originates from the power-law equation, first introduced by Giersiepen et al. [1990], and reads

$$H(\bar{\tau}, t) = C\bar{\tau}^{\alpha}t^{\beta}. \tag{2.58}$$

The hemolysis index H denotes a scalar measure for the released hemoglobin to the total hemoglobin within a RBC. It refers to a stress-based model since hemolysis is directly related to a scalar stress representative, $\bar{\tau}$ and an exposure time t, which represents the duration for which the RBC is exposed to the stress. It becomes evident that the foundation of this model assumes a homogeneous stress representation. This is a strong assumption for most practical applications and hardly holds for complex cases. However, it has been shown that when relatively comparing different geometries, this model provides sufficiently reliable results (Taskin et al. [2012]).

The set of constants (C, α, β) appearing in Eq. (2.58) are introduced to fit experimental data. Several sets of these constants have been proposed by different researchers and in some cases differences of up to 1 order of magnitude can be found. Nevertheless, the relationship between hemolysis and stress as well as exposure time is non-linear with $\alpha > 1$ and $\beta < 1$. The latter implies that when an RBC is exposed to a constant shear stress $\bar{\tau}$, its hemolysis potential is decreased with time. This is biologically justifiable since an RBC leaking hemoglobin reduces in volume, which results in a decrease of the tension in which its membrane is exposed to, and due to the hardening of the membrane of an RBC when submitted to stress (Yu et al. [2017]). The parameter sets predominantly employed in this thesis are collected in Table 2.1.

The driving force of the phenomenon is assumed to be $\bar{\tau}$. In fluid flows, shear stress of a Newtonian fluid is represented by the tensor $\tau_{ij} = 2\mu S_{ij}$ and therefore a suitable metric is required to relate τ_{ij} to the scalar $\bar{\tau}$. A popular group of descriptions for the scalar

Table 2.1: Power-law hemolysis model parameters. The notation corresponds to the initials of the investigators that performed the experiments (Giersiepen et al. [1990] (GW), Heuser and Opitz [1980] (HO), Zhang et al. [2011] (ZT)). The final two columns correspond to the type of blood that was used and to the maximum stress that was applied during the experiments.

Notation	Values (C, α, β)	Type of Blood	Max. Stress (Pa)
GW	$(3.6 \cdot 10^{-7}, 2.416, 0.785)$	Human	255
HO	$(1.8 \cdot 10^{-8}, 1.991, 0.765)$	Porcine	600
ZT	$(1.2 \cdot 10^{-7}, 1.992, 0.661)$	Ovine	320

representative is based on the second invariant of the stress tensor, viz.

$$I_{\tau_2} = \frac{1}{2}\Big[\left(\mathrm{tr}(\tau_{ij})^2 - \mathrm{tr}(\tau_{ij}^2)\right)\Big]. \tag{2.59}$$

It is noted here, that $\mathrm{tr}(\tau_{ij}) \sim \partial v_i/\partial x_i$ and therefore on a converged state of an incompressible fluid, the first term on the RHS of Eq. (2.59) identically vanishes due to the continuity equation. The scalar representative of shear stress is then frequently computed as

$$\bar{\tau} = \sqrt{-kI_{\tau_2}}, \tag{2.60}$$

where k refers to a positive integer parameter. The choice of this parameter is based on the flow scenario. In the case of a one-dimensional shear flow $k = 1$ is the most appropriate choice while for $k = 3$ one gets the popular von Mises stress.

2.2.2 Eulerian Formulation

Equation (2.58) is simple in nature but not suitable for numerical implementation in a CFD framework. This is due to the non-linear dependency of the hemolysis index with time and due to the Lagrangian type of the equation, since it involves observations based on a CM rather than a CV. A solution to these issues was given by Garon and Farinas [2004]. A linearization of Eq. (2.58) w.r.t. time reads

$$H_L = H^{\frac{1}{\beta}} = C^{\frac{1}{\beta}}\bar{\tau}^{\frac{\alpha}{\beta}}t. \tag{2.61}$$

If one assumes that Eq. (2.61) holds for any experimental exposure time interval and that it describes the blood damage for any volume of CM, then one can formulate the problem in a weaker form as

$$\int\limits_{V_{\mathrm{CM}}} \left(H_L - C^{\frac{1}{\beta}}\bar{\tau}^{\frac{\alpha}{\beta}}t\right) \mathrm{d}V = 0 \rightarrow \frac{\mathrm{d}}{\mathrm{d}t}\int\limits_{V_{\mathrm{CM}}} \left(H_L - C^{\frac{1}{\beta}}\bar{\tau}^{\frac{\alpha}{\beta}}t\right) \mathrm{d}V = 0 \tag{2.62}$$

and by application of the RTT for a fixed CV based on an Eulerian viewpoint

$$\frac{\mathrm{d}}{\mathrm{d}t}\int\limits_{V_{\mathrm{CM}}}\left(H_L - C^{\frac{1}{\beta}}\bar{\tau}^{\frac{\alpha}{\beta}}t\right)\mathrm{d}V = \int\limits_{\mathrm{CV}}\left[\left(\frac{\partial H_L}{\partial t} - C^{\frac{1}{\beta}}\bar{\tau}^{\frac{\alpha}{\beta}}\right) + v_i\left(\frac{\partial H_L}{\partial x_i} - \frac{\partial(C^{\frac{1}{\beta}}\bar{\tau}^{\frac{\alpha}{\beta}}t)}{\partial x_i}\right)\right]\mathrm{d}V = 0. \tag{2.63}$$

The employed model assumes a homogeneous stress application, since the relevant experiments have been performed using a Couette viscosimeter. As already discussed this is a strong assumption to be made, however necessary if the experimentally derived set of hemolysis constant parameters are to be employed on the computational model. Therefore Eq. (2.63) simplifies to

$$\int\limits_{\mathrm{CV}}\left[\left(\frac{\partial H_L}{\partial t} - C^{\frac{1}{\beta}}\bar{\tau}^{\frac{\alpha}{\beta}}\right) + v_i\frac{\partial H_L}{\partial x_i}\right]\mathrm{d}V = 0 \qquad \text{or}$$

$$\int\limits_{\mathrm{CV}}\left[\frac{\partial H_L}{\partial t} + v_i\frac{\partial H_L}{\partial x_i}\right]\mathrm{d}V = \int\limits_{\mathrm{CV}} C^{\frac{1}{\beta}}\bar{\tau}^{\frac{\alpha}{\beta}}\,\mathrm{d}V \tag{2.64}$$

and for a steady-state case

$$\int\limits_{\mathrm{CV}} v_i\frac{\partial H_L}{\partial x_i}\,\mathrm{d}V = \int\limits_{\mathrm{CV}} C^{\frac{1}{\beta}}\bar{\tau}^{\frac{\alpha}{\beta}}\,\mathrm{d}V. \tag{2.65}$$

Equation (2.65) is now described in a suitable form for its numerical solution using the FV method described in Section 2.1.

Threshold consideration

Experimental studies indicate that hemolysis occurs above a certain level of applied stress. To account for this, several studies introduce in the hemolysis model a threshold for $\bar{\tau}$. However, in addition to the level of ambiguity in computing $\bar{\tau}$, a widely accepted threshold does not exist. Leverett et al. [1972] suggest a threshold of 150 Pa while others consider even time-dependent thresholds, see e.g., Sharp and Mohammad [1998], to account for the time-dependent response of RBCs to stress. Regardless of an accurate estimation of the threshold value, an introduction of this concept to Eq. (2.65) is frequently realized as

$$\int\limits_{\mathrm{CV}} v_i\frac{\partial H_L}{\partial x_i}\,\mathrm{d}V = \int\limits_{\mathrm{CV}} \delta C^{\frac{1}{\beta}}\bar{\tau}^{\frac{\alpha}{\beta}}\,\mathrm{d}V \quad \text{with} \quad \delta = \begin{cases} 0, & \text{if } \bar{\tau} < \bar{\tau}_t \\ 1, & \text{if } \bar{\tau} \geq \bar{\tau}_t \end{cases}, \tag{2.66}$$

where $\bar{\tau}_t$ denotes the threshold value for shear stress. The threshold introduced in Eq. (2.66) is prone to create strong discontinuities on the source term of adjacent cells. To avoid this, a threshold

$$\hat{\delta} = \begin{cases} \left(\frac{\bar{\tau}}{\bar{\tau}_t}\right)^n, & \text{if } \bar{\tau} < \bar{\tau}_t \\ 1, & \text{if } \bar{\tau} \geq \bar{\tau}_t \end{cases}, \tag{2.67}$$

where n is a positive integer, can also be considered. This threshold allows for a smoother transition between adjacent cells, considering that the distribution of $\bar{\tau}$ is also smooth by construction.

Source term modification

The scalar hemolysis index H is bounded, by virtue of its definition, as $0 \leq H \leq 1$ and therefore so is its linearized version, i.e., $0 \leq H_L \leq 1$. However, the RHS of Eq. (2.65) is not bounded and can therefore result in unphysical values of H_L larger than 1. A solution to that is given by multiplying the source term by $(1 - H_L)$, as suggested by Lacasse et al. [2007],

$$\int\limits_{\mathrm{CV}} v_i \frac{\partial H_L}{\partial x_i} \,\mathrm{d}V = \int\limits_{\mathrm{CV}} C^{\frac{1}{\beta}} \bar{\tau}^{\frac{\alpha}{\beta}} (1 - H_L) \,\mathrm{d}V. \tag{2.68}$$

This modification of the RHS also holds physical meaning as it ensures that the hemolysis induction reduces with time, for an unsteady simulation. This is true due to the response of RBCs to stress as discussed above.

2.2.3 Numerical Aspects

Equation (2.65) refers to the transport of the scalar hemolysis index H_L through a fixed domain. With reference to Eq. (2.12), the hemolysis equation involves only a convective and a source term. This means that if $\phi = H_L$, $S = C^{\frac{1}{\beta}} \bar{\tau}^{\frac{\alpha}{\beta}}$ and the diffusive term is dropped, then the discretization strategies presented in Section 2.1.3 can be followed.

The one-way coupling of the hemolysis model with the NS equations allow also for an algorithmic decoupling. The solution of the flow field can precede the hemolysis equation. Once the converged solution is obtained, the velocity field can be used as input for the solution of the hemolysis equation. This feature of the algorithm is significantly advantageous in studies targeting exclusively on the hemolysis model. For example, consider a case in which interest is given on the response of the model for different hemolysis modeling parameters. The costly NS solution can then be computed only once and act as the basis for multiple (fast) numerical evaluations of the hemolysis equation. The benefits of this strategy will be further highlighted in Chapter 5.

Boundary conditions

In all applications it is assumed that blood entering the fluid domain Ω is undamaged and therefore the Dirichlet condition $H_L = 0$ is set on (Γ_{in}). In the remaining boundary patches, a zero Neumann boundary condition is set, i.e., $\partial H_L / \partial n = 0$ is set.

2.2.4 Objective Functional

In order to evaluate the extent to which the flow has damaged the blood, a scalar quantity is sought. A usual strategy is to collect the hemolysis field variables, i.e., $H = H_L^{\beta}$, on the outlet of the domain as a mass flow average, viz.

$$\mathrm{HI} = \frac{\int\limits_{\Gamma_{\mathrm{out}}} H_L^{\beta} \rho v_i n_i \,\mathrm{d}S}{\int\limits_{\Gamma_{\mathrm{out}}} \rho v_i n_i \,\mathrm{d}S}. \tag{2.69}$$

Note that the denominator of Eq. (2.69) is constant in steady flows of incompressible flows. The numerator can therefore be used as an appropriate metric for the development of an optimization method targeting its minimization.

The numerical computation of HI is based on the midpoint rule, viz.

$$\mathrm{HI} = \frac{\int\limits_{\Gamma_{\text{out}}} H_L^{\beta} \rho v_i n_i \, \mathrm{d}S}{\int\limits_{\Gamma_{\text{out}}} \rho v_i n_i \, \mathrm{d}S} = \frac{\sum\limits_{\mathrm{F}(\Gamma_{\text{out}})} \int\limits_{\Delta\Gamma} H_L^{\beta} \rho v_i n_i \, \mathrm{d}\Gamma}{\sum\limits_{\mathrm{F}(\Gamma_{\text{out}})} \int\limits_{\Delta\Gamma} \rho v_i n_i \, \mathrm{d}\Gamma} \approx \frac{\sum\limits_{\mathrm{F}(\Gamma_{\text{out}})} \left[\dot{m} H_L^{\beta}\right]^{\mathrm{F}}}{\sum\limits_{\mathrm{F}(\Gamma_{\text{out}})} \left[\dot{m}\right]^{\mathrm{F}}}, \tag{2.70}$$

where $\mathrm{F}(\Gamma_{\text{out}})$ denotes the number of computational faces used to discretize the outlet boundary patch. This metric is computed once after the convergence of the NS and hemolysis equations.

2.2.5 Verification Studies

Regardless of the accuracy of a hemolysis model in predicting the damage induced during a blood flow, a crucial aspect is the verification of the numerical implementation. As outlined by AIAA [1998] in the guide for the verification and validation of CFD simulations, the former refers to the process of determining that the implementation accurately represents the developer's conceptual description of the model while the latter targets to determine the degree to which a model is accurately representing reality. To this extent and with the growing interest of the biomedical community in hemolysis modeling, the FDA proposes several benchmark cases with which such verification studies can be conducted (Hariharan et al. [2015]).

Verification studies optimally compare the numerical solution with analytical solutions. To this end, the benchmark problems considered in Hariharan et al. [2015], are accompanied with analytical solutions, the derivation of which is briefly outlined below (however, some derivations presented herein are novel to the best of my knowledge). Since the hemolysis model also involves the velocity field, the benchmark problems considered, correspond to cases where the NS equations can be analytically solved. These refer to a fully developed Hagen-Poiseuille pipe flow and a Couette flow.

Hagen-Poiseuille pipe flow

This benchmark problem refers to a fully developed three-dimensional (3D) pipe flow, which is sketched in Fig. 2.4. In this case and by considering that the coordinate origin coincides with the center of the inlet cross-section, the velocity vector reduces to $v_i = (0, 0, v_z(r))$ with

$$v_z(r) = V_{\max} \left(1 - \left(\frac{r}{R}\right)^2\right) \tag{2.71}$$

and the only component of the shear stress tensor that doesn't vanish is

$$\tau^*(r) = \mu \frac{\partial v_z(r)}{\partial r} = -2\mu V_{\max} \frac{r}{R^2}. \tag{2.72}$$

In the context of hemolysis modeling, a scalar representative of the shear stress tensor is required, which usually follows from Eq. (2.60). To be consistent with the flow conditions, the metric needs to reduce to the expression given by Eq. (2.72). By considering the continuity equation and expanding Eq. (2.60), one gets

$$\begin{aligned}\bar{\tau} &= \sqrt{-kI_{\tau_2}} = \sqrt{k\frac{1}{2}\mathrm{tr}(\tau_{ij}^2)} = \sqrt{2k\mu^2\mathrm{tr}(S_{ik}S_{kj})}\\ &= \sqrt{2k\mu^2\frac{1}{2}\left(\frac{\partial v_z(r)}{\partial r}\right)^2} = \sqrt{k}\mu\frac{\partial v_z(r)}{\partial r} \qquad (2.73)\end{aligned}$$

and thus, $k = 1$ is chosen to ensure consistency with the Hagen-Poiseuille results (2.72). Based on the velocity profile, the strong form of the Eulerian formulation of the power-law hemolysis model reduces to

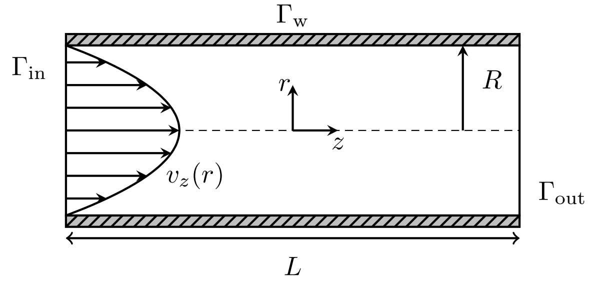

Figure 2.4: Sketch of the fully-developed 3D laminar pipe flow.

$$v_z(r)\frac{\partial H_L}{\partial z} = C^{\frac{1}{\beta}}\bar{\tau}^{\frac{\alpha}{\beta}} \rightarrow H_L = \frac{C^{\frac{1}{\beta}}\bar{\tau}^{\frac{\alpha}{\beta}}}{v_z(r)}z + C_0 \quad \text{in } \Omega. \qquad (2.74)$$

By considering that $H_L = H^{\frac{1}{\beta}}$ and assuming that blood enters the computational domain undamaged, the analytical solution for the hemolysis field reads

$$H = \frac{C\bar{\tau}^{\alpha}}{v_z^{\beta}(r)}z^{\beta} \quad \text{in } \Omega, \qquad (2.75)$$

and with that, the objective function (2.69) results in

$$\mathrm{HI} = \Lambda\sum_{k=0}^{\infty}\frac{\Gamma(2-\beta)}{\Gamma(k+1)\Gamma(2-\beta-k)}\frac{(-1)^k}{(a+2+2k)}, \qquad (2.76)$$

with $\Lambda = 4CL^{\beta}V_{\max}^{(\alpha-\beta)}(2\mu/R)^{\alpha}$ and Γ denoting the gamma function. The derivation of expression (2.76) can be found in Appendix A.2. The infinite series is numerically approximated and converges for $k > 100$ based on the constant parameters considered in this benchmark case.

The geometric parameters are set to $L = 0.5$ m and $R = 2$ mm. The fluid properties are set to $\mu = 3.5$ mPa $\cdot$ s and $\rho = 1056$ kg/m^3 to emulate blood. The maximum velocity is set to $V_{\max} = 1.24$ m/s so that a Reynolds number Re$= 2\,\rho V_{\max}R/\mu = 1500$ is attained and laminar conditions are guaranteed.

Two three-dimensional computational meshes are employed for this verification study, as shown in Fig. 2.5. The coarser one employs approximately 650k CVs while the denser one 900k. The two grids are essentially distinguished based on their refinement near the pipe wall. In terms of the specific numerics, the convective term of the momentum and hemolysis equations are discretized based on the QUICK method.

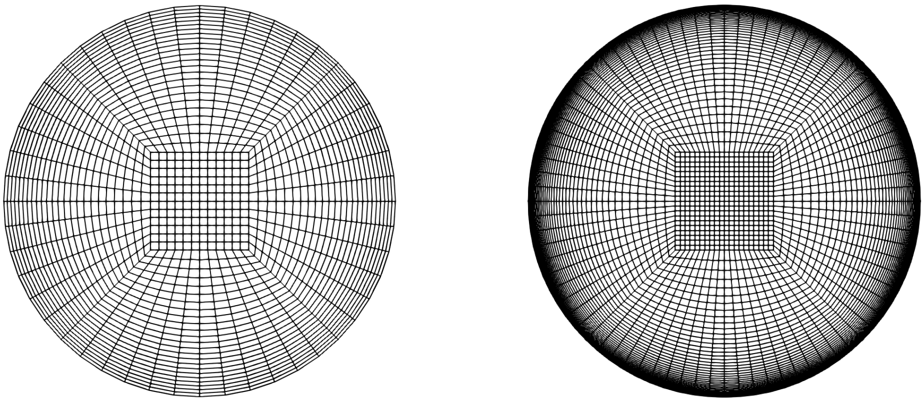

Figure 2.5: Cross-section of the pipe mesh based on (left) refinement 1 (Ref. 1) and (right) refinement 2 (Ref. 2).

Figure 2.6 compares the computed hemolysis solution (using the mesh Ref. 2) against the analytical values, as computed by Eq. (2.75), for three longitudinal positions, namely $z = 0.2L, 0.4L, 0.6L$. The comparison is realized for all three sets of hemolysis model parameters (cf. Table 2.1). As can be seen, all computed values are fitting the analytical solutions to a satisfying degree.

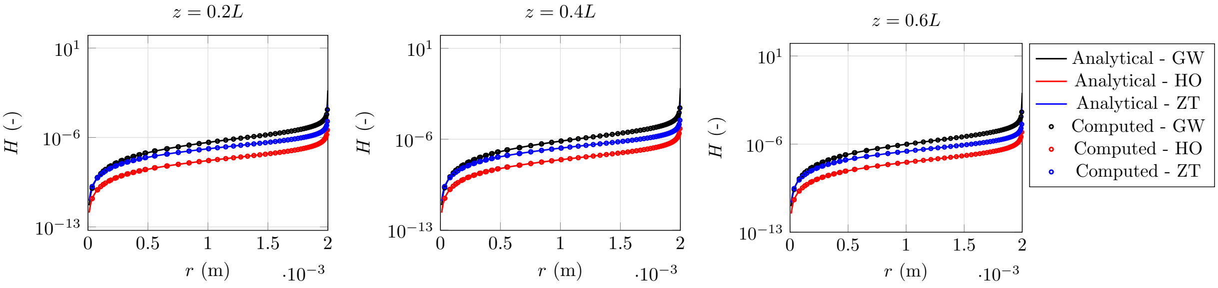

Figure 2.6: Hemolysis profiles at three distinct longitudinal positions of the pipe flow. Continuous lines correspond to analytical solutions while points indicate computed values. Vertical axis in logarithmic scale.

In addition to the hemolysis field comparisons, Table 2.2 compares the computed value of HI with the analytical solution. The comparison considers the computed values from both employed meshes. It is shown that the error significantly decreases when the finer mesh is used. This is due to the refinement near the walls. As shown in Fig. 2.6, the larger values of hemolysis are encountered in the boundary layer region, near the pipe wall. This highlights the necessity of a near-wall refinement, even in fully laminar cases, so that this section is properly resolved.

Table 2.2: Comparison of computed HI based on Eq. (2.70) and analytical based on (2.76) for different sets of hemolysis parameters (cf. Table 2.1). The computed value of both employed meshes is presented and distinguished as Ref. 1 and Ref. 2 in accordance to Fig. 2.5.

Parameter Set	Analytical	Computed	Error (%)
GW	$4.07 \cdot 10^{-6}$	Ref. 1: $3.93 \cdot 10^{-6}$	-3.43
		Ref. 2: $3.99 \cdot 10^{-6}$	-1.96
HO	$1.22 \cdot 10^{-7}$	Ref. 1: $1.18 \cdot 10^{-7}$	-3.23
		Ref. 2: $1.20 \cdot 10^{-7}$	-1.63
ZT	$7.88 \cdot 10^{-7}$	Ref. 1: $7.67 \cdot 10^{-7}$	-2.66
		Ref. 2: $7.76 \cdot 10^{-7}$	-1.52

Couette flow

The second benchmark case refers to a two-dimensional (2D) Couette flow, as sketched in Fig. 2.7. The velocity field is then given by

$$v_z(y) = V_{\mathrm{w}}(1 - \frac{y}{D}) \tag{2.77}$$

and the shear stress tensor reduces to the scalar constant expression of

$$\tau' = \mu \frac{V_{\mathrm{w}}}{D}. \tag{2.78}$$

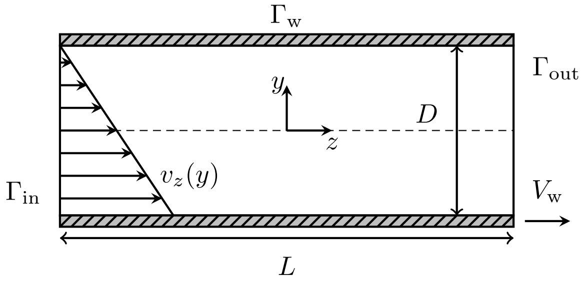

Figure 2.7: Sketch of the 2D Couette flow.

The analytical hemolysis field solution is equivalently given by Eq. (2.75) and the objective function results in

$$\mathrm{HI} = \frac{2L^{\beta}\mu^{\alpha}CV_{\mathrm{w}}^{(\alpha-\beta)}}{(2-\beta)D^{\alpha}}. \tag{2.79}$$

The derivation of this expression is trivial and is therefore omitted.

The case is set up using $L = 0.5$ m and $D = 2$ mm. The fluid properties are the same as the ones used for the pipe flow while a wall velocity $V_{\mathrm{w}} = 2.48$ m/s is employed to assure a Reynolds number Re$= \rho V_{\mathrm{w}} D/\mu = 1500$. The domain is discretized using 40k CVs with a progressive refinement near the walls.

Figure 2.8 shows the computed hemolysis solution against the analytical values. As shown, an excellent agreement is observed for all three longitudinal positions and hemolysis parameter sets studied. This is further verified by the computed objective functional value which amounts exactly to the analytical solution as shown in Table 2.3.

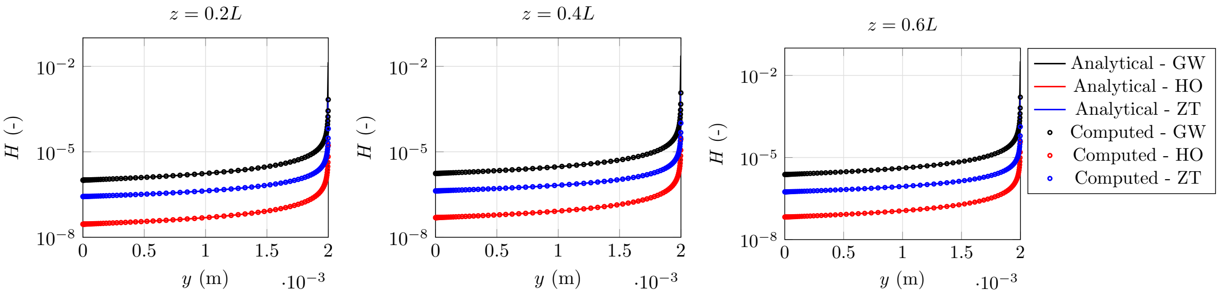

Figure 2.8: Hemolysis profiles at three distinct longitudinal positions of the Couette flow. Continuous lines correspond to analytical solutions while points indicate computed values. Vertical axis in logarithmic scale.

Table 2.3: Comparison of computed HI based on Eq. (2.70) and analytical based on (2.79) for different sets of hemolysis parameters.

Parameter Set	Analytical	Computed	Error (%)
GW	$5.87 \cdot 10^{-6}$	$5.87 \cdot 10^{-6}$	0
HO	$1.60 \cdot 10^{-7}$	$1.60 \cdot 10^{-7}$	0
ZT	$1.16 \cdot 10^{-6}$	$1.16 \cdot 10^{-6}$	0

In view of the satisfactory agreement between computed and analytical results for both benchmark cases studied, the implementation of the hemolysis model in the FV software, is considered verified.

2.3 Non-Newtonian Properties

Blood consists of four main components: blood plasma, RBCs (also known as erythrocrytes), white blood cells (leukocytes) and platelets (thrombocytes). The last three are suspended into the plasma that acts as the carrier fluid. The plasma and the RBCs amount to approximately 99% of blood. Therefore, hemodynamics are in large governed by the fluid properties of plasma and the interaction and concentration of RBCs. However and in the extent to which blood is treated as a continuous fluid medium, the discrete description of RBCs is omitted and instead fluid properties try to account for this omission. To a certain extent this is achieved by considering blood to be a non-Newtonian fluid. Several experimental studies (Brooks et al. [1970], Chien et al. [1966], Cokelet [1963]) have verified the non-Newtonian nature of blood which is mainly attributed to the RBCs.

Newtonian and non-Newtonian fluids differ on how they describe the relationship between shear stress and the magnitude of the strain rate tensor. For brevity reason, the (scalar) magnitude of the strain rate tensor is referred to as shear rate ($\dot{\gamma}$) and is not to be confused with the strain rate tensor. For a Newtonian fluid the relationship is linear and the constant ratio between shear stress and shear rate refers to the (apparent) viscosity of the fluid. In contrast to this, non-Newtonian fluids generally exhibit a non-linear dependency between shear rate and shear stress and the viscosity is thus modeled as a function of the former. The shear rate is frequently modeled as the second invariant of the strain rate tensor S_{ij}, viz.

$$\dot{\gamma} = \sqrt{2S_{ij}S_{ij}}. \tag{2.80}$$

In case of non-Newtonian fluids the apparent viscosity of the fluid is hereafter denoted as $\tilde{\mu} := \tilde{\mu}(\dot{\gamma})$. Generally, non-Newtonian models are distinguished based on the following categories:

Dilatant or shear-thickening fluids. In these fluids the viscosity increases with the shear rate and the shear rate-stress curve is convex. A well-known shear-thickening fluid is the Oobleck, a suspension of cornstarch and water. In general the viscosity of a shear-thickening fluid can be described as

$$\tilde{\mu} = k\dot{\gamma}^{n-1} \quad \text{with } n > 1. \tag{2.81}$$

Pseudoplastic or shear-thinning fluids. The viscosity decreases with the increase of shear rate and the shear rate-stress curve is concave. An example of such a fluid is quicksand, which when undisturbed it appears as a solid (i.e., high viscosity) but a slight change in the stress causes a sudden decrease of viscosity and thus appears to liquefy. The viscosity of such fluids can be described as

$$\tilde{\mu} = k\dot{\gamma}^{n-1} \quad \text{with } n < 1. \tag{2.82}$$

Bingham plastic fluids. In these fluids no deformation is observed below a threshold stress value (yield stress). For stresses larger than the yield stress, the relationship between shear rate-stress is linear. An example of this type of fluids is toothpaste.

A schematic illustration of the dependency of the shear rate-stress for the different non-Newtonian fluids is presented in Fig. 2.9.

For the sake of completeness, it is worth mentioning some additional categories often encountered in literature, such as the *plastic fluid* in which the thinning effects are much

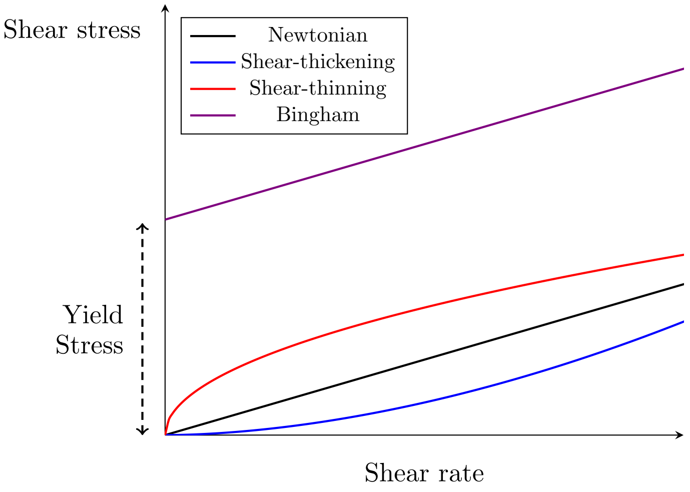

Figure 2.9: Shear stress against shear rate diagram for different non-Newtonian fluids.

stronger than in the case of the *pseudoplastic fluids*. In this case, the convexity of the curve presented in Fig. 2.9 is the same as with the shear-thinning fluid but the curve is significantly steeper. Furthermore, the above mentioned models relate shear stress exclusively with strain-rate and viscoelastic effects are neglected. These usually refer to time-dependant deformations such as *creep* or *stress relaxation*.

Experimental studies indicate that blood exhibits a shear-thinning as well as a nonlinear viscoelastic behavior. The latter is sparsely considered in employed models – see however Yeleswarapu [1996] for such a case – due to the complexity that it presents in computational studies. In contrast, several models have been proposed to model the shear-thinning nature of blood, which is experimentally justified by the *Rouleaux* formation phenomenon. When the shear rates are low, RBCs aggregate into the Rouleaux formation, a formation resembling a stacking of coins. When the aggregation grows so does the viscosity. When the shear rates are sufficiently high the RBCs disaggregate and remain present as individual corpuscles that are deformed by shearing. This results in a decrease of apparent viscosity (Baskurt et al. [2011]).

This thesis considers three frequently employed non-Newtonian models to describe the shear-thinning nature of blood. These are:

1. Power-law (see, e.g., Shibeshi and Collins [2005]):

$$\tilde{\mu} = k\dot{\gamma}^{n-1} \quad \text{with } n < 1. \tag{2.83}$$

This model accurately represents the conceptual description of a shear-thinning fluid as introduced above. However, an inherent problem of this model is that for $\dot{\gamma} \to 0$, $\tilde{\mu} \to \infty$ and that for large enough shear rates the model rapidly diverges from an experimentally observed Newtonian viscosity. Therefore, in this thesis the model is employed as

$$\tilde{\mu} = \begin{cases} \mu_0, & \text{if } \dot{\gamma} \leq \dot{\gamma}^{\mathrm{LT}} \\ k\dot{\gamma}^{n-1}, & \text{if } \dot{\gamma}^{\mathrm{UT}} \leq \dot{\gamma} \leq \dot{\gamma}^{\mathrm{LT}} \\ \mu_\infty, & \text{if } \dot{\gamma} \geq \dot{\gamma}^{\mathrm{UT}} \end{cases} \quad \text{with } n < 1, \tag{2.84}$$

where $\dot{\gamma}^{\mathrm{UT}}$ and $\dot{\gamma}^{\mathrm{LT}}$ denote an upper and a lower threshold for the shear rate, respectively. The values of these thresholds are implicitly determined based on the prescribed μ_0 and μ_∞. That is, $\dot{\gamma}^{\mathrm{LT}} = (\mu_0/k)^{1/(n-1)}$ and $\dot{\gamma}^{\mathrm{UT}} = (\mu_\infty/k)^{1/(n-1)}$.

2. Casson law (see, e.g., Blair [1959]):

$$\sqrt{\tau} = \sqrt{\tau_0} + \sqrt{\mu_c \dot{\gamma}}. \tag{2.85}$$

Equation (2.85) while shear-thinning in nature, it incorporates characteristics of a Bingham fluid as it relates a scalar representative of the shear stress, i.e., τ, with a yield stress τ_0 and the Casson viscosity μ_c. An apparent viscosity can be defined based on Eq. (2.85) which reads

$$\tilde{\mu} = \left(\sqrt{\mu_c} + \frac{\sqrt{\tau_0}}{\sqrt{\dot{\gamma}}} \right)^2 . \tag{2.86}$$

However, similarly to the drawback of the original Power-law equation, Eq. (2.86) results in viscosity tending to infinity for shear rate values tending to zero. To avoid this shortcoming, in this thesis a modified version of the Casson law is employed which reads,

$$\tilde{\mu} = \left(\sqrt{\mu_c} + \frac{\sqrt{\tau_0}}{\sqrt{\lambda} + \sqrt{\dot{\gamma}}} \right)^2 , \tag{2.87}$$

introducing a regularization constant λ as suggested by González and Moraga [2005].

3. Carreau law (see, e.g., Johnston et al. [2004], Cho [1991]):

$$\tilde{\mu} = \left(\mu_\infty + (\mu_0 - \mu_\infty) \left(1 + (\lambda \dot{\gamma})^2 \right)^{\frac{n-1}{2}} \right) . \tag{2.88}$$

The parameters μ_0 and μ_∞ are sometimes considered as a function of the RBC concentration of blood (Quarteroni et al. [2000]). However, such a property is not considered herein since it would essentially require a coupling between the viscosity and hemolysis models. Such a coupling is not yet established and therefore similar considerations are omitted. Having said that, the physiological correlation between hematocrit (i.e., the percentage by volume of RBCs in blood) and viscosity should not be undermined (see e.g., Kishimoto et al. [2020]). To this extent, a hemolysis model coupled with a viscosity model is of high importance even though significantly difficult to construct for reasons outlined in Section 2.2.

The above models along with the parameter values employed in this thesis, unless stated otherwise, are collected in Table 2.4. The parameters appearing for each model are extracted from Shibeshi and Collins [2005] (PL), González and Moraga [2005] (MC) and Johnston et al. [2004] (C). Note that certain parameters are slightly modified so that all models converge to the Newtonian viscosity for high shear rates. Figure 2.10 shows the apparent viscosity of each investigated model w.r.t. the shear rate.

Several other models have been proposed in literature to account for the non-Newtonian properties of blood, see e.g., Yeleswarapu [1996]. Nevertheless and to the extent that a proposed model relates the apparent viscosity exclusively to shear rate, i.e., $\tilde{\mu} := \tilde{\mu}(\dot{\gamma})$, it can be incorporated to a consistent adjoint model, as shown in Chapter 4 .

Table 2.4: Constitutive models for the description of apparent viscosity. Models denoted by (N), (PL), (MC) and (C) correspond to the Newtonian, Power-law, modified-Casson and Carreau models, respectively.

Model	$\tilde{\mu}$	List of constants	Units
(N)	μ	$\mu = 3.5$	$(\mathrm{mPa \cdot s})$
(PL)	Eq. (2.84)	$(k,\, n,\, \mu_0,\, \mu_\infty) = (17, 0.708, 50, 3.5)$	$(\mathrm{mPa \cdot s}^n, -, \mathrm{mPa \cdot s}, \mathrm{mPa \cdot s})$
(MC)	Eq. (2.87)	$(\tau_0,\, \lambda,\, \mu_c) = (21, 11.5, 3.5)$	$(\mathrm{mPa}, \mathrm{s}^{-1}, \mathrm{mPa \cdot s})$
(C)	Eq. (2.88)	$(\lambda,\, n,\, \mu_0,\, \mu_\infty) = (3.313, 0.357, 56, 3.5)$	$(\mathrm{s}, -, \mathrm{mPa \cdot s}, \mathrm{mPa \cdot s})$

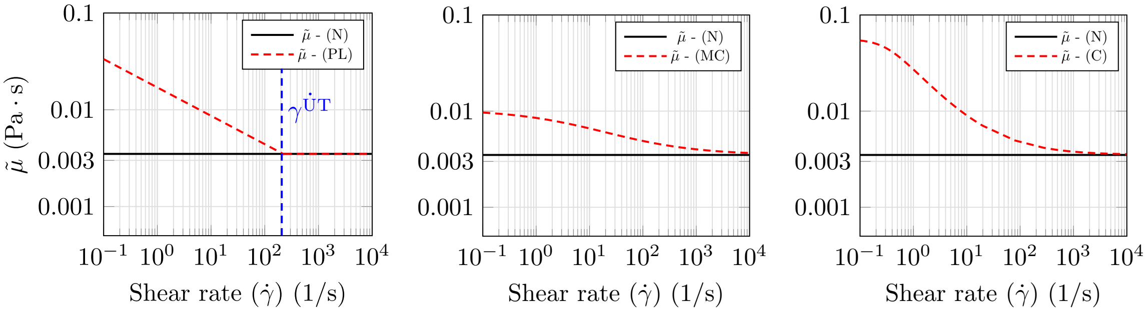

Figure 2.10: Apparent viscosity for (left) Power-law, (middle) modified-Casson and (right) Carreau viscosity models. The Newtonian viscosity is included in black [continuous] line. Axes in logarithmic scale.

Furthermore, it must be noted that it is generally accepted that for high shear rates (the exact number is ambiguous but a general consensus of $\dot{\gamma} > 100\,\mathrm{s}^{-1}$ (Berger and Jou [2000], Pedley [1980]) exists) blood behaves as a Newtonian fluid. Therefore, in several applications presented in this thesis, this assumption is going to be employed if deemed sufficient to describe the rheology of blood.

2.3.1 Numerical Aspects

Each of the aforementioned viscosity models describe the apparent viscosity as a non-linear function of the strain rate tensor and introduce an additional non-linearity to the momentum equations. This issue is resolved by an iterative strategy, where the apparent viscosity is evaluated at each CV based on the velocity of the previous iteration. The face-based value required then for the discretization of the diffusive term is computed based on a linear interpolation, as in Eq. (2.19). The non-Newtonian equations considered in this work are algebraic in nature and therefore require no BCs or initial conditions. However, since many quantities of interest require the viscosity on the boundaries, the values of viscosity are extrapolated there based on a zero-order extrapolation from the nearest cell.

2.3.2 Verification Studies

The verification studies conducted in this section refer exclusively to a 3D fully-developed pipe flow, as sketched in Fig. 2.4. For this reason, the same geometric parameters as the ones employed in Section 2.2.5 as well as the same discretized domain, employing 900k

CVs, are used. The verification is conducted by means of velocity profile comparisons. The analytical solution of the velocity profile for a Newtonian fluid is repeated here and reads

$$v_z(r) = V_{\max}\left(1-\left(\frac{r}{R}\right)^2\right) = \frac{|c|R^2}{4\mu}\left(1-\left(\frac{r}{R}\right)^2\right), \tag{2.89}$$

where the maximum velocity $V_{\max}$ has been substituted by $|c|R^2/(4\mu)$ where c is used to denote a constant pressure gradient, i.e., $\partial p/\partial z = c$, characterizing the flow. This is done so to avoid prescribing a velocity profile on the inlet of the domain and instead enables a consideration of fixed pressure boundaries for both the inlet and outlet. Based on the geometric parameters discussed in Section 2.2.5, $c = 1000$ is set to ensure laminar conditions for the range of investigated non-Newtonian parameters. The velocity profiles are therefore exclusively an outcome of the simulation and the comparisons conducted herein can serve as a valid measure for verification.

For this benchmark case, the velocity profile for a Power-law fluid reads

$$v_z^{\mathrm{PL}}(r) = \frac{nR}{n+1}\left(\frac{|c|R}{2k}\right)^{\frac{1}{n}}\left[1-\left(\frac{r}{R}\right)^{\frac{1}{n}+1}\right], \tag{2.90}$$

where n, k refer to the Power-law constant parameters. The derivation of (2.90) is trivial and can be found in many standard textbooks, e.g., Irgens [2014].

In addition to the velocity profiles, a comparison can be made between the analytically computed volume fluxes which read

$$Q^{\mathrm{N}} = \int\limits_{\Gamma} v_z(r)\,\mathrm{d}S = \frac{1}{2}\pi V_{\max}R^2 = \frac{\pi R^4}{8\mu}|c|, \tag{2.91}$$

$$Q^{\mathrm{PL}} = \int\limits_{\Gamma} v_z^{\mathrm{PL}}(r)\,\mathrm{d}S = \left(\frac{|c|R}{2k}\right)^{\frac{1}{n}}\frac{n}{1+3n}\pi R^3, \tag{2.92}$$

for a Newtonian and a Power-law fluid, respectively. Figure 2.11 compares the analytically derived velocity profiles with the computed ones. Note that for $n = 1$ the Power-law model reduces to the Newtonian model with a viscosity $\mu = k$. In all cases an excellent agreement is shown between computed and analytical values. The comparison between the computed volume flux and the analytical one for different sets of (k, n) is shown in Table 2.5. The computed values do not exceed an error of 1%.

Table 2.5: Comparison of computed volume flux and analytical based on (2.92) for different sets of (k, n) parameters.

Parameter k (mPa $\cdot$ s^n)	Parameter n (-)	Analytical (m^3/s)	Computed (m^3/s)	Error (%)
10	0.8	$4.44 \cdot 10^{-6}$	$4.43 \cdot 10^{-6}$	-0.22
	1	$1.25 \cdot 10^{-6}$	$1.25 \cdot 10^{-6}$	0
	1.2	$5.42 \cdot 10^{-7}$	$5.43 \cdot 10^{-7}$	0.18
20	0.8	$1.87 \cdot 10^{-6}$	$1.86 \cdot 10^{-6}$	-0.53
	1	$6.28 \cdot 10^{-7}$	$6.28 \cdot 10^{-7}$	0
	1.2	$3.04 \cdot 10^{-7}$	$3.05 \cdot 10^{-7}$	0.32

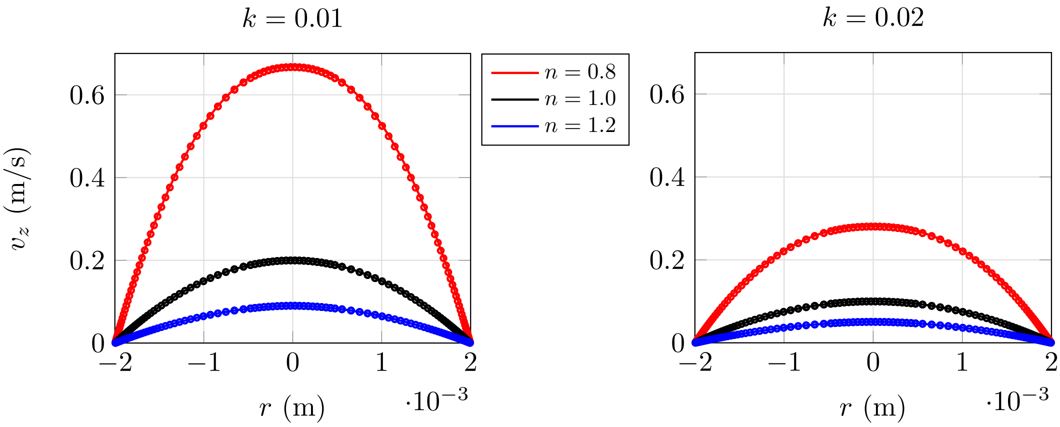

Figure 2.11: Velocity profiles of a Power-law fluid for (left) $k = 0.01$ and (right) $k = 0.02$ and different n values. Continuous lines display the analytical solution, given by Eq. (2.90), points display the computed values.

Even though the verification studies included herein consider only a Power-law fluid model, the algorithmic implementation of all viscosity models is exactly the same. Therefore, verifying the implementation of one model implies the verification of the rest.

2.4 Fluid-Structure Interaction

In what is covered so far in this chapter, the walls surrounding the blood flow are assumed to be rigid. This essentially means that regardless of the forces produced by the flow (or any external forces) the walls are bound to their initial position. This assumption is indeed sufficient for a certain range of hemodynamic applications, e.g., extravascular machinery, but falls short in a range of intravascular applications. To this end, a computational method able to account for the mechanical interdependence between fluid and structure, i.e., fluid-structure interaction, is crucial. Note that in the case of blood flow in the cardiovascular system, blood does not only mechanically interact with the vascular tissue but also biochemically. Computational modeling of such interactions have been previously investigated in literature through the addition of advection-diffusion equations describing the concentration of substances soluted in blood, see e.g., Rappitsch and Perktold [1996], but are not considered herein.

The ever-growing advances in computational resources have resulted in an increasing interest in FSI problems of several engineering fields, such as the aeronautical (Cavagna et al. [2007], Farhat et al. [2006]), marine (Radtke et al. [2021], Lee et al. [2014]), wind energy (Bazilevs et al. [2015], Hsu and Bazilevs [2012]), automotive (Broniszewski and Piechna [2019], Shangguan and Zhen-Hua Lu [2004]) and biomedical (Radtke et al. [2016], Bazilevs et al. [2010]). While the application changes from field to field, a common ground for all is the solution approach followed to tackle the FSI problem, which can be either monolithic or partitioned.

The FSI problem is constructed by the conservation laws of mass and momentum of both the fluid and the structure. In monolithic approaches, these equations are solved as a whole, usually using the same numerical method and discretized domain which also implies the same dependent variables. In contrast, a partitioned approach considers the subproblems separately. The interaction is then realized by a communication of the necessary quantities between the common interface boundaries of the fluid and structural domains. This thesis exclusively considers partitioned FSI approaches. This section is not meant to provide an in depth explanation of the many features involved in FSI simulations or structural mechanics. Instead, it targets to provide a necessary background for a more involved discussion on the application. For an in depth explanation of FSI solution approaches (with a special interest on cardiovascular applications) see Radtke [2020], Bazilevs et al. [2013]. A comprehensive discussion on the high-order FE method, employed in this thesis for the discretization of the structural problem, can be found in Düster et al. [2017].

For each subproblem, the governing equations are formulated with a different viewpoint. To this extent, a brief description of each subproblem is presented below.

2.4.1 Structure Subproblem

The structure subproblem follows a Lagrangian viewpoint. Consider Ω_0^{s} to be the undeformed reference domain of a structure and let Ω_t^{s}, $t \in (0, T)$ be the current configuration, where it is assumed $\Omega_0^{\mathrm{s}} = \Omega_{t=0}^{\mathrm{s}}$. To distinguish between the coordinates of the reference and current configuration consider X_I and x_i, respectively. Note that a capital index is used for the former to indicate a possible change of the coordinate basis, e.g., from a Cartesian to a curvilinear coordinate system. However, in all FSI applications studied in this thesis, a Cartesian coordinate is preserved for both reference and current domains and therefore capital indices are dropped in what follows. The two domains are related through the displacement vector $d_i^\mathrm{s}(X_i, t)$ which allows the mapping

$$x_i = X_i + d_i^\mathrm{s}, \tag{2.93}$$

as shown in Fig. 2.12.

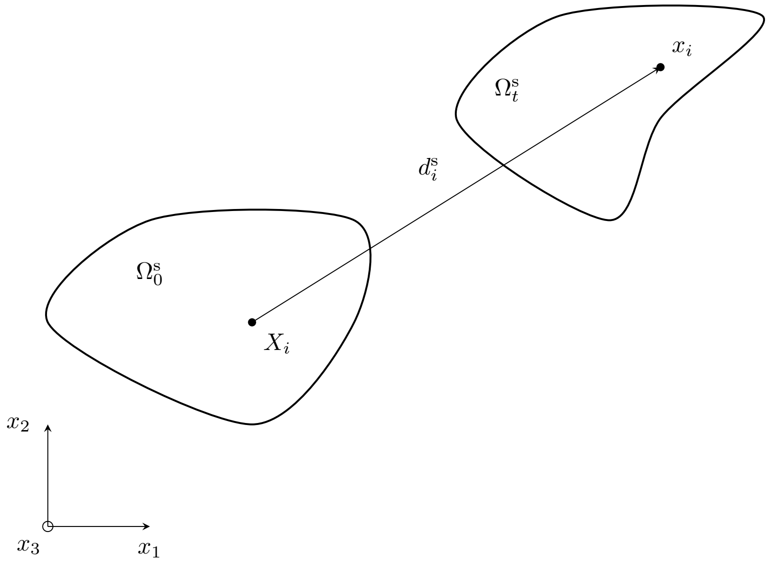

Figure 2.12: Sketch of reference and current domains.

A deformation gradient F_{ij} can then be written as

$$F_{ij} = \frac{\partial x_i}{\partial X_j} = \delta_{ij} + \frac{\partial d_i^\mathrm{s}}{\partial X_j} \tag{2.94}$$

and its determinant as

$$J = \det(F_{ij}), \tag{2.95}$$

which allows us to express the volume change from an element of the reference domain $\mathrm{d}\Omega_0^\mathrm{s}$ to an element of the current $\mathrm{d}\Omega_t^\mathrm{s}$ based on

$$\mathrm{d}\Omega_t^\mathrm{s} = J\mathrm{d}\Omega_0^\mathrm{s}. \tag{2.96}$$

Furthermore, the Green-Lagrange strain tensor E_{kl} is defined as

$$E_{kl} = \frac{1}{2}\left(F_{ik}F_{il} - \delta_{kl}\right), \tag{2.97}$$

which is completely defined in Ω_0^s since the first indices of the deformation gradient, which refer to the coordinates of the current domain, contract. Based on these definitions one can consider the conservation laws of the structure from a Lagrangian viewpoint.

Conservation of mass

Similar to a control mass consideration of the fluid, the conservation of mass for a structure reads

$$\frac{\mathrm{d}}{\mathrm{d}t}\int\limits_{\Omega_t^{\mathrm{s}}} \rho_t^s \,\mathrm{d}V = \int\limits_{\Omega_0^{\mathrm{s}}} \frac{\mathrm{d}(J\rho_t^s)}{\mathrm{d}t}\,\mathrm{d}V = 0, \tag{2.98}$$

where ρ_t^{s} refers to the density of the current configuration and Eq. (2.96) was applied to transfer from the current to the reference domain. Equation (2.98) implies for a material point that

$$\rho_0^{\mathrm{s}} = J\rho_t^{\mathrm{s}}, \tag{2.99}$$

where ρ_0^{s} denotes the known density in the undeformed configuration. Equation (2.99) can be used to calculate the density at a material point in the current configuration. In what follows, the index t is dropped from the structural density and unless specified, it always refers to the density of the current configuration.

Conservation of momentum

Once again following the same conceptual road as the one followed for the fluid, Newton's law of motion for the structure can be written as

$$\frac{\mathrm{d}}{\mathrm{d}t}\int\limits_{\Omega_t^{\mathrm{s}}} \rho^{\mathrm{s}}\dot{d}_i^{\mathrm{s}}\,\mathrm{d}V = F_i, \tag{2.100}$$

where $\dot{d}_i^{\mathrm{s}}$ is used to denote the first temporal derivative of the displacement vector and F_i denotes the sum of all forces acting on the arbitrarily defined material volume Ω_t^{s} in the i^{th} direction. The latter can be written through the use of the symmetric Cauchy stress tensor σ_{ij} as

$$F_i = \int\limits_{\Omega_t^{\mathrm{s}}} \left(\frac{\partial}{\partial x_j}(\sigma_{ij}) + \rho^{\mathrm{s}} b_i\right)\mathrm{d}V, \tag{2.101}$$

where b_i denotes a source term in the form of external volume forces. If Eq. (2.101) is substituted in Eq. (2.100) and both LHS and RHS are pulled back to the reference domain

$$\begin{aligned}
&\int\limits_{\Omega_0^{\mathrm{s}}} \frac{\mathrm{d}}{\mathrm{d}t}\left(J\rho^{\mathrm{s}}\dot{d}_i^{\mathrm{s}}\right)\mathrm{d}V = \int\limits_{\Omega_0^{\mathrm{s}}} J\left(\frac{\partial}{\partial x_j}(\sigma_{ij}) + \rho^{\mathrm{s}} b_i\right)\mathrm{d}V,\\
&\int\limits_{\Omega_0^{\mathrm{s}}} \rho_0^{\mathrm{s}}\ddot{d}_i^{\mathrm{s}}\,\mathrm{d}V = \int\limits_{\Omega_0^{\mathrm{s}}} \left[\frac{\partial}{\partial X_k}\left(J\frac{\partial X_k}{\partial x_j}\sigma_{ij}\right) + \rho_0^{\mathrm{s}} b_i\right]\mathrm{d}V,\\
&\int\limits_{\Omega_0^{\mathrm{s}}} \left[\rho_0^{\mathrm{s}}\ddot{d}_i^{\mathrm{s}} - \frac{\partial}{\partial X_k}\left(J\frac{\partial X_k}{\partial x_j}\sigma_{ij}\right) - \rho_0^{\mathrm{s}} b_i\right]\mathrm{d}V = 0.
\end{aligned} \tag{2.102}$$

Considering the first Piola-Kirchhoff stress tensor

$$P_{ik} = J\frac{\partial X_k}{\partial x_j}\sigma_{ij}, \tag{2.103}$$

the linear momentum equations for the structure can be written in strong form (neglecting the necessary BCs and initial conditions) as

$$\rho_0^{\mathrm{s}}\left(\ddot{d}_i^{\mathrm{s}} - b_i\right) - \frac{\partial}{\partial X_k}(P_{ik}) = 0 \quad \text{in} \quad \Omega_0^{\mathrm{s}}, \tag{2.104}$$

from which the unknown variable d_i^{s} can be computed.

A weak form of Eq. (2.104) reads

$$\int\limits_{\Omega_0^{\mathrm{s}}} \rho_0^{\mathrm{s}} \delta d_i^{\mathrm{s}} \ddot{d}_i^{\mathrm{s}} \, \mathrm{d}V + \int\limits_{\Omega_0^{\mathrm{s}}} \delta E_{ij} S_{ij}^{\mathrm{s}} \, \mathrm{d}V = \int\limits_{\Omega_0^{\mathrm{s}}} \rho_0^{\mathrm{s}} \delta d_i^{\mathrm{s}} b_i \, \mathrm{d}V + \int\limits_{\Gamma_0^{\mathrm{s}}} \delta d_i^{\mathrm{s}} t_i \, \mathrm{d}S, \tag{2.105}$$

where δd_i^{s} is introduced as a test function, δE_{ij} is the variation of the Green-Lagrange strain, $S_{ij}^{\mathrm{s}} = (\partial X_i / \partial x_k) P_{kj}$ is the second Piola-Kirchhoff stress tensor and $t_i = F_{ij} S_{jk}^{\mathrm{s}} N_k$ with N_k being the normal vector to the boundary of the reference domain Γ_0^{s}. In this work, hyperelastic constitutive equations are used to describe the material. Based on this, the second Piola-Kirchhoff stress tensor can be written as

$$S_{ij}^{\mathrm{s}} = \frac{\partial W}{\partial E_{ij}}, \tag{2.106}$$

where W is the *strain energy density function* (SEDF) and is defined differently depending on the material model employed. This will be given separately for each application so that to close the structure subproblem. The weak form is then discretized using high-order finite elements which yields a system of nonlinear ordinary differential equations. This procedure is realized through the use of the high-order FE code *AdhoC* (Düster and Kollmannsberger [2010]). For further details on the numerics of the FE method, see Szabo and Babuska [1991].

2.4.2 Fluid Subproblem

In the previous sections of this chapter relating to fluid dynamics, all equations are considered based on an Eulerian viewpoint and defined on non-moving domains. In the context of FSI this is not sufficient since the walls confining the blood flow are allowed to move based on the forces exerted to them. To this end, an ALE viewpoint is followed to arrive at the fluid equations of state for an FSI simulation. Based on an ALE description of motion, neither a material-fixed configuration (Lagrangian) nor a fixed spatial configuration (Eulerian) are taken as the reference. Instead, a third domain is introduced, i.e., the referential domain, the coordinates of which identify the grid points. A mapping of the referential domain to the spatial domain reveals the motion of the grid points in the spatial domain and suggests a mesh velocity, $\tilde{v}_i$. Further details on the concept of ALE can be found in (Donea et al. [2004]).

The conservation equations based on an ALE description are derived by a proper application of the Leibniz's rule in 3D domains. For a scalar quantity ϕ this can be written in an integral form over an arbitrary volume Ω_t whose boundary moves with the mesh velocity $\tilde{v}_i$ as

$$\frac{\mathrm{d}}{\mathrm{d}t}\int\limits_{\Omega_t}\phi\,\mathrm{d}\Omega+\int\limits_{O(\Omega_t)}\phi(v_i-\tilde{v}_i)n_i\,\mathrm{d}S=S^{\phi}, \tag{2.107}$$

where the RHS refers to source terms. If $\tilde{v}_i = 0$ the Eulerian description is recovered while if $\tilde{v}_i = v_i$ one gets the Lagrangian description. Now if ϕ is substituted by ρ, ρv_1, ρv_2, ρv_3 and H_L one arrives at the ALE equations of state.

Collectively, the governing equations of the (incompressible) fluid subproblem are written in a strong form (without the BCs) as

$$\frac{\partial v_i}{\partial x_i}=0 \qquad \text{in } \Omega_t^{\mathrm{f}}, \tag{2.108}$$

$$\frac{\partial v_i}{\partial t}+(v_j-\tilde{v}_j)\frac{\partial v_i}{\partial x_j}-\frac{1}{\rho^{\mathrm{f}}}\frac{\partial}{\partial x_j}\left(2\mu^{\mathrm{f}}S_{ij}-p\delta_{ij}\right)=0 \quad \text{in } \Omega_t^{\mathrm{f}} \tag{2.109}$$

$$\frac{\partial H_L}{\partial t}+(v_j-\tilde{v}_j)\frac{\partial H_L}{\partial x_j}-C^{\frac{1}{\beta}}\bar{\tau}^{\frac{\alpha}{\beta}}=0 \qquad \text{in } \Omega_t^{\mathrm{f}}, \tag{2.110}$$

where the quantities ρ^{f}, μ^{f} and Ω_t^{f} have been introduced to denote the fluid density, viscosity and domain in the context of FSI. As shown, the ALE formulation of the governing equations is very similar to the one of the Eulerian with the exception of an additional contribution introduced on the convective terms which accounts for the movement of the mesh.

An inspection of Eq. (2.108), i.e., the continuity equation for an incompressible fluid in ALE, with regards to the integral formulation of Eq. (2.107) reveals a missing piece in the rational followed up to this point. Consider the conservation of mass based on Eq. (2.107), then in the absence of mass sources and for constant density,

$$\frac{\mathrm{d}}{\mathrm{d}t}\int\limits_{\Omega_t}\mathrm{d}\Omega+\int\limits_{O(\Omega_t)}(v_i-\tilde{v}_i)n_i\,\mathrm{d}S=0. \tag{2.111}$$

This reveals that the conservation is more involved than it appears to be in its differential form. However, one must consider that space is also conserved and therefore enforce the *space conservation law* (SCL) (Demirdžić and Perić [1988]) which reads

$$\frac{\mathrm{d}}{\mathrm{d}t}\int\limits_{\Omega_t}\mathrm{d}\Omega-\int\limits_{O(\Omega_t)}\tilde{v}_i n_i\,\mathrm{d}S=0. \tag{2.112}$$

By substitution of Eq. (2.112) to Eq. (2.111) one arrives at

$$\int\limits_{O(\Omega_t)}v_i n_i\,\mathrm{d}S=\int\limits_{\Omega_t}\frac{\partial v_i}{\partial x_i}\,\mathrm{d}V=0. \tag{2.113}$$

Numerical aspects

Treatment of the SCL:

In essence the numerical process for the solution of the fluid subproblem differs to what is described in Section 2.1 only due to the consideration of the SCL. If one considers an exemplary implicit backward Euler discretization method for the temporal derivative and the midpoint rule for the surface integral, the SCL (2.112) for the P-centered CV reads

$$\frac{V^{\mathrm{P},t} - V^{\mathrm{P},t-1}}{\Delta t} = \sum_{\mathrm{N(P)}} [\tilde{v}_i n_i]^{\mathrm{F},t}. \tag{2.114}$$

The difference between CV volumes at consecutive time levels can be expressed as the sum of the swept volumes by each CV face (δV^{F}) when moving from the old to the new position. This is illustrated for a 2D example in Fig. 2.13. Equation (2.114) can thus be written as

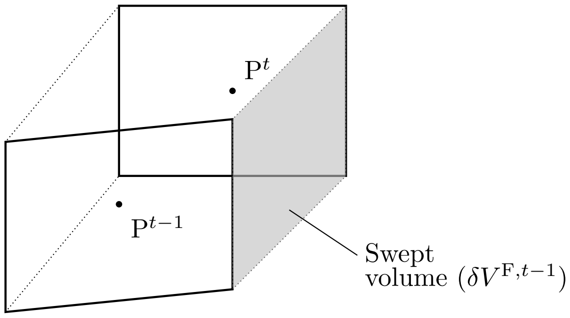

Figure 2.13: The two-dimensional P-centered CV at time instances t and $t-1$. In light gray the volume swept by one cell face.

$$\frac{1}{\Delta t} \sum_{\mathrm{N(P)}} \delta V^{\mathrm{F},t-1} = \sum_{\mathrm{N(P)}} [\tilde{v}_i n_i]^{\mathrm{F},t}. \tag{2.115}$$

A possible solution of Eq. (2.115) is given by assuming that each term of the sums on the LHS and RHS is equal. This results into an update of the volume (or mass if both sides are multiplied by the constant density) fluxes through each face, viz.

$$\dot{m'}^{\mathrm{F,t}} = \frac{\rho^{\mathrm{f}}}{\Delta t} \delta V^{\mathrm{F},t-1}. \tag{2.116}$$

Therefore, if the displacement of the mesh is known to the solver, there is no need to explicitly define the velocity $\tilde{v}_i$ but instead the flux corrections can be computed based on the swept volume of each face. Note that the computation in 3D is relatively involved and requires triangulation of the swept areas. In addition, if the second-order accurate in time ITTL method is considered for the discretization of the temporal term in Eq. (2.112) then the mass flux correction reads

$$\dot{m'}^{\mathrm{F,t}} = \frac{\rho^{\mathrm{f}}}{2\Delta t} (3\delta V^{\mathrm{F},t-1} - \delta V^{\mathrm{F},t-2}). \tag{2.117}$$

Note that Eq. (2.117) is not used for the results shown in this work.

In terms of the SIMPLE algorithm, the mass flux at each face, computed as described in Section 2.1, is updated by subtracting the contribution (2.116) in each time iteration. Note that the correction only relates to the previous time step(s) and therefore it can be done once per time step.

Mesh update:

It is easy to conceptualize that the numerical coupling between a structural and a fluid solver is meant to provide displacements exclusively at the interacting boundary of the two domains. If these displacements are applied to the boundary faces and the internal faces remain unmoved then it is (more than) probable that the boundary faces will collide with the internal ones and the numerical process will terminate. It is therefore necessary that a rule is devised so that the internal mesh is moved in accordance to the boundary movement. In the context of FSI simulations this is done exclusively by the solution of the Laplace problem, viz.

$$\begin{aligned} \frac{\partial}{\partial x_k}(\mu^{\mathrm{w}}\frac{\partial d_i^{\mathrm{f}}}{\partial x_k}) &= 0 \quad \text{in } \Omega_t^{\mathrm{f}} \\ d_i^{\mathrm{f}} &= d_i^{\mathrm{s}} \quad \text{on } \Gamma_t^{\mathrm{FSI}} \\ d_i^{\mathrm{f}} &= 0 \quad \text{on } \Gamma_t^{\mathrm{f}} \setminus \Gamma_t^{\mathrm{FSI}}, \end{aligned} \tag{2.118}$$

where $\partial\Omega_t^{\mathrm{f}} = \Gamma_t^{\mathrm{f}}$ and $\Gamma_t^{\mathrm{FSI}} \subset \Gamma_{\mathrm{w}}^{\mathrm{f}}$ denotes the interface between the structure and fluid domains. The vector d_i^{f} is introduced to denote the displacements of the fluid mesh and can only be logically perceived in its discrete counterpart, while d_i^{s} corresponds to the solution of the structure subproblem on Γ_t^{FSI}. The diffusivity coefficient μ^{w} corresponds to the reciprocal of the distance from the nearest wall boundary.

Equation (2.118) is discretized and assembled based on the FV techniques discussed for a diffusive term. Therefore, the discrete values d_i^{f} refer to cell/face-centered values. This implies that a) d_i^{s} needs to be provided by the FE solver at the position of the centers of the faces comprising Γ_t^{FSI} and b) an update of the nodes of each CV is necessary. The former is realized by the finite element shape functions. The latter uses an inverse distance weighting, also known as Shepard's interpolation (Shepard [1968]). That is, once the d_i^{f} cell-centered displacements are known, the displacement vector at a node is computed as

$$d_i^{\mathrm{f,node}} = \frac{1}{N^{\mathrm{n}}} \sum_{k=1}^{N^{\mathrm{n}}} d_i^{\mathrm{f},k} \left(1 - \frac{\|x_j^{\mathrm{f,node}} - x_j^{\mathrm{f},k}\|_2}{\sum\limits_{m=1}^{N^{\mathrm{n}}} \|x_j^{\mathrm{f,node}} - x_j^{\mathrm{f},m}\|_2} \right), \tag{2.119}$$

where $d_i^{\mathrm{f,node}}$ denotes the computed displacement of a node with N^{n} adjacent cells. To assist the notation, $d_i^{\mathrm{f},k}$ was introduced to denote the k^{th} adjacent to the node cell-centered displacement as computed from Eq. (2.118) while $x_j^{\mathrm{f,node}}$ and $x_j^{\mathrm{f},k/m}$ denote the Cartesian coordinates of the node and $k^{\mathrm{th}}/m^{\mathrm{th}}$ cell-center, respectively. The symbol $\|.\|_2$ refers to the Euclidean norm. To assist comprehension in view of the admittedly tedious notation of Eq. (2.119), Fig. 2.14 is presented.

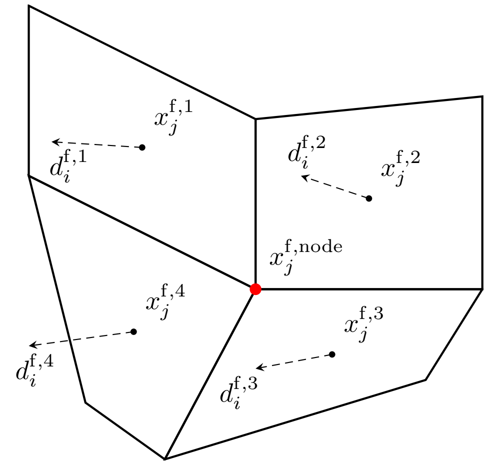

Figure 2.14: A node surrounded by $N^{\mathrm{n}} = 4$ CVs. Dashed arrows represent the cell-centered, computed from Eq. (2.118), displacements $d_i^{\mathrm{f},1,..,4}$.

2.4.3 Partitioned Solution Approach

In addition to the BCs required for each subproblem, the FSI problem demands that the following coupling conditions are fulfilled on the coupling interface Γ_t^{FSI},

$$v_i = \tilde{v}_i = \dot{d}_i^{\mathrm{s}} \qquad \text{on } \Gamma_t^{\mathrm{FSI}} \tag{2.120}$$

$$t_i = -\left(2\mu^{\mathrm{f}} S_{ij} - p\delta_{ij}\right) n_j \qquad \text{on } \Gamma_t^{\mathrm{FSI}}. \tag{2.121}$$

Equations (2.120) and (2.121) are enforced through the partitioned solution scheme, which considers the individual field solvers as black boxes. In specific, Eq. (2.120) refers to the transmission of information from the solid to the fluid while Eq. (2.121) from the fluid to the solid. This is illustrated by an operator formulation, where

$$D_{ji}^t = \mathcal{S}(T_{ki}^t) \quad \text{for } j = 1, ..., \mathrm{N}^{\mathrm{fc}} \quad \text{and } k = 1, ..., \mathrm{N}^{\mathrm{qp}} \tag{2.122}$$

denotes the solution at the time step t of the structure subproblem, which yields D_{ji}^t given the tractions T_{ki}^t. The former represents a matrix of N^{fc} rows where each row contains the displacement vector d_i^{s} computed at one discrete face center of Γ_t^{FSI}, where N^{fc} is used to denote the total number of discrete fluid faces on the interface. Equivalently, T_{ki}^t contains at each row the traction vector t_i for one quadrature point discretizing the structure domain, where N^{qp} is used to denote the total number of discrete structure elements on the interface. Similarly one can write

$$T_{ki}^t = \mathcal{F}(D_{ji}^t) \quad \text{for } j = 1, ..., \mathrm{N}^{\mathrm{fc}} \quad \text{and } k = 1, ..., \mathrm{N}^{\mathrm{qp}}, \tag{2.123}$$

to represent the fluid subproblem solution. In a coupled problem it must hold

$$D_{ji}^t = \mathcal{S}(\mathcal{F}(D_{ji}^t)) \quad \text{and} \quad T_{ki}^t = \mathcal{F}(\mathcal{S}(T_{ki}^t)). \tag{2.124}$$

A solution to these fixed-point equations can be found using an accelerated fixed-point iteration with the following three steps:

$$\begin{aligned} T_{ki}^{t,l} &= \mathcal{F}(D_{ji}^{t,l-1}) && \text{1. call fluid solver} \\ \tilde{D}_{ji}^{t,l} &= \mathcal{S}(T_{ki}^{t,l}) && \text{2. call structure solver} \\ D_{ji}^{t,l} &= \mathcal{A}(\tilde{D}_{ji}^{t,l}) && \text{3. accelerate convergence} \end{aligned}$$

where l is used to indicate the coupling iteration and $\tilde{D}_{ji}^{t,l}$ is used to denote an intermediate solution of the structure solver. The acceleration operator $\mathcal{A}$ introduced as a third step of the algorithmic process might refer to a wide variety of choices. In this work the Quasi-Newton least squares (QNLS) method is used to accelerate the convergence (Degroote et al. [2009, 2010]). The iterative solution of the FSI problem is realized with the use of the coupling tool *comana* (König et al. [2016]).

2.4.4 Benchmark Problem

Even though both the structure solver (AdhoC) and the fluid solver (FreSCo$^+$) have been extensively and individually tested in their respective regime of application, their coupling needs to be evaluated. To this end, this section targets to perform such an evaluation by simulating the well-known 2D lid-driven cavity flow benchmark problem. A sketch of the problem is shown in Fig. 2.15 (left). The computational grid for the fluid subproblem, which is shown in a deformed state in Fig. 2.15 (right), consists of 1521 CVs.

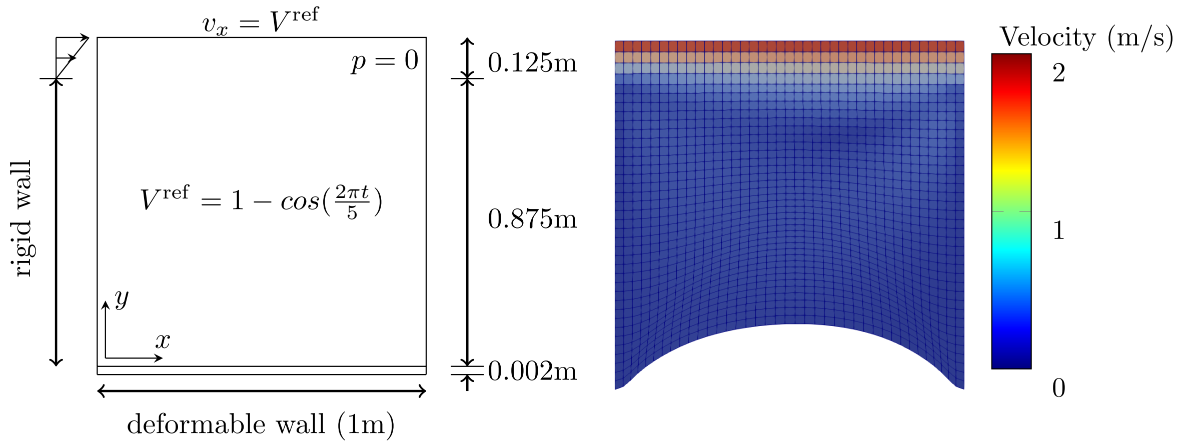

Figure 2.15: Left: Sketch of the 2D lid-driven cavity flow case. Right: Deformed fluid computational mesh at $t = 27.5$s coloured by the magnitude of the fluid velocity vector.

A linear pulsating velocity profile with a period of $T = 5$s is prescribed on the inlet patch. An outlet, in which $p = 0$ is set, is located at the exact opposite position of the inlet. The top wall is moving with the maximum velocity of the inlet (V^{ref}) while the vertical walls are modelled as rigid and non-moving. The bottom wall is assumed to be deformable. Density and viscosity of the fluid are set to $\rho^{\text{f}} = 1\frac{\text{kg}}{\text{m}^3}$ and $\mu^{\text{f}} = 0.01\text{Pa}\cdot\text{s}$, resulting to an average (in time) Re=12.5.

For the deformable wall, the *St. Venant-Kirchhoff* constitutive model is employed, which is an extension of the geometrically linear elastic material model to the geometrically nonlinear regime. Based on this model the SEDF is given by

$$W = \frac{\lambda^{\mathrm{s}}}{2}\left(\mathrm{tr}(E_{ij})\right)^2 + \mu^{\mathrm{s}}\mathrm{tr}(E_{ij}E_{ij}), \tag{2.125}$$

where $\lambda^{\mathrm{s}}, \mu^{\mathrm{s}}$ refer to the *Lamé constants* and are given by

$$\lambda^{\mathrm{s}} = \frac{E\nu^{\mathrm{s}}}{(1+\nu^{\mathrm{s}})(1-2\nu^{\mathrm{s}})} \quad \text{and} \quad \mu^{\mathrm{s}} = \frac{E}{2(1+\nu^{\mathrm{s}})}, \tag{2.126}$$

where E and ν^{s} refer to the Young's modulus and Poisson's ratio, respectively. For the application at hand, these are set to $E = 250$ Pa and $\nu^{\mathrm{s}} = 0$ while density is set to $\rho^{\mathrm{s}} = 500\rho^{\mathrm{f}}$. For the structure discretization, 16 isoparametric finite elements with quadratic shape functions are used. The BCs closing the structure problem refer to a zero displacement at the left and rightmost position of the deformable wall while zero traction is set at the bottom part. As shown by Eq. (2.121), on the top side the traction is set by the fluid loads. The case is simulated for a total of $10T$ with a constant step size (on both the fluid and structure solver) $\Delta t = 0.002T$.

The case is assessed by monitoring the displacement of the midpoint of the deformable wall and by subsequent comparison with literature-reported results, as shown in Fig. 2.16. A comparison between the present work and the results presented in Radtke [2020] show an excellent agreement. These results were obtained using a different fluid solver with however the same numerical settings. On the other hand, the results presented in Valdés Vázquez [2007] were obtained by using the generalized-α method for time integration while this work (and the one of Radtke [2020]) employ an implicit Euler method for the fluid solver. The obvious discrepancy noted with the results of Mok [2001] are due to a lack of necessary BCs information given. However, it can be noted that the results of the latter correspond solely to a shift of the mean vertical displacement.

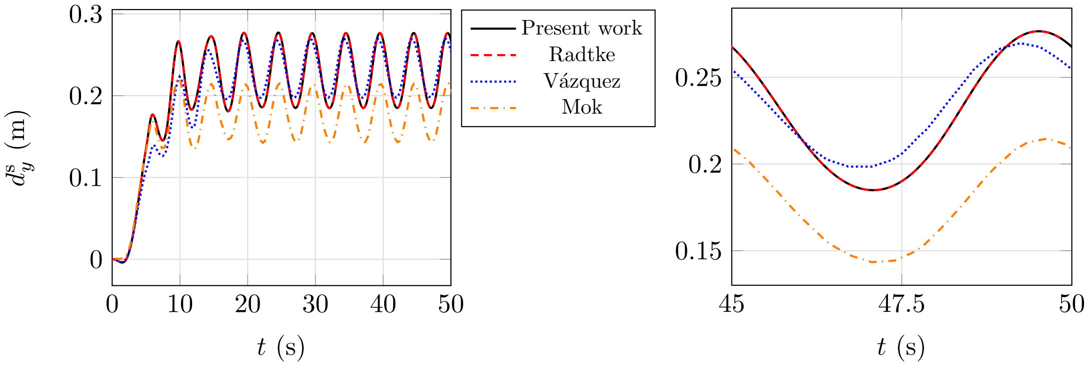

Figure 2.16: Vertical displacement of deformable's wall midpoint. Left: Complete simulation results. Right: Last period results. Continuous line refers to the results obtained for this work, discontinuous refer to those presented in the dissertations of Radtke [2020], Valdés Vázquez [2007] and Mok [2001].

Nevertheless, the excellent agreement between the results presented in this work and in the work of Radtke [2020] serves to verify the coupling between the two solvers.

3 Parameter-free Shape Optimization

This chapter discusses the shape optimization problem as considered in this thesis. A key aspect of the discussion conducted herein is the definition of the shape's control, i.e., the set of elements the modification of which results in corresponding modifications of the shape. As already discussed in the introduction, a frequent practice is the parameterization of the shape. This can be done by using e.g., volumetric B-splines (Farhikhteh et al. [2023], Papoutsis-Kiachagias et al. [2019]), geometric characteristics of the shape (Abraham et al. [2005a]), Free-Form Deformation (FFD) boxes (Dick et al. [2022]) or other conceivable CAD descriptions. Even though such approaches are appealing due to their (often) inherent features of sustaining certain characteristics of the initial shape, such as smoothness, or due to their ease of dealing with CAD-based geometric constraints, they constrict the design space based on a (frequently small) finite number of parameters. This thesis is concerned with parameter-free approaches, in which the control is the shape itself. This can be conceived as an infinitely large set of control points. The numerical optimization is then realized by updating the position of the elements used to discretize its surface. The strategy refers to a parameter-free (or CAD-free) shape optimization approach.

Section 3.1 presents the general optimization problem. Therein the approximation of a descent direction[1] given a sensitivity field is discussed. Section 3.2 presents various approaches for the algorithmic approximation of an appropriate descent direction for the complete discretized domain. Section 3.3 discusses additional optimization aspects of interest, such as a step-size control. This chapter closes with an illustrative CFD-based example, in which some of the presented methods are applied. Emphasis is given on aspects of computational interest.

3.1 General Shape Optimization Problem

Shape optimization is a particularly involved topic that is based on notions of shape calculus. An in-depth discussion on some of the mathematical aspects briefly presented in this chapter can be found in Radtke et al. [2023], Allaire et al. [2021], Sokolowski and Zolesio [1992]. The optimization problem is formulated in the context of optimization with PDE constraints, a topic extensively discussed in Hinze et al. [2008].

Let a shape $\Gamma = \Gamma_{\text{in}} \cup \Gamma_{\text{out}} \cup \Gamma_{\text{w}}$ associated with a domain $\Omega \subset \mathbb{R}^d$, with $d = 2$ or $d = 3$. Consider that its operational performance in the context of a physical condition can be described based on a scalar objective functional J, the value of which is antiproportional to the conceived efficiency of the shape. Then a general shape optimization problem can

---

[1] In most cases, the term "descent direction" may be used in place of "gradient". This is because the latter implies a direction of steepest descent which is usually hard or even impossible to determine. Instead, descent direction refers, as the name suggests, to a direction in which the objective functional is minimized.

be stated as

$$\min_{y_n,\Omega} J(y_n,\Omega) \quad \text{s.t.} \quad R_k(y_n,\Omega)=0. \tag{3.1}$$

Here "s.t." abbreviates "subject to". The vector y_n represents the state which can be conceived as the solution of the physical problem given a shape and collectively presented by $R_k(y_n,\Omega)=0$. The latter represents a system of N^{k} PDEs. If it is assumed that a unique solution of $R_k(y_n,\Omega)=0$ exists for each shape then one can write $\Omega \mapsto y_n(\Omega)$. This allows us to formulate the initially posed optimization problem based on a reduced objective functional, i.e., $\hat{J}(\Omega) := J(y_n(\Omega),\Omega)$. A minimum of $\hat{J}$ is also a minimum of J under the condition that the shape is admissible.

This thesis is concerned with iterative strategies such that $\hat{J}(\Omega^{i+1}) < \hat{J}(\Omega^i)$ where i denotes the iterate and

$$\Omega^{i+1} = \left\{ \tilde{x}_j : \tilde{x}_j = x_j + t^i\theta_j(x_j) \quad \forall x_j \in \Omega^i \right\}, \tag{3.2}$$

where t^i is a positive small step size that might change from iteration to iteration. Assuming that the necessary conditions as set on Allaire et al. [2021] (Definition 4.1) hold, then a first-order approximation reads

$$\hat{J}(\Omega^{i+1}) \approx \hat{J}(\Omega^i) + \hat{J}'(\Omega^i)(\theta_j), \tag{3.3}$$

where $\hat{J}'(\Omega^i)(\theta_j)$ denotes the shape derivative at Ω^i in a sufficiently smooth direction θ_j. Note that $\hat{J}'(\Omega^i)(\theta_j)$ amounts to a scalar quantity and can be loosely associated with an inner product. It becomes evident that θ_j corresponds to a descent direction for $\hat{J}$ if

$$\hat{J}'(\Omega^i)(\theta_j) < 0. \tag{3.4}$$

Our optimization problem is therefore concerned with finding θ_j such that Eq. (3.4) holds. In general, a shape derivative can be expressed as

$$\hat{J}'(\Omega^i)(\theta_j) = \int\limits_{\Gamma} \theta_j n_j s \, \mathrm{d}\Gamma, \tag{3.5}$$

where s is called the *sensitivity* and n_j refers to the normal vector to the surface. Equation (3.5) is the *Hadamard form* of a shape derivative.

Assuming that s is given to us, an obvious choice is to set $\theta_j = -n_j s$. Equation (3.3) can be then written as

$$\hat{J}(\Omega^{i+1}) \approx \hat{J}(\Omega^i) - \int\limits_{\Gamma} s^2 \, \mathrm{d}\Gamma \leq \hat{J}(\Omega^i), \tag{3.6}$$

However, several mathematical and practical restrictions do not allow for this choice. An obvious practical drawback of a descent direction pointing in the normal of a surface with an inhomogeneous sensitivity is illustrated in Fig. 3.1. As discussed in Section 2.4, the computed displacement values (same logic of a mesh update applies both in FSI and shape optimization considerations) are on a face/cell center. Therefore, as shown in Fig. 3.1 an irregular negative s field and a consideration of $\theta_j = -n_j s$ would theoretically rip apart the mesh in one shape update. Note that this is a straightforward rather simplistic thought experiment and in reality no discontinuities would appear on a discrete level since the real deformation would somewhat be implicitly filtered by the update rule of the nodes, cf. Eq. (2.119).

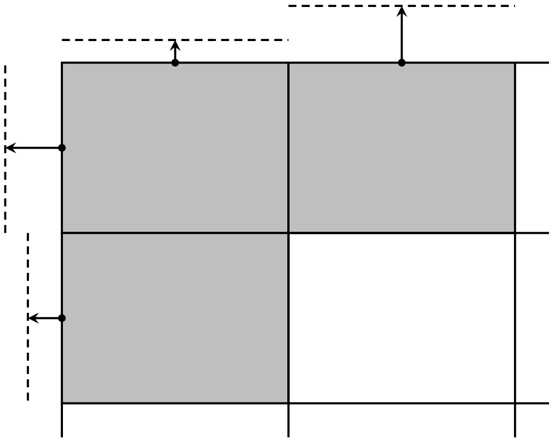

Figure 3.1: Four CVs at the edge of a discretized domain. In lightgray the three CVs with a boundary face. Arrows denote an arbitrary update of the boundary faces in the normal direction. Dashed lines denote the assumed position of the boundary faces after the update.

Furthermore, it must be noted that in the context of internal blood flows where the boundary can be assumed as the union of Γ_{in}, Γ_{out} and Γ_{w}, only the latter is a candidate for design. In fact, it is often the case that only part of the wall boundary is free for design while the remainder is fixed to its initial configuration. This is denoted as $\Gamma_{\text{d}} \subset \Gamma_{\text{w}}$ and it implies that $\theta_j(x_i) = 0 \; \forall x_i \in \Gamma \setminus \Gamma_{\text{d}}$. While this is straightforward and requires minimal implementation effort, it often leads to a rapid deterioration of the mesh quality around the sections where design and non-design boundaries meet. An approach on how such an issue can be circumvented is discussed in Section 3.3.

Algorithm 1 General parameter-free shape update algorithm.

```
Require: initial shape $\Gamma^0$, $\epsilon > 0$
for $i = 0, 1, ...$ do
    Compute the primal problem $R_k(y_n, \Omega^i)=0$ to find $\hat{J}(\Omega^i)$.
    Compute a sensitivity distribution $s$ on $\Gamma^i$.
    Compute a descent direction $\theta_j \in \Omega^i$.
    if $|\hat{J}'(\Omega^i)(\theta_j)| \leq \epsilon$ then
        break
    end if
    Determine step size $t^i$.
    Update shape based on Eq. (3.2).
end for
```

A general algorithmic strategy for parameter-free shape optimization can be schematically summarized as in Algorithm 1. In this chapter, steps 2 and 3 of the algorithm are considered as a black box and focus is given on how step 4 can be realized given a sensitivity. A key aspect of the above outlined procedure is that no re-meshing is required. This means that topological relationships remain unaltered and a simulation can continue by restarting from the previous optimization step, as long as the update of the mesh does not heavily deteriorate its quality, since the state of two consecutive shapes is usually similar. This results to a significant speed-up in total computational time. Therefore, approaches that sustain the quality of the employed discretization are highly favorable in the context of CAD-free shape optimization.

The remainder of this chapter discusses approaches that provide descent directions θ_j smoother than $-n_j s$ as well as additional aspects relevant to the optimization.

3.2 Shape Update Methods

This section describes approaches in which a descent direction can be evaluated based on a sensitivity field. Section 3.2.1 presents methods in which a descent direction is initially determined on the discretized shape (Γ) and subsequently extended on the domain (Ω). To assist the notation, therein the descent direction on the boundary is denoted as θ_j^Γ while θ_j refers to the collective discrete descent direction field on both Γ and Ω. Section 3.2.2 discusses methods in which the complete θ_j field can be made available with the solution of one additional PDE.

3.2.1 Two-Step Methods

Two methods of a two-step nature are considered herein. The first can be conceived exclusively on the discrete level while the second is based on a *Hilbertian extension* procedure. In both cases an extension of the deformation field to the domain is required and is subsequently realized by the solution of a Laplace equation.

Sensitivity filtering

One of the most straightforward approaches to finding a descent direction smoother than $-sn_j$ is to filter the sensitivity field (Kröger and Rung [2015], Stavropoulou et al. [2014]). Consider a discretized domain in which the sensitivity field is directly given at the nodes of the boundary elements, i.e., s^{n}, rather than the face centers. Then a filtered shape update direction at one node can be computed by

$$\theta_j^{\Gamma,\mathrm{n}} = -\sum_{i=1}^{N^{\mathrm{n}}} w^{\mathrm{n},i} s^{\mathrm{n},i} n_j^{\mathrm{n},i}, \tag{3.7}$$

where N^{n} is the number of nodes in the neighborhood of the node in which the descent direction is currently computed. The weights are denoted by $w^{\mathrm{n},i}$ while $n_j^{\mathrm{n},i}$ refers to an interpolated value of the face-based normal vectors to the nodal positions. Note that for weights $w^{\mathrm{n},i} = 1$ for all i, the approach reduces to the unfiltered choice.

Having considered this explicit filtering directly on the nodal positions, we can now return to the mindset of a FV-based solution. In this, the sensitivity values would be computed and stored in the centers of the boundary faces comprising Γ_d. Now assume that indeed one sets $\theta_j^\Gamma = -sn_j$ for every design face center. Then the domain update would again be realized by means of nodal displacements that still need to be evaluated. If one follows a scheme to compute the nodal displacements based on the surrounding cell/face values as the one described by Eq. (2.119) then it becomes clear that the computed nodal displacements are of the same nature as in Eq. (3.7). Therefore, the "naive" application of $\theta_j^\Gamma = -sn_j$ in the discrete setting of a FV-based tool inheres some level of smoothness by the interpolated computation of descent direction at the nodes. Therefore, the thought experiment illustrated in Fig. 3.1 is usually avoided.

Laplace-Beltrami

The concept of the Laplace-Beltrami method is based on a consideration of a Hilbertian framework. Consider the Hilbert space $H = H^1(\Gamma)$ with the associated inner product $a(\cdot,\cdot) : H \times H \to \mathbb{R}$, which reads

$$\begin{aligned} a(u,v) &= \int\limits_\Gamma u \cdot v \,\mathrm{d}\Gamma + \int\limits_\Gamma \nabla_\Gamma u : \nabla_\Gamma v \,\mathrm{d}\Gamma \\ &= \int\limits_\Gamma u \cdot v \,\mathrm{d}\Gamma - \int\limits_\Gamma v \Delta_\Gamma u \,\mathrm{d}\Gamma + \int\limits_{\partial\Gamma} v \nabla_\Gamma u \,\mathrm{d}\partial\Gamma, \end{aligned} \tag{3.8}$$

where ∇_Γ refers to a gradient defined exclusively on the surface of the shape and thus on its tangential direction.

Based on this framework, the gradient of $\hat{J}$ at Ω, i.e., $g_j \in H$, is identified as the Riesz representative of the shape derivative which is an element of the dual space H^*. The gradient g_j corresponds to the solution of the variational form

$$a(g_j, w_j) = \hat{J}'(\Omega)(w_j) \quad \forall w_j \in H, \tag{3.9}$$

which results in the strong formulation (Vassberg and Jameson [2006])

$$\begin{aligned} g_j - k\Delta_\Gamma g_j &= sn_j \quad \text{on } \Gamma_\mathrm{d} \\ g_j &= 0 \qquad \text{on } \Gamma \setminus \Gamma_\mathrm{d}, \end{aligned} \tag{3.10}$$

where Δ_Γ refers to the Laplace-Beltrami operator, i.e., the Laplacian in the tangent directions of the surface, from which this method often takes its name. In index notation this can be represented as

$$\Delta_\Gamma g_j = \frac{\partial}{\partial x_i}\left(\frac{\partial g_j}{\partial x_i}\right) - n_k \frac{\partial}{\partial x_k}\left(\frac{\partial g_j}{\partial x_i} n_i\right). \tag{3.11}$$

If one considers Eq. (3.10) as a smoothing operation then the parameter k is introduced to allow control over the extent to which the initial sensitivity field is smoothed. This becomes obvious by considering that for $k = 0$ the solution identically reduces to sn_j. Note that k is a dimensional unit with $[k] = m^2$. This implies that while k is usually arbitrarily chosen, it should actually be related to a length unit, characteristic to the case. An admissible descent direction can then be obtained by setting $\theta_j^\Gamma = -g_j$.

Domain update

Once the boundary field θ_j^Γ has been identified, it is necessary that it is extended in the domain for the reasons outlined in Section 2.4. Similarly to what was discussed therein, the internal field is updated by the solution of a Laplace problem that reads

$$\begin{aligned} \frac{\partial}{\partial x_k}\left(\mu^{\mathrm{w}} \frac{\partial \theta_j}{\partial x_k}\right) &= 0 \quad \text{in } \Omega \\ \theta_j &= \theta_j^\Gamma \quad \text{on } \Gamma. \end{aligned} \tag{3.12}$$

The diffusivity coefficient μ^{w} corresponds to the reciprocal of the distance from the nearest wall boundary. The choice of this diffusivity coefficient is made so that the deformation near the design boundaries, where the diffusivity is high, emulates a rigid body motion and thus sustains, as much as possible, the beneficial characteristics of the undeformed configuration. The coefficient then vanishes far away from the design section to allow for zero deformation. The update of the nodes is then computed in accordance to (2.119).

3.2.2 One-Step Methods

Section 3.2.1 discusses methods for which a descent direction can be found on the shape itself. This section presents two methods in which the said direction is found for the complete domain Ω and no extension is necessary. This is done by the solution of an additional PDE after the sensitivity field is found.

Steklov-Poincaré

This approach builds on the concept of an identification problem based on Steklov-Poincaré metrics (Welker [2016]). The problem in a strong formulation reads

$$\begin{aligned} \frac{\partial}{\partial x_k}\left(k^{\mathrm{sp}} \frac{\partial g_j}{\partial x_k}\right) &= 0 \quad \text{in } \Omega \\ k^{\mathrm{sp}} \frac{\partial g_j}{\partial x_i} n_i &= s n_j \quad \text{on } \Gamma_{\mathrm{d}} \\ g_j &= 0 \quad \text{on } \Gamma \setminus \Gamma_{\mathrm{d}}, \end{aligned} \tag{3.13}$$

where k^{sp} corresponds to a diffusivity coefficient that allows for a certain extent of control, similar to the Laplace-Beltrami approach. This allows for a choice of k^{sp} such that it resembles the constitutive tensor of a material and the whole method is then associated with linear elasticity, see e.g., Azegami and Wu [1996]. However, in this thesis the diffusivity is set equal to the reciprocal of the distance from the nearest wall boundary, as is done for the extension to the domain in the one-step methods. Such a method is also employed in Kühl [2021] where it is successfully applied for large-scale engineering applications. Once the field g_j is identified, an admissible descent direction is set to $\theta_j = -g_j$

In addition to the fact that this method requires no subsequent extension to the domain, it is also very suitable for a FV-based environment. The equation can be discretized based on the techniques discussed in Section 2.1 for a diffusive term.

p-Laplace

A recently proposed method (Müller et al. [2021], Müller [2023]) refers to an identification problem stemming from a p-Laplace relaxation of the steepest descent direction. This approach results in a strong formulation that reads

$$\begin{aligned}
\frac{\partial}{\partial x_k}\left(\left(\left(\frac{\partial g_m}{\partial x_l}\right)^2\right)^{\frac{p-2}{2}}\frac{\partial g_j}{\partial x_k}\right) &= 0 \qquad \text{in } \Omega \\
\left(\left(\frac{\partial g_m}{\partial x_l}\right)^2\right)^{\frac{p-2}{2}}\frac{\partial g_j}{\partial x_i} n_i &= s n_j \qquad \text{on } \Gamma_\mathrm{d} \\
g_j &= 0 \qquad \text{on } \Gamma \setminus \Gamma_\mathrm{d}
\end{aligned} \tag{3.14}$$

and approximates a steepest descent direction for $p \to \infty$. It is noted that in terms of its structure, the problem described by Eq. (3.14) differs to the one described by Eq. (3.13) only to the coefficient, which creates a non-linearity for the former. In fact, if one sets $p = 2$ then the p-Laplace problem reduces to the Steklov-Poincaré for $k^\mathrm{sp} = 1$. Of course, in this case it becomes hard to argue that $p \to \infty$ and the conceptual origins of this method are questioned. Once again, a suitable descent direction is set by $\theta_j = -g_j$

While this method guarantees both mathematical and practical advantages, the computational effort becomes higher as the value of p increases. In certain cases, the solution approach of Eq. (3.14) can in fact require a wall-clock time equivalent to the solution of the primal problem. To this end, a hybrid approach trying to combine the positive aspects of both the Steklov-Poincaré and p-Laplace methods is proposed in Müller et al. [2023].

3.3 Auxiliary Optimization Aspects

In addition to finding an admissible descent direction, the numerical solution of the optimization problem should address certain auxiliary, practical aspects. Two of such aspects explicitly discussed in this section are the determination of a suitable step size and the smoothing of the descent direction field around a neighborhood where Γ_d and $\Gamma \setminus \Gamma_\mathrm{d}$ meet.

3.3.1 Step Size Control

In gradient-based optimization approaches, the choice of a step size can be either beneficial or detrimental to the complete process. On the one hand, a large step size can significantly speed up the optimization but at the same time might lead to a significant deterioration of the computational mesh, an increase of the objective functional or to fluctuating solutions around an optimum. On the other hand, a small step size can prolong the optimization process “wasting” computational resources. However, in most engineering applications, in which the nature of the optimization problem can hardly be a priori determined, devising an appropriate rule for the step size is oftentimes rather difficult. To this end, several researchers employ a constant step size, see e.g., Kühl et al. [2022], Antonau et al. [2021], Papoutsis-Kiachagias and Giannakoglou [2016].

Even though this is a straightforward choice, the determination of the constant value is not and it can in fact require a significant amount of resources (depending on the case) to find. To this extent when a constant step size is used in this thesis, this is a priori determined in the first iteration based on

$$t = \theta^{\max} \left(\max_{x_k \in \Gamma_\mathrm{d}} \left(\sqrt{\theta_j^2(x_k)} \right) \right)^{-1}, \tag{3.15}$$

where $\theta^{\max}$ refers to a constant scalar value that is usually related to a characteristic length of the shape. In essence, $\theta^{\max}$ serves as a user-defined parameter based on which the descent direction field is scaled. While this is an intuitive choice for circumventing the need for directly prescribing t, it still requires user experience on the investigated case, to determine a suitable candidate for $\theta^{\max}$. This is usually chosen as a fraction of a characteristic length L of the investigated case, e.g., in the order of $\mathcal{O}(L/100)$ or $\mathcal{O}(L/1000)$.

From the constant step size of (3.15) one can conceptualize an iterative rule that reads

$$t^i = \theta^{\max} \left(\max_{x_k \in \Gamma_\mathrm{d}} \left(\sqrt{\theta_j^2(x_k^i)} \right) \right)^{-1}, \tag{3.16}$$

which simply follows the concept of Eq. (3.15) for each optimization iteration. An inherent problem of this rule is that as the optimization progresses, one expects the field of θ_j to decrease in value and by extension also reduce the maximum value of the norm. Due to the anti-proportional relationship of the maximum value of the norm with the step size t, it is often the case that this method leads to significantly large step sizes near an optimum.

An additional popular criterion is based on the sufficient decrease of the objective functional, as measured by the inequality

$$\hat{J}(\Omega^{i+1}) \leq \hat{J}(\Omega^i) + c\, t\, \hat{J}'(\Omega^i)(\theta_j) \tag{3.17}$$

for some constant $c \in (0,1)$. Inequality (3.17) is often called the *Armijo condition.* Based on this, a backtracking rule can be devised for controlling the step size which is summarized by the following steps:

1. Choose $\bar{t}$, $\tau \in (0,1)$, $c \in (0,1)$; Set $t \leftarrow \bar{t}$;
2. If inequality (3.17) is satisfied continue; Else set $t \leftarrow \tau t$ and repeat optimization step.
3. Terminate Armijo loop with $t^i = t$

This rule allows to start from a relatively large step size $\bar{t}$ the choice of which is based on Eq. (3.15). While this technique allows to circumvent the fluctuating solutions around a minimum, it doesn't necessarily speed up the process. Therefore in addition to this, a similar approach where $\bar{t}$ corresponds to a small value and is progressively increased, is also considered. However, both such approaches are usually met with technical restrictions in terms of CFD-based optimization. A backtracking Armijo condition is based on a sufficiently large initial step size that is progressively minimized based on the satisfaction of condition (3.17). However, the choice of the step size is restricted by the quality of the computational mesh which doesn't allow for an arbitrarily chosen large step size. Therefore, in most investigated cases herein, the success of this method appears near an optimum where the step size is decreased when a fluctuation (increase) of the objective functional appears, thus smoothing the minimization history of the last steps. On the other hand, one can start by a small step size and progressively increase it until a condition, such as the objective to be increased, is met. However, even on this scenario it is frequent that the mesh is heavily deteriorated before the set condition is met and therefore the optimization process prematurely terminates.

3.3.2 Filtering of Descent Direction Field

Each shape update method discussed in Section 3.2 considers $\theta_j(x_k) = 0 \; \forall x_k \in \Gamma \backslash \Gamma_\mathrm{d}$ which while mathematically consistent with the formulation of the problem, it is prone to create practical problems. If the distribution of the sensitivity, and consequently the descent direction field, results in large deformations in the neighborhood connecting design and non-design sections of the shape, a kink is bound to appear which inevitably deteriorates the quality of the mesh. A practical way of dealing with this aspect of the optimization is to filter the computed descent direction field in such a way that a smooth transition from Γ_d to $\Gamma \setminus \Gamma_\mathrm{d}$ is achieved. For instance, in a 2D case one can filter the already computed descent direction θ_j by applying

$$\tilde{\theta}_j = \begin{cases} \frac{1}{2}\theta_j \left(1 - \cos\left(\pi \frac{r}{r_0}\right)\right), & \text{if } r \leq r_0 \\ \theta_j, & \text{if } r > r_0 \end{cases} \tag{3.18}$$

as also suggested in Müller et al. [2023]. This filter operates based on a radius r_0, defined by the user and

$$r = \|x_k - \tilde{x}_k\|_2, \tag{3.19}$$

where $\tilde{x}_k$ denotes the Cartesian coordinates vector of a computational node connecting Γ_d and $\Gamma \setminus \Gamma_\mathrm{d}$.

In a 3D case, an equivalent filter can be constructed by building on the idea of a torus. In specific, a 2D circular intersection at nodes connecting Γ_d and $\Gamma \setminus \Gamma_\mathrm{d}$ is considered perpendicular to the main flow direction. The radius can then be computed as

$$r = \sqrt{\left(\sqrt{(x_1 - \bar{x}_1)^2 + (x_2 - \bar{x}_2)^2} - r_1\right)^2 + \left(x_3 - \bar{x}_3)\right)^2}, \tag{3.20}$$

where it is assumed that the main flow direction is pointing in the third Cartesian coordinate. Here $\bar{x}$ is used to denote the position vector of the center of the assumed intersection and r_1 its radius. The filter can then be equivalently applied in a 3D case as proposed by Eq. (3.18).

Note that the filter is applied on the complete computational domain and not only on the shape surface. Equation (3.18) is numerically applied on the cell/face centers and just before the nodal interpolation (2.119) is realized and the mesh is transformed. In specific, after the application of the filter, the procedure continues by interpolating $\tilde{\theta}_j$ to the nodes instead of the original θ_j.

3.4 Illustrative Example

In this section a 2D CFD-based shape optimization application is investigated with respect to certain of the introduced shape update approaches. Emphasis is given to practical aspects and restrictions that arise during an optimization procedure. The investigated application refers to steady, laminar external flows and therefore the optimization problem as posed in Eq. (3.1) is constrained by the NS equations that in a suitable residual form read

$$R^{\mathrm{p}} = \frac{\partial v_i}{\partial x_i} = 0 \tag{3.21}$$

$$R_i^{\mathrm{v}} = v_j \frac{\partial v_i}{\partial x_j} - \frac{1}{\rho} \frac{\partial}{\partial x_j} \left(2\mu S_{ij} - p\delta_{ij} \right) = 0. \tag{3.22}$$

The geometry refers to a 2D cylinder as schematically depicted in Fig. 3.2 (left). This example targets to minimize the flow-induced drag of the cylinder by optimizing parts of its shape. The objective reads

$$\hat{J}(\Omega) = \int\limits_{\Gamma} \left(p\delta_{ij} - 2\mu S_{ij} \right) n_i e_j^x \, \mathrm{d}\Gamma, \tag{3.23}$$

where e_j^x denotes the basis vector in the x-direction, i.e., the main flow direction. As already discussed, in this chapter the sensitivity is assumed to be given to us, however the interested reader is referred to Kühl et al. [2019] for a detailed explanation on how the sensitivity of this benchmark problem can be efficiently found. Note that the objective is evaluated along the complete circular obstacle Γ, but its shape derivative is evaluated only along the section under design Γ_{d}, cf., Fig. 3.2. The decision of optimizing a section of the obstacle's shape instead of the complete shape is made to avoid trivial solutions such as, e.g. a singular point or a straight line, in the absence of additional geometric constraints. The steady and laminar study is performed at $\mathrm{Re}_{\mathrm{D}} = \rho \, U_{\mathrm{in}} \, D/\mu = 20$ based on the cylinder's diameter D and the inflow velocity U_{in}. The two-dimensional domain has a length and height of $40\,D$ and $20\,D$, respectively.

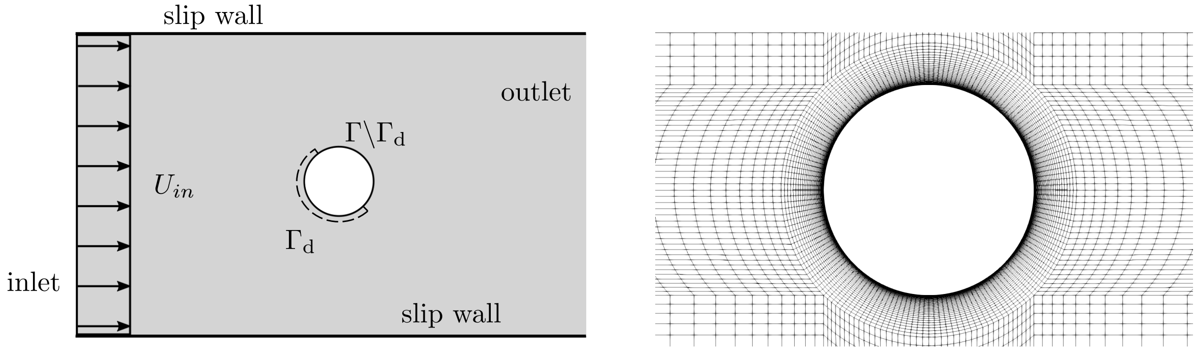

Figure 3.2: Left: Sketch of the investigated 2D cylinder optimization problem where the dashed line denotes the section free for design Γ_{d}. Right: Detail of the employed numerical grid near the cylinder.

To ensure the independence of the objective functional $\hat{J}$ w.r.t. spatial discretization, a grid study is first conducted, as presented in Table 3.1. Since the monitored integral quantity does not show a significant change from refinement level 3 on, level 3 is employed for all following optimizations. The utilized structured numerical grid consists of approximately 19000 CVs. The cylinder is discretized with 160 surface patches along its circumference. A detail of the mesh in the neighborhood of the cylinder is shown in Fig. 3.2 (right). The average dimensionless near-wall spacing around the cylinder is $y^+ \approx \mathcal{O}(10^{-3})$.

Table 3.1: Results of the mesh dependence study. Index i refers here to the mesh refinement level. Note $\rho = 20$ kg/m^3, $\mu = 1$ Pa $\cdot$ s, $U_{in} = 1$ m/s and $D = 1$ m.

refinement level	number of FV	$\frac{2\hat{J}_i}{\rho U_{in}^2 D^2}$	$\frac{\hat{J}_i - \hat{J}_{i-1}}{\hat{J}_{i-1}}(\%)$
M0	300	2.1637	-
M1	1200	2.1370	-1.23
M2	4800	2.1317	-0.25
M3	**19200**	**2.1334**	**0.08**
M4	76800	2.1334	-0.003
M5	307200	2.1334	-0.001

3.4.1 Results - Without Filter

This case is investigated w.r.t. the applied descent direction. In specific, the methods that are investigated are:

1. the direct application of the sensitivity field, i.e., $\theta_j = -n_j s$ (for each cell/face center on Γ_d), abbreviated as DS.
2. the Laplace-Beltrami method as described by Eq. (3.10) for different parameter values of k and abbreviated as LB.
3. the Steklov-Poincaré method, abbreviated as SP.

In all applications presented below the step size is determined based on the Armijo condition with the constant parameters $c = 0.5$ and $\tau = 0.5$. The initial step size $\bar{t}$ is prescribed on the first iteration based on Eq. (3.15), where $\theta^{\max} = 0.005\, D$ is chosen.

Figure 3.3 (left) shows the relative decrease of $\hat{J}(\Omega)$ w.r.t. the initial shape, for all aforementioned approaches. The SP approach reaches the maximum reduction, greater than 10%. As expected, the DS approach is the first to terminate with the lowest reduction while the LB approach increases its "efficiency" as the smoothing parameter k increases, while for a small value of k the descent history is identical to that of the DS approach. However, as illustrated in Fig. 3.3 (right), where the shape derivative is computed based on Eq. (3.5), none of the methods converge to a (local) minimum. Furthermore, no simulation satisfied a convergence criterion set to $(\hat{J}_i - \hat{J}_{i-1}) \cdot 100\% / \hat{J}_{i-1} \leq \epsilon$, with $\epsilon = 0.001$. Instead, all applications are terminated prematurely due to the deterioration of the mesh quality.

This shortcoming of the optimization is visualized in Fig. 3.4. On the left, the discretized rightmost connection between design and non-design areas is shown for the last produced shape by the DS approach. As initially speculated and in the absence of a filter, a kink

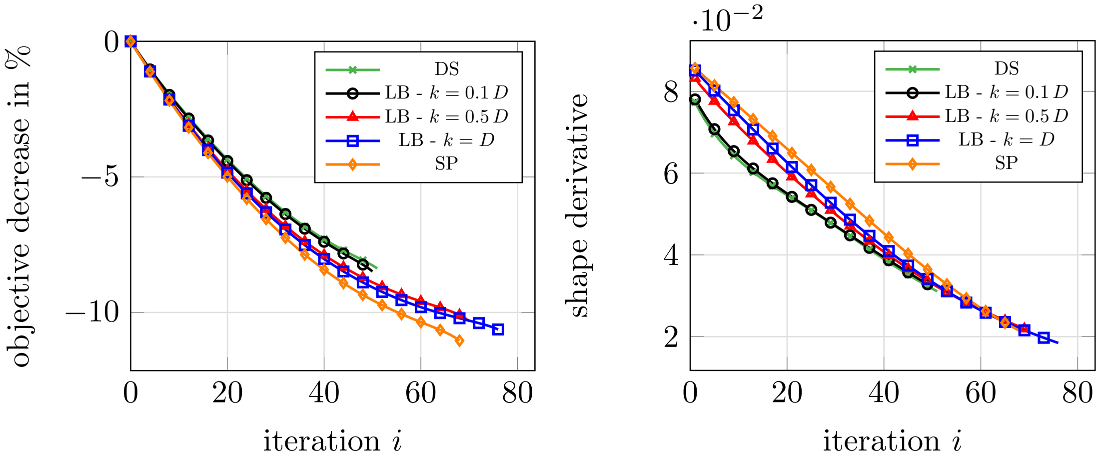

Figure 3.3: Left: Relative decrease $(\hat{J}_i - \hat{J}_0) \cdot 100\%/\hat{J}_0$ of objective. Right: History of shape derivative (3.5) during the optimization.

appears on the neighborhood of the faces connecting the two sections of the shape. The numerical procedure cannot continue without re-meshing or without a change of the numerical settings, since the primal problem diverges. To further illustrate the aspect of mesh quality preservation, Fig. 3.4 (right) is presented where the minimum cell orthogonality of the computational meshes is monitored during the optimization. Herein the orthogonality

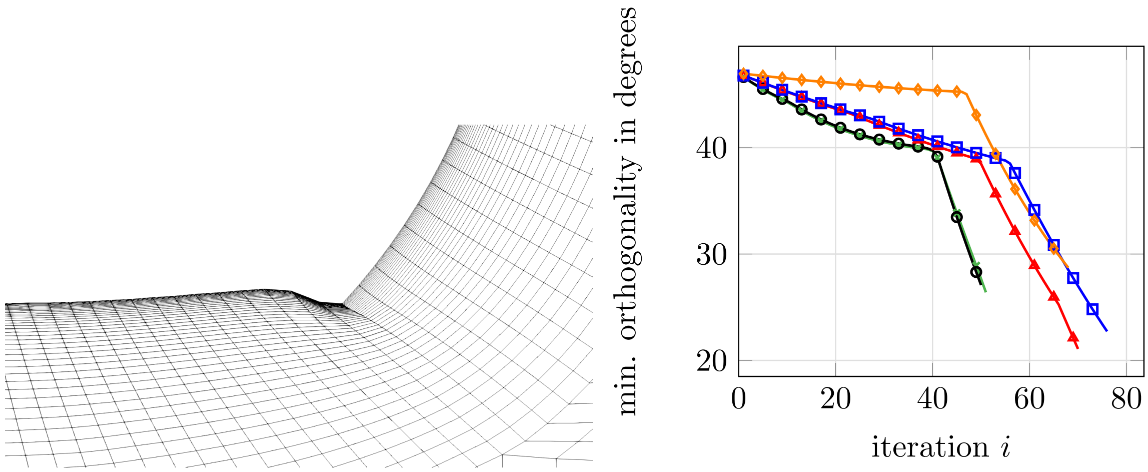

Figure 3.4: Left: Detail of the numerical grid at the rightmost connection between Γ_{d} and $\Gamma \backslash \Gamma_{\mathrm{d}}$ in the last optimization iteration with the DS approach. Right: Minimum cell orthogonality of the computational mesh. Legend as in Fig. 3.3.

of each cell is computed as

$$\alpha = \min_{n \in N} \left(90^\circ - \beta^n\right), \tag{3.24}$$

where β^n refers to the n^{th} angle between a face normal and the connecting line between the adjacent cell center and N denotes the total number of adjacent cells. The monitored minimum orthogonality of the computational mesh corresponds to the minimum value of α out of all cells. The SP method sustains a good mesh quality for the longest number of iterations while the LB method maintains a better mesh quality for larger numbers of k. It can be seen that all optimization procedures terminate on a critical value of approximately 25°.

Furthermore it is interesting to note the differences between the last produced shape by each approach. This is displayed in Fig. 3.5. It is noted that the application of the DS approach results in the "roughest" shape while the SP approach to the "smoothest". It is also interesting to note that for $k \to 0$ the LB approach results in an almost identical configuration as the DS approach while as k increases the obtained shape closer matches the one produced by SP.

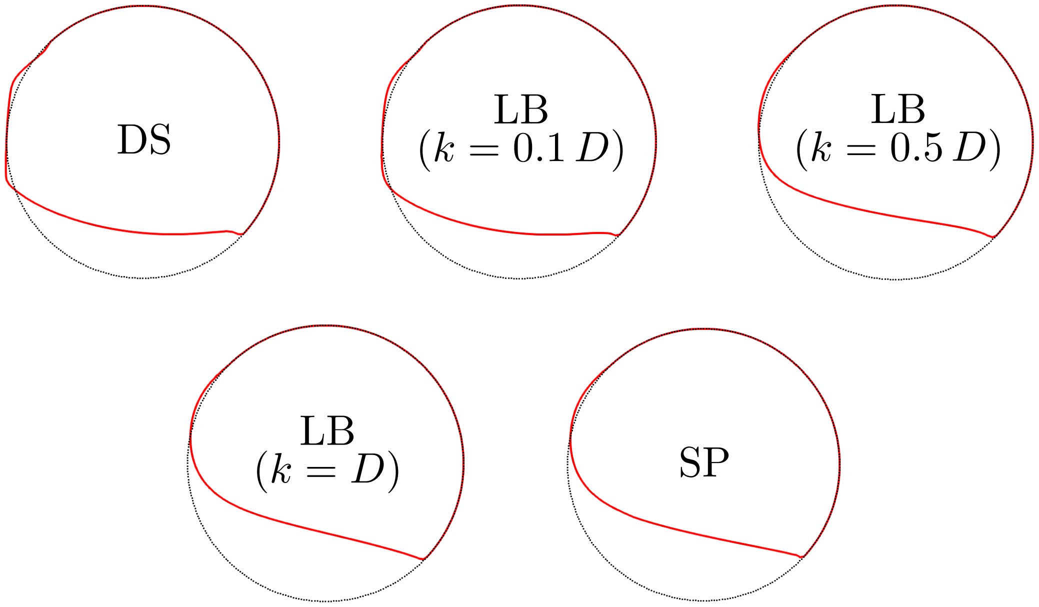

Figure 3.5: Outlines of initial (black line) shape compared to optimized (red lines) shapes. Descent direction employed: DS, LB - $k = 0.1\,D$, LB - $k = 0.5\,D$, LB - $k = D$, SP. The order follows from left to right and from top to bottom.

All simulations are parallelized using 10 CPU cores. The total wall clock time of each optimization process is monitored and then divided by the total number of (converged) shapes produced by each approach, to get an average wall clock time per shape update T^{wc}. This results in $T^{\mathrm{wc}} \approx 0.1$ hr for all update methods with small deviations that are attributed to the different convergence rate of the primal problem for each shape on the sequence. This shows that even though LB is herein classified as a two-step approach, the computational expense of estimating the descent direction field over Γ_{d} is small compared to the more time consuming extension to the domain, whose expense is comparable to the complete SP process. Overall, it must be noted that for most available shape update approaches in CFD optimization, the shape update procedure requires only a fraction of the time required for the solution of the primal problem.

Re-meshing

In order to validate that the predicted objective decrease is accurate and not an element of the mesh-morphing approach followed during the optimization, the optimized shapes are re-evaluated on a new mesh. The newly generated meshes consist of 20800 CVs and

160 surface patches along the circumference of the cylinder. It is ensured that the average dimensionless near-wall spacing around the optimized cylinders is of the same order of magnitude as in the initial mesh. Table 3.2 shows the predicted objective functional of the last optimized shape using the original morphed grid and the new mesh. For all cases it is noted that the deviation does not exceed 1% and therefore the results predicted by the optimization process are relatively accurate and cannot be attributed to the mesh distortion.

Table 3.2: Deviation of the computed objective functional $\hat{J}$ at the final achieved optimization iteration for each descent direction using the original mesh ($\hat{J}^{\mathrm{o}}$) and a new mesh ($\hat{J}^{\mathrm{n}}$).

descent direction	$\frac{2\hat{J}^{\mathrm{o}}}{\rho U_{in}^2 D^2}$	$\frac{2\hat{J}^{\mathrm{n}}}{\rho U_{in}^2 D^2}$	$\frac{\lvert\hat{J}^{\mathrm{o}}-\hat{J}^{\mathrm{n}}\rvert}{\hat{J}^{\mathrm{n}}}$(%)
DS	1.951	1.957	0.31
LB ($k = 0.1\,D$)	1.948	1.953	0.28
LB ($k = 0.5\,D$)	1.897	1.914	0.85
LB ($k = D$)	1.905	1.908	0.18
SP	1.897	1.916	0.95

It is interesting to note that the largest deviation appears for the SP approach. As shown in Fig. 3.6 the shape corresponding to the original mesh exhibits a kink near the connection between design and non-design sections. The reasons behind this kink are outlined above. However, this feature of the optimized shape refers only to couple of numerical faces and during the re-meshing process it is lost, cf. Fig. 3.6 (right). The existence of such kinks can induce both numerical but also manufacturability issues since such details often exceed the capabilities of the manufacturing process. To this extent, a proper smoothing of the connection between design and non-design segments is often advantageous even though it might alter the result of the initially posed optimization problem.

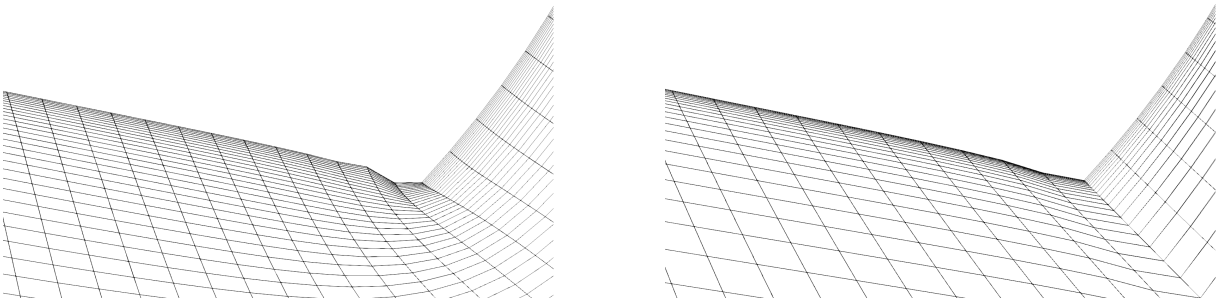

Figure 3.6: Detail of the numerical grid at the rightmost connection between Γ_{d} and $\Gamma \setminus \Gamma_{\mathrm{d}}$ in the last optimization iteration with the SP approach. Left: Mesh produced by the mesh-morphing approach of the optimization process. Right: Mesh produced by re-meshing the optimized shape.

3.4.2 Results - With Filter

For all presented methods, the quality of the mesh is heavily deteriorated in the vicinity of the connection between Γ_d and $\Gamma \backslash \Gamma_\mathrm{d}$. Figure 3.7 shows the optimization results of this case by applying the LB - $k = 0.1\,D$ method and using the filter suggested in Eq. (3.18). As can be seen the application of the filter produces shapes of a smoother transition from design to non-design. However, depending on the filtering radius applied, not only does the descent history change but also the final solution. It is interesting to note that while the application of a filter with a small filtering radius produces similar results to the unfiltered solution, the procedure terminates even faster since the sharp change from one section to the other is simply propagated upstream. This is an element of the computed sensitivity field and is case-specific. However, by increasing the filtering radius to $r_0 = 0.3\,D$ a converged solution (meeting the convergance criterion) is obtained, even though it is significantly different from the initially proposed shape.

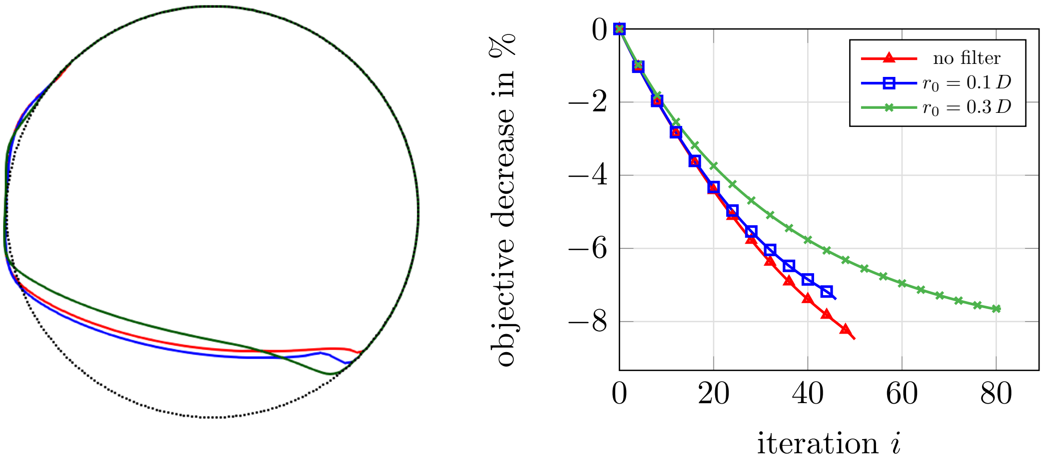

Figure 3.7: Cylinder optimization using LB - $k = 0.1\,D$ and descent direction filter (3.18). Left: Outlines of initial (black line) shape compared to optimized using no filter (red line), filtering radius $r_0 = 0.1\,D$ (blue line) and filtering radius $r_0 = 0.3\,D$ (green line). Right: Relative decrease $(\hat{J}_i - \hat{J}_0) \cdot 100\% / \hat{J}_0$ of objective.

This study shows that while the application of an explicit filter on the descent direction field can indeed result in smoother and numerically converged solutions, it might also lead to slower convergence and a different solution from the one obtained from an unfiltered method.

4 The Adjoint Method

In the previous chapter the parameter-free shape optimization problem was considered with the assumption of a given sensitivity field. In this chapter the adjoint method for efficiently estimating this field is presented. In the context of parameter-free gradient-based CFD shape optimization, the *adjoint method* constitutes perhaps the only computationally feasible approach to determining the sensitivity field. This is because the computational effort required by the adjoint method is detached from the number of design variables, which is assumed to span to infinity for a continuous shape description or a significantly large finite number for the discrete shape representation.

This chapter is dedicated to the presentation of the continuous adjoint method for fluid dynamics and its extension to incorporate aspects of hemodynamic interest. The adjoint problem is inherently dependant on the primal problem and the objective to be minimized. Therefore a general formulation is virtually impossible to be stated. However, certain aspects on the derivation process remain identical in the context of fluid dynamics. These derivations are presented in the context of a generalized problem and built upon to derive a generalized non-Newtonian adjoint formulation as well as a dual[1] to the hemolysis-based primal problem.

The chapter is organized in five sections. Section 4.1 presents a general theoretical background that motivates the use of the adjoint method. Section 4.2 follows with a presentation of generalized derivations in the context of continuous adjoint NS equations. Numerical aspects are discussed and a verification case is investigated by means of a second-order accurate FD study. Section 4.3 discusses the dual problem to the NS equations with hemolysis modeling for a Newtonian fluid. The chapter continues with Section 4.4 where a generalized adjoint problem for non-Newtonian blood models is presented. The former two sections include verification studies to assess the novel derivations as well as discussions to indicate the necessary numerical implementations on a FV-based CFD code. The chapter closes with Section 4.5 where the novel adjoint hemolysis and non-Newtonian systems are combined to allow for the minimization of hemolysis while employing a non-Newtonian model to describe the rheology of blood.

4.1 General Motivation for the Adjoint Formalism

Consider the function $F(x_i)$, $x_i \in \mathbb{R}^N$, $F : \mathbb{R}^N \mapsto \mathbb{R}$ and the optimization problem

$$\min_{x_i \in \mathbb{R}^N} F(x_i) \quad \text{s.t.} \quad C_k(x_i) = 0, \quad \text{with} \quad k = 1, \dots, M \tag{4.1}$$

where $C_k(x_i) = 0$ denotes a set of M equality constraints for the design variables x_i. Let's neglect the constraints for now and assume that F is continuously differentiable. Then a

---

[1] Note that *dual* and *adjoint* are oftentimes used interchangeably. The former indicates the dependence of the adjoint problem to the primal.

first order approximation of F reads

$$F(x_i + \delta x_i) \approx F(x_i) + \frac{\partial F}{\partial x_i}\delta x_i, \tag{4.2}$$

where $\delta x_i \in \mathbb{R}^N$ is a variation of the current design x_i. As already discussed in the previous chapter, δx_i is a descent direction for F if the second term on the RHS of Eq. (4.2) is negative. In fact, the descent direction becomes the steepest when

$$\delta x_i^* = \arg \min_{\delta x_i \in \mathbb{R}^N} \frac{\partial F}{\partial x_i}\delta x_i \tag{4.3}$$

and by considering a Euclidean space, the inner product can be written as

$$\frac{\partial F}{\partial x_i}\delta x_i = \left\| \frac{\partial F}{\partial x_i} \right\| \|\delta x_i\| \cos\theta, \tag{4.4}$$

where θ is the angle between the vectors dF/dx_i and δx_i. It is clear that, if one assumes a unit length for both vectors, Eq. (4.4) becomes minimum for $\cos\theta = -1$. Therefore, Eq. (4.3) reduces to

$$\delta x_i^* = -\frac{\partial F}{\partial x_i}. \tag{4.5}$$

Therefore, the steepest descent optimization method requires the estimation of the partial derivative of F w.r.t. the components of x_i. Note that while the constraints of the optimization problem (4.1) are neglected so far, their existence implies a subset of admissible solutions of x_i, i.e. $x_i \in X^{\text{ad}} \subset \mathbb{R}^N$ which also restricts the set of available descent directions δx_i.

The following sections discuss different methods for the estimation of these partial derivatives and compare them in terms of the necessary computational effort required for each.

4.1.1 Finite Difference Method

The most straightforward approach to approximate the sought partial derivatives is the FD method. Based on this method, a first-order approximation of the derivatives can be written as

$$\frac{\partial F}{\partial x_i} = \frac{F(x_i + \epsilon e_i^x) - F(x_i)}{\epsilon} + \mathcal{O}(\epsilon) \quad : \text{forward FD} \quad \text{or} \tag{4.6}$$

$$= \frac{F(x_i) - F(x_i - \epsilon e_i^x)}{\epsilon} + \mathcal{O}(\epsilon) \quad : \text{backward FD}, \tag{4.7}$$

where e_i^x denotes a unit vector of the same size as x_i and ϵ denotes a (small) perturbation magnitude in the direction e_i^x. A second-order accurate formula can be obtained by subtracting the Taylor expansions of $F(x_i + \epsilon e_i^x)$ and $F(x_i - \epsilon e_i^x)$ and reads

$$\frac{\partial F}{\partial x_i} = \frac{F(x_i + \epsilon e_i^x) - F(x_i - \epsilon e_i^x)}{2\epsilon} + \mathcal{O}(\epsilon^2) \quad : \text{central FD}. \tag{4.8}$$

The approximations are schematically illustrated in Fig. 4.1 in which the better estimation of the partial derivative based on a central difference scheme becomes obvious. The higher accuracy of the central FD scheme comes however at an extra cost. In the applications studied in this thesis, the equality constraints of the optimization problem (4.1) correspond to a set of PDEs, the satisfaction of which results on an admissible design x_i. It is therefore required that any perturbed design also satisfy the PDEs, otherwise it cannot be classified as admissible. In order to guarantee the satisfaction of the constraining PDEs, for each perturbed design, the PDEs are solved. This means that for the estimation of $F(x_i \pm \epsilon e_i^x)$, the constraints $C_k(x_i \pm \epsilon e_i^x) = 0$ need to be solved N times, i.e., the length of the x_i vector. Based on this, the computational cost for Eq. (4.6) and (4.7) is $N+1$ PDE solutions, while for the higher accuracy central difference scheme (4.8) it is $2N$ (+1, which implies that a solution at the reference value is also usually sought). If one associates the cost of satisfying the, so far vaguely described, equality constraints with the numerical solution of the NS equations and N with the total number of design variables in the context of parameter-free shape optimization, it becomes clear that the FD method is computationally demanding, if not unsuitable, to accompany a gradient-based optimizer.

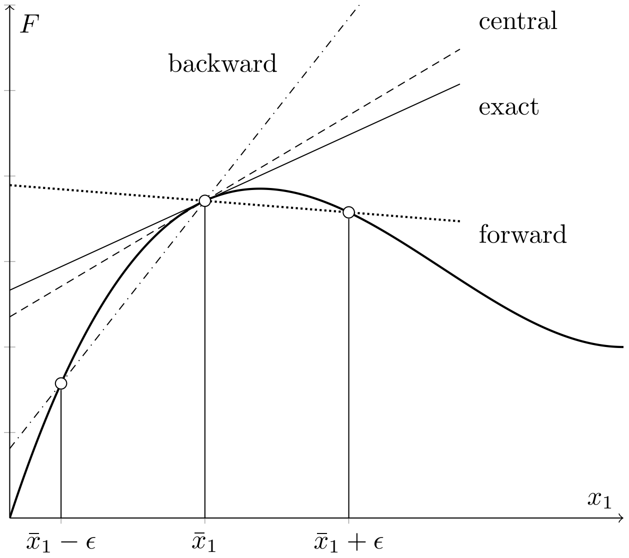

Figure 4.1: Approximation of $\partial F/\partial x_1$ at $\bar{x}_1$ using different FD schemes.

Additionally, the choice of an appropriate perturbation magnitude ϵ is not trivial. As can be seen, the truncation error of the schemes scale with ϵ or ϵ^2 and therefore a sufficiently small perturbation magnitude is sought. However, the smaller the perturbation gets the closer the value of $F(x_i \pm \epsilon e_i^x)$ is to the reference value. This can lead to the numerical error of *subtractive cancellation*. In essence, one looks for a step size small enough to guarantee that the approximation is in the linear region of the exact solution, cf. Fig. 4.1, but large enough to circumvent cancellation errors.

Even though the computational cost of FD does not allow its use in a parameter-free shape optimization procedure, its straightforward implementation makes the method a useful tool to validate derivatives obtained by other approaches (Kavvadias et al. [2015], Carnarius et al. [2010], Othmer [2008], Papadimitriou and Giannakoglou [2007]).

4.1.2 Complex Step Method

Another method that is based on a Taylor series expansion of F is the complex step method, in which the state is expanded based on an imaginary step. This method originates from Lyness and Moler [1967] and later popularized by Squire and Trapp [1998]. The second-order accurate approximation reads

$$\frac{\partial F}{\partial x_j} = \frac{\operatorname{Im}\left(F(x_j + i\epsilon e_j^x)\right)}{\epsilon} + \mathcal{O}(\epsilon^2), \tag{4.9}$$

where i is the imaginary unit. The advantage of this method is that there is no error due to subtractive cancellation, which implies that the value of ϵ can be arbitrarily decreased as compared to FD, and that a second-order accuracy is attained at the cost of N PDE solutions instead of $2N$ required by FD. However, the application of the method requires access to the source code since it must be modified so that all real variables and computations are replaced with complex ones. This is also accompanied by an increase in the memory requirements since complex variables require double the memory in comparison to real variables.

4.1.3 Direct Method

In the considerations so far, the minimization problem is presented in a simplified form where the objective and the constraints are only a function of the variables x_i. However, in the context of the applications investigated in this thesis, the problem can be extended to

$$\min_{y_m \in \mathbb{R}^M, x_i \in \mathbb{R}^N} F(y_m(x_i), x_i) \quad \text{s.t.} \quad C_k(y_m(x_i), x_i) = 0, \tag{4.10}$$

where $y_m : \mathbb{R}^N \mapsto \mathbb{R}^M$ denotes the vector of state variables. If we assume existence and uniqueness of this mapping then the optimization problems (4.1) and (4.10) are equivalent. However, the latter allows us to follow a different conceptual path as regards the sought derivative for the gradient-based optimization problem. Based on the chain rule, the total derivatives of F are

$$\frac{dF}{dx_i} = \frac{\partial F}{\partial x_i} + \frac{\partial F}{\partial y_m}\frac{dy_m}{dx_i}. \tag{4.11}$$

The partial derivative of F in the direction of x_i represents the change of the former w.r.t. variations of the latter while keeping the state constant. Instead, the total derivative takes into account the changes also induced to the state and therefore basically represent a direct relation of the constraint to the computation of the sought derivative. In the methods presented in Sections 4.1.1 and 4.1.2, the partial derivatives are computed and the constraints are indirectly satisfied by their solution on a perturbed design.

The constraints must indeed always be satisfied which implies

$$\frac{dC_k}{dx_i} = \frac{\partial C_k}{\partial x_i} + \frac{\partial C_k}{\partial y_m}\frac{dy_m}{dx_i} = 0 \rightarrow \frac{\partial C_k}{\partial y_m}\frac{dy_m}{dx_i} = -\frac{\partial C_k}{\partial x_i}. \tag{4.12}$$

The computational cumbersome part of Eq. (4.11) is dy_m/dx_i. If this is substituted based on Eq. (4.12) then

$$\frac{dF}{dx_i} = \frac{\partial F}{\partial x_i} - \frac{\partial F}{\partial y_m}\left(\frac{\partial C_k}{\partial y_m}\right)^{-1}\frac{\partial C_k}{\partial x_i}. \tag{4.13}$$

This equation reveals two possible approaches on computing the sought derivative, i.e., the direct and the adjoint method.

The direct method computes the matrix dy_m/dx_i directly from Eq. (4.12) and then substitutes the result in Eq. (4.11) which results in the symbolic formulation of Eq. (4.13). In order to illustrate the computational cost of this method consider a discrete computational mesh of K CVs. Then the length of the vectors C_k and y_m would be equal to $M = K \times Y$, where Y denotes the number of state variables, e.g., pressure and velocity components for a laminar flow of an incompressible, Newtonian fluid. Equation (4.12) then corresponds to a linear system with a LHS matrix of size $M \times M$ and a RHS matrix of size $M \times N$. The LHS matrix corresponds to the partial derivatives of the constraints w.r.t. the state. The RHS instead requires every design variable to be perturbed on a fixed state. For each column of the $\partial C_k/\partial x_i$ we can then compute a column of the dy_m/dx_i matrix. The direct method then requires the solution of N linear equation systems as well as storing the $M \times M$ matrix $\partial C_k/\partial y_m$.

4.1.4 Adjoint Method

The adjoint method is based on reversing the principle between design and objective. Instead of varying the design variables and computing the induced changes of the state and subsequently the objective, as done in the direct method, the adjoint method demands a change of the objective related to a modification of the design.

The starting point of the method is the formulation of a *Lagrangian* function that reads

$$\mathcal{L}(y_m, \hat{y}_k, x_i) = F(y_m, x_i) + \hat{y}_k C_k(y_m, x_i), \tag{4.14}$$

where $\hat{y}_k$ corresponds to Lagrange multipliers, or in this context *the adjoint variables*. Note that based on the discrete example discussed in Section 4.1.3, the length of y_m and C_k is the same. The (necessary) satisfaction of the constraints implies that $\mathcal{L} = F$. The total derivative of the Lagrangian then reads

$$\frac{d\mathcal{L}}{dx_i} = \frac{\partial F}{\partial x_i} + \frac{\partial F}{\partial y_m}\frac{dy_m}{dx_i} + \hat{y}_k\left(\frac{\partial C_k}{\partial x_i} + \frac{\partial C_k}{\partial y_m}\frac{dy_m}{dx_i}\right). \tag{4.15}$$

Rearranging the equation results in

$$\frac{d\mathcal{L}}{dx_i} = \left(\frac{\partial F}{\partial x_i} + \hat{y}_k\frac{\partial C_k}{\partial x_i}\right) + \left(\frac{\partial F}{\partial y_m} + \hat{y}_k\frac{\partial C_k}{\partial y_m}\right)\frac{dy_m}{dx_i}. \tag{4.16}$$

The concept of the adjoint method is to choose the adjoint variables $\hat{y}_k$ in such a way that the second term on the RHS of Eq. (4.16) vanishes, viz.

$$\hat{y}_k\frac{\partial C_k}{\partial y_m} = -\frac{\partial F}{\partial y_m} \rightarrow \hat{y}_k = -\frac{\partial F}{\partial y_m}\left(\frac{\partial C_k}{\partial y_m}\right)^{-1}, \tag{4.17}$$

which if substituted in Eq. (4.13) results in the computation of the sensitivity based on

$$\frac{dF}{dx_i} = \frac{\partial F}{\partial x_i} + \hat{y}_k \frac{\partial C_k}{\partial x_i}. \tag{4.18}$$

This approach renders the costly computation of dy_m/dx_i obsolete and instead requires the solution of Eq. (4.17) for the proper determination of the adjoint variables. Consider now again the discrete example described in Section 4.1.3. The solution of the linear Eq. (4.17) requires the determination of the $M \times M$ matrix $\partial C_k/\partial y_m$ and the M vector $\partial F/\partial y_m$ irrespective of the number of design variables N. Therefore, the total cost of the adjoint method is equal to just one numerical solution of a linear system of $M \times M$ equations for any number of N design variables.

To summarize, in every possible method for computing the necessary partial derivative outlined above the computational cost scales linearly with the number of design variables. However, it must be noted that while in the FD and complex step methods the cost refers to the numerical solution of usually non-linear equations, the direct method refers to the solution of linear equations, cf. Eq. (4.12). Nevertheless, even for the FD and complex step methods, the solution process can be warm started from a previous solution thus making the cost often comparable to that of the direct method. By considering that in CFD-based applications the cost refers to the computationally expensive numerical solution of the NS equations and that in parameter-free shape optimization the number of design variables corresponds (from a discrete perspective) to the number of faces discretizing the design section, it becomes clear that the adjoint is the only viable method to accompany the gradient-based optimizer in practical applications.

4.2 Continuous Adjoint Navier-Stokes Equations for Incompressible Fluids

Section 4.1 was devoted to presenting the motivation behind the use of the adjoint method in the context of parameter-free gradient-based shape optimization. Therein, the discussion was confined to examples most suitable to highlight the discrete adjoint method. In this section, the continuous adjoint method is presented for a general fluid dynamics case where the constraints refer to the NS equations. The principal difference between the discrete and the continuous adjoint method refers to how one arrives at the numerical representation of the adjoint problem. On the one hand, the discrete adjoint method follows a *discretize-then-derive* approach, where the underlying problem is first discretized and then used to derive the discrete adjoint problem. On the other hand, the continuous adjoint problem follows the *derive-then-discretize* approach in which the adjoint problem is initially formulated on a continuous level and then discretized for its numerical solution. As outlined in Chapter 1, a key feature of the continuous method is that it allows the use of similar numerical tools as those used for the solution of the primal problem. Therefore, even though source-code access is inherently required by the adjoint method due to its dependency on the objective functional and the constraining primal problem, the continuous adjoint method allows for a certain level of flexibility as regards its numerical implementation. The notation used herein serves as a conceptual bridge between the "continuous" notation used in Chapter 3 and the "discrete" notation of Section 4.1.

Let $J(y_m, u_k)$, $J : Y \times U \to \mathbb{R}$ be the objective functional to be minimized based on the optimization problem

$$\min_{(y_m,u_k)\in W^{\mathrm{ad}}} J(y_m(u_k), u_k) \quad \text{s.t.} \quad R_l(y_m(u_k), u_k) = 0, \tag{4.19}$$

where $W^{\mathrm{ad}} := Y \times U$ is an admissible space, with Y and U the Banach spaces of the state and control, respectively. Based on what is presented in Chapter 3, the control u_k can be thought as a vector representation of the shape Ω and it can be associated to x_i based on the notation of Section 4.1. The assumption of existence and uniqueness of the mapping $u_k \mapsto y_m(u_k)$ is again employed to arrive at the reduced objective functional $\hat{J}(u_k) := J(y_m(u_k), u_k)$. In this section, the constraints represent the NS equations in residual, strong form (without the boundary conditions) for an incompressible, Newtonian fluid in laminar, steady-state flow and can be written as

$$R^p = -\frac{\partial v_j}{\partial x_j} = 0 \tag{4.20}$$

$$R_i^v = \rho v_j \frac{\partial v_i}{\partial x_j} - \frac{\partial}{\partial x_j}\left[2\mu S_{ij} - p\delta_{ij}\right] = 0. \tag{4.21}$$

The solution of the constraints, given a shape, results in the state

$$y_m = (p, v_1, v_2(, v_3)), \tag{4.22}$$

where the last component of the velocity vector is in parentheses to allow for possible 2D flows.

Furthermore and in order to keep the derivations as general as possible, allow $\hat{J}$ to be decomposed as (Heners et al. [2018], Othmer [2008])

$$\hat{J} = \int_{\Gamma} j_{\Gamma}\,\mathrm{d}\Gamma + \int_{\Omega} j_{\Omega}\,\mathrm{d}\Omega, \tag{4.23}$$

where the first term on the RHS refers to boundary contributions while the second term to volume contributions.

As discussed in Section 4.1.4, the starting point of the adjoint method is the formulation of an *augmented objective functional* or Lagrangian, viz.

$$\mathcal{L} = \hat{J} + \int_{\Omega} \hat{y}_l R_l\,\mathrm{d}\Omega = \hat{J} + \int_{\Omega} \left[\hat{p}R^p + \hat{v}_i R_i^v\right]\,\mathrm{d}\Omega. \tag{4.24}$$

Since the constraints need to be satisfied for every admissible shape, Eq. (4.24) allows to formulate the initially constrained optimization problem (4.19) as an equivalent unconstrained problem. A saddle point of the Lagrangian is given when its total variation vanishes, viz.

$$\delta\mathcal{L} = \delta_{y_m}\mathcal{L}\cdot\delta y_m + \delta_{u_k}\mathcal{L}\cdot\delta u_k = 0, \tag{4.25}$$

where the first term on the RHS denotes the directional derivative of the Lagrangian in the direction of the primal state and the second term in the direction of the control (shape). In this sense, $\delta_{u_k}\mathcal{L}\cdot\delta u_k$ can be associated with the shape derivative and we thus search for a formulation of the Hadamard form as presented in Eq. (3.5), where δu_k represents a descent direction. Furthermore and based on the concept set forth in Section 4.1.4, $\delta_{y_m}\mathcal{L}\cdot\delta y_m$ is the means for obtaining the adjoint equations. In specific, we require that the variation of the Lagrangian is independent of δy_m, i.e., the variations of the state are independent of the variations in the control, and therefore demand

$$\delta_{y_m}\mathcal{L}\cdot\delta y_m = \left\{\begin{array}{c}\delta_p\mathcal{L}\cdot\delta p\\ \delta_{v_i}\mathcal{L}\cdot\delta v_i\end{array}\right\} = 0 \quad \forall\delta y_m. \tag{4.26}$$

Equation (4.26) gives rise to the adjoint equations, the satisfaction of which leads to the determination of

$$\hat{y}_l = (\hat{p}, \hat{v}_1, \hat{v}_2(, \hat{v}_3)) \tag{4.27}$$

such that the directional derivative of the Lagrangian in the direction of the primal state vanishes for every δy_m.

The variation $\delta_{y_m}\mathcal{L}\cdot\delta y_m$ can be expanded as

$$\delta_{y_m}\mathcal{L}\cdot\delta y_m = \delta_{y_m}\hat{J}\cdot\delta y_m + \int_{\Omega} \hat{y}_l\left(\delta_{y_m}R_l\cdot\delta y_m\right)\,\mathrm{d}\Omega, \tag{4.28}$$

where based on the decomposition of Eq. (4.23)

$$\delta_{y_m}\hat{J}\cdot\delta y_m = \int_{\Gamma} \delta y_m \frac{\partial j_{\Gamma}}{\partial y_m}\,\mathrm{d}\Gamma + \int_{\Omega} \delta y_m \frac{\partial j_{\Omega}}{\partial y_m}\,\mathrm{d}\Omega. \tag{4.29}$$

If one splits the volume integral of Eq. (4.24) into subintegrals consisting of isolated terms of the primal equations, viz.

$$\underbrace{\int_\Omega \hat{p}\Big(-\frac{\partial v_j}{\partial x_j}\Big)\,\mathrm{d}\Omega}_{I_1} + \Bigg[\underbrace{\int_\Omega \hat{v}_i\Big(\rho v_j\frac{\partial v_i}{\partial x_j}\Big)\,\mathrm{d}\Omega}_{I_2} + \underbrace{\int_\Omega \hat{v}_i\Big(-\frac{\partial}{\partial x_j}(2\mu S_{ij})\Big)\,\mathrm{d}\Omega}_{I_3} + \underbrace{\int_\Omega \hat{v}_i\Big(\frac{\partial p}{\partial x_i}\Big)\,\mathrm{d}\Omega}_{I_4}\Bigg],$$

where in accordance with Eq. (4.24)

$$\int_\Omega \hat{p}R^p d\Omega = I_1\,, \qquad \int_\Omega \hat{v}_i R_i^v d\Omega = I_2 + I_3 + I_4,$$

the computation of Eqs. (4.28) can be written as

$$\delta_{y_m}\mathcal{L}\cdot\delta y_m = \delta_{y_m}\Big(J + \sum_{l=1}^{4} I_l\Big)\cdot\delta y_m = \delta_{y_m}J\cdot\delta y_m + \sum_{l=1}^{4}(\delta_{y_m}I_l\cdot\delta y_m) = 0. \tag{4.30}$$

4.2.1 Variations of the Steady Navier-Stokes Equations

Each term of the sum in Eq. (4.30) is treated separately to arrive at the collective expression of the adjoint equations. In the following enumerated list, the number refers to the respective subintegral.

1. Since I_1 doesn't directly depend on p it follows that $\delta_p I_1\cdot\delta p = 0$. The variation in the direction of v_i reads

$$\delta_{v_i}I_1\cdot\delta v_i = -\int_\Gamma (\delta v_i n_i)\hat{p}\,\mathrm{d}\Gamma + \int_\Omega (\delta v_i)\frac{\partial\hat{p}}{\partial x_i}\,\mathrm{d}\Omega, \tag{4.31}$$

   where n_i denotes the normal vector to the boundary.

2. Similarly to I_1, $\delta_p I_2\cdot\delta p = 0$ and

$$\delta_{v_i}I_2\cdot\delta v_i = \int_\Gamma \delta v_i\hat{v}_i\rho(v_j n_j)\,\mathrm{d}\Gamma - \int_\Omega (\delta v_i)\left(v_j\rho\frac{\partial\hat{v}_i}{\partial x_j} - \hat{v}_j\rho\frac{\partial v_j}{\partial x_i}\right)\mathrm{d}\Omega. \tag{4.32}$$

3. Since $S_{ij} = 0.5\,(\partial v_i/\partial x_j + \partial v_j/\partial x_i)$ is a function of velocity only, it again follows that $\delta_p I_3\cdot\delta p = 0$ and

$$\delta_{v_i}I_3\cdot\delta v_i = \underbrace{-\int_\Gamma \hat{v}_i\mu\Big(\frac{\partial\delta v_i}{\partial x_j} + \frac{\partial\delta v_j}{\partial x_i}\Big)n_j\,\mathrm{d}\Gamma}_{\Gamma_1} + \underbrace{\int_\Omega \frac{\partial\hat{v}_i}{\partial x_j}\mu\Big(\frac{\partial\delta v_i}{\partial x_j} + \frac{\partial\delta v_j}{\partial x_i}\Big)\,\mathrm{d}\Omega}_{I_3^*}, \tag{4.33}$$

where I_3^* can be expanded further using a second integration by parts as

$$\begin{aligned} I_3^* &= \int\limits_\Omega \frac{\partial \hat{v}_i}{\partial x_j}\mu\frac{\partial \delta v_i}{\partial x_j}\,\mathrm{d}\Omega + \int\limits_\Omega \frac{\partial \hat{v}_i}{\partial x_j}\mu\frac{\partial \delta v_j}{\partial x_i}\,\mathrm{d}\Omega \\ &= \underbrace{\int\limits_\Gamma (\delta v_i)\mu\left[\frac{\partial \hat{v}_i}{\partial x_j}+\frac{\partial \hat{v}_j}{\partial x_i}\right]n_j\,\mathrm{d}\Gamma}_{\Gamma_2} - \int\limits_\Omega (\delta v_i)\frac{\partial}{\partial x_j}\left[\mu\Big(\frac{\partial \hat{v}_i}{\partial x_j}+\frac{\partial \hat{v}_j}{\partial x_i}\Big)\right]\mathrm{d}\Omega. \end{aligned} \tag{4.34}$$

Combining the surface integrals of Eqs. (4.33) and (4.34) results in

$$\Gamma_1+\Gamma_2 = \int\limits_\Gamma \mu n_j\left(\frac{\partial \hat{v}_j}{\partial x_i}\delta v_i - \frac{\partial \delta v_j}{\partial x_i}\hat{v}_i\right)\mathrm{d}\Gamma + \int\limits_\Gamma \mu n_j\left(\frac{\partial \hat{v}_i}{\partial x_j}\delta v_i - \frac{\partial \delta v_i}{\partial x_j}\hat{v}_i\right)\mathrm{d}\Gamma. \tag{4.35}$$

Expanding the first integral of Eq. (4.35) leads to

$$\begin{aligned} &\int\limits_\Gamma \mu n_j\left(\frac{\partial \hat{v}_j}{\partial x_i}\delta v_i - \frac{\partial \delta v_j}{\partial x_i}\hat{v}_i\right)\mathrm{d}\Gamma = \int\limits_\Gamma \mu\frac{\partial \hat{v}_n}{\partial x_i}\delta v_i\,\mathrm{d}\Gamma - \int\limits_\Gamma \mu\frac{\partial \delta v_n}{\partial x_i}\hat{v}_i\,\mathrm{d}\Gamma \\ &= \Bigg[\mu\hat{v}_n\underbrace{\delta v_i n_i}_{\delta v_n}\Bigg]_{\partial\Gamma} - \Bigg[\mu\underbrace{\hat{v}_i n_i}_{\hat{v}_n}\delta v_n\Bigg]_{\partial\Gamma} - \int_\Gamma \hat{v}_n\mu\frac{\partial \delta v_i}{\partial x_i}\,\mathrm{d}\Gamma + \int\limits_\Gamma \delta v_n\mu\frac{\partial \hat{v}_i}{\partial x_i}\,\mathrm{d}\Gamma \\ &= 0, \end{aligned} \tag{4.36}$$

where $(.)_n$ denotes the normal to the surface component of a vector. Herein the assumption is made that $\partial n_j/\partial x_i$, i.e., the local curvature of the boundary, is negligible and that the variation of the primal continuity asymptotically holds along the boundary of the domain. The former assumption is frequently applied, also throughout the primal equations, and is called *plane Couette* flow assumption. Furthermore, as it will be shown in the following derivations, in the absence of a volume-based objective involving pressure contributions, the adjoint velocity field must be solenoidal which is also assumed to asymptotically hold on the boundary, thus allowing us to neglect the last surface integral of Eq. (4.36).

Based on the above, the variation of I_3 in the direction of v_i reads

$$\delta_{v_i} I_3\cdot\delta v_i = \int\limits_\Gamma (\delta v_i)\mu n_j\frac{\partial \hat{v}_i}{\partial x_j}\,\mathrm{d}\Gamma - \int\limits_\Gamma \hat{v}_i\mu n_j\frac{\partial \delta v_i}{\partial x_j}\,\mathrm{d}\Gamma - \int\limits_\Omega (\delta v_i)\frac{\partial}{\partial x_j}\left(2\mu\hat{S}_{ij}\right)\mathrm{d}\Omega, \tag{4.37}$$

where in an analogy to the primal flow $\hat{S}_{ij} = 0.5\,(\partial\hat{v}_i/\partial x_j + \partial\hat{v}_j/\partial x_i)$.

4. The subintegral I_4 doesn't directly depend on the velocity vector and thus $\delta_{v_i} I_4\cdot\delta v_i = 0$. The variation in the direction of pressure reads

$$\delta_p I_4\cdot\delta p = \int\limits_\Gamma (\delta p)\hat{v}_i n_i\,\mathrm{d}\Gamma - \int\limits_\Omega (\delta p)\frac{\partial \hat{v}_i}{\partial x_i}\,\mathrm{d}\Omega. \tag{4.38}$$

Having expressed all subintegrals in the form of surface and volume integrals we can superpose all contributions into the directional derivatives of the Lagrange functional, viz.

$$\delta_p \mathcal{L} \cdot \delta_p = \int\limits_{\Gamma} (\delta p) \left(\hat{v}_i n_i + \frac{\partial j_\Gamma}{\partial p} \right) \mathrm{d}\Gamma - \int\limits_{\Omega} (\delta p) \left(\frac{\partial \hat{v}_i}{\partial x_i} - \frac{\partial j_\Omega}{\partial p} \right) \mathrm{d}\Omega, \tag{4.39}$$

$$\begin{aligned} \delta_{v_i} \mathcal{L} \cdot \delta v_i = & \int\limits_{\Gamma} (\delta v_i) \left[-\hat{p} n_i + \rho \hat{v}_i v_j n_j + \mu n_j \frac{\partial \hat{v}_i}{\partial x_j} + \frac{\partial j_\Gamma}{\partial v_i} \right] \mathrm{d}\Gamma \\ & - \int\limits_{\Gamma} \mu \hat{v}_i \frac{\partial \delta v_i}{\partial x_j} n_j \, \mathrm{d}\Gamma \\ & + \int\limits_{\Omega} (\delta v_i) \left[\hat{v}_j \rho \frac{\partial v_j}{\partial x_i} - v_j \rho \frac{\partial \hat{v}_i}{\partial x_j} - \frac{\partial}{\partial x_j} \left(2\mu \hat{S}_{ij} - \hat{p} \delta_{ij} \right) + \frac{\partial j_\Omega}{\partial v_i} \right] \mathrm{d}\Omega. \end{aligned} \tag{4.40}$$

The conditions (4.26) require that the all integrals in Eqs. (4.39) and (4.40) vanish for any admissible δp and δv_i.

4.2.2 Field Adjoint Equations

For the volume integrals, the satisfaction of conditions (4.26) leads to the *field adjoint equations*, viz.

$$\hat{R}^p = -\frac{\partial \hat{v}_i}{\partial x_i} + \frac{\partial j_\Omega}{\partial p} = 0 \tag{4.41}$$

$$\hat{R}_i^v = \hat{v}_j \rho \frac{\partial v_j}{\partial x_i} - v_j \rho \frac{\partial \hat{v}_i}{\partial x_j} - \frac{\partial}{\partial x_j} \left(2\mu \hat{S}_{ij} - \hat{p} \delta_{ij} \right) + \frac{\partial j_\Omega}{\partial v_i} = 0. \tag{4.42}$$

Equation (4.41) refers to the adjoint continuity equation while Eq(s). (4.42) to the adjoint momentum equation(s) due to their similarity with the respective primal equations. Note that these equations are linear in the unknowns $\hat{p}$ and $\hat{v}_i$. However, their similarities with the (non-linear) primal equations suggest a similar numerical implementation for their solution. Furthermore, it is worth noting that no assumption is made to arrive at the field adjoint equations as presented by (4.41), (4.42), apart from the nature of the fluid and the flow. Nevertheless, the equations are augmented by an additional source term involving volume contributions of the objective functional. This necessitates the specification of the objective before the numerical solution of the adjoint. In addition, the adjoint equations involve the primal state, cf., (4.22), thus suggesting a sequential solution approach, i.e., the numerical solution of the adjoint equations needs to follow the solution of the primal for a given control.

4.2.3 Boundary Adjoint Conditions

The solution of the field adjoint equations results in vanishing volume integrals of Eqs. (4.39) and (4.40). Instead, the requirement of vanishing surface integrals is used to deduce the necessary BCs for closing the field adjoint equations. Similarly to the concept applied for the field adjoint equations, a straightforward approach is to demand that the integrand vanishes for any possible δy_m. However, due to the BCs applied to the primal problem, certain simplifications can be made for the deduction of the adjoint BCs. These simplifications are therefore dependent on the primal problem. In this section certain assumptions are made based on what is frequently applied in the context of blood flows where the domain boundary can be split as $\Gamma = \Gamma_{\text{in}} \cup \Gamma_{\text{out}} \cup \Gamma_{\text{w}}$. A similar analysis to what follows herein can also be found in Othmer [2008].

Inlet and non-design wall

The primal velocity is usually fixed on Γ_{in} and Γ_{w}, based on a prescribed velocity and the no-slip condition, respectively. This implies that any variation of the shape will not induce a variation of the velocity in the respective boundaries and so $\delta v_i = 0$ on Γ_{in} and Γ_{w}. Therefore, the remaining surface integrals that need to vanish are

$$\int\limits_{\Gamma_{\text{in}}\cup\Gamma_{\text{w}}} (\delta p)\left(\hat{v}_i n_i + \frac{\partial j_\Gamma}{\partial p}\right) \mathrm{d}\Gamma := 0 \quad \text{and} \quad \int\limits_{\Gamma_{\text{in}}\cup\Gamma_{\text{w}}} \mu \hat{v}_i \frac{\partial \delta v_i}{\partial x_j} n_j \, \mathrm{d}\Gamma := 0. \tag{4.43}$$

Assuming that the primal continuity equation asymptotically holds also on the boundaries of the domain, then its variation must also hold and one can write

$$\frac{\partial \delta v_i}{\partial x_i} = \frac{\partial \delta v_n}{\partial n} + \frac{\partial \delta v_i^t}{\partial x_i^t} = 0, \tag{4.44}$$

where the divergence has been decomposed into normal and tangential contributions. Hereafter, a standalone n refers to the spatial normal direction while the two (one) tangential directions are (is) represented by a superscript of t for a three (two) dimensional problem. Since $\delta v_i = 0$ is assumed everywhere on Γ_{in} and Γ_{w}, it holds that $\partial \delta v_i^t / \partial x_i^t = 0$ and therefore following from Eq. (4.44)

$$\frac{\partial \delta v_n}{\partial n} = 0 \quad \text{on } \Gamma_{\text{in}} \cup \Gamma_{\text{w}}. \tag{4.45}$$

Based on this, the necessity of satisfying the second equation of (4.43) simplifies to

$$\int\limits_{\Gamma_{\text{in}}\cup\Gamma_{\text{w}}} \mu \hat{v}_i^t \frac{\partial \delta v_i^t}{\partial n} \, \mathrm{d}\Gamma = 0. \tag{4.46}$$

Therefore the BCs simultaneously satisfying the first equation of (4.43) and (4.46) are

$$\hat{v}_n = -\frac{\partial j_\Gamma}{\partial p} \quad \text{and} \quad \hat{v}_i^t = 0 \quad \text{on } \Gamma_{\text{in}} \cup \Gamma_{\text{w}}. \tag{4.47}$$

From the above deductions we managed to obtain BCs for the adjoint velocity on the respective boundary patches. However, there is no remaining information for the deduction of the necessary BCs for adjoint pressure. Since the latter enters the adjoint field equations similarly to its primal counterpart, the same BCs are set as in the primal problem, i.e., zero Neumann conditions.

Outlet

Pressure is usually fixed and zero Neumann is set for velocity on Γ_{out}. Based on these assumptions one can write

$$\delta p = 0 \quad \text{and} \quad \frac{\partial \delta v_i}{\partial x_j} n_j = 0. \tag{4.48}$$

Therefore, the only boundary integral that needs to be eliminated is

$$\int_{\Gamma_{\text{out}}} (\delta v_i) \left[-\hat{p} n_i + \rho \hat{v}_i v_j n_j + \mu n_j \frac{\partial \hat{v}_i}{\partial x_j} + \frac{\partial j_\Gamma}{\partial v_i} \right] \mathrm{d}\Gamma := 0. \tag{4.49}$$

The integrand in brackets is set to zero and split into normal and tangential components to arrive at

$$-\hat{p} + \rho \hat{v}_n v_n + \mu \frac{\partial \hat{v}_n}{\partial n} + \frac{\partial j_\Gamma}{\partial v_n} = 0 \quad \text{on } \Gamma_{\text{out}}, \tag{4.50}$$

$$\rho \hat{v}_i^t v_n + \mu \frac{\partial \hat{v}_i^t}{\partial n} + \frac{\partial j_\Gamma}{\partial v_i^t} = 0 \quad \text{on } \Gamma_{\text{out}}. \tag{4.51}$$

Equations (4.50) and (4.51) can be used to set BCs for the adjoint pressure and the tangential adjoint velocity components, respectively. The normal component of the adjoint velocity can be set by assuming that Eq. (4.41) holds on the boundary and the computed tangential adjoint velocity components.

The necessary assumptions to arrive at the BCs outlined above are summarized as follows:

- It is assumed that $\partial j_\Omega / \partial p = 0$ and $\partial n_j / \partial x_i \approx 0$ on Γ so that Eq. (4.36) holds.
- It is assumed that a Dirichlet condition is set for primal velocity on the inlet and wall patches.
- It is assumed that a Dirichlet condition is set for primal pressure and a zero Neumann condition is set for velocity on the outlet.
- It is assumed that the primal and adjoint continuity equations asymptotically hold on the boundary of the domain.

If these assumptions hold, then the field adjoint equations as well as the BCs outlined above hold for any case in which the constraining primal problem refers to the NS equations for an incompressible, Newtonian fluid in laminar, steady-state flow conditions.

4.2.4 Shape Sensitivity

If the field adjoint equations and their respective BCs are satisfied, then $\delta_{y_m}\mathcal{L} \cdot \delta y_m = 0$ and the total variation of the Lagrangian involves only the directional derivative in the direction of the control u_k, cf. Eq. (4.25). This can be written as

$$\delta_{u_k}\mathcal{L} \cdot \delta u_k = \delta_{u_k} J \cdot \delta u_k + \int_\Omega \hat{y}_l (\delta_{u_k} R_l \cdot \delta u_k) \, \mathrm{d}\Omega. \tag{4.52}$$

Note that in the expression of Eq. (4.52), an additional term involving the variation of dΩ in the direction of the control, often referred to as the Leibniz term, is omitted. This is made based on the assumption that the flow equations are satisfied along the boundary, an assumption already made on the analysis above, cf. Section 4.2.3. From a numerical perspective, this assumption is usually well justified when the employed grids are fine near the boundaries and the Re number is small. As regards the latter, this is frequently the case in blood flows, with the value of Re number rarely exceeding 7500. Nevertheless, for a consistent treatment of this term, the interested reader is referred to Kavvadias et al. [2015].

It holds that the total variation of the residual primal equations vanishes, viz.

$$\delta R_l = \delta_{y_m} R_l \cdot \delta y_m + \delta_{u_k} R_l \cdot \delta u_k = 0, \tag{4.53}$$

which leads to

$$\delta_{u_k} R_l \cdot \delta u_k = -\delta_{y_m} R_l \cdot \delta y_m, \tag{4.54}$$

Substituting Eq. (4.54) into Eq. (4.52) results in

$$\delta_{u_k} \mathcal{L} \cdot \delta u_k = \delta_{u_k} J \cdot \delta u_k - \int\limits_{\Omega} \hat{y}_l (\delta_{y_m} R_l \cdot \delta y_m) \, \mathrm{d}\Omega, \tag{4.55}$$

where the volume integral of Eq. (4.55) has already been computed for the construction of the adjoint equations, cf. Eq. (4.30). Employing the derived expressions and accordingly expanding Eq. (4.55) leads to

$$\begin{aligned}
\delta_{u_k} \mathcal{L} \cdot \delta u_k = {} & \delta_{u_k} \hat{J} \cdot \delta u_k - \int\limits_{\Gamma} (\delta p) \, (\hat{v}_i n_i) \, \mathrm{d}\Gamma + \int\limits_{\Omega} (\delta p) \left(\frac{\partial \hat{v}_i}{\partial x_i} \right) \mathrm{d}\Omega \\
& - \int\limits_{\Gamma} (\delta v_i) \left[-\hat{p} n_i + \rho \hat{v}_i v_j n_j + \mu n_j \frac{\partial \hat{v}_i}{\partial x_j} \right] \mathrm{d}\Gamma + \int\limits_{\Gamma} \mu \hat{v}_i \frac{\partial \delta v_i}{\partial x_j} n_j \, \mathrm{d}\Gamma \\
& - \int\limits_{\Omega} (\delta v_i) \left[\hat{v}_j \rho \frac{\partial v_j}{\partial x_i} - v_j \rho \frac{\partial \hat{v}_i}{\partial x_j} - \frac{\partial}{\partial x_j} \Big(2\mu \hat{S}_{ij} - \hat{p} \delta_{ij} \Big) \right] \mathrm{d}\Omega.
\end{aligned} \tag{4.56}$$

This expression is general and requires only the assumptions made for the satisfaction of Eq. (4.36). However, the goal of the analysis is to arrive at an expression for $\delta_{u_k} \mathcal{L} \cdot \delta u_k$ of the Hadamard form, cf. Eq. (3.5), where δu_k is associated with θ_j therein. To do so, certain aspects regarding the objective functional need to be specified.

It is usual in the context of blood flows that the objective functional is defined exclusively on Γ_{in} or Γ_{out}. Therefore, $\partial j_\Omega / \partial y_m = 0$ everywhere and the field adjoint equations, Eqs. (4.41), (4.42), include no contributions from the objective. Their satisfaction therefore leads to vanishing volume integrals in Eq. (4.56). Furthermore, the variation of the control δu_k is only defined in sections under design that are a subset of the wall patch, i.e. $\Gamma_{\text{d}} \subset \Gamma_{\text{w}}$. Based on the assumption that $\hat{J}$ is defined on Γ_{in} or Γ_{out}, this leads to $\delta_{u_k} \hat{J} \cdot \delta u_k = 0$. Furthermore, as shown in Section 4.2.3, it is deduced that $\hat{v}_i = 0$ on Γ_{w}

and thus Γ_d which finally allows us to simplify Eq. (4.56) to

$$\delta_{u_k}\mathcal{L} \cdot \delta u_k = \int\limits_{\Gamma_\mathrm{d}} (\delta v_i) \left[\hat{p} n_i - \mu n_j \frac{\partial \hat{v}_i}{\partial x_j}\right] \mathrm{d}\Gamma. \tag{4.57}$$

Finally it is required that δv_i is associated with δu_k. This is done by a first order Taylor series expansion on the wall as suggested by Soto and Löhner [2004], viz.

$$\begin{aligned} v_i\left(u_j + (\delta u_k n_k) n_j\right) &\approx v_i(u_j) + \frac{\partial v_i}{\partial x_j} n_j (\delta u_k n_k) \\ v_i\left(u_j + (\delta u_k n_k) n_j\right) - v_i(u_j) := \delta v_i &\approx \frac{\partial v_i}{\partial x_j} n_j (\delta u_k n_k), \end{aligned} \tag{4.58}$$

where it is assumed that any possible small variation of the control (shape) is in the normal direction of the surface. Substituting Eq. (4.58) in Eq. (4.57) leads to

$$\delta_{u_k}\mathcal{L} \cdot \delta u_k = \int\limits_{\Gamma_\mathrm{d}} \delta u_k n_k \left[\hat{p} \frac{\partial v_i}{\partial n} n_i - \mu \frac{\partial \hat{v}_i}{\partial n} \frac{\partial v_i}{\partial n}\right] \mathrm{d}\Gamma, \tag{4.59}$$

which is of the Hadamard form and we can thus set based on Eq. (3.5)

$$s = \hat{p} \frac{\partial v_i}{\partial n} n_i - \mu \frac{\partial \hat{v}_i}{\partial n} \frac{\partial v_i}{\partial n}. \tag{4.60}$$

The use of Eq. (4.60) to obtain the shape sensitivity requires the following assumptions:

- The assumptions made in Section 4.2.3 must hold.
- The objective must be defined exclusively on Γ_in, Γ_out or $\Gamma_\mathrm{in} \cup \Gamma_\mathrm{out}$.

These assumptions are frequently valid for the shape optimization of blood-related geometries and in the absence of additional constraints, Eq. (4.60) holds for an approximation of the shape sensitivity.

4.2.5 Numerical Solution

The numerical solution of the adjoint field equations (4.41), (4.42) closely follows the FV procedure described in Chapter 2. The equations are (similarly) discretized and then for each equation an under-relaxed algebraic equation system is solved to acquire the discrete adjoint solution. Even though the adjoint system is inherently linear to the unknowns, the coupling of adjoint pressure and adjoint velocity is similar to the primal problem and thus an adjoint counterpart to the SIMPLE algorithm is used, see Stück and Rung [2013]. Furthermore, due to the dependence of the adjoint problem to the primal variables, its numerical solution is based on a restart from the corresponding converged primal solution. This enables the exchange of the primal variables from the last outer iteration (or time step, if applicable) of the primal solver. Therefore, during the numerical solution of the adjoint problem, all the corresponding primal variables are assumed as known.

The main differences between the primal problem and the dual in terms of the discretization strategy relate to

- the change of information transfer for the convective term and
- the additional term $\hat{v}_j \rho \frac{\partial v_j}{\partial x_i}$ in the adjoint momentum equations, usually denoted as the *advection term* or *ATC term*.

The objective contributions are by definition independent of the adjoint variables and are thus always treated explicitly as RHS contributions to the adjoint algebraic equation system. Their treatment follows the discretization strategy outlined for the source term of the primal system.

Convective term

As discussed in Section 2.1.3, the convective term of the primal problem results in LHS contributions of the algebraic equation system in the form of $\dot{m}^{\mathrm{F}} \phi^{\mathrm{F}}$, where the face values follow from interpolation strategies of the cell-centered values of the adjacent cells. However, in the adjoint momentum equations the corresponding convective term exhibits two peculiarities that don't allow for the direct application of the primal strategy. Firstly, the adjoint velocity is transported based on the primal velocity, which also results in the linearity of the equations in contrast to their primal counterpart. Secondly, the sign of the term is reversed in comparison to the primal term due to the application of Gauss divergence theorem during the derivation process, cf. Eq. (4.32).

The adjoint convective term for the P CV (see notation of Section 2.1.3) reads

$$-\int\limits_{V^{\mathrm{P}}} v_j\, \rho \frac{\partial \hat{v}_i}{\partial x_j}\, \mathrm{d}V = -\int\limits_{O(V^{\mathrm{P}})} \rho\, v_j n_j \hat{v}_i \, \mathrm{d}S = -\sum_{\mathrm{N(P)}} \int\limits_{\Delta\Gamma} \rho v_j n_j \hat{v}_i \, \mathrm{d}\Gamma. \tag{4.61}$$

Similarly to the primal considerations, one can consider one face and write based on the midpoint rule

$$-\int\limits_{\Delta\Gamma} \rho v_j n_j \hat{v}_i \, \mathrm{d}\Gamma \approx -[\rho v_j n_j \Delta\Gamma]^{\mathrm{F}} \hat{v}_i^{\mathrm{F}} = -\dot{m}^{\mathrm{F}}\, \hat{v}_i^{\mathrm{F}}. \tag{4.62}$$

Therefore, each i^{th} component of the discretized adjoint momentum equations inheres LHS contributions in the form of Eq. (4.62). Note that in contrast to the primal system, $\dot{m}^{\mathrm{F}}$ doesn't increase the number of unknowns and doesn't require Picard-linearization since it involves only primal velocity, which is considered known. The approximation of $\hat{v}_i^{\mathrm{F}}$ based on cell-centered values can follow the same procedure as the ones mentioned in Section 2.1.3. Mind that the information transfer is reversed thus implying a direction reversal of the employed schemes, e.g., upwind schemes are replaced by downwind.

Advection term

The advection term for the P CV reads

$$\int\limits_{V^{\mathrm{P}}} \rho\, \hat{v}_j \frac{\partial v_j}{\partial x_i}\, \mathrm{d}V. \tag{4.63}$$

A straightforward approach is to explicitly treat this term in a Picard-linearized fashion, i.e., Eq. (4.63) is discretized as a source term where the cell-centered value of $\hat{v}_j$ is used from the previous iteration. In all applications presented in this thesis, this is the approach used for the advection term.

However, it must be noted that in high Re flows the advection term can often result in numerical instabilities of the adjoint system. Therefore, different approaches have been proposed for its treatment, see e.g., Stück [2012]. In certain cases, it can also be omitted to ensure the stability of the equation system in the expense of dual consistency.

Furthermore, it is interesting to note that the advection term can have different formulations based on the derivation path followed to arrive at the adjoint equations. Particularly interesting is the approach followed in Othmer [2008]. The I_2 subintegral of the Lagrangian can be equivalently written as

$$\underbrace{\int\limits_{\Omega} \hat{v}_i \Big(\rho \frac{\partial(v_j v_i)}{\partial x_j}\Big)\,\mathrm{d}\Omega}_{I_2^*}, \tag{4.64}$$

where the convective term is not simplified based on the continuity equation for an incompressible fluid. The variation of I_2^* in the direction of velocity then reads

$$\begin{aligned}\delta_{v_i} I_2^* \cdot \delta v_i &= \int\limits_{\Omega} \hat{v}_i \Big(\rho \frac{\partial(\delta v_j v_i)}{\partial x_j}\Big)\,\mathrm{d}\Omega + \int\limits_{\Omega} \hat{v}_i \Big(\rho \frac{\partial(v_j \delta v_i)}{\partial x_j}\Big)\,\mathrm{d}\Omega \\ &= \int\limits_{\Gamma} \rho\,\delta v_i\,(\hat{v}_j v_j n_i + \hat{v}_i v_j n_j)\,\mathrm{d}\Gamma - \int\limits_{\Omega} (\delta v_i)\rho v_j \left(\frac{\partial \hat{v}_i}{\partial x_j} + \frac{\partial \hat{v}_j}{\partial x_i}\right)\mathrm{d}\Omega.\end{aligned} \tag{4.65}$$

Based on this, the advection term reads

$$-\int\limits_{V^{\mathrm{P}}} \rho\, v_j \frac{\partial \hat{v}_j}{\partial x_i}\,\mathrm{d}V, \tag{4.66}$$

which in comparison to the term of Eq. (4.63) differs only by a change of the sign and a swap of adjoint and primal velocity. Note that this derivation approach also alters the applied BCs due to an additional term appearing on the corresponding surface integral. The discrete treatment of this term can also be explicitly realized.

Optimization process with the adjoint method

A general algorithmic strategy for parameter-free shape optimization is schematically presented in Chapter 3, Algorithm 1. Therein, it is assumed that a sensitivity distribution s on Γ is given. Herein this step is extended to include the algorithmic consideration of the adjoint method. The modified process is presented in Algorithm 2. The notation is also modified to stay consistent with this section.

It must be noted that step 4 of Algorithm 2 corresponds to a post-processing step of the adjoint problem and doesn't amount to any substantial computational cost. Based on the above, it becomes clear that with the use of the adjoint method the computational cost for the determination of the sensitivity distribution amounts only to the cost of realizing step 3, i.e. the computation of the adjoint problem, independent of the number of faces used to discretize Γ. Overall, based on Algorithm 2 the computational cost for one shape update in CFD-based applications is equal to the cost of steps 2, 3 and 5. Considering that the

Algorithm 2 General parameter-free shape optimization algorithm using the adjoint method.

```
Require: initial shape $\Gamma^0$, $\epsilon > 0$
for $i = 0, 1, ...$ do
    Compute the primal problem to find $\hat{J}(u_k^i)$ and the primal state $y_m^i(u_k^i)$.
    $\boxed{\text{Compute the adjoint problem to find the adjoint state } \hat{y}_l^i}$.
    Calculate the sensitivity distribution $s$ on $\Gamma^i$ based on $y_m^i$ and $\hat{y}_l^i$.
    Compute a descent direction $\delta u_k \in \Omega^i$ based on one of the methods presented in Chapter 3.
    if $|\hat{J}'(\Omega^i)(\delta u_k)| \leq \epsilon$ then
        break
    end if
    Determine step size $t^i$.
    Update shape based on Eq. (3.2).
end for
```

cost for computing the adjoint problem is usually comparable to that of the primal solution and that for most presented methods in Chapter 3 the cost of computing an appropriate descent direction is trivial compared to the solution of the primal problem, the total cost amounts to approximately 2 CFD solutions per shape update.

4.2.6 Verification Study

This section targets to verify the proposed sensitivity, cf. Eq. (4.60). In contrast to the verification examples shown in Chapter 2, an analytical solution for the derived sensitivity field is oftentimes impossible to obtain. To this extent, the derived expression is verified against the sensitivity computed based on second-order accurate FD, see Section 4.1.1. Due to the substantial cost of performing FD, the study is restricted to a 2D example and the sensitivity is computed only for the initial shape. The exemplary application is chosen so that it relates to characteristics relevant to blood flows. In specific, a stenosed geometry which relates to a generic arterial stenosis (Jeong and Rhee [2009]) is investigated, as shown in Fig. 4.2 (left). The shape of the stenosis is modeled based on a cosine curve, namely

$$h^s(x) = \frac{\delta}{2}\left[1 + cos\Big(\pi\frac{x - x_1}{x_0}\Big)\right] \quad \text{in} \quad (x_1 - x_0) \leq x \leq (x_1 + x_0), \tag{4.67}$$

where $x_1 = L/2$ denotes the longitudinal position of the stenosis center, x_0 refers to half the length of the stenosis and $\delta = H/4$ to its maximum height. The geometry is discretized with 12000 CVs with an average dimensionless near-wall spacing on Γ_d of approximately $y^+ \approx \mathcal{O}(10^{-2})$. The employed structured grid is progressively refined towards the design section, as shown in Fig. 4.2 (right). On the inlet patch a parabolic Poiseuille velocity

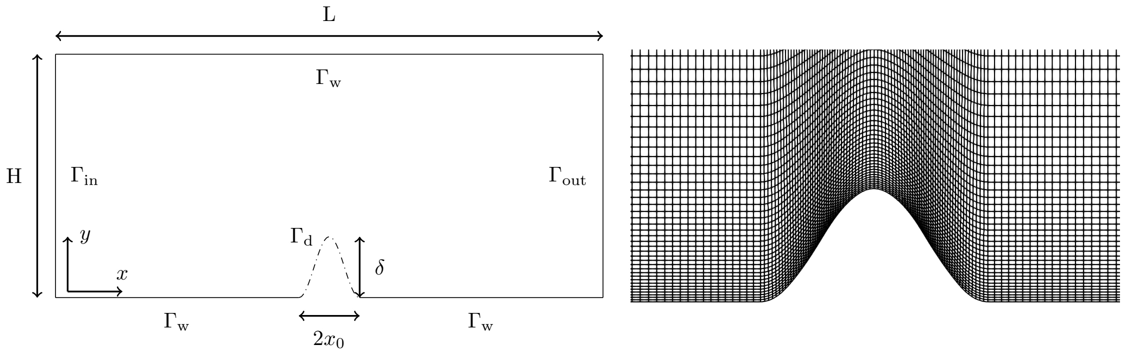

Figure 4.2: Left: Sketch of the 2D geometry for the FD study. Dashed line corresponds to the design section (Γ_d). The origin coincides with the leftmost lowest point of the geometry. Right: Detail of the employed numerical grid near the design section.

profile is set, viz.

$$v_x^\mathrm{in} = 2\,V\left(1 - \left(\frac{2y - \mathrm{H}}{\mathrm{H}}\right)^2\right). \tag{4.68}$$

The static pressure is set to zero on the outlet, while the walls follow a no-slip boundary condition. The molecular viscosity is set equal to the Newtonian blood viscosity, i.e., $\mu = 3.5$ mPa·s, cf. Table 2.4, and the density is set to $\rho = 1056$ kg/m^3 amounting to $\mathrm{Re} = \rho V \mathrm{H}/\mu = 12$.

The verification study is realized for the dissipated power objective functional, i.e.

$$\hat{J} = -\int_\Gamma \left(p + \frac{1}{2}\rho(v_k v_k)\right) v_i n_i \,\mathrm{d}\Gamma, \tag{4.69}$$

which corresponds to a quantity of frequent engineering interest due to its obvious correlation with power losses caused by the flow. Even in biomedical applications the impact of the quantity is not trivial. Studies have suggested the use of energy dissipation as an index to quantify the severity of aortic stenosis (Garcia et al. [2000]) or discussed the metric as a crucial parameter in certain surgical techniques (Grigioni et al. [2006]), such as Fontan-type interventions (Fontan and Baudet [1971]).

Note that due to the no-slip BC on the wall, the objective functional relates exclusively to Γ_in and Γ_out. Furthermore, due to the no-slip condition, $j_\Gamma = 0$ on Γ_d and therefore the necessary assumptions made in Section 4.2.4 are fulfilled. For the sake of completeness, the necessary derivatives of the objective functional in the direction of the state read

$$\begin{aligned} &\frac{\partial j_\Omega}{\partial y_m} = 0, \quad \frac{\partial j_\Gamma}{\partial p} = -v_i n_i \quad \text{and} \\ &\frac{\partial j_\Gamma}{\partial v_i} = -\left(p + \frac{1}{2}\rho(v_k v_k)\right) n_i - \rho(v_j n_j) v_i. \end{aligned} \tag{4.70}$$

The FD study is realized by perturbing individual faces of the discretized design surface in their normal direction, as shown in Fig. 4.3. The center and corresponding nodes of each discrete face, included in the study, is perturbed in both positive and negative

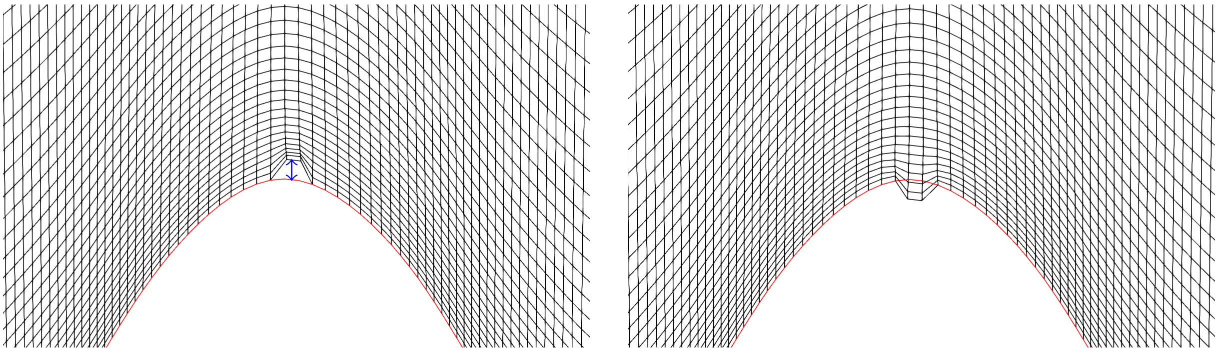

Figure 4.3: Perturbed numerical grid for the determination of sensitivity near the midpoint of the stenosis. Red line indicates the initial design surface, blue arrow denotes the length ϵ of the perturbation. Left: Perturbation in the negative normal direction. Right: Equal perturbation in the positive normal direction. Perturbation size is exaggerated for visual purposes.

normal directions by ϵ to facilitate a second-order accurate sensitivity approximation. The internal mesh is deformed based on Eq. (3.12). Each simulation is warm started from the unperturbed primal solution, thus allowing a significant gain in computational effort. Once the FD simulations are converged, the local surface sensitivity is estimated for a surface patch F based on

$$s^{\mathrm{F,FD}} = \frac{[\hat{J}(u_k^{\mathrm{F}} + \epsilon\, n_k^{\mathrm{F}}) - \hat{J}(u_k^{\mathrm{F}} - \epsilon\, n_k^{\mathrm{F}})]}{2\epsilon} \frac{1}{2\, A^{\mathrm{F}}}, \tag{4.71}$$

where u_k^{F} represents the position vector of the design face center and A^{F} is the corresponding perturbed area, which is used as a support area for unit consistency. As regards the latter, the nodes of the perturbed face are also nodes of the two neighbouring faces which results in them being also perturbed, cf. Fig 4.3. Assuming that neighbouring faces have approximately the same area, this means that the total area perturbed by ϵ is approximately equal to twice the area of the intended face (half contribution from each neighbour), which results in dividing the expression by $2A^{\mathrm{F}}$ in Eq. (4.71) instead of A^{F}.

For a reliable comparison of FD-based ($\epsilon = \delta \cdot 10^{-4}$) sensitivities against adjoint-based ones, it is important to verify that the chosen perturbation magnitude ϵ is sufficiently small and the approximated derivative lies satisfactorily within a regime dominated by a linear response, as discussed in Section 4.1.1. This is done by estimating the response of the objective functional for different perturbation sizes on one design face, as shown in Fig. 4.4 (right). Figure 4.4 (left) shows the FD-based and adjoint-based shape sensitivity estimations. As shown therein, the "continuous" results of the adjoint method based on expression (4.60) match satisfactorily the FD-based local results.

This study serves to verify the numerical implementation of the adjoint solver as well as its mathematical validity in terms of computational studies.

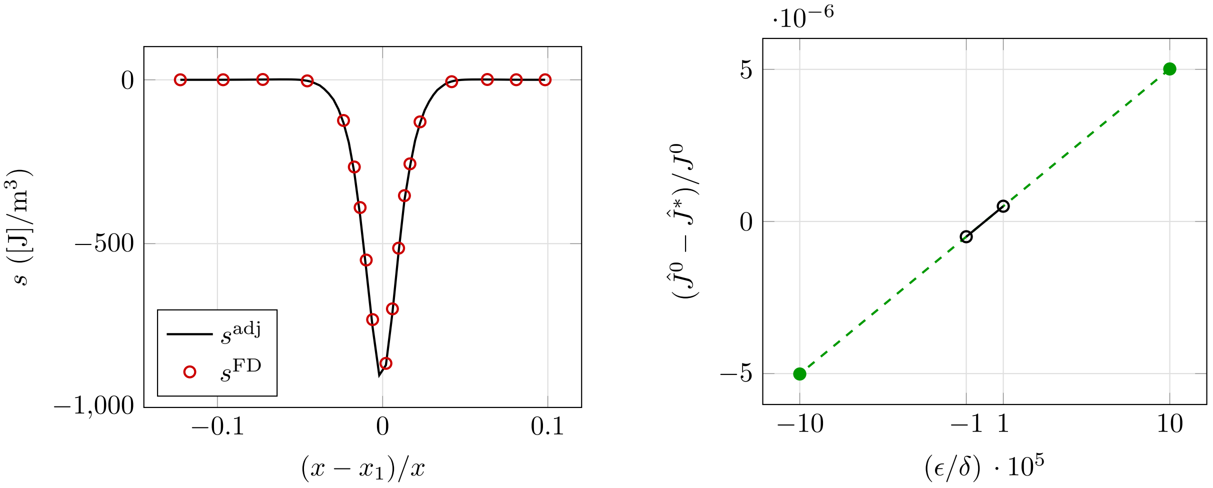

Figure 4.4: Left: Shape sensitivity estimations based on the adjoint method (continuous black line) and the FD method for $\epsilon = \delta \cdot 10^{-4}$ (red circles). Right: Influence of perturbation magnitude ϵ on $s^{\mathrm{F,FD}}$ for $u_k^{\mathrm{F}} = (x_1, \delta)$. The computed objective functionals of the unperturbed and perturbed shapes are denoted by $\hat{J}^0$ and $\hat{J}^*$, respectively.

4.3 Continuous Adjoint Navier-Stokes Equations with Hemolysis Modeling

Section 4.2 presented the derivation of the continuous adjoint equations for a primal flow described by the NS equations on a steady-state, laminar flow for an incompressible, Newtonian fluid. Assumptions relevant to the usual conditions applied in blood flow simulations were made to simplify the dual problem and derive a sensitivity expression. While the derived expressions presented therein are sufficiently general to be used in various blood-flow related optimization problems, they fall short on explicitly accounting for hemolysis. This section is therefore devoted to the derivation and implementation of a novel adjoint system, consistent to the primal problem involving hemolysis modeling. The foundation of the necessary additional derivations, as well as the employed notation, are based on Section 4.2. The problem described therein will be referred to as the *initial problem* in this section.

When hemolysis modeling is included in the primal problem, in addition to the NS equations (4.20), (4.21) the residual equation for hemolysis must be considered. In the derivations that follow, the threshold consideration described in Section 2.2 is neglected and the residual hemolysis equation reads

$$R^H = v_i \frac{\partial H_L}{\partial x_i} - C^{\frac{1}{\beta}} \bar{\tau}^{\frac{\alpha}{\beta}} \left(1 - H_L\right) = 0. \tag{4.72}$$

Note that due to the one-way coupling of the employed hemolysis model, the residual NS equations remain unchanged. The primal state is augmented to include the linearized hemolysis index, viz.

$$y_m = (p, v_1, v_2(, v_3), H_L). \tag{4.73}$$

The goal of the optimization problem is to minimize hemolysis. To this extent and in the context of adjoint-based optimization a suitable scalar functional able to serve as an objective functional for the derivation of the adjoint system is needed. As discussed in Section 2.2.4, Eq. (2.69) serves as an appropriate scalar quantity to evaluate the extent to which the flow has damaged the blood. In fact, given that the inlet and outlet surfaces are bound to their initial configuration, the denominator of HI (cf., Eq. (2.69)) is constant. Hence the numerator of HI is considered as an appropriate objective functional, viz.

$$\hat{J} = \int\limits_{\Gamma_{\text{out}}} H_L^{\beta} \rho v_i n_i \, \mathrm{d}\Gamma = \int\limits_{\Gamma_{\text{out}}} j_{\Gamma} \, \mathrm{d}\Gamma \tag{4.74}$$

and its variations in the direction of the primal state read

$$\begin{aligned} \delta_p \hat{J} \cdot \delta p = 0, \quad \delta_{v_i} \hat{J} \cdot \delta v_i &= \int\limits_{\Gamma_{\text{out}}} \delta v_i \left(\rho H_L^{\beta} n_i\right) \mathrm{d}\Gamma, \\ \delta_{H_L} \hat{J} \cdot \delta H_L &= \int\limits_{\Gamma_{\text{out}}} \delta H_L \left(\rho \beta H_L^{(\beta-1)} v_i n_i\right) \mathrm{d}\Gamma. \end{aligned} \tag{4.75}$$

The Lagrangian is then formulated as

$$\mathcal{L} = \hat{J} + \int\limits_{\Omega} \hat{y}_l R_l \, \mathrm{d}\Omega = \hat{J} + \int\limits_{\Omega} \left[\hat{p} R^p + \hat{v}_i R_i^v + \hat{h} R^H \right] \mathrm{d}\Omega, \tag{4.76}$$

where the adjoint state is accordingly augmented with adjoint hemolysis, i.e., $\hat{h}$, to account for the primal hemolysis equation. If the same process as in Section 4.2 is followed and the volume integral is decomposed to subintegrals consisting of isolated terms of the primal equations then due to the one-way coupling, integrals $I_1, \ldots, I_4$ are the same and two additional subintegrals are introduced,

$$\sum_{l=1}^{4} I_l + \underbrace{\int\limits_{\Omega} \hat{h} \Big(v_i \frac{\partial H_L}{\partial x_i} \Big) \mathrm{d}\Omega}_{I_5} + \underbrace{\int\limits_{\Omega} \hat{h} \Big(- C^{\frac{1}{\beta}} \bar{\tau}^{\frac{\alpha}{\beta}} \left(1 - H_L\right) \Big) \mathrm{d}\Omega}_{I_6} .$$

For conditions (4.30) to hold, one has to account for the variations of the hemolysis equation in the direction of the state, i.e., $\delta_{y_m} I_5 \cdot \delta y_m$ and $\delta_{y_m} I_6 \cdot \delta y_m$.

4.3.1 Variations of the Hemolysis Equation

Similar to Section 4.2.1, each subintegral is treated separately and the number of the enumerated list refers to the considerations made for the respective subintegral.

5. Since I_5 doesn't directly depend on p it follows that $\delta_p I_5 \cdot \delta p = 0$. The variation in the direction of v_i reads

$$\delta_{v_i} I_5 \cdot \delta v_i = \int\limits_{\Gamma} (\delta v_i n_i) \hat{h} H_L \, \mathrm{d}\Gamma - \int\limits_{\Omega} \delta v_i H_L \frac{\partial \hat{h}}{\partial x_i} \mathrm{d}\Omega, \tag{4.77}$$

if the Gauss divergence theorem is applied or if not

$$\delta_{v_i} I_5 \cdot \delta v_i = \int\limits_{\Omega} \delta v_i \hat{h} \frac{\partial H_L}{\partial x_i} \mathrm{d}\Omega. \tag{4.78}$$

The variation of I_5 in the direction of H_L reads

$$\delta_{H_L} I_5 \cdot \delta H_L = \int\limits_{\Gamma} \delta H_L \left(v_i n_i \hat{h} \right) \mathrm{d}\Gamma - \int\limits_{\Omega} \delta H_L \left(v_i \frac{\partial \hat{h}}{\partial x_i} \right) \mathrm{d}\Omega. \tag{4.79}$$

6. The variation of I_6 in the direction of pressure vanishes, i.e., $\delta_p I_6 \cdot \delta p = 0$. For the variation in the direction of velocity one needs to consider that $\bar{\tau}$ is a function of velocity and treat the term accordingly. Recall from Eqs. (2.59) and (2.60) that in a converged state of the primal, the scalar representative of shear stress can be computed as

$$\bar{\tau} = \sqrt{-k I_{\tau_2}} = \left(2 k \mu^2 S_{ij} S_{ij} \right)^{\frac{1}{2}} := {\tau^*}^{\frac{1}{2}}, \tag{4.80}$$

where τ^* is introduced to simplify the derivation process, by once linearizing w.r.t. velocity. Furthermore, one can denote $M = C^{\frac{1}{\beta}}(1 - H_L)$ and write

$$I_6 = -\int\limits_{\Omega} \hat{h} M \tau^{*\frac{\alpha}{2\beta}} \,\mathrm{d}\Omega,$$

where its variation in the direction of velocity reads

$$\delta_{v_i} I_6 \cdot \delta v_i = -\int\limits_{\Omega} \hat{h} \left(4k\mu^2 M \frac{\alpha}{2\beta} \tau^{*(\frac{\alpha}{2\beta}-1)} S_{ij} \right) \delta S_{ij} \,\mathrm{d}\Omega, \tag{4.81}$$

where $\delta S_{ij} = 0.5\,(\partial \delta v_i / \partial x_j + \partial \delta v_j / \partial x_i)$. By defining $B_{ij} = 2Mk\mu^2 \frac{\alpha}{\beta} \tau^{*(\frac{\alpha}{2\beta}-1)} S_{ij}$ and taking advantage of $B_{ij} \sim S_{ij} \rightarrow B_{ij} = B_{ji}$, a compact form of Eq. (4.81) is further expanded as

$$\begin{aligned}
\delta_{v_i} I_6 \cdot \delta v_i &= -\int\limits_{\Omega} \hat{h} \frac{1}{2} B_{ij} \left(\frac{\partial \delta v_i}{\partial x_j} + \frac{\partial \delta v_j}{\partial x_i} \right) \mathrm{d}\Omega = -\int\limits_{\Omega} \hat{h} B_{ij} \left(\frac{\partial \delta v_i}{\partial x_j} \right) \mathrm{d}\Omega \\
&= -\int\limits_{\Gamma} \delta v_i \left(\hat{h} B_{ij} n_j \right) \mathrm{d}\Gamma + \int\limits_{\Omega} \delta v_i \left(\frac{\partial (\hat{h} B_{ij})}{\partial x_j} \right) \mathrm{d}\Omega,
\end{aligned} \tag{4.82}$$

which results in a suitable formulation to be used in the optimality conditions. Finally, the variation of I_6 in the direction of hemolysis reads

$$\delta_{H_L} I_6 \cdot \delta H_L = \int\limits_{\Omega} \delta H_L \left(\hat{h} C^{\frac{1}{\beta}} \bar{\tau}^{\frac{\alpha}{\beta}} \right) \mathrm{d}\Omega. \tag{4.83}$$

4.3.2 Field Adjoint Hemolysis Equations

Based on the additional volume integrals arising from the variations of I_5 and I_6 and the specification of the objective functional based on Eq. (4.74), the field adjoint equations are reformulated to

$$\hat{R}^p = -\frac{\partial \hat{v}_i}{\partial x_i} = 0 \tag{4.84}$$

$$\hat{R}_i^v = \hat{v}_j \rho \frac{\partial v_j}{\partial x_i} - v_j \rho \frac{\partial \hat{v}_i}{\partial x_j} - \frac{\partial}{\partial x_j} \left(2\mu \hat{S}_{ij} - \hat{p}\delta_{ij} - \boxed{\hat{h} B_{ij}} \right) - \boxed{H_L \frac{\partial \hat{h}}{\partial x_i}} = 0 \tag{4.85}$$

$$\hat{R}^H = v_i \frac{\partial \hat{h}}{\partial x_i} - C^{\frac{1}{\beta}} \bar{\tau}^{\frac{\alpha}{\beta}} \hat{h} = 0. \tag{4.86}$$

Note that these equations employ Eq. (4.77) instead of Eq. (4.78). The adjoint momentum equations are augmented with the two additional boxed terms, relating to primal and adjoint hemolysis. An additional linear equation, Eq. (4.86), is introduced and referred to as adjoint hemolysis equation. Its solution results in the determination of adjoint hemolysis.

The additional terms enhancing the adjoint momentum equations are independent of adjoint velocity and therefore act as source terms. These terms act similar to the adjoint pressure term and the viscous term and thereby enhance the adjoint flow mechanics based on the adjoint hemolysis. Furthermore, it is interesting to note that in contrast to its primal counterpart, the adjoint hemolysis equation does not require any information from the solution of the adjoint continuity and momentum equations. Once again, we have a one-way coupling but this time the direction of the coupling and thereby the algorithmic order of sequence is reversed. The derived expressions resemble adjoint systems where the NS equations are augmented by a convection equation, e.g. the adjoint complement of the Volume of Fluid (VoF) method for multi-phase applications (Kühl et al. [2021], Kröger et al. [2018]).

4.3.3 Boundary Adjoint Hemolysis Conditions

Similar to the initial problem of Section 4.2, the boundary conditions are deduced by demanding that the surface integrals appearing in the state variations of the Lagrangian vanish. The surface integrals that need to disappear in the context of the adjoint complement to hemolysis are

$$\begin{aligned}\delta_{y_m}\mathcal{L}\cdot\delta y_m\Big|_{\Gamma} &= \int\limits_{\Gamma}(\delta p)\left(\hat{v}_i n_i\right)\,\mathrm{d}\Gamma - \int\limits_{\Gamma}\mu\hat{v}_i\frac{\partial\delta v_i}{\partial x_j}n_j\,\mathrm{d}\Gamma \\ &+ \int\limits_{\Gamma}(\delta v_i)\left[-\hat{p}n_i + \rho\hat{v}_i v_j n_j + \mu n_j\frac{\partial\hat{v}_i}{\partial x_j} + \boxed{H_L\hat{h}n_i} - \boxed{\hat{h}B_{ij}n_j} + \frac{\partial j_\Gamma}{\partial v_i}\right]\mathrm{d}\Gamma \\ &+ \boxed{\int\limits_{\Gamma}(\delta H_L)\left(\hat{h}v_i n_i + \frac{\partial j_\Gamma}{\partial H_L}\right)\mathrm{d}\Gamma},\end{aligned} \tag{4.87}$$

where the boxed terms denote the additional contributions due to the consideration of hemolysis.

Similarly to Section 4.2.3, the analysis that follows is subdivided to each boundary section of the domain.

Inlet and non-design wall

On the inlet, blood is assumed to enter the domain undamaged, i.e., a zero Dirichlet boundary condition is set for H_L which implies $\delta H_L = 0$ and thus the last integral of Eq. (4.87) naturally vanishes. Furthermore, on the wall even though the boundary condition for hemolysis is zero Neumann, the no-slip boundary condition for velocity in addition to $\partial j_\Gamma/\partial H_L = 0$ therein leads again to the natural cancellation of the last integral of Eq. (4.87) by virtue of the primal problem. Similarly to the initial problem, the third integral (second line) of Eq. (4.87) vanishes by virtue of the Dirichlet velocity BCs. The remaining integrals that ought to be cancelled are therefore the same integrals as for the initial problem, since they don't include any novel contributions from the consideration of hemolysis. Based on the argumentation followed in Section 4.2.3, these integrals vanish for

$$\hat{v}_i = 0 \quad \text{on } \Gamma_{\text{in}} \cup \Gamma_{\text{w}}. \tag{4.88}$$

However, similarly to adjoint pressure, the analysis falls short on providing the necessary information for deducing the adjoint hemolysis variable. Since, adjoint hemolysis acts on the adjoint momentum equations similarly to the adjoint pressure term, a zero Neumann condition is set for both to close the dual problem, i.e.

$$\frac{\partial \hat{p}}{\partial n} = 0 \quad \text{and} \quad \frac{\partial \hat{h}}{\partial n} = 0 \quad \text{on } \Gamma_{\text{in}} \cup \Gamma_{\text{w}}. \tag{4.89}$$

Outlet

On the outlet the first two integrals of Eq. (4.87) naturally vanish by virtue of the primal BCs. Starting from the last integral, its cancellation for every δH_L suggests

$$\hat{h} v_i n_i + \rho\beta H_L^{\beta-1} v_i n_i = 0 \rightarrow \hat{h} = -\rho\beta H_L^{\beta-1} \quad \text{on } \Gamma_{\text{out}}, \tag{4.90}$$

providing the necessary BC for the adjoint hemolysis variable. Note that this condition creates a strong link between primal and adjoint hemolysis which implies that the resulting adjoint hemolysis field strongly depends on the outcome of hemolysis on the outlet. This is due to the definition of the objective. The remaining integral vanishes for every δv_i if

$$-\hat{p} + \rho\hat{v}_n v_n + \mu\frac{\partial \hat{v}_n}{\partial n} + H_L\hat{h} - \hat{h}\cancel{B_{ij}n_in_j} + \rho H_L^{\beta} = 0 \quad \text{on } \Gamma_{\text{out}}, \tag{4.91}$$

$$\rho\hat{v}_i^t v_n + \mu\frac{\partial \hat{v}_i^t}{\partial n} - \hat{h}B_{in}^t = 0 \quad \text{on } \Gamma_{\text{out}}. \tag{4.92}$$

where $B_{ij}n_in_j$ cancels out for incompressible fluids by virtue of $B_{ij} \sim S_{ij}$ and the zero Neumann BC applied on the outlet for primal velocity. Furthermore, if $\hat{h}$ from Eq. (4.90) is substituted in Eq. (4.91), then the latter simplifies to

$$-\hat{p} + \rho\hat{v}_n v_n + \mu\frac{\partial \hat{v}_n}{\partial n} + \rho H_L^{\beta}(1-\beta) = 0 \quad \text{on } \Gamma_{\text{out}}. \tag{4.93}$$

Equations (4.93) and (4.92) can be used to set BCs for adjoint pressure and tangential velocity component(s), respectively while similarly to the initial problem the normal adjoint velocity can be approximated by the satisfaction of adjoint continuity on the outlet boundary.

The assumptions set forth in the initial problem must also hold so that the above derived expressions are valid. In addition, the BCs described in Section 2.2.3 for primal hemolysis must hold.

4.3.4 Shape Sensitivity for Hemolysis

The same methodology as the one outlined in Section 4.2.4 is followed herein. In the absence of a volume-based objective functional, the satisfaction of the adjoint equations leads to the cancellation of the volume integrals. Keeping in mind that $\hat{v}_i, v_i = 0$ on the wall and that the objective is again defined in a section of the boundary not coinciding with the design wall, the sensitivity expression reads

$$\delta_{u_k}\mathcal{L}\cdot\delta u_k = \int\limits_{\Gamma_\text{d}} \delta u_k n_k \left[\left(\hat{p} - \boxed{H_L\hat{h}}\right)\frac{\partial v_i}{\partial n}n_i - \left(\mu\frac{\partial \hat{v}_i}{\partial n} - \boxed{\hat{h}B_{ij}n_j}\right)\frac{\partial v_i}{\partial n}\right] \mathrm{d}\Gamma, \tag{4.94}$$

where the boxed terms refer to the additional contributions in the sensitivity expression as compared to the one derived for the initial problem, cf., Eq. (4.59). At this point it is worth noting that given the assumption that continuity also holds on the boundary of the domain, the first term on the sensitivity expression vanishes by virtue of $(\partial v_i/\partial n)n_i$ being equal to zero on a wall boundary.

4.3.5 Numerical Solution

The numerical solution of the adjoint equations involving hemolysis, i.e., (4.84), (4.85) and (4.86), differ to the initial problem in two key aspects,

- the solution of the additional adjoint hemolysis equation and
- the treatment of the additional contributions to the adjoint momentum equations.

Each aspect is discussed separately below.

Adjoint hemolysis equation

As discussed in Section 4.3.2, the adjoint hemolysis equation is inherently decoupled from the adjoint NS equations and requires information only from the primal problem. This allows for a similar algorithmic strategy to its primal counterpart, only this time in reverse mode. That is, following the solution of the primal problem, the adjoint hemolysis equation can be first independently solved and its solution can be used for the solution of the adjoint NS equations.

Similar to primal hemolysis, its dual involves only a convective and source term. In adjoint mode, the convective term is usually treated by using the negative of the primal mass (or volume) face flux. Therefore, in order to stay consistent with the discretization techniques used for the adjoint momentum equation, the adjoint hemolysis equation is discretized in the form of $-\hat{R}^H = 0$. The approximation of face values of adjoint hemolysis follow the same schemes as the ones mentioned in Section 2.1.3. The source term refers to the cell-centered values $S = -C^{\frac{1}{\beta}}\tau^{\frac{\alpha}{\beta}}\hat{h}$.

It must be noted that the solution of this equation usually requires only a small fraction of the wall-clock time required for the solution of the adjoint NS equations.

Additional contributions to adjoint momentum

The adjoint momentum equations are augmented with two additional terms, cf. Eq. (4.85), as compared to the initial problem. These terms act as source terms and drive the adjoint flow. Note that both of these terms include exclusively primal variables and adjoint hemolysis. Therefore, their contribution in the RHS of the discretized adjoint momentum equation system needs to be computed only once after the solution of the adjoint hemolysis equation.

The first additional term appearing in Eq. (4.85) is moved to the RHS and is treated based on Gauss divergence theorem for the P CV as

$$-\int\limits_{V^{\mathrm{P}}} \frac{\partial(\hat{h}B_{ij})}{\partial x_j}\,\mathrm{d}V = -\int\limits_{O(V^{\mathrm{P}})} \hat{h}B_{ij}n_j\,\mathrm{d}S = -\sum_{\mathrm{N(P)}}\int\limits_{\Delta\Gamma} \hat{h}B_{ij}n_j\,\mathrm{d}\Gamma, \tag{4.95}$$

which based on the midpoint rule can be computed on each face comprising the P CV as

$$-\int_{\Delta\Gamma} \hat{h} B_{ij} n_j \,\mathrm{d}\Gamma \approx -\hat{h}^{\mathrm{F}} B_{ij}^{\mathrm{F}} n_j^{\mathrm{F}} \Delta\Gamma^{\mathrm{F}}, \tag{4.96}$$

where $\hat{h}^{\mathrm{F}}$ is computed based on Eq. (2.21), since its gradients are already known from the solution of adjoint hemolysis and B_{ij}^{F} is computed based on Eq. (2.19). Note that while the latter equation refers to scalar quantities, the same process is realized for each component of B_{ij}. The sum of these contributions are then added to the RHS of the discrete adjoint momentum equations for the P CV.

Special attention needs to be given to the CVs with at least one boundary face, in particular if the face refers to a wall boundary. On $\Gamma_{\mathrm{in}} \cup \Gamma_{\mathrm{w}}$, due to the zero Neumann boundary condition, adjoint hemolysis is set to the cell-centered value of the CV in which the face belongs, while on Γ_{out} the Dirichlet BC (Eq. (4.90)) is used to approximate $\hat{h}^{\mathrm{B}}$.

The approximation of B_{ij}^{B} is based on a zero-order extrapolation from the CV on $\Gamma_{\mathrm{in}} \cup \Gamma_{\mathrm{out}}$. However, recall that B_{ij} corresponds to a scaled version of the S_{ij} tensor and therefore its treatment on the wall is based on the latter. In specific, a local wall-mounted coordinate system is considered for the treatment of the strain rate tensor. Therein, and due to the continuity equation and the no-slip condition, the only components not cancelling out are those involving $\frac{\partial v_k^t}{\partial n}$, which need to be approximated. Using the plane Couette flow assumption, a first-order accurate approximation of this term reads

$$\frac{\partial v_k^t}{\partial n} = \frac{\left(v_k^{\mathrm{B}} - v_k^{\mathrm{P}}\right)^t}{\Delta n}, \tag{4.97}$$

where $\Delta n = |n_j(x_j^{\mathrm{B}} - x_j^{\mathrm{P}})|$ is the normal distance of the boundary face to the cell-center. The tangential difference of the velocities on the numerator can be computed as

$$\left(v_k^{\mathrm{B}} - v_k^{\mathrm{P}}\right)^t = \Delta v_k^t = \Delta v_k - (\Delta v_j n_j) n_k, \quad \text{where} \quad \Delta v_k = v_k^{\mathrm{B}} - v_k^{\mathrm{P}}. \tag{4.98}$$

Based on this, one can compute the normalized vector tangential to the surface as

$$t_k = \frac{\Delta v_k^t}{\sqrt{(\Delta v_i^t)^2}}. \tag{4.99}$$

Now as regards the treatment of B_{ij}^{B}, the quantities that need to be addressed are τ^*, cf. Eq. (4.80), which is involved in the scalar component of B_{ij} and $S_{ij} n_j$. The former can be computed on the wall as

$$(\tau^*)^{\mathrm{B}} = 2k\mu^2 (S_{ij} S_{ij})^{\mathrm{B}} \approx k\mu^2 \frac{\partial v_k^t}{\partial n} \frac{\partial v_k^t}{\partial n} \approx k \left(\mu \frac{\Delta v_k^t}{\Delta n}\right)^2. \tag{4.100}$$

Finally, the inner product of $S_{ij} n_j$ is computed based on the first order approximation (4.97) as

$$S_{ij} n_j \approx \frac{1}{2} \frac{(\Delta v_k t_k)}{\Delta n} t_i n_j n_j = \frac{1}{2} \frac{(\Delta v_k t_k)}{\Delta n} t_i. \tag{4.101}$$

Note that the same expression as in Eq. (4.96) appears in the sensitivity expression (4.94).

Therein, since $\Gamma_{\mathrm{d}} \subset \Gamma_{\mathrm{w}}$, the same discrete treatment as the one described above for a wall boundary is followed.

The second contribution on the adjoint momentum equations is treated as a usual source term, based on cell-centered values, viz.

$$\int\limits_{V^{\mathrm{P}}} H_L \frac{\partial \hat{h}}{\partial x_i} \, \mathrm{d}V \approx H_L^{\mathrm{P}} \left(\frac{\partial \hat{h}}{\partial x_i} \right)^{\mathrm{P}} V^{\mathrm{P}}. \tag{4.102}$$

The remaining terms in the adjoint NS equations are treated as in the initial problem.

4.3.6 Verification Studies

The verification studies conducted in this section serve a twofold purpose. Initially, the numerical implementation of the novel adjoint hemolysis equation is verified against analytical solutions. These are possible to derive due to the existence of analytical solutions to the primal problem (see Section 2.2.5) and its decoupled nature w.r.t. the adjoint NS. Secondly and similarly to the initial problem, the derived sensitivity expression is assessed based on a second-order accurate FD study.

The Hagen-Poiseuille pipe flow of Section 2.2.5 is considered. This allows us to arrive at the analytical solution of the primal velocity, shear stress and hemolysis, repeated herein for the convenience of the reader,

$$v_z(r) = V_{\max} \left(1 - \left(\frac{r}{R} \right)^2 \right) \quad \text{and} \quad \bar{\tau} = -2\mu V_{\max} \frac{r}{R^2} \quad \text{and} \quad H = \frac{C \bar{\tau}^{\alpha}}{v_z^{\beta}(r)} z^{\beta}. \tag{4.103}$$

Based on the above, the adjoint hemolysis equation reduces to the ordinary differential equation (ODE)

$$v_z(r) \frac{d\hat{h}}{dz} - C^{\frac{1}{\beta}} \bar{\tau}^{\frac{\alpha}{\beta}} \hat{h} = 0, \tag{4.104}$$

with the solution

$$\hat{h} = K e^{\frac{\Lambda}{v_z} z}, \tag{4.105}$$

where $\Lambda = C^{\frac{1}{\beta}} \bar{\tau}^{\frac{\alpha}{\beta}}$ and K is the integration constant. The latter is deduced based on the Dirichlet BC of adjoint hemolysis set on the outlet, cf. Eq. (4.90), which results in

$$\hat{h}(z, r) = -\rho \beta H_L^{\beta - 1} \Big|_{z_{\max}} e^{\frac{\Lambda}{v_z}(z - z_{\max})}, \tag{4.106}$$

where $z_{\max}$ denotes the longitudinal position of the outlet plane. Therefore, based on the analytical solutions (4.103), Eq. (4.106) serves as an analytical solution for the adjoint hemolysis equation in the case of a fully developed pipe flow.

Note that for the biological reasons described in Section 2.2, it always holds that $\beta < 1 \to (\beta - 1) < 0$ and since $H_L \in [0, 1]$, it is advised that the BC at the outlet is reformulated to $\hat{h}\Big|_{\Gamma_{\mathrm{out}}} = -\rho\beta \left(H_L + \epsilon \right)^{\beta - 1}$, with $\epsilon \approx \mathcal{O}(10^{-20})$, to avoid potential segmentation faults.

The computations are realized by restarting from the primal cases presented in Section 2.2.5 with a dense spatial discretization of 900k CVs. The convective term of the adjoint hemolysis equation is discretized using the corresponding downwind analogy to the QUICK scheme to allow for discretization consistency between the primal and dual problems. Figure 4.5 compares the computed adjoint hemolysis field against the derived analytical expression (4.106) for the three sets of hemolysis constants, cf. Table 2.1. The agreement between the two fields is excellent thus verifying the FV implementation for the solution of the adjoint hemolysis field. It should be noted that due to the nature of the BCs of the adjoint hemolysis equation, the field values are negative and thus the absolute values are presented to support a log-scale of the ordinate. Furthermore, it is worth noting that the complete adjoint hemolysis field is dominated by the BC set on the outlet and thus minimal changes are observed along the longitudinal direction of the pipe. This is due to the fully developed primal flow field and the geometry of the benchmark problem and does not generally hold for cases where the flow phenomena are more involved.

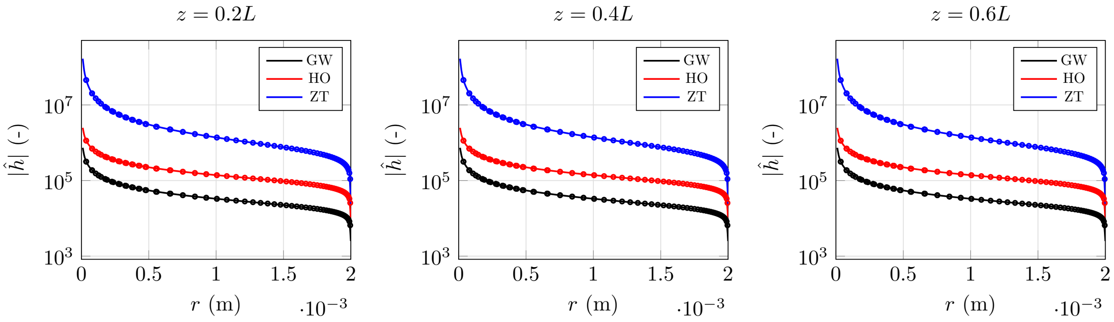

Figure 4.5: Absolute value of adjoint hemolysis profiles at three distinct longitudinal positions of the pipe flow. Continuous lines correspond to analytical solutions while points indicate computed values. Vertical axis in logarithmic scale.

The verification of the sensitivity expression of Eq. (4.94) is realized by means of a second-order accurate FD study, similar to what is done for the initial problem. The geometry considered for this study refers to a 2D symmetrically stenosed duct, as shown in Fig. 4.6. This geometry is chosen so that to include flow characteristics in which hemolysis has been shown to occur. It is also used as a simplified two-dimensional replicate of the optimization study conducted in Chapter 6, Section 6.1. The shape of the stenosis on the

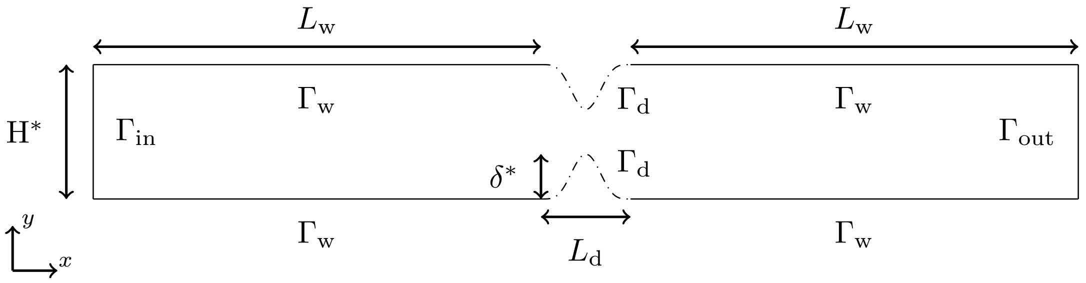

Figure 4.6: Sketch of the 2D double-stenosed geometry for the adjoint hemolysis FD study. The origin coincides with the leftmost lowest point of the geometry. Dashed lines correspond to the design section (Γ_d).

bottom wall follows from

$$y = \delta^* \left(\sin\left(\frac{\pi}{L_\mathrm{d}} x - \frac{\pi}{1000} \right) \right)^4, \quad \forall x \in [L_\mathrm{w}, L_\mathrm{w} + L_\mathrm{d}], \tag{4.107}$$

where δ^* is the height of the bump and amounts to $\delta^* = \mathrm{H}^*/3$, with H^* denoting the total height of the duct. The geometry is discretized with approximately 67000 CVs with an average dimensionless near-wall spacing on Γ_d of $y^+ \approx \mathcal{O}(10^{-2})$ for the flow conditions employed in this study. On the leftmost inlet boundary patch, a parabolic Poiseuille velocity profile is set, see Eq. (4.68). A zero static pressure is set on the outlet and all the walls follow a no-slip BC. The properties of the fluid are set to the Newtonian blood properties, $\mu = 3.5$ mPa·s and $\rho = 1056$ kg/m^3. The Reynolds number is set to $\mathrm{Re} = \rho V H^*/\mu \approx 30$.

All primal convective terms are discretized based on the QUICK scheme and the adjoint ones based on the downwind counterpart of QUICK. As regards, the primal and adjoint hemolysis equations, the study employs the GW set of hemolysis parameters, cf. Table 2.1 while $k = 1$ is used to compute the scalar representative of shear stress, see Eq. (2.60). The FD study is conducted as described in Section 4.2.6 with $\hat{J}$ standing for the numerator of HI, see Eq. (4.74).

In order to evaluate the reliability of the FD results, a perturbation magnitude study is initially conducted. The results, as shown in Fig. 4.7 (right), suggest that a perturbation magnitude of $\epsilon = \delta^* \cdot 10^{-5}$ lies satisfactorily within a linear response regime.

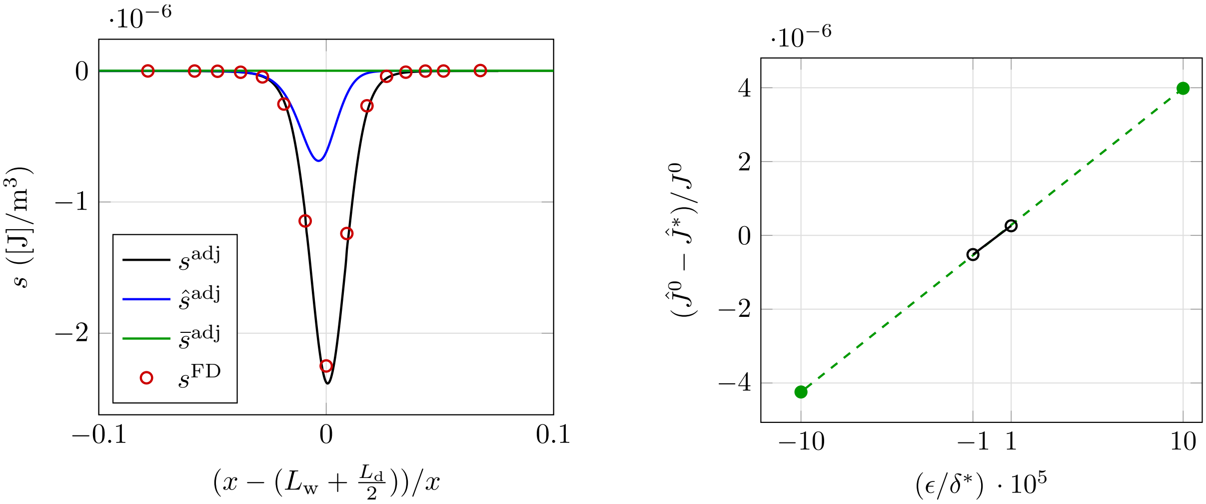

Figure 4.7: Left: Shape sensitivity estimations based on the consistent adjoint hemolysis model (continuous black line, s^adj), a semi-reduced adjoint model neglecting additional contributions in the adjoint momentum equations (continuous blue line, $\hat{s}^\mathrm{adj}$), a reduced adjoint model neglecting all additional contributions (continuous green line, $\bar{s}^\mathrm{adj}$) and the FD method for $\epsilon = \delta^* \cdot 10^{-5}$ (red circles). Right: Influence of perturbation magnitude ϵ on $s^\mathrm{F,FD}$ for $u_k^\mathrm{F} = (L_\mathrm{w} + \frac{L_\mathrm{d}}{2}, \delta^*)$. The computed objective functionals of the unperturbed and perturbed shapes are denoted by $\hat{J}^0$ and $\hat{J}^*$, respectively.

As regards the adjoint-based sensitivity, three individual cases are constructed. In all cases, the computed quantity refers to the bottom design wall. The first one considers the complete and consistent adjoint system as described in this section and the sensitivity is denoted as s^{adj}. The second one considers the possibility of neglecting contributions of adjoint hemolysis from the field adjoint momentum equations, i.e., neglecting the boxed terms in Eq. (4.85), thus resulting to only the additional contributions in the sensitivity expression, which require solely the solution of the (computationally inexpensive) adjoint hemolysis equation and the primal problem. This is denoted as $\hat{s}^{\mathrm{adj}}$. The third case neglects all additional contributions to the adjoint system, i.e., boxed terms from both the adjoint momentum and sensitivity expression are neglected, and is denoted as $\bar{s}^{\mathrm{adj}}$.

As shown in Fig. 4.7 (left), the consistent adjoint sensitivity satisfactorily matches the FD results. In contrast, the reduced quantity $\hat{s}^{\mathrm{adj}}$ falls short in estimating the sought sensitivity. Even though the additional boxed terms in (4.94) are the same as in the consistent case, the adjoint velocity is not properly predicted since the necessary additional terms in the adjoint momentum are neglected. Therefore, the terms involving adjoint velocity in the sensitivity expression are inaccurate, thus leading to an inaccurate sensitivity estimation. Finally, the case that neglects every additional hemolysis-based contribution results in a constant sensitivity of zero. This is to be expected, since neither the adjoint flow can be developed without the contributions from adjoint hemolysis nor do the decoupled contributions of adjoint hemolysis are taken into account.

Overall, the satisfactory agreement between the FD-based results and those predicted by the complete adjoint system verify the derivations of this section as well as their numerical implementation. Furthermore, this study highlights the importance of a consistent adjoint system, since reduced expressions might lead to inaccurate estimations that could potentially drive the optimization problem away from an optimal solution.

4.4 Continuous Adjoint non-Newtonian Navier-Stokes Equations

Having derived a suitable adjoint model able to account for hemolysis in Section 4.3, this section turns its focus on the non-Newtonian nature of blood and the necessary adjustments that need to be made in the adjoint problem to account for it. Some adjoint sensitivity studies have already been conducted based on non-Newtonian blood flows, see e.g. Abraham et al. [2005a,b]. However, in these studies viscosity is considered “frozen” on the dual problem, i.e., the variation of viscosity w.r.t. the state is omitted. The goal of this section is to present a consistent dual problem to the generalized NS equations using non-Newtonian blood models, in which the corresponding viscosity model is also varied. Similarly to Section 4.3, the foundation of the derivations presented herein, as well as the employed notation, are based on Section 4.2 and the problem described therein is also referred to here as the initial problem. Nevertheless, a discussion on how the derivations presented herein and in Section 4.3 can be combined is included at the end of this chapter.

The analysis that follows is based on the three non-Newtonian models presented in Table 2.4. All models are algebraic in nature and depend exclusively on a set of constant parameters and the shear rate parameter $\dot{\gamma}$, cf. Eq. (2.80). To describe therefore the viscosity model in a residual equation form, one can write

$$R^{\tilde{\mu}} = \tilde{\mu} - f(\dot{\gamma}) = 0, \tag{4.108}$$

where $f(\dot{\gamma})$ corresponds to the shear rate function describing each respective non-Newtonian model. Two possible approaches are conceivable on how to proceed with the adjoint analysis. On the one hand, one can directly substitute $f(\dot{\gamma})$ in place of the non-Newtonian viscosity on the NS equations. On the other hand, Eq. (4.108) can be used as an additional equality constraint in the formulation of the Lagrangian. In this thesis, the second approach is pursued since it simplifies the derivation process as well as highlights the effect of the non-Newtonian viscosity in the dual problem. The non-Newtonian viscosity can therefore serve as a state variable and the overall primal state can be described as

$$y_m = (p, v_1, v_2(, v_3), \tilde{\mu}). \tag{4.109}$$

Since the non-Newtonian models refer to the nature of the fluid rather than an auxiliary phenomenon that we wish to study and intervene on, as in the case of hemolysis, the analysis that follows is based on a general description of the objective functional as in Eq. (4.23).

The Lagrangian is formulated as

$$\mathcal{L} = \hat{J} + \int\limits_{\Omega} \hat{y}_l R_l \, \mathrm{d}\Omega = \hat{J} + \int\limits_{\Omega} \left[\hat{p} R^p + \hat{v}_i R_i^v + \hat{\mu} R^{\tilde{\mu}} \right] \, \mathrm{d}\Omega, \tag{4.110}$$

where $\hat{\mu}$ refers to the adjoint viscosity multiplying the additional algebraic equality constraint (4.108). Similarly to the previous sections, the volume integral in the Lagrangian is decomposed to subintegrals consisting of isolated terms of the primal equations,

$$I_1 + I_2 + I_3' + I_4 + \underbrace{\int\limits_{\Omega} \hat{\mu}\Big(\tilde{\mu} - f(\dot{\gamma})\Big)\,\mathrm{d}\Omega}_{I_5'},$$

where $I_{1,2,4}$ are the same as in the initial problem while I_3 is adjusted based on the introduction of non-Newtonian viscosity, denoted here as I_3'. I_5' is introduced to account for the additional term. Noting therefore that $I_{1,2,4}$ are independent of the newly introduced state variable, the only variations that need to be further investigated refer to those of I_3' and I_5'.

4.4.1 Variations of the non-Newtonian Models

Similar to before, each subintegral is treated separately and the number of the enumerated list refers to the derivations made for the respective subintegral.

3. Keeping in mind that $\tilde{\mu}$ is introduced as an additional primal state variable, $\delta_{v_i} I_3' \cdot \delta v_i$ is the same as in the initial problem, cf. Eq. (4.37), and $\delta_p I_3' \cdot \delta p = 0$. The variation of I_3' in the direction of $\tilde{\mu}$ reads

$$\begin{aligned}\delta_{\tilde{\mu}} I_3' \cdot \delta\tilde{\mu} &= -\int\limits_{\Omega} \hat{v}_i \left(\frac{\partial}{\partial x_j}\left(\delta\tilde{\mu}\, 2S_{ij}\right)\right) \mathrm{d}\Omega \\ &= -\int\limits_{\Gamma} (\delta\tilde{\mu}) 2\hat{v}_i S_{ij} n_j \,\mathrm{d}\Gamma + \int\limits_{\Omega} (\delta\tilde{\mu}) 2 S_{ij} \frac{\partial \hat{v}_i}{\partial x_j}\,\mathrm{d}\Omega. \end{aligned} \tag{4.111}$$

5. The variation of I_5' in the direction of pressure is identically equal to zero. The remaining variations read

$$\delta_{v_i} I_5' \cdot \delta v_i = -\int_{\Gamma} (\delta v_i) \hat{\mu} X_{ij} n_j \,\mathrm{d}\Gamma + \int_{\Omega} (\delta v_i) \frac{\partial}{\partial x_j}\Big[\hat{\mu} X_{ij}\Big]\,\mathrm{d}\Omega, \tag{4.112}$$

$$\delta_{\tilde{\mu}} I_5' \cdot \delta\tilde{\mu} = \int_{\Omega} (\delta\tilde{\mu}) \hat{\mu}\,\mathrm{d}\Omega. \tag{4.113}$$

   Here, X_{ij} is a symmetric tensor proportional to the strain-rate tensor S_{ij}, similar to the B_{ij} tensor derived for the adjoint hemolysis equations. The derivation of Eq. (4.112) is presented in Appendix A.3. The derivation process is realized for the three non-Newtonian models presented in Table 2.4 as well as the Newtonian model to allow for a generalization of the adjoint problem. Each model results in a different X_{ij} tensor and they are all collectively presented in Table 4.1. Note that the parameters appearing in X_{ij} refer to the constants of Table 2.4 for each respective model.

Table 4.1: Tensor X_{ij} for each viscosity model. The units of its components are $[X_{ij}]=[\mathrm{Pa}\cdot\mathrm{s}^2]$.

Model	X_{ij}
Newtonian (N)	0
Power-law (PL)	$\left[2k(n-1)\dot{\gamma}^{(n-3)}\right]\ S_{ij}$
Modified-Casson (MC)	$\left[-2\left(\frac{\sqrt{\tau_0}}{\sqrt{\lambda}+\sqrt{\dot{\gamma}}}+\sqrt{\mu_c}\right)\left(\frac{\sqrt{\tau_0}}{(\sqrt{\lambda}+\sqrt{\dot{\gamma}})^2}\right)\frac{1}{\dot{\gamma}^{\frac{3}{2}}}\right]\ S_{ij}$
Carreau (C)	$\left[2(n-1)(\mu_0-\mu_\infty)\left(1+(\lambda\dot{\gamma})^2\right)^{\frac{n-3}{2}}\lambda^2\right]\ S_{ij}$

4.4.2 Field Adjoint non-Newtonian Equations

Based on the additional volume integrals arising from the variations of I_3' and I_5', the field adjoint equations considering non-Newtonian blood properties are reformulated to

$$\hat{R}^p = -\frac{\partial \hat{v}_i}{\partial x_i} + \frac{\partial j_\Omega}{\partial p} = 0 \tag{4.114}$$

$$\hat{R}_i^v = \hat{v}_j \rho \frac{\partial v_j}{\partial x_i} - v_j \rho \frac{\partial \hat{v}_i}{\partial x_j} - \frac{\partial}{\partial x_j}\Big(2\mu \hat{S}_{ij} - \hat{p}\delta_{ij} - \boxed{\hat{\mu} X_{ij}}\Big) + \frac{\partial j_\Omega}{\partial v_i} = 0 \tag{4.115}$$

$$\hat{R}^\mu = \hat{\mu} + 2S_{ij}\frac{\partial \hat{v}_i}{\partial x_j} + \frac{\partial j_\Omega}{\partial \tilde{\mu}} = 0. \tag{4.116}$$

The boxed term refers to the additional contribution to the adjoint momentum equations due to the consideration of adjoint viscosity. In line with its primal companion, Eq. (4.116) is algebraic w.r.t. the adjoint viscosity and therefore one can write

$$\hat{\mu} = -\Big(2S_{ij}\frac{\partial \hat{v}_i}{\partial x_j} + \frac{\partial j_\Omega}{\partial \tilde{\mu}}\Big) = -\Big(2S_{ij}(\hat{S}_{ij} + \hat{\Gamma}_{ij}) + \frac{\partial j_\Omega}{\partial \tilde{\mu}}\Big) = -\Big(2S_{ij}\hat{S}_{ij} + \frac{\partial j_\Omega}{\partial \tilde{\mu}}\Big), \tag{4.117}$$

where $\hat{\Gamma}_{ij}$ denotes the anti-symmetric part of the adjoint velocity gradient and thus its inner product with the symmetric S_{ij} vanishes.

Equations (4.115) are enhanced in comparison to the initial problem only by an additional term, that for the case of a Newtonian fluid vanishes by virtue of $X_{ij} = 0$, thus keeping the formulation general to both Newtonian and non-Newtonian fluids. In the case of Newtonian fluids the adjoint viscosity equation then becomes obsolete due to its multiplication with $X_{ij} = 0$ and mathematically irrelevant since any variation of the viscosity, i.e., $\delta\tilde{\mu}$, is identically equal to zero.

Furthermore, it is interesting to note the similarities between the additional contributions in the adjoint momentum equation for the case of hemolysis consideration, Eq. (4.85) and non-Newtonian consideration, Eq. (4.115). In both cases, an additional term appears corresponding to the primal strain-rate tensor multiplied by a scalar quantity and an adjoint variable, i.e., adjoint hemolysis and adjoint viscosity, respectively. The term acts similarly in both cases with the difference that in the case of adjoint hemolysis, the term is completely decoupled from the adjoint NS while in the case of non-Newtonian fluids the term is coupled with the adjoint momentum equations due to the necessary determination of adjoint velocity components for the computation of adjoint viscosity, cf. Eq. (4.116). It is this author's belief that the similarities are not coincidental but are rather based on the biological correlation between hemolysis and non-Newtonian properties. As discussed in Section 2.3, non-Newtonian blood models attempt to capture the interaction and concentration of RBCs, that are otherwise neglected in view of a continuous fluid medium assumption. Similarly, hemolysis models attempt to describe the damage of RBCs, from a continuous perspective, thus changing the concentration of active RBCs in the investigated volume of blood. In view of the decoupled nature from the flow dynamics of a large volume of prominent hemolysis models, the (continuous) adjoint can provide insights on the development of coupled continuous primal hemolysis models using information from the adjoint non-Newtonian equations by e.g., correlating the B_{ij} and X_{ij} matrices. This idea is not pursued in this work but is rather stated to highlight the advantageous nature of the continuous adjoint as regards our fundamental understanding of the companion primal problem.

4.4.3 Boundary Adjoint non-Newtonian Conditions

Similarly to the initial problem, the boundary conditions are deduced by demanding that the surface integrals of the state variation of the Lagrangian vanish. For the case of non-Newtonian considerations these read

$$\begin{aligned}\delta_{y_m}\mathcal{L}\cdot\delta y_m\Big|_\Gamma = {} & \int\limits_\Gamma (\delta p)\left(\hat{v}_i n_i + \frac{\partial j_\Gamma}{\partial p}\right)\mathrm{d}\Gamma - \int\limits_\Gamma \tilde{\mu}\hat{v}_i\frac{\partial \delta v_i}{\partial x_j}n_j\,\mathrm{d}\Gamma \\ & + \int\limits_\Gamma (\delta v_i)\left[-\hat{p}n_i + \rho\hat{v}_i v_j n_j + \tilde{\mu}n_j\frac{\partial \hat{v}_i}{\partial x_j} + \boxed{\hat{v}_j\left(\frac{\partial\tilde{\mu}}{\partial x_j}n_i - \frac{\partial\tilde{\mu}}{\partial x_i}n_j\right)} - \boxed{\tilde{\mu}X_{ij}n_j} + \frac{\partial j_\Gamma}{\partial v_i}\right]\mathrm{d}\Gamma \\ & + \boxed{\int\limits_\Gamma (\delta\tilde{\mu})\left(\frac{\partial j_\Gamma}{\partial\tilde{\mu}} - 2\hat{v}_i S_{ij}n_j\right)\mathrm{d}\Gamma},\end{aligned} \tag{4.118}$$

where boxed terms denote the additional terms in comparison to the initial problem. Note that the first boxed term in the second line of Eq. (4.118) does not appear in the derivations above but instead appears in Eq. (4.36), since the Gauss divergence theorem applied therein needs to also account for gradients of viscosity. Similar to the previous sections, the deduction of BCs is realized for each boundary patch individually.

Inlet and non-design wall

Due to $\delta v_i = 0$ on $\Gamma_{\text{in}} \cup \Gamma_{\text{w}}$, the condition that leads to the cancellation of the remaining terms is

$$\hat{v}_n = -\frac{\partial j_\Gamma}{\partial p} \quad \text{and} \quad \hat{v}_i^t = 0 \quad \text{on } \Gamma_{\text{in}} \cup \Gamma_{\text{w}}. \tag{4.119}$$

Note that these conditions are sufficient to cancel the remaining terms only in the case that $\partial j_\Gamma / \partial\tilde{\mu} = 0$ on $\Gamma_{\text{in}} \cup \Gamma_{\text{w}}$. This is indeed the case for all applications studied in this thesis but it should be considered as an additional assumption. Similarly to what was done in the previous sections, a zero Neumann boundary condition is assumed for adjoint pressure on $\Gamma_{\mathrm{in}} \cup \Gamma_{\mathrm{w}}$.

Outlet

On the outlet the equations that need to be satisfied are

$$-\hat{p} n_i + \rho \hat{v}_i v_j n_j + \tilde{\mu} n_j \frac{\partial \hat{v}_i}{\partial x_j} + \hat{v}_j \left(\frac{\partial \tilde{\mu}}{\partial x_j} n_i - \frac{\partial \tilde{\mu}}{\partial x_i} n_j \right) - \hat{\mu} X_{ij} n_j + \frac{\partial j_\Gamma}{\partial v_i} = 0 \quad \text{on } \Gamma_{\mathrm{out}}, \tag{4.120}$$

$$\left(\frac{\partial j_\Gamma}{\partial \tilde{\mu}} - 2 \hat{v}_i S_{ij} n_j \right) = 0 \quad \text{on } \Gamma_{\mathrm{out}}. \tag{4.121}$$

Assuming that $\partial j_\Gamma / \partial \tilde{\mu} = 0$ also on the outlet, we can decompose in normal and tangential components the remaining term of Eq. (4.121) and write

$$2 \hat{v}_i S_{ij} n_j = \hat{v}_n \frac{\partial v_n}{\partial n} + \hat{v}_i^t \frac{\partial v_n}{\partial x_i^t} = 0. \tag{4.122}$$

By virtue of the zero Neumann BC set for primal velocity on Γ_{out}, $\partial v_n / \partial n = 0$ and thus for the satisfaction of Eq. (4.122) one needs to apply $\hat{v}_i^t = 0$.

Subsequently, one can decompose Eq. (4.120) into its normal and tangential components, viz.

$$-\hat{p} + \rho \hat{v}_n v_n + \overbrace{\hat{v}_j \frac{\partial \tilde{\mu}}{\partial x_j} - \hat{v}_n \frac{\partial \tilde{\mu}}{\partial n}}^{\mathrm{T1}} + \tilde{\mu} \frac{\partial \hat{v}_n}{\partial n} - \overbrace{\hat{\mu} X_{ij} n_j n_i}^{\mathrm{T2}} + \frac{\partial j_\Gamma}{\partial v_n} = 0, \tag{4.123}$$

$$\rho \hat{v}_i^t v_n - \hat{v}_n \frac{\partial \tilde{\mu}}{\partial x_i^t} + \tilde{\mu} \frac{\partial \hat{v}_i^t}{\partial n} - \hat{\mu} (X_{ij} n_j)^t + \frac{\partial j_\Gamma}{\partial v_i^t} = 0. \tag{4.124}$$

By further developing term T1 of Eqn. (4.123), it is shown that

$$\mathrm{T1}: \quad \hat{v}_j \frac{\partial \tilde{\mu}}{\partial x_j} - \hat{v}_n \frac{\partial \tilde{\mu}}{\partial n} = \hat{v}_n \frac{\partial \tilde{\mu}}{\partial n} + \hat{v}_i^t \frac{\partial \tilde{\mu}}{\partial x_i^t} - \hat{v}_n \frac{\partial \tilde{\mu}}{\partial n} = \hat{v}_i^t \frac{\partial \tilde{\mu}}{\partial x_i^t} = 0, \tag{4.125}$$

since $\hat{v}_i^t = 0$ is already imposed on Γ_{out}. Furthermore, term T2 also vanishes owing to the incompressible assumption and $X_{ij} \sim S_{ij}$. Equation (4.123) thus reduces to

$$-\hat{p} + \rho \hat{u}_n u_n + \tilde{\mu} \frac{\partial \hat{u}_n}{\partial n} + \frac{\partial j_\Gamma}{\partial u_n} = 0 \quad \text{on } \Gamma_{\mathrm{out}}, \tag{4.126}$$

which can be used to set a Dirichlet BC for adjoint pressure. Furthermore, given that $\hat{v}_i^t$ is already set to zero, Eq. (4.124) can be used to determine $\hat{v}_n$ on Γ_{out}.

Adjoint viscosity refers to an algebraic equation and thus requires no explicit BC for its solution. However, boundary values are required for the computation of related expressions. Therefore, in all investigated cases, adjoint viscosity is approximated by a zero gradient extrapolation to boundary patches from the nearest cell.

4.4.4 Shape Sensitivity for non-Newtonian Models

Following the same methodology as the one outlined in Section 4.2.4 and considering that $\hat{v}_i = 0$ on Γ_d and that a boundary-based objective defined on Γ_in, Γ_out or $\Gamma_\mathrm{in} \cup \Gamma_\mathrm{out}$ is targeted, one arrives at the sensitivity expression

$$\delta_{u_k}\mathcal{L} \cdot \delta u_k = \int\limits_{\Gamma_\mathrm{d}} \delta u_k n_k \left[\hat{p}\frac{\partial v_i}{\partial n} n_i - \left(\tilde{\mu}\frac{\partial \hat{v}_i}{\partial n} - \boxed{\hat{\mu} X_{ij} n_j}\right)\frac{\partial v_i}{\partial n}\right] \mathrm{d}\Gamma. \tag{4.127}$$

The sensitivity expression is again augmented by an additional boxed term that is similar in nature with the term appearing in the hemolysis-based sensitivity expression.

The assumptions that need to hold to arrive at the sensitivity expression of Eq. (4.127) and the BCs as outlined in Section 4.4.3 are summarized as follows:

- The assumptions made for the initial problem must hold.

- The objective functional must be independent of the effective viscosity, i.e. $\partial j_\Gamma / \partial \tilde{\mu} = 0$ must hold on Γ.

4.4.5 Numerical Solution

Even though the additional term introduced in the adjoint momentum equations is similar to the term involving B_{ij} for hemolysis, its algorithmic treatment is slightly different due to the nature of the adjoint variable multiplying each respective term. On the one hand, adjoint hemolysis is decoupled from the adjoint NS system of equations and therefore its computation can precede the solution of the latter. On the other hand, adjoint viscosity is coupled with the adjoint momentum equations since it involves $\hat{S}_{ij}$, cf. Eq. (4.117). Therefore, similar to its primal counterpart and in the context of the iterative process followed for the computation of the adjoint NS system, adjoint viscosity is computed from the algebraic Eq. (4.117) based on the adjoint velocity of the previous iteration. The non-boundary face-based values required for the adjoint viscosity are computed based on a linear interpolation from the adjacent CVs, as in Eq. (2.19).

Overall, the additional non-Newtonian based contribution is treated explicitly as a source term based on Gauss divergence theorem for the P CV as

$$-\int\limits_{V^\mathrm{P}} \frac{\partial(\hat{\mu} X_{ij})}{\partial x_j}\,\mathrm{d}V = -\int\limits_{O(V^\mathrm{P})} \hat{\mu} X_{ij} n_j\,\mathrm{d}S = -\sum_{\mathrm{N(P)}} \int\limits_{\Delta\Gamma} \hat{\mu} X_{ij} n_j\,\mathrm{d}\Gamma, \tag{4.128}$$

which based on the midpoint rule can be computed on each face comprising the P CV as

$$-\int\limits_{\Delta\Gamma} \hat{\mu} X_{ij} n_j\,\mathrm{d}\Gamma \approx -\hat{\mu}^\mathrm{F} X_{ij}^\mathrm{F} n_j^\mathrm{F} \Delta\Gamma^\mathrm{F}. \tag{4.129}$$

The computation of X_{ij}^F follows the same procedure as the one discussed for B_{ij}^F in Section 4.3.5, since both quantities are simply a scaled version of the primal strain rate tensor.

4.4.6 Verification Studies

The goal of this section is twofold. On the one hand, the sensitivity expression, as derived in Eq. (4.127), for a non-Newtonian blood model is assessed against second-order accurate FD. The validity of the newly derived expression is investigated for two different flow conditions of non-Newtonian interest for a blood model, i.e., low shear rates. On the other hand, the effect of the usually assumed “frozen” non-Newtonian viscosity is studied by neglecting any additional term introduced in the adjoint system and sensitivity expression w.r.t. the initial problem.

In order to highlight the latter, the investigated flow scenarios are simulated using the same geometry and discretization as the one studied in Section 4.2.6. The objective functional is chosen to be the dissipated power, which covers the necessary assumptions for Eq. (4.127). The necessary derivatives of the objective functional in the direction of the state are presented in Eq. (4.70).

The flow conditions are the same as in Section 4.2.6 with the exception that an additional case of a lower Re number is investigated by changing the inlet velocity magnitude. In specific, the FD study is conducted for Re = 1.2 and Re = 12. Figure 4.8 is presented to visualize the differences of these two virtually similar cases on the apparent viscosity of blood using a non-Newtonian model. As shown, the higher Re case results in a shear rate neighborhood of viscosities close to the Newtonian one (see Section 2.3 for the physical justification of this observation) while the lower Re case results in a neighborhood of maximum viscosity differences from the Newtonian.

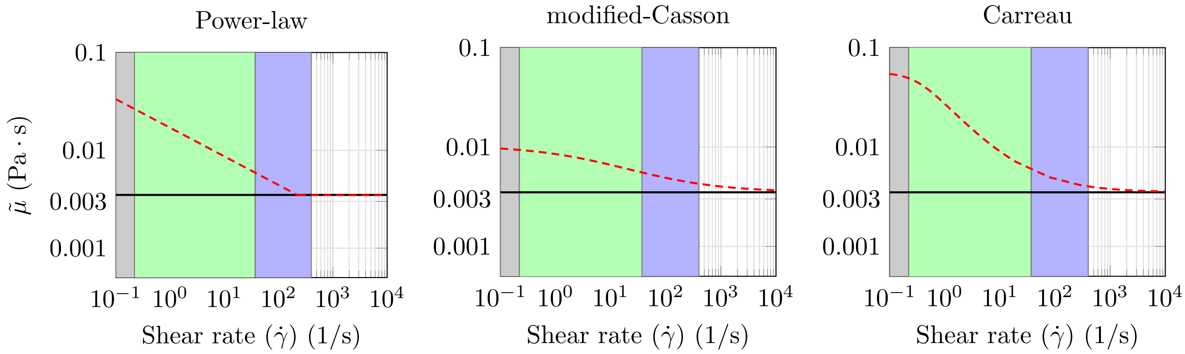

Figure 4.8: Shear rate ranges appearing for the investigated FD studies and the corresponding apparent viscosity for each of the employed non-Newtonian models. Gray area corresponds to shear rates appearing for the Re = 1.2 case, blue area for Re = 12 and light green for both cases. Dashed line denotes the non-Newtonian viscosity and solid line the Newtonian viscosity of blood.

Figures 4.9 and 4.10 compare the FD-based and adjoint-based shape sensitivity estimations for Re = 1.2 and Re = 12, respectively. In specific, computations are realized for both Newtonian and non-Newtonian fluid models. For the latter, a reduced non-Newtonian description is investigated in which the primal problem employs the respective non-Newtonian description while the dual follows from the Newtonian set of adjoint equations, i.e., the primal viscosity is assumed “frozen” on the dual. As shown, the FD-based results satisfactorily match their adjoint counterparts for both Newtonian and non-Newtonian fluids and for both considered Re numbers. However, when the reduced non-Newtonian model is considered, the adjoint-based shape sensitivity estimation deviates from the respective FD results, thus highlighting the importance of adjoint consistency w.r.t. the primal problem.

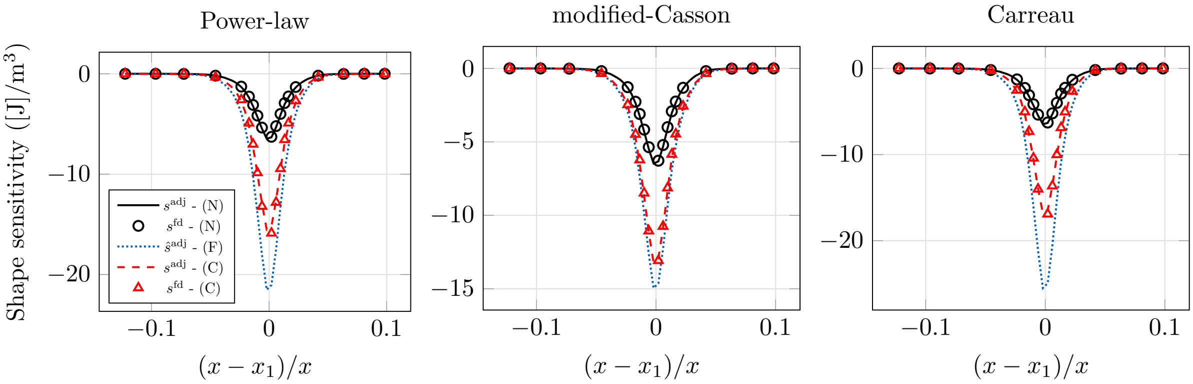

Figure 4.9: Study for Re = 1.2. Shape estimations for a Power-law (left), modified-Casson (middle) and Carreau (right) viscosity model. Black (continuous), red (dashed) and blue (densely dotted) lines correspond to Newtonian, consistent non-Newtonian (C) and reduced non-Newtonian (F) adjoint-based estimations, respectively. Circles and triangles denote discrete FD results for a Newtonian and non-Newtonian fluid, respectively. Perturbation magnitude $\epsilon = \delta \cdot 10^{-4}$, cf. Fig. 4.2 for reference.

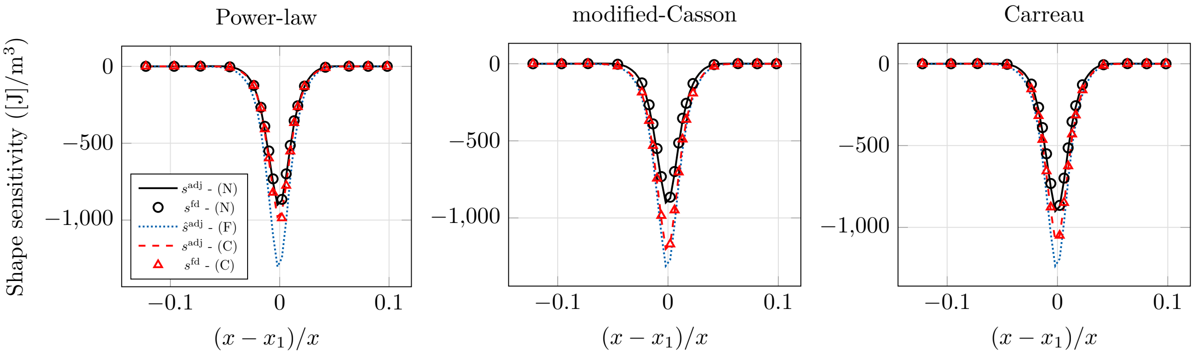

Figure 4.10: Study for Re = 12. Caption and legends as in Fig. 4.9.

Furthermore, it is interesting to note the trend exhibited in the sensitivity of a non-Newtonian fluid w.r.t. the Newtonian fluid for the two different Re number configurations as well as the impact of the “frozen” viscosity assumption. As expected, for the higher Re number case the Newtonian and non-Newtonian results are fairly close to each other since the range of shear rates, especially in a neighborhood near the stenosed investigated section of the geometry, results in viscosities similar to the Newtonian one for all employed non-Newtonian models. On the other hand, the non-Newtonian and Newtonian results significantly deviate from each other for Re = 1.2 where the shear rate range is lower, cf. Fig. 4.8.

As regards the “frozen” viscosity assumption, it is shown that the error of the estimated sensitivity increases as the Re number decreases. This is also attributed to the shear-thinning nature of blood. As the shear rates increase the non-Newtonian viscosity exhibits an asymptotic convergence towards the Newtonian viscosity and thus the assumption of neglecting the variations of viscosity for the derivation of the adjoint is stronger.

Note that the aforementioned observations consider a direct relation between viscous diffusion and shape sensitivity, which does not naturally hold. It is assumed that the difference between the FD-based sensitivity results and the reduced adjoint results exclusively depends on the difference between Newtonian and non-Newtonian effective viscosity. While there is indeed a direct dependence between the adjoint-based sensitivity outlined in Eq. (4.127) and the apparent viscosity, the expression is far more involved than that. However, due to the low Re numbers considered, the transport of momentum is governed by viscous diffusion. This primal flow behavior naturally reflects on the adjoint problem and the shape sensitivity estimation.

Finally, a remark ought to be made as regards the trend of s^{adj} (complete non-Newtonian adjoint-based shape sensitivity) and $\hat{s}^{\mathrm{adj}}$ (reduced non-Newtonian adjoint). As shown in these verification studies, the differences can be quite significant, especially in regions where non-Newtonian properties are dominant. However, the overall trend of the two curves is fairly similar, i.e., one could approximate $\hat{s}^{\mathrm{adj}} \approx \kappa s^{\mathrm{adj}}$, where κ represents a constant value. Naturally, one cannot have an a priori knowledge of κ, however in the context of a gradient-descent optimization algorithm, the difference between a reduced and a complete non-Newtonian adjoint model would essentially boil down to a step-size issue. Nevertheless, while this observation virtually holds for the cases studied in this section, it does not necessarily hold for more involved cases and therefore the consistency of the adjoint should be preserved to ensure a proper descent direction.

4.5 Continuous Adjoint non-Newtonian and Hemolysis Equations

The two novel adjoint problems presented in Sections 4.3 and 4.4 are herein combined to allow for the derivation of an adjoint-based shape sensitivity for the minimization of hemolysis while concurrently employing a non-Newtonian rheological model for blood. The foundation of the necessary additional derivations presented in this section as well as the notation employed herein are based on the work presented in the three previous sections.

Targeting the minimization of hemolysis induction, the objective functional considered herein is confined to the description of Eq. (4.74), with its variations in the direction of the primal state given in Eqs. (4.75). Note that the latter are not enhanced by variations in the direction of apparent viscosity since there is no direct dependence on the definition of the functional.

The complete Lagrangian can now be stated as

$$\mathcal{L} = \hat{J} + \int\limits_{\Omega} \left[\hat{p} R^p + \hat{v}_i R_i^v + \hat{h} R^H + \hat{\mu} R^{\tilde{\mu}} \right] \mathrm{d}\Omega, \tag{4.130}$$

and following the decomposition approach outlined in the previous sections, the volume integral can be decomposed in subintegrals, viz.

$$I_1 + I_2 + I_3' + I_4 + I_5 + I_6 + I_5',$$

following the order of the Lagrangian constraints in Eq. (4.130). In essence and as compared to the derivations of the previous sections, in the scope of this work one searches for auxiliary contributions that might arise by considering the variations of each respective problem in the direction of the additional primal variable, i.e., hemolysis or non-Newtonian viscosity. These variations are

$$\delta_{H_L} I_3' \cdot \delta H_L, \quad \delta_{\tilde{\mu}} I_5 \cdot \delta \tilde{\mu}, \quad \delta_{\tilde{\mu}} I_6 \cdot \delta \tilde{\mu}, \quad \delta_{H_L} I_5' \cdot \delta H_L.$$

All of the above derivatives are identically equal to zero except $\delta_{\tilde{\mu}} I_6 \cdot \delta \tilde{\mu}$ due to the direct dependence of $\bar{\tau}$ with $\tilde{\mu}$, cf. Eq. (4.80). Employing the notation of Section 4.3.1, this variation reads

$$\delta_{\tilde{\mu}} I_6 \cdot \delta \tilde{\mu} = -\int\limits_{\Omega} (\delta \tilde{\mu}) \Lambda \, \mathrm{d}\Omega, \tag{4.131}$$

where $\Lambda = 2\hat{h}\frac{\alpha}{\beta} k \tilde{\mu} M \tau^{*(\frac{\alpha}{2\beta}-1)} S_{ij} S_{ij}$.

4.5.1 Field Adjoint Combined Equations

The changes induced to the derivation process by combining the hemolysis equation and the non-Newtonian blood properties are minimal and reflect only on the adjoint non-Newtonian equation. Collectively, the field adjoint equations for the combined problem read

$$\hat{R}^p = -\frac{\partial \hat{v}_i}{\partial x_i} = 0 \tag{4.132}$$

$$\hat{R}_i^v = \hat{v}_j \rho \frac{\partial v_j}{\partial x_i} - v_j \rho \frac{\partial \hat{v}_i}{\partial x_j} - \frac{\partial}{\partial x_j}\left(2\mu \hat{S}_{ij} - \hat{p}\delta_{ij} - \hat{\mu} X_{ij} - \hat{h} B_{ij}\right) - H_L \frac{\partial \hat{h}}{\partial x_i} = 0 \tag{4.133}$$

$$\hat{R}^H = v_i \frac{\partial \hat{h}}{\partial x_i} - C^{\frac{1}{\beta}} \bar{\tau}^{\frac{\alpha}{\beta}} \hat{h} = 0 \tag{4.134}$$

$$\hat{R}^\mu = \left(\hat{\mu} - \boxed{\Lambda}\right) + 2S_{ij} \frac{\partial \hat{v}_i}{\partial x_j} = 0. \tag{4.135}$$

The boxed scalar quantity Λ denotes the only additional contribution that needs to be considered due to the combination of the hemolysis and non-Newtonian problems. Note that the nature of the derived expressions sustain their individual characteristics, i.e., adjoint hemolysis is one-way coupled and adjoint viscosity is algrebraic, thus allowing for a similar algorithmic strategy to what is presented in the previous sections.

4.5.2 Boundary Adjoint Combined Conditions

The cross derivatives between hemolysis and non-Newtonian terms do not increase the number of boundary integrals. Therefore the BCs of the combined problem are deduced by demanding that the combined boundary integral expressions of Sections 4.3 and 4.4 vanish, viz.

$$\begin{aligned}
\delta_{y_m}\mathcal{L} \cdot \delta y_m\Big|_\Gamma = & \int\limits_\Gamma (\delta p)\left(\hat{v}_i n_i\right) \mathrm{d}\Gamma - \int\limits_\Gamma \mu \hat{v}_i \frac{\partial \delta v_i}{\partial x_j} n_j \, \mathrm{d}\Gamma \\
& + \int\limits_\Gamma (\delta v_i)\left[-\hat{p} n_i + \rho \hat{v}_i v_j n_j + \tilde{\mu} n_j \frac{\partial \hat{v}_i}{\partial x_j} + H_L \hat{h} n_i - \hat{h} B_{ij} n_j + \frac{\partial j_\Gamma}{\partial v_i}\right] \mathrm{d}\Gamma \\
& + \int\limits_\Gamma (\delta v_i)\left[\hat{v}_j \left(\frac{\partial \tilde{\mu}}{\partial x_j} n_i - \frac{\partial \tilde{\mu}}{\partial x_i} n_j\right) - \hat{\mu} X_{ij} n_j\right] \mathrm{d}\Gamma \\
& + \int\limits_\Gamma (\delta H_L)\left(\hat{h} v_i n_i + \frac{\partial j_\Gamma}{\partial H_L}\right) \mathrm{d}\Gamma - \int\limits_\Gamma (\delta \tilde{\mu})\left(2\hat{v}_i S_{ij} n_j\right) \mathrm{d}\Gamma.
\end{aligned} \tag{4.136}$$

Inlet and non-design wall

Bearing in mind that the objective functional refers to the expression of Eq. (4.74), the BCs for adjoint velocity on $\Gamma_{\text{in}} \cup \Gamma_{\text{w}}$ are the same for both individual problems and are also sufficient to cancel all integrals of Eq. (4.136), i.e.

$$\hat{v}_i = 0 \quad \text{on } \Gamma_{\text{in}} \cup \Gamma_{\text{w}}, \tag{4.137}$$

is set. Adjoint pressure and hemolysis are computed based on a zero Neumann BC, similar to the adjoint hemolysis problem.

Outlet

On the outlet the cancellation of the last integral of Eq. (4.136) calls for $\hat{v}_i^t = 0$ on Γ_{out}, as discussed in Section 4.4.3. Adjoint hemolysis is computed based on Eq. (4.90), while adjoint pressure is computed based on

$$-\hat{p} + \rho \hat{v}_n v_n + \tilde{\mu} \frac{\partial \hat{v}_n}{\partial n} + \rho H_L^{\beta} (1-\beta) = 0 \quad \text{on } \Gamma_{\text{out}}. \tag{4.138}$$

The remaining terms appearing in the third and fourth integral of Eq. (4.136) naturally vanish on the outlet as discussed in the previous sections. The adjoint normal velocity component can be approximated by the tangential decomposition of the complete expression multiplying δv_i.

4.5.3 Shape Sensitivity for Combined Problem

Similar to the BCs, since the combined problem does not increase the number of surface integrals, the combined surface sensitivity results from a linear combination of the shape sensitivities derived in Sections 4.3 and 4.4 and reads

$$\delta_{u_k} \mathcal{L} \cdot \delta u_k = \int\limits_{\Gamma_{\text{d}}} \delta u_k n_k \left[\left(\hat{p} - H_L \hat{h} \right) \frac{\partial v_i}{\partial n} n_i - \left(\tilde{\mu} \frac{\partial \hat{v}_i}{\partial n} - \hat{h} B_{ij} n_j - \hat{\mu} X_{ij} n_j \right) \frac{\partial v_i}{\partial n} \right] \mathrm{d}\Gamma. \tag{4.139}$$

Note that both B_{ij} and X_{ij} refer to scaled versions of the primal strain rate tensor and can therefore be combined in one term.

4.5.4 Numerical Solution

Since the combination of the two individual problems does not change the general characteristics of each novel contribution, the algorithmic and discretization strategies presented in the previous sections can also be sustained. In specific, the adjoint hemolysis equation can precede the solution of the adjoint non-Newtonian NS equations and its solution can be used to feed the necessary terms of Eqs. (4.132), (4.133) and (4.135). The procedure can then continue by the algebraic computation of $\hat{\mu}$ and its Picard-like implementation in the adjoint momentum equations. The discretization of all additional terms, as compared to the initial problem, introduced in the adjoint momentum equations is based on the strategies discussed in Sections 4.3 and 4.4.

5 Robust Shape Optimization

Chapters 3 and 4 were dedicated to the presentation of gradient-based parameter-free shape optimization techniques using the adjoint method. Therein, the investigated problems were assumed to be deterministic. In that context, with precise knowledge of the underlying primal problem, one can find an optimal (or optimized) solution of the control, i.e., the shape, for a given objective. However, precise knowledge of the conditions, under which a flow phenomenon occurs, is often challenging to attain, particularly in blood flow-related applications.

As discussed in previous chapters, modeling blood-specific phenomena such as hemolysis or the non-Newtonian rheological behavior of blood relies on parameters typically deduced from fitting models to experimental data. Although experiments are conducted under sterile, well-controlled conditions (Wurzinger et al. [1985], Heuser and Opitz [1980]), the same parameter sets are frequently used for more complex computational studies (Yu et al. [2017], Thamsen et al. [2015]). Furthermore, the uncertainty introduced by these parameters is evident from the significantly different parameter sets found in the literature, see e.g., Table 2.1. These uncertainties are classified as epistemic, since they can be reduced through more accurate computational and experimental modeling. Additionally, the cardiovascular system is influenced by aleatoric uncertainties stemming from the complex, unpredictable fluctuations of a human heart rate.

While these two types of uncertainty differ conceptually and prompt reflection on the nature of the underlying phenomena, they are not distinguished in the subsequent discussion, as their mathematical and numerical treatment remains the same. Furthermore, it should be noted that one might also justifiably consider the shape to be uncertain. This scenario is not considered in this thesis and uncertainties relate exclusively to the conditions and parameters used to model the blood flow.

This chapter presents an extension of the already described optimization techniques to increase their robustness against the underlying uncertainties of the conditions or the modeling parameters. To this end, the optimization problem searches for shape configurations that are optimized w.r.t. the statistical moments of a QoI in a range of probable outcomes of an uncertain variable or a vector of uncertain variables. The chapter is organized in four sections. Section 5.1 formulates the robust shape optimization problem. Section 5.2 presents the stochastic gradient descent method as well as a related modification of the original formulation. Both formulations employ the adjoint method for the efficient computation of necessary derivatives. The chapter continues with Section 5.3 where a shape optimization procedure is discussed based on the first-order second-moment (FOSM) method and the assistance of the continuous adjoint method. The chapter closes with Section 5.4 where a CFD-based illustrative example is presented to highlight the characteristics of each aforementioned method.

5.1 Problem Formulation

In what was discussed up to this point, the goal of the optimization problems was to minimize an objective functional by updating a set of design variables given a state. The state was assumed to be a function of the design and was acquired from the solution of a set of PDEs including fully determined parameters and BCs. This problem was mathematically described by Eq. (4.19). The gradient-based solution of this problem results in an admissible design u_k^* for which $J(y_m^*(u_k^*), u_k^*) \in \mathbb{R}$ is (at least locally) minimal. However, consider that the state is unpredictably perturbed due to reasons unrelated to the design, e.g., due to our false estimation of the state. The solution found by the deterministic problem is likely not to be optimal anymore.

To illustrate this concept further, consider a mechanical hand performing a coin toss experiment under fully-controlled air conditions. Then, based on the initial placement of the coin on the hand, one can calculate and apply the necessary employed force by the hand (design) so a desired outcome is always achieved (objective). This renders the problem deterministic. However, if we replace now the mechanical hand with a human hand, it is logical to arrive at the conclusion that the lack of exact control on its motion might result in different outcomes, rendering the problem stochastic.

The goal of robust optimization is not to arrive at a set of optimal solutions for each probable state but rather to arrive at a design that likely performs better than the initial for each probable state as well as exhibits minimum variations on its outcome w.r.t. the uncertain input. To this end, the objective functional is considered as a statistical quantity and the optimization targets the minimization of its statistical moments rather than its value at each probable state. To highlight this distinction, what is considered as an objective functional in the previous chapters is here referred to as QoI and denoted as $F \in \mathbb{R}$. The objective functional is then defined as

$$J = w_1 \mu_F + w_2 \sigma_F, \tag{5.1}$$

where μ_F and σ_F correspond to the mean value (first statistical moment) and to the standard deviation (square root of second statistical moment) of the QoI, respectively. The weights w_1 and w_2 can be chosen by the designer before the optimization process, so that to decide which quantity should be mainly targeted. A reasonable assumption for w_1 and w_2, although not necessary, is to decide for $w_1 + w_2 = 1$, thus making the objective functional the convex combination of the first two statistical moments of the QoI.

To properly account for uncertainties in the optimization problem, consider a probability space $(\Omega^*, \mathcal{F}, \mathbb{P})$[1], which consists of a sample space Ω^*, a σ-algebra $\mathcal{F} \subset \mathbb{P}(\Omega^*)$ and a probability measure $\mathbb{P} : \Omega^* \to [0, 1]$. Based on this, $\omega_i \in \Omega^* \subset \mathbb{R}^M$ denotes the vector of uncertain variables, which when prescribed refers to a stochastic outcome.

As discussed above, this thesis considers a deterministic control (design) while the uncertainties influence only the state, i.e., $y_m(\omega_i, u_k)$. For a given stochastic outcome, the state vector refers to a realization in view of the stochastic process. A realization is therefore determined by the solution of the underlying primal problem, given a stochastic outcome, which based on the notation of Chapter 4 is denoted by $R_l(y_m(\omega_i, u_k), u_k, \omega_i) = 0$. The

---

[1] Note that Ω^* is used in this context instead of the usual Ω notation to distinguish the sample space from the volume occupied by a fluid.

optimization problem is then formulated as

$$\min_{(y_m,u_k)\in W^{\mathrm{ad}}} J(y_m(u_k,\omega_i),u_k) \quad \text{s.t.} \quad R_l(y_m(u_k,\omega_i),u_k,\omega_i)=0, \tag{5.2}$$

Note that while the constraints explicitly depend on the uncertain variables, the definition of Eq. (5.1) allows us to consider only an implicit dependence between the objective functional and the uncertainty vector. In fact, due to the unique mapping from a control to a state for a given stochastic outcome, one can reduce the objective functional to a function of the control only, as was done in the previous chapters. For a thorough mathematical discussion on stochastic optimization problems of a similar ansatz as the one of Eq. (5.2), the reader is referred to Geiersbach et al. [2023, 2021], Geiersbach and Wollner [2020], Ali et al. [2017].

A key aspect of the robust optimization problem is the definition and computation of the statistical moments of the QoI. The identification of these moments is usually referred to as UQ. In this thesis the UQ is based on two different approaches. In both approaches and in view of the independence between design and uncertain variables, the statistical moments are evaluated for a given design. Therefore, to simplify the notation, u_k is omitted everywhere unless deemed necessary. The first approach computes the statistical moments by evaluating N realizations, where N should correspond to a sufficiently large sample size able to capture the moments. The moments are then computed as

$$\mu_F = \frac{1}{N}\sum_{n=1}^{N} F(y_m(\omega_i^{(n)})), \tag{5.3}$$

$$\sigma_F = \sqrt{\frac{1}{N-1}\sum_{n=1}^{N}\left(F(y_m(\omega_i^{(n)}))-\mu_F\right)^2}, \tag{5.4}$$

where $F(y_m(\omega_i^{(n)}))$ denotes the QoI computed at the n^{th} realization of the observed sample. Note that Bessel's correction is applied for the computation of the standard deviation. This approach of UQ has the obvious disadvantage that N needs to correspond to a sufficiently large number. In the context of shape optimization this suggests the need of N CFD solutions per shape update. In the absence of an appropriate surrogate model, the application of this method becomes often unfeasible unless "suitably" modified.

The second approach relies on the MoM. Initially, it is noted that for a given design, the QoI depends solely on the state which in turn depends only on the uncertain variables. This allows us to define the reduced function $\hat{F}(\omega_i) := F(y_m(\omega_i))$ for each shape. Consider now that the vector of uncertain variables is associated with a probability density function (PDF) $f(\omega_i) = f_1(\omega_1)f_2(\omega_2)...f_M(\omega_M)$ for independent uncertain variables, where f_i denotes the individual PDF of the i^{th} variable. Based on this, we can write

$$\mu_F = \int_{-\infty}^{\infty} \hat{F}(\omega_i)f(\omega_i)\,\mathrm{d}\omega, \tag{5.5}$$

$$\sigma_F^2 = \int_{-\infty}^{\infty} \left(\hat{F}(\omega_i)-\mu_F\right)^2 f(\omega_i)\,\mathrm{d}\omega = \int_{-\infty}^{\infty} \hat{F}(\omega_i)^2 f(\omega_i)\,\mathrm{d}\omega - \mu_F^2. \tag{5.6}$$

The handling of these expressions in the context of the MoM is further discussed in Section 5.3.

Overall, the solution of the optimization problem is based on gradient-based techniques, similar to the previous chapters. Therefore, one searches for an expression of $\delta_{u_k} J \cdot \delta u_k$. In a slight abuse of notation w.r.t. the previous chapter, allow $\delta_{u_k} J$ to be expressed as dJ/du_k and neglect the direction δu_k. Note that in large, this chapter employs the notation of $d(.)/d(.)$ instead of $\partial(.)/\partial(.)$ to highlight the interdependence of the state to both control and uncertain variables. Therefore, the necessary chain rule is implied and taken into account for the computation of the sought quantities.

5.2 Stochastic Gradient Descent Method

The section presents a method for the solution of the optimization problem (5.2) by employing a stochastic gradient descent method. The foundation of the method is on the approximation of a stochastic gradient which can then be employed to iteratively update the shape. In contrast to what is presented in Section 5.3, the SGD method relies on evaluating realizations from randomly selected stochastic outcomes. Given that a sufficiently large number of realizations is evaluated, the statistical moments can then be numerically approximated based on Eqs. (5.3) and (5.4). To simplify the notation, allow a QoI evaluated at the n^{th} realization to be denoted as $F_n := F(y_m(\omega_i^{(n)}))$. The derivatives of the statistical moments in the direction of the control then read

$$\frac{d\mu_F}{du_k} = \frac{1}{N} \sum_{n=1}^{N} \frac{dF_n}{du_k}, \tag{5.7}$$

$$\frac{d\sigma_F}{du_k} = \frac{1}{\sigma_F (N-1)} \sum_{n=1}^{N} \left[(F_n - \mu_F) \left(\frac{dF_n}{du_k} - \frac{d\mu_F}{du_k} \right) \right]. \tag{5.8}$$

These expressions can then be used to compute the derivative of the objective per shape update, viz.

$$\frac{dJ}{du_k} = w_1 \frac{d\mu_F}{du_k} + w_2 \frac{d\sigma_F}{du_k}. \tag{5.9}$$

Note that Eqs. (5.7) and (5.8) require only the computation of the QoI at each realization as well as their derivatives in the direction of the control. Given a stochastic outcome, the former can be computed by the solution of a primal problem while the latter by the solution of the corresponding dual problem at the stochastic outcome.

An obvious drawback of the SGD method is the necessity of evaluating a large number of realizations. If the evaluations refer to CFD solutions, the necessary cost to evaluate a representative sample size becomes often rapidly unfeasible in the context of engineering applications and other approaches need to be considered. To this extent however, the scenario in which the hemolysis parameters are considered uncertain must be highlighted. Due to the one-way coupling of the hemolysis equation with the NS, evaluating different realizations requires only the computation of the hemolysis equation using the same flow solution. Since the solution of hemolysis requires a trivial amount of time in comparison to the complete flow solution, the number of realizations can be significantly increased using a reasonable amount of computational resources. Furthermore, each realization is by definition independent from another. Therefore, given a high performance computing facility, the N (or a subset of N) realizations can be trivially parallelized, thus reducing the required wall-clock time per shape update.

Even though the aforementioned points allow for an application of the method also on CFD applications, the computational cost can still be significant. A possible solution to circumvent this issue is the use of reduced-order models that can approximate the QoI given a stochastic outcome without the need of a complete CFD simulation. However, even this approach may conceptually lag behind since the QoI needs to be evaluated for each shape update. Therefore, even though a suitable reduced-order model may be built for the initial shape, it might prove below par in its estimations for the subsequent shapes during the optimization history. To this extent, this thesis investigates a modification of the original method to alleviate some of the computational effort, cf. Section 5.2.1.

5.2.1 Binning Variant

Consider a scenario in which the primal problem depends on a single uncertain variable ω. Given a PDF $f(\omega)$ associated with ω, the SGD method relies on the evaluation of the objective (and its derivative in the direction of the control) for randomly selected samples. For example, if the sample space corresponds to $[\omega_{\min}, \omega_{\max}] = [-1, 1]$ and the probability distribution refers to a Gaussian distribution, the PDF corresponds to Fig. 5.1 (left), truncated before and after -1 and 1, respectively. If the sample size N corresponds to a computationally feasible relatively small number, i.e., in the order of $\mathcal{O}(10)$, then it is most likely that the stochastic gradient is approximated by information stemming only from the most probable outcomes. Therefore, the information from the more unlikely stochastic outcomes are neglected and the optimization procedure is prone to fluctuate a lot since the direction of the descent direction may significantly change per shape update.

To this extent, this thesis proposes a variant of the original SGD method so that the evaluated realizations scan the complete sample space in each shape update. The foundation of the variant is based on binning the sample space into N equidistant bins with a width $(\omega_{\max} - \omega_{\min})/N$. In each bin a uniform constant PDF $f^b(\omega) = N/(\omega_{\max} - \omega_{\min})$ is assigned. The sampling is then based on the newly created bins thus assuring that the complete sample space is uniformly scanned during the estimation of the stochastic gradient. For example, the first stochastic outcome is selected from the first bin, the second from the second bin and so on until all N stochastic outcomes are created. However, if the process continues now as in the case of SGD, the impact of the underlying PDF, for example the Gaussian distribution, is completely lost.

In order to recover the information of the underlying PDF $f(\omega)$ and to assure a discrete partition of unity, the derivatives of the statistical moments in the direction of the control are weighted by the normalized probability density of each stochastic outcome based on the underlying PDF, viz.

$$\frac{d\mu_F}{du_k} = \frac{1}{N} \sum_{n=1}^{N} \frac{dF_n}{du_k} \hat{f}(\omega^{(n)}), \tag{5.10}$$

$$\frac{d\sigma_F}{du_k} = \frac{1}{\sigma_F (N-1)} \sum_{n=1}^{N} \left[(F_n - \mu_F) \left(\frac{dF_n}{du_k} - \frac{d\mu_F}{du_k} \right) \right] \hat{f}(\omega^{(n)}), \tag{5.11}$$

with

$$\hat{f}(\omega^{(n)}) = \frac{f(\omega^{(n)})}{\sum_{n=1}^{N} f(\omega^{(n)})}, \tag{5.12}$$

where $f(\omega^{(n)})$ corresponds to the probability density of the underlying PDF for the stochastic outcome $\omega^{(n)}$ selected from the uniform distribution of the n^{th} bin. The binning process in the context of the SGD method is schematically visualized in Fig. 5.1 (right).

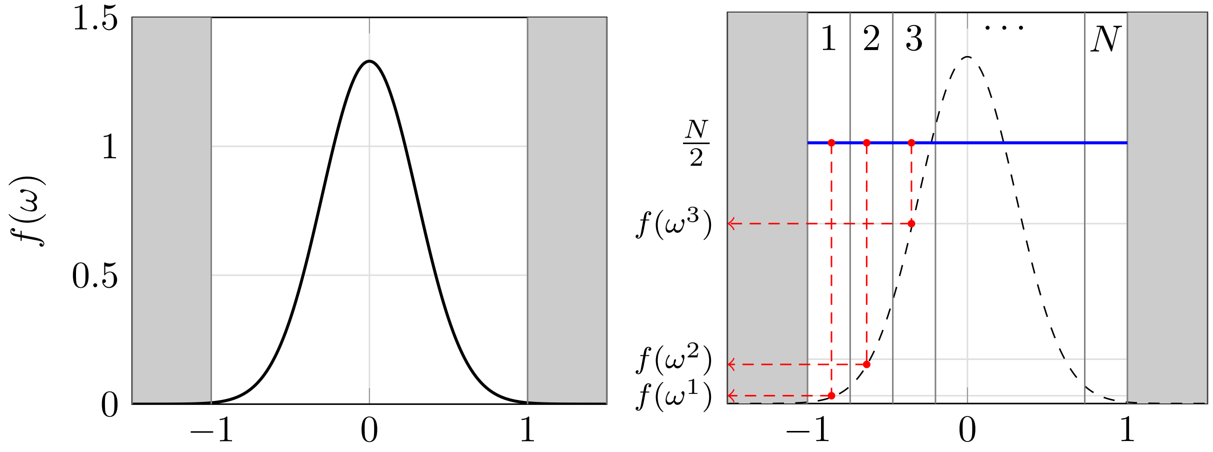

Figure 5.1: Left: Gaussian PDF for mean and standard deviation equal to 0 and 0.3, respectively. Right: Schematic representation of the SGD binning variant. Note that the figure has been created for illustrative purposes and does not correspond to an accurate representation of the PDFs. In specific, the area under each bin should correspond to the area under the underlying PDF (in dashed line) equal to unity.

In case the primal problem depends on a vector of M uncertain variables, the same process is followed for each individual variable and the normalized weight is computed based on

$$\hat{f}(\omega^{(n)}) = \frac{\sum_{i=1}^{M} f_i(\omega_i^{(n)})}{\sum_{n=1}^{N}\left(\sum_{i=1}^{M} f_i(\omega_i^{(n)})\right)}, \tag{5.13}$$

where f_i corresponds to the underlying PDF associated with the i^{th} uncertain variable.

It must be noted that even on the original SGD method, this kind of weighting is implicitly applied by the sampling process. The random choice of the stochastic outcome is dependant on the underlying PDF and therefore the frequency with which an outcome appears in the approximation of the stochastic gradient corresponds to an implicit weighting of the estimation. The essential difference between the proposed modification and the original method is that the modification targets to explicitly consider this weight and allow for a scan of the complete sample space using a reduced sample size N.

5.2.2 Optimization Algorithm

The numerical realization of the SGD-based optimization methods is illustrated in Algorithm 3. As previously discussed, due to the independence of the realizations, the loops in lines 2-5 and 7-9 can be trivially parallelized given the necessary computational resources.

Algorithm 3 SGD-based robust parameter-free shape optimization algorithm using the adjoint method.

```
Require: initial shape $\Gamma^0$, $l^{\max} \geq 1$, $N \geq 1$
1:  for $l = 0, 1, ...$ do
2:      for $n = 0, 1, ..., N$ do
3:          Generate stochastic outcome $\omega_i^{(n)}$.
4:          Compute the primal problem at $(\omega_i^{(n)}, u_k^l)$ to find $F_n$.
5:      end for
6:      Calculate $\mu_F$ and $\sigma_F$ based on Eqs. (5.3) and (5.4), respectively.
7:      for $n = 0, 1, ..., N$ do
8:          Compute the adjoint problem at $(\omega_i^{(n)}, u_k^l)$ to find $dF_n/du_k$.
9:      end for
10:     Calculate $d\mu_F/du_k$ and $d\sigma_F/du_k$ based on Eqs. (5.7) or (5.10) and (5.8) or (5.11),
        respectively.
11:     Calculate the shape sensitivity based on Eq. (5.9).
12:     Compute a descent direction $\delta u_k \in \Omega^l$ based on one of the methods presented in
        Chapter 3.
13:     Determine step size $t^l$.
14:     Update shape based on Eq. (3.2).
15:     if $l = l^{\max}$ then
16:         break
17:     end if
18: end for
```

The adjoint problem is dependent on the underlying primal and for the applications considered in this work, it refers to one of the problems presented in Chapter 4. Furthermore, in contrast to deterministic optimization, the necessary information for the computation of the shape sensitivity are produced by different simulations. Therefore, an intermediate computational level is created where all the necessary information are collected. The same level is used to compute an appropriate descent direction and update the shape. The operations of lines 10-14 are thus realized therein.

The convergence of a SGD method is a challenging issue. Convergence criteria as those employed in the case of deterministic optimization can hardly suffice since the evaluated sample can even lead to an increase of the objective functional in some iterations. Therefore, as shown in Algorithm 3 the complete process terminates when a pre-defined number of iterations $l^{\max}$ is reached. An a priori knowledge of this number is especially difficult to attain in the context of SGD. However, it should be chosen based on the computational capabilities of the designer and the available resources.

In this regard, the choice of an appropriate step size t^l is also crucial. As discussed in Geiersbach et al. [2021], the Armijo backtracing condition shown in Section 3.3.1 generally fails in stochastic approximations. Therefore, the "Robbins-Monro" step size rule, originally introduced by Robbins and Monro [1951], is recommended to determine an appropriate step size per optimization iteration. The rule reads

$$t^l \leq 0, \quad \sum_{l=1}^{\infty} t^l = \infty, \quad \sum_{l=1}^{\infty} (t^l)^2 < \infty. \tag{5.14}$$

A straightforward step size sequence that satisfies the aforementioned rule is $t^l = c^*/l$, where c^* is a user-defined constant. Though this step size rule satisfies the "Robbins-Monro" criteria, it can rapidly lead to (undesirably) minor shape updates. For example, if the randomly chosen samples in the first couple iterations lead to opposing shape update directions, the deformation field will reduce in magnitude not because we are approaching a local optimum but because the step size has decreased by virtue of the applied rule. Therefore, in this work the step size per optimization iteration l is chosen as

$$t^l = \begin{cases} c^*, & \text{for } l \leq l^{\mathrm{RM}} \\ c^*/\left(l - l^{\mathrm{RM}}\right), & \text{for } l > l^{\mathrm{RM}} \end{cases} \tag{5.15}$$

where c^* is computed based on the maximum displacement rule of the first iteration (cf. Eq. (3.15)) and $l^{\mathrm{RM}} < l^{\max}$ corresponds to an intermediate iteration after which the estimated objective of the last couple iterations has sufficiently decreased w.r.t. the initial. Note that the step size sequence of Eq. (5.15) satisfies the conditions of (5.14).

5.3 Adjoint-based First-Order Second-Moment (FOSM) Method

This section presents a methodology for the solution of the optimization problem (5.2) by employing the MoM for the determination of the statistical moments of the QoI. This approach has previously been applied in the context of engineering robust optimization applications in, e.g., Krüger et al. [2023], Fragkos et al. [2019], Papadimitriou and Giannakoglou [2013]. As discussed in Section 5.1, each uncertain variable is associated with a PDF, which implies a mean and a standard deviation for each variable. Let $\bar{\omega}_i \in \mathbb{R}^M$ and $\sigma_i \in \mathbb{R}^M$ denote the vectors of mean values and standard deviations, respectively. A Taylor series expansion of the (reduced) QoI around the mean values of the uncertainty variables then reads

$$\hat{F}(\bar{\omega}_i + \delta\omega_i) = \hat{F}(\bar{\omega}_i) + \frac{d\hat{F}}{d\omega_i}\delta\omega_i + \frac{1}{2}\frac{d^2\hat{F}}{d\omega_i d\omega_j}\delta\omega_i\delta\omega_j + \text{HoT}. \tag{5.16}$$

Even though not explicitly shown, it is implied that all derivative expressions are computed at $\bar{\omega}_i$ unless stated otherwise. This assumption holds also for what follows. Truncating the expansion after the second term on the RHS results in a first order approximation and is thus used to derive the FOSM method. Note that this truncation implies that the approximation is accurate for any $\delta\omega_i$ if the relationship between the QoI and the uncertain variables is linear. Based on the first order truncation of Eq. (5.16), the QoI computed at an arbitrary stochastic outcome ω_i can be written as

$$\hat{F}(\omega_i) = \hat{F}(\bar{\omega}_i + \delta\omega_i) = \hat{F}(\bar{\omega}_i) + \frac{d\hat{F}}{d\omega_i}\delta\omega_i + \mathcal{O}(\delta\omega_i^2). \tag{5.17}$$

Substituting Eq. (5.17) in Eq. (5.5) and neglecting the HoT gives

$$\begin{aligned}
\mu_F &= \int_{-\infty}^{\infty} \left[\hat{F}(\bar{\omega}_i) + \frac{d\hat{F}}{d\omega_i}\delta\omega_i\right] f(\omega_i)\,\mathrm{d}\omega \\
&= \hat{F}(\bar{\omega}_i) \underbrace{\int_{-\infty}^{\infty} f(\omega_i)\,\mathrm{d}\omega}_{1} + \frac{d\hat{F}}{d\omega_i} \underbrace{\int_{-\infty}^{\infty} \delta\omega_i f(\omega_i)\,\mathrm{d}\omega}_{0} = \hat{F}(\bar{\omega}_i),
\end{aligned} \tag{5.18}$$

since the first integral on the last line of Eq. (5.18) is identically equal to 1 and the second integral for $\delta\omega_i = (\omega_i - \bar{\omega}_i)$ corresponds to the first central moment which is zero for any distribution that has a mean. Applying the same process to the definition of the variance

(5.6) results in

$$\sigma_F^2 = \int_{-\infty}^{\infty} \left[\hat{F}(\bar{\omega}_i) + \frac{d\hat{F}}{d\omega_i}\delta\omega_i \right]^2 f(\omega_i)\,\mathrm{d}\omega - \mu_F^2.$$

$$= \underbrace{\hat{F}(\bar{\omega}_i)^2}_{\mu_F^2} + 2\hat{F}(\bar{\omega}_i)\frac{d\hat{F}}{d\omega_i}\underbrace{\int_{-\infty}^{\infty} \delta\omega_i f(\omega_i)\,\mathrm{d}\omega}_{0} + \frac{d\hat{F}}{d\omega_i}\frac{d\hat{F}}{d\omega_j}\underbrace{\int_{-\infty}^{\infty} \delta\omega_i\delta\omega_j f(\omega_i)\,\mathrm{d}\omega}_{C_{ij}} - \mu_F^2$$

$$= \frac{d\hat{F}}{d\omega_i}\frac{d\hat{F}}{d\omega_j}C_{ij}, \tag{5.19}$$

where C_{ij} denotes the covariance matrix of the uncertain variables. As already implied but not explicitly said, this thesis assumes the uncertain variables of a problem to be independent of each other. In this case, the covariance matrix is a diagonal matrix, with its diagonal corresponding to the vector σ_i^2. Based on this assumption, Eq. (5.19) can be written in a compact form as

$$\sigma_F^2 = \left[\frac{d\hat{F}}{d\omega_i}\right]^2 \sigma_i^2 \rightarrow \sigma_F = \sqrt{\left[\frac{d\hat{F}}{d\omega_i}\right]^2 \sigma_i^2}. \tag{5.20}$$

Therefore, with knowledge of $\bar{\omega}_i$ and σ_i, one can approximate the two statistical moments based on the first order approximation outlined in Eq. (5.17). Note that the method is independent of the underlying choice of the PDF and can be equivalently applied, given the sole knowledge of the mean and variance values. This is especially advantageous in applications where the underlying particular probability distribution is unknown to the designer.

Based on the above moment approximations the objective functional reads

$$J = w_1\hat{F}(\bar{\omega}_i) + w_2\sqrt{\left[\frac{d\hat{F}}{d\omega_i}\right]^2 \sigma_i^2} \tag{5.21}$$

and the sought derivative in the direction of the control

$$\frac{dJ}{du_k} = w_1\frac{d\hat{F}}{du_k} + w_2\frac{1}{\sigma_F}\frac{d^2\hat{F}}{d\omega_i du_k}\lambda_i, \tag{5.22}$$

where the vector $\lambda_i \in \mathbb{R}^M$ corresponds to

$$\lambda_i = \left(\frac{d\hat{F}}{d\omega_1}\sigma_1^2, \frac{d\hat{F}}{d\omega_2}\sigma_2^2, \ldots, \frac{d\hat{F}}{d\omega_M}\sigma_M^2 \right).$$

To perform the computation of the sought derivative (5.22), the method requires the calculation of the following quantities at each shape update:

- The derivative of the QoI in the direction of the control, $d\hat{F}/du_k$.

- The derivative of the QoI in the direction of the uncertain variables, $d\hat{F}/d\omega_i$.
- The mixed derivative of the QoI in both aforementioned directions, $d^2\hat{F}/d\omega_i du_k$.

5.3.1 First-Order Derivative in the Direction of the Control

Due to the independence between the uncertain variables and the control, the computation of $d\hat{F}/du_k$ does not require any additional uncertainty-related changes. Therefore, its computation can be realized using any of the methods outlined in Section 4.1. Naturally, the preferable method is the adjoint method since the control corresponds exclusively to the shape in the context of this thesis. Depending on the underlying primal problem, the expression of this derivative can thus be found in Sections 4.2.4, 4.3.4, 4.4.4 or 4.5.3, where the adjoint problems related to biomedical applications are presented. The total computational cost for its estimation thus amounts to one primal and one adjoint solution at the prescribed state of uncertainty $\omega_i = \bar{\omega}_i$.

5.3.2 First-Order Derivative in the Direction of the Uncertain Variables

The analysis made above is based on the reduced QoI $\hat{F}$, however in the context of computing the first-order derivative of the QoI in the direction of the uncertain variables it is illustrative to consider an expanded formulation for the QoI, i.e., $F(y_m(\omega_i), u_k, \omega_i)$. Note that $\hat{F} =: F$ and this distinction is only made for better comprehension. The sought derivative can therefore be stated based on the chain rule as

$$\frac{dF}{d\omega_i} = \frac{\partial F}{\partial \omega_i} + \frac{\partial F}{\partial y_m}\frac{dy_m}{d\omega_i}. \tag{5.23}$$

Note that this expression is essentially equivalent to the expression of Eq. (4.11) by simply swapping the control vector with the uncertainty variable vector. It is interesting therefore to examine whether what was applied therein can be equivalently transferred to the identification of $dF/d\omega_i$.

Our constraints are now represented by $R_l(y_m(\omega_i, u_k), u_k, \omega_i) = 0$ and must always be satisfied, even at perturbations of the uncertain variables, which implies that

$$\frac{dR_l}{d\omega_i} = \frac{\partial R_l}{\partial \omega_i} + \frac{\partial R_l}{\partial y_m}\frac{dy_m}{d\omega_i} = 0 \rightarrow \frac{\partial R_l}{\partial y_m}\frac{dy_m}{d\omega_i} = -\frac{\partial R_l}{\partial \omega_i}, \tag{5.24}$$

which can be used to finally arrive at an equivalent expression of (4.13)

$$\frac{dF}{d\omega_i} = \frac{\partial F}{\partial \omega_i} - \frac{\partial F}{\partial y_m}\left(\frac{\partial R_l}{\partial y_m}\right)^{-1}\frac{\partial R_l}{\partial \omega_i}. \tag{5.25}$$

This shows that the use of the adjoint method is indeed reasonable for approximating $d\hat{F}/d\omega_i$. However, as outlined in Chapter 4, the adjoint method is motivated in cases where the control (here uncertainties) vector is substantially large since it decouples the necessary additional computations from the number of control (uncertainty) variables. If the uncertainty vector is small, even the straightforward FD method can provide the necessary information at a reasonable cost.

Finite difference method

The sought derivative can be computed based on a first-order accurate finite differences approach as

$$\frac{dF}{d\omega_i} = \frac{F(y_m(\bar{\omega}_i + \delta\omega_i), u_k, \bar{\omega}_i + \delta\omega_i) - F(y_m(\bar{\omega}_i), u_k, \bar{\omega}_i)}{\delta\omega_i} + \mathcal{O}(\delta\omega_i). \tag{5.26}$$

This requires the computation of M more simulations[2], in addition to the necessary simulation computed at $\omega_i = \bar{\omega}_i$. Note that the approximation is only first-order accurate. A higher order approximation of the derivative, while possible, can be omitted due to the initial assumption of linearity between the QoI and the uncertain variables.

Naturally, the larger the number of uncertain variables, the larger the additional computational effort required to approximate the sought derivative from FD. The case of uncertain hemolysis parameters must again be highlighted in this context. If one considers the hemolysis parameters to be uncertain, i.e., $\omega_i = (C, \alpha, \beta)$ and $M = 3$, cf. Table 2.1, the numerical approximation of Eq. (5.26) becomes computationally trivial. Due to the one-way coupling of the hemolysis model, any variation of ω_i will not induce a variation in the flow field. Therefore, the computationally expensive solution of the NS needs to be realized only once at $\omega_i = \bar{\omega}_i$ and then used for 3 solutions of the (perturbed) hemolysis equations.

Adjoint method

Equation (5.25) motivates the use of the adjoint method for the determination of the sought derivative. If the same conceptual process as the one presented in Section 4.1.4 is followed, then one easily arrives at the conclusion that

$$\frac{dF}{d\omega_i} = \frac{\partial F}{\partial \omega_i} - \hat{y}_l \frac{\partial R_l}{\partial \omega_i} \quad \text{with} \quad \hat{y}_l = -\frac{\partial F}{\partial y_m} \left(\frac{\partial R_l}{\partial y_m} \right)^{-1}. \tag{5.27}$$

Note that $\hat{y}_l$ results from the same equation as in the case of dF/du_k. This implies that the adjoint solution needs to be computed only once and concurrently provide the necessary information for the computation of both required first derivatives.

To illustrate the adjoint method further in the context of computing $dF/d\omega_i$, consider the following example. A 2D channel flow is obscured by three circular objects, namely C1, C2, C3, with diameters $D = H/11$, $d = D/2$ and D, respectively. The total length of the domain is $L \approx 3H$. The longitudinal distance from the inlet and vertical distance from the top wall for the centers of C1, C2 and C3 are (H, $H/2$), (1.36H, 0.38H) and (1.9H, 0.63H), respectively. A sketch of this configuration is shown in Fig. 5.2 (left). The case includes uncertainties by means of the inlet velocity profile, which is given by a truncated

---

[2] Note that as already discussed in Chapter 4, these simulations correspond to restart cases from a converged solution and therefore their cost is usually smaller than a complete CFD simulation from scratch.

Karhunen-Lòeve expansion, see Benner et al. [2020], viz.

$$\begin{aligned} v_n(y) &= [v(y)]^{\text{mean}} + \sum_{i=1}^{M} v^R \left(i^{(-\gamma-0.5)} \sin\left(\frac{2\pi i y}{H}\right)\right) \omega_i, && (5.28)\\ v_t(y) &= 0, && (5.29) \end{aligned}$$

where the mean velocity profile ($[v(y)]^{\text{mean}}$) is given by a fully developed parabolic velocity profile and the indices t, n mark the y, x direction along the inlet. Figure 5.2 (right) illustrates the differences between the mean flow profile and a perturbed one based on Eq. (5.28) with $M = 5$, a decay rate $\gamma = 0.1$ and a stochastic outcome $\omega_i = 0.5\ \forall i \in \{1, 2, \dots, 5\}$. Consider that the QoI stands for the power loss, which for the convenience of the reader is repeated here,

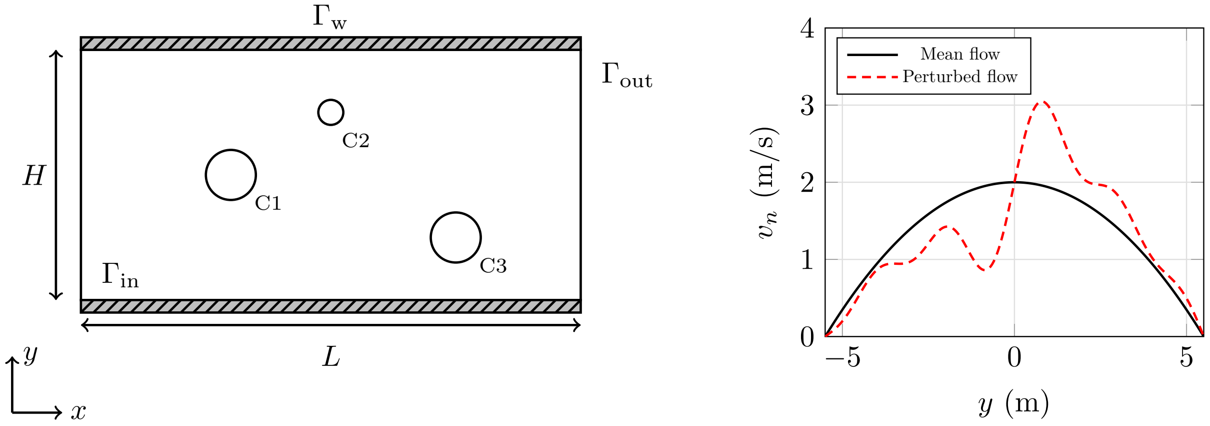

Figure 5.2: Left: Sketch of the 2D flow with 3 circular obstacles. Right: Mean and perturbed inlet velocity profile for the example case.

$$F = -\int_{\Gamma} \left(p + \frac{1}{2}\rho(v_k v_k)\right) v_i n_i \,\mathrm{d}\Gamma = -\int_{\Gamma} f_{\Gamma} \,\mathrm{d}\Gamma.$$

In view of the integral formulation of our constraints, Eq. (5.27) can be written as

$$\frac{dF}{d\omega_i} = \frac{\partial F}{\partial \omega_i} - \int_{\Omega} \hat{y}_l \frac{\partial R_l}{\partial \omega_i} \,\mathrm{d}\Omega. \tag{5.30}$$

Note that in contrast to the previous chapter, where inserting the derivative inside the integral required an assumption for cancelling out an additional Leibniz term (see discussion in Section 4.2.4), the formulation here is exact due to the independence of the shape and the uncertain variables. The first term on the RHS of Eq. (5.30) can be explicitly treated as

$$\frac{\partial F}{\partial \omega_i} = -\left[\frac{\partial}{\partial \omega_i}\int\limits_{\Gamma_{in}} f_\Gamma \,\mathrm{d}\Gamma + \underbrace{\frac{\partial}{\partial \omega_i}\int\limits_{\Gamma\backslash\Gamma_{in}} f_\Gamma \,\mathrm{d}\Gamma}_{=0}\right]$$
$$= -\int\limits_{\Gamma_{in}}\left(p\frac{\partial v_n}{\partial \omega_i} + \frac{3}{2}\rho v_n^2 \frac{\partial v_n}{\partial \omega_i}\right)\mathrm{d}\Gamma. \tag{5.31}$$

Based on Eq. (5.28),

$$\frac{\partial v_n}{\partial \omega_i} = \cancelto{0}{\frac{\partial v^{\text{mean}}}{\partial \omega_i}} + A_i \quad \text{with} \quad A_i = -v^R\left(i^{(-\gamma-0.5)}\sin\left(\frac{2\pi i y}{H}\right)\right), \tag{5.32}$$

which if substituted in Eq. (5.31) results in

$$\frac{\partial F}{\partial \omega_i} = \int\limits_{\Gamma_{in}} A_i\left(p + \frac{3}{2}\rho v_n^2\right)\mathrm{d}\Gamma. \tag{5.33}$$

Having found an expression for $\partial F/\partial \omega_i$, the remaining term of Eq. (5.30) is handled based on adjoint techniques. It is reminded that the adjoint variables are deduced by the same adjoint problem as in the case of computing dF/du_k. This means that for the example case considered here, the adjoint field equations and adjoint boundary conditions correspond to the expressions of Section 4.2. Furthermore, using Eq. (5.24) one can substitute $\partial R_l/\partial \omega_i$ with the exact same expression as the one used for the derivation of the shape sensitivity. Therefore, the second term of Eq. (5.30) can be expressed as in (4.56) by substituting the variation of the state variables w.r.t. the control to variations w.r.t. the uncertain variables, viz.

$$-\int\limits_{\Omega}\hat{y}_l\frac{\partial R_l}{\partial \omega_i}\,\mathrm{d}\Omega = -\int\limits_{\Gamma}\frac{\partial p}{\partial \omega_i}\left(\hat{v}_k n_k\right)\mathrm{d}\Gamma + \int\limits_{\Omega}\frac{\partial p}{\partial \omega_i}\left(\frac{\partial \hat{v}_k}{\partial x_k}\right)\mathrm{d}\Omega$$
$$-\int\limits_{\Gamma}\frac{\partial v_k}{\partial \omega_i}\left[-\hat{p}n_k + \rho\hat{v}_k v_j n_j + \mu n_j\frac{\partial \hat{v}_k}{\partial x_j}\right]\mathrm{d}\Gamma + \int\limits_{\Gamma}\mu\hat{v}_k\frac{\partial}{\partial x_j}\left(\frac{\partial v_k}{\partial \omega_i}\right)n_j\,\mathrm{d}\Gamma$$
$$-\int\limits_{\Omega}\frac{\partial v_k}{\partial \omega_i}\left[\hat{v}_j\rho\frac{\partial v_j}{\partial x_k} - v_j\rho\frac{\partial \hat{v}_k}{\partial x_j} - \frac{\partial}{\partial x_j}\left(2\mu\hat{S}_{kj} - \hat{p}\delta_{kj}\right)\right]\mathrm{d}\Omega. \tag{5.34}$$

The QoI (objective functional in the context of the previous chapter) is defined exclusively on Γ and therefore the volume integrals vanish by virtue of the adjoint field equations' solution. Furthermore, taking into account that pressure does not explicitly depend on the uncertain variables, the above expression simplifies to

$$
\begin{aligned}
-\int\limits_{\Omega} \hat{y}_l \frac{\partial R_l}{\partial \omega_i}\, \mathrm{d}\Omega = & -\int\limits_{\Gamma} \frac{\partial v_k}{\partial \omega_i} \left[-\hat{p} n_k + \rho \hat{v}_k v_j n_j + \mu n_j \frac{\partial \hat{v}_k}{\partial x_j} \right] \mathrm{d}\Gamma \\
& + \int\limits_{\Gamma} \mu \hat{v}_k \frac{\partial}{\partial x_j} \left(\frac{\partial v_k}{\partial \omega_i} \right) n_j \, \mathrm{d}\Gamma. \qquad (5.35)
\end{aligned}
$$

The only boundary in which we have an explicit dependence between velocity and uncertain variables is Γ_{in}. Based on this, the second term on the RHS of Eq. (5.35) can be written as

$$
\int\limits_{\Gamma_{\mathrm{in}}} \mu \hat{v}_k \frac{\partial}{\partial x_j} \left(\frac{\partial v_k}{\partial \omega_i} \right) n_j \, \mathrm{d}\Gamma = \int\limits_{\Gamma_{\mathrm{in}}} \mu \hat{v}_t \frac{\partial}{\partial \omega_i} \left(\frac{\partial v_t}{\partial n} \right) \mathrm{d}\Gamma + \int\limits_{\Gamma_{\mathrm{in}}} \mu \hat{v}_n \frac{\partial}{\partial \omega_i} \left(\frac{\partial v_n}{\partial n} \right) \mathrm{d}\Gamma = 0. \qquad (5.36)
$$

Based on the deductions of Section 4.2.3, which are also applicable here, $\hat{v}_t = 0$ on Γ_{in} thus leading to the cancellation of the first integral in Eq. (5.36). The second term is also equal to zero by virtue of $v_t = 0$ on Γ_{in} and the assumption that continuity asymptotically holds on the boundaries.

Following the same conceptual path, $\partial \hat{v}_t / \partial x_t = 0$ on Γ_{in} and by applying $\hat{v}_n = v_n$ on Γ_{in} for the power loss QoI, one arrives at

$$
-\int\limits_{\Omega} \hat{y}_l \frac{\partial R_l}{\partial \omega_i}\, \mathrm{d}\Omega = \int\limits_{\Gamma_{\mathrm{in}}} A_i \left[\hat{p} - \rho v_n^2 \right] \mathrm{d}\Gamma. \qquad (5.37)
$$

Combining Eqs. (5.33) and (5.37) results in an expression for the initially sought derivative

$$
\frac{dF}{d\omega_i} = \int\limits_{\Gamma_{\mathrm{in}}} A_i \left[(\hat{p} + p) + \frac{1}{2} \rho v_n^2 \right] \mathrm{d}\Gamma. \qquad (5.38)
$$

The computation of Eq. (5.38) requires no additional computational effort, apart from the numerical estimation of the integrand expression, since both primal and adjoint variables are already known. The derivation process outlined above can be followed for any QoI and primal problem, thus making the adjoint method an appealing tool even in this context and especially for uncertain cases with large M.

For the sake of completeness, the validity of expression (5.38) is assessed against a FD study. The study is conducted based on the parameters described above and $\bar{\omega}_i = 0.5\ \forall i \in \{1, 2, \dots, 5\}$, which results in the inlet velocity profile presented in Fig. 5.2 (right). The 2D computational grid consists of 22400 CVs. The solution of the velocity magnitude field at $\bar{\omega}_i$ is presented in Fig. 5.3 (left). The sought derivative is computed based on a first-order accurate FD study (5.26), for which 5 additional computations are realized for $\bar{\omega}_i + \delta\omega_i$, with $\delta\omega_i = 10^{-4}\ \forall i \in \{1, 2, \dots, 5\}$. The results of the study are visualized in Fig. 5.3 (right) where they are compared with the corresponding adjoint solution (5.38). The necessary adjoint field equations and BCs can be found in Section 4.2. As can be seen, the adjoint and FD-based solutions satisfactorily match (no deviation is larger than 2%), with a slight under-estimation from the adjoint solver. This can be attributed to the accuracy of the

FD approximation. Overall, the adjoint-based results are acceptable, especially in view of the computational efficiency of the method, thus showcasing the beneficial characteristics of the method even for the computation of the first-order derivative of the QoI in the direction of the uncertain variables.

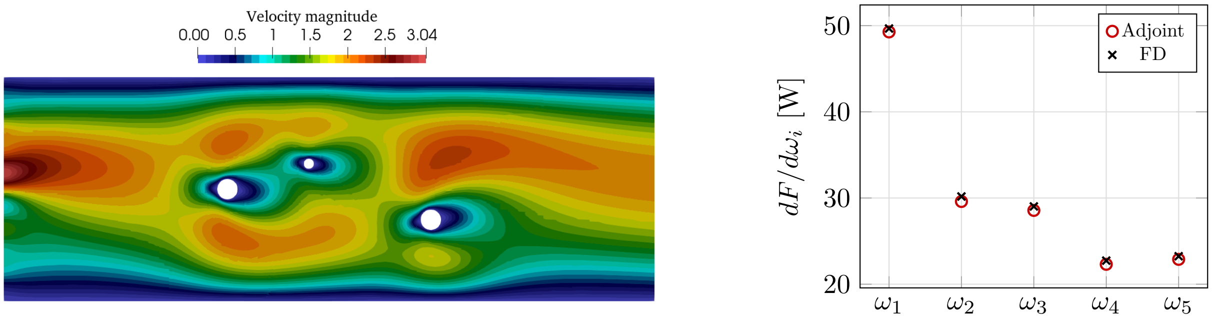

Figure 5.3: Left: Velocity magnitude contours for $\bar{\omega}_i$. Right: Comparison of estimated first-order derivative based on FD (5.26) with $\delta\omega_i = 10^{-4}$ $\forall i \in \{1, 2, \ldots, 5\}$ and adjoint (5.38).

5.3.3 Second-Order Mixed Derivative

While the required first derivatives can be computed from the same adjoint problem, thus requiring the same computational effort as in deterministic shape optimization, the mixed second derivative requires additional computations. One straightforward option is to compute the sought derivative based on a second-order accurate FD scheme, viz.

$$\frac{d^2\hat{F}}{d\omega_i du_k} = \frac{\frac{d\hat{F}}{du_k}(\bar{\omega}_i + \delta\omega_i) - \frac{d\hat{F}}{du_k}(\bar{\omega}_i - \delta\omega_i)}{2\delta\omega_i} + \mathcal{O}(\delta\omega_i^2). \tag{5.39}$$

This method requires $4M$ additional simulations, i.e., $2M$ primal simulations at $\bar{\omega}_i + \delta\omega_i$ and $\bar{\omega}_i - \delta\omega_i$, and their respective duals for the computation of the first derivatives. This cost can, of course, be halved by using a first-order scheme, at the expense of the accuracy of the approximation. Nevertheless, depending on the size of the uncertain variables, the cost of this approximation can rapidly become unbearable in view of the often expensive underlying CFD simulations and the several iterations needed for convergence of the optimization.

However, as well-noted by Fragkos et al. [2019] and Krüger et al. [2023], the computation of Eq. (5.22) does not require the explicit computation of the mixed second derivative but instead its projection on the λ_i vector. Computing the projected quantity instead of the mixed derivative renders the necessary cost independent of the number of uncertain variables. Fragkos et al. [2019] proposes to estimate the sought quantity through the solution of an additional primal and adjoint system of equations while Krüger et al. [2023] suggests that the quantity is computed through the application of FD in the principal direction. This thesis employs the methodology proposed by Krüger et al. [2023] and thus the concept of the approach is briefly presented in what follows. For further details, the reader is pointed to the original paper.

Consider the Taylor series expansion of the first derivative of the QoI in the direction of the control at the "uncertainty location" $\bar{\omega}_i$, viz.

$$\frac{d\hat{F}}{du_k}(\bar{\omega}_i + \delta\omega_i) = \frac{d\hat{F}}{du_k}(\bar{\omega}_i) + \frac{d^2\hat{F}}{du_k d\omega_i}\delta\omega_i + \mathcal{O}(\delta\omega_i^2). \tag{5.40}$$

If the perturbation vector is not arbitrarily chosen but instead equated with a scaled version of the λ_i vector, i.e., $\delta\omega_i = \epsilon^* \lambda_i$, then Eq. (5.40) results in

$$\frac{d^2\hat{F}}{du_k d\omega_i}\lambda_i = \frac{1}{\epsilon^*}\left[\frac{d\hat{F}}{du_k}(\bar{\omega}_i + \epsilon^*\lambda_i) - \frac{d\hat{F}}{du_k}(\bar{\omega}_i)\right] + \mathcal{O}(\epsilon^*\lambda_i^2), \tag{5.41}$$

while a second-order accurate approximation of the projected quantity reads

$$\frac{d^2\hat{F}}{du_k d\omega_i}\lambda_i = \frac{1}{2\,\epsilon^*}\left[\frac{d\hat{F}}{du_k}(\bar{\omega}_i + \epsilon^*\lambda_i) - \frac{d\hat{F}}{du_k}(\bar{\omega}_i - \epsilon^*\lambda_i)\right] + \mathcal{O}(\epsilon^{*2}\lambda_i^2). \tag{5.42}$$

Note that the essential difference between expressions (5.39) and (5.42), that admittedly might be hidden based on the employed index notation, is that the former needs to perturb each individual uncertain variable while keeping the rest constant at their mean values while the latter perturbs the complete mean value vector simultaneously. This leads to expression (5.39) requiring 4M additional simulations while expression (5.42) is resolved with only 4 additional simulations – or 2 for the first-order accurate expression (5.41) – independent of the number of uncertain variables.

The value of ϵ^* is control-dependent and throughout this work it is set based on

$$\epsilon^* = \hat{\epsilon}\frac{1}{\sqrt{\lambda_i^2}}, \tag{5.43}$$

where $\hat{\epsilon}$ is fixed, as the authors of Krüger et al. [2023] suggest.

5.3.4 Optimization Algorithm

The adjoint-assisted optimization algorithm for robust shape optimization using the FOSM method is presented in Algorithm 4.

Note that the presented algorithms in this chapter differentiate between statements with the keyword "Compute" and "Calculate". The lines including the former require a substantial computational effort, since they involve (full or restart) CFD simulations, while those including the latter amount to trivial resources for the computation of sought quantities. Furthermore, the computations of lines 9 and 10 can be realized in parallel since they are independent of each other. Overall, one shape update requires 6 CFD simulations[3] and 1 simulation for the computation of the descent direction. As regards the latter, it must be highlighted that the expression of Eq. (5.22) corresponds to a shape sensitivity and thus similarly to the deterministic optimization cases, a proper descent direction must be identified for the update of the shape (see Chapter 3). However, this issue becomes

---

[3] Note that the 2 simulations of line 9 are substantially faster than the other 4 in the case where hemolysis parameters are considered uncertain since the primal flow does not need to be recomputed.

Algorithm 4 FOSM-based robust parameter-free shape optimization algorithm using the adjoint method.

```
Require: initial shape $\Gamma^0$, $\bar{\omega}_i$, $\sigma_i$, $\hat{\epsilon} > 0$, $\epsilon > 0$
 1: for $l = 0, 1, ...$ do
 2:     Compute the primal problem at $(\bar{\omega}_i, u_k^l)$ to find $\hat{F}(\bar{\omega}_i)$.
 3:     Compute the adjoint problem at $(\bar{\omega}_i, u_k^l)$ to find $d\hat{F}/du_k$, $d\hat{F}/d\omega_i$ and $\lambda_i$.
 4:     Calculate the objective functional $J$ based on Eq. (5.21).
 5:     if $|J(u_k^l) - J(u_k^{l-1})|/J(u_k^{l-1}) \leq \epsilon$ then
 6:         break
 7:     end if
 8:     Calculate $\epsilon^*$ based on Eq. (5.43).
 9:     Compute the primal problem at $(\bar{\omega}_i + \epsilon^* \lambda_i, u_k^l)$ and $(\bar{\omega}_i - \epsilon^* \lambda_i, u_k^l)$ restating from
        the primal solution at $(\bar{\omega}_i, u_k^l)$.
10:     Compute the adjoint problem at $(\bar{\omega}_i + \epsilon^* \lambda_i, u_k^l)$ and $(\bar{\omega}_i - \epsilon^* \lambda_i, u_k^l)$ to find $d\hat{F}/du_k$
        for each respective state.
11:     Calculate the projected mixed derivative based on Eq. (5.42).
12:     Calculate the shape sensitivity based on Eq. (5.22).
13:     Compute a descent direction $\delta u_k \in \Omega^l$ based on one of the methods presented in
        Chapter 3.
14:     Determine step size $t^l$.
15:     Update shape based on Eq. (3.2).
16: end for
```

slightly more involved in the case of robust parameter-free shape optimization. For the computation of a descent direction in the deterministic optimization case, the necessary information, i.e., the sensitivity distribution over Γ_d, can be fully obtained as soon as the adjoint system is solved. Therefore, the shape update can be computationally realized by restarting from the last adjoint solution. In the case of robust shape optimization however, the necessary sensitivity is computed on different algorithmic levels and therefore it needs to be collected on the same level to allow for the identification of a descent direction. To this end, line 12 of Algorithm 4 is responsible for the collection of the individual sensitivity components and the computation of the complete expression at each discretized design face of the computational grid. Given this information, the algorithm proceeds at lines 13-15 to update the shape from which the next primal simulation can start.

5.4 Illustrative Example

This section studies the 2D channel flow, initially presented in Section 5.3.2 in the context of the adjoint method, for the application of the robust optimization methods presented in this chapter. The flow configuration is schematically illustrated in Fig. 5.2 (left) and the geometrical characteristics are as described in Section 5.3.2, with the exemption that the inlet boundary is moved closer to the circular objects by $H/2$ so that to allow a bigger influence of the uncertainties on the flow field even in highly diffusive flow scenarios at low Reynolds numbers.

The 2D computational grid is refined near the circular object walls and consists of approximately 31000 CVs. The average dimensionless near-wall spacing around all cylinders is estimated at $y^+ \approx \mathcal{O}(10^{-3})$ for an unpertrubed flow scenario with $\mathrm{Re_D} = \rho\, v^R\, D/\mu = 20$.

As originally discussed in Section 5.3.2, the flow is considered uncertain by means of its inlet velocity profile, which is given by a truncated Karhunen–Lòeve expansion. In all investigated cases, the size of the uncertainty vector is $M = 20$ and a decay rate of $\gamma = 1.5$ is set, which signifies that the first perturbing sinusoidals govern the overall perturbation of the inlet velocity. Furthermore, the complete expansion is multiplied by 0.5 to guarantee that all resulting boundary inlet velocity vectors point inside the domain.

The investigated robust shape optimization methods are:

- Stochastic gradient descent method (SGD),
- Stochastic gradient descent method - binning variant (SGD-B),
- Adjoint-assisted FOSM method (FOSM).

The sample space is $[-1, 1]$ for all uncertain variables. Each variable is associated with a normal distribution with a mean of 0 and standard deviation 0.3, i.e., $\bar{\omega}_i = 0$ and $\sigma_i = 0.3$ $\forall i \in \{1, 2, \ldots, M\}$. The PDF of this distribution is visualized in Fig. 5.1 (left). The SGD and SGD-B employ a sample size $N = 15$. The QoI corresponds to power-loss and FOSM employs the adjoint method to compute the first-order derivative in the direction of the uncertain variables based on Eq. (5.38). The second-order mixed derivative required by the FOSM method is computed based on a second-order accurate FD approximation, cf. Eq. (5.42).

To avoid trivial solutions in the absence of a geometric constraint, as also discussed in Section 3.4, certain sections of the cylinders are considered free for design while the remaining sections are fixed to their initial configuration, as displayed in Fig. 5.4. All investigated methods employ the Steklov-Poincaré method for the identification of a descent direction

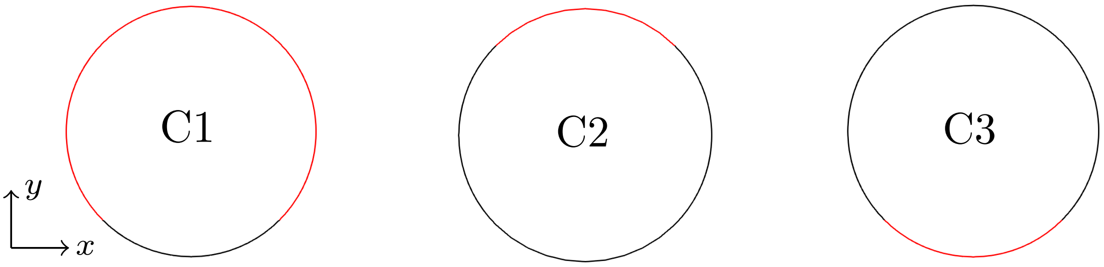

Figure 5.4: Design (in red) and non-design (in black) sections of the three 2D cylinders.

from the sensitivity derivative (see Section 3.2.2). To allow for a smooth transition from design to non-design sections the 2D filter presented in Eq. (3.18) is employed for each cylinder. Based on the results of Section 3.4.1, the filtering radii are chosen as $r_0^1 = 0.3\,D$, $r_0^2 = 0.3\,d$, $r_0^3 = 0.3\,D$ for C1, C2 and C3, respectively.

All optimization cases initially employ a step size t^0 based on the maximum displacement approach described by Eq. (3.15) with $\theta^{\max} = D/100$. The FOSM-based optimizations then employ the Armijo-backtracking rule, described in Section 3.3.1, with $c \approx 0$ and $\tau = 0.5$. The SGD-based optimizations employ the “Robbis-Monro” step size rule given in Eq. (5.15), where l^{RM} is chosen based on experience on the investigated case.

5.4.1 Optimization of Mean

The robust shape optimizations are initially applied for the minimization of the mean value of the QoI, i.e., μ_F, which is realized by setting the weights of the objective functional J to $(w_1, w_2) = (1, 0)$. A convergence criterion of $(J_l - J_{l-1}) \cdot 100\%/J_{l-1} \leq 0.001$ is set for the FOSM case while a maximum number of 50 optimization iterations is set for the SGD-based cases. Furthermore, the latter initiate the “Robbis-Monro” step size reduction method after 40 iterations, i.e. $l^{\mathrm{RM}} = 40$.

Figure 5.5 shows the estimated mean and standard deviation changes w.r.t. the initial shape. The continuous lines denote the changes monitored by each respective method on the fly. For example, the SGD-based methods compute the mean and standard deviation based on Eqs. (5.3) and (5.4), respectively, using their sample size of $N = 15$. The FOSM method uses expressions (5.18) and (5.20) instead. However, these are only approximations of the statistical moments. To this extent, the initial and final shapes produced by each optimization process are assessed based on MC simulations using a sample size of $N^{\mathrm{MC}} = 1000$. For all cases, the samples are randomly picked from the same normal distribution as the one employed for the sampling of the SGD and SGD-B methods. The estimated change of the statistical moments based on the MC simulations are visualized by filled circles for each robust optimization method in Fig. 5.5.

The results indicate that all three methods managed to arrive at a solution minimizing μ_F, which is ultimately the goal of the optimization, by approximately 9%. The comparison between the MC-based estimated decrease and those predicted by each method shows that all of them manage to arrive at a reasonable prediction as regards the mean value. Though it must be noted that the SGD method shows significant fluctuations during the optimization history due to under-sampling. The picture changes however as regards the estimation of σ_F. While the optimization employs $w_2 = 0$ and therefore doesn’t explicitly target the minimization of standard deviation, its approximation by the FOSM and SGD method reveals a significant mismatch w.r.t. the results of the MC simulations. On the other hand, the SGD-B method manages to satisfactorily capture the relative change even with a sample size of $N = 15$. Furthermore, the fluctuations of the estimated σ_F-value using the SGD method become even more prominent in the case of the standard deviation.

As easily noted by the MC-reported results, all optimized shapes suggest a similar relative change of the mean and standard deviation w.r.t. the initial. This is further validated by examining the optimized shapes in Fig. 5.6. All three methods managed to arrive at almost exactly the same result for all three cylinders in the flow.

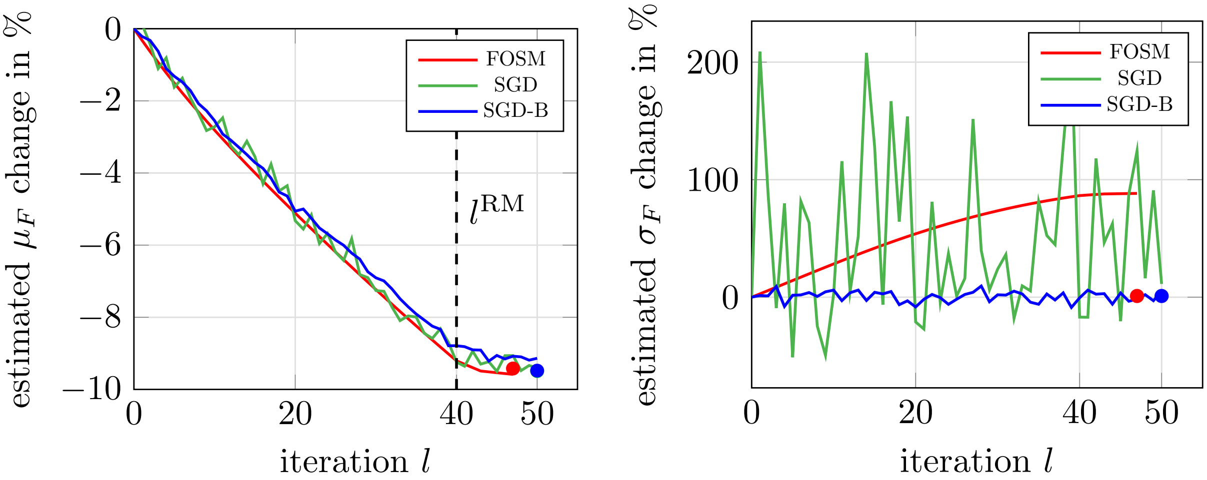

Figure 5.5: Optimization cases for $(w_1, w_2) = (1, 0)$, i.e., optimization of the mean. Left: Estimated change of the mean value of the QoI in continuous line. Right: Estimated change of the standard deviation of the QoI in continuous line. Filled circles denote the estimated decrease from the initial to the final shapes based on MC simulations. Green (SGD) and blue (SGD-B) circles align perfectly on top of each other.

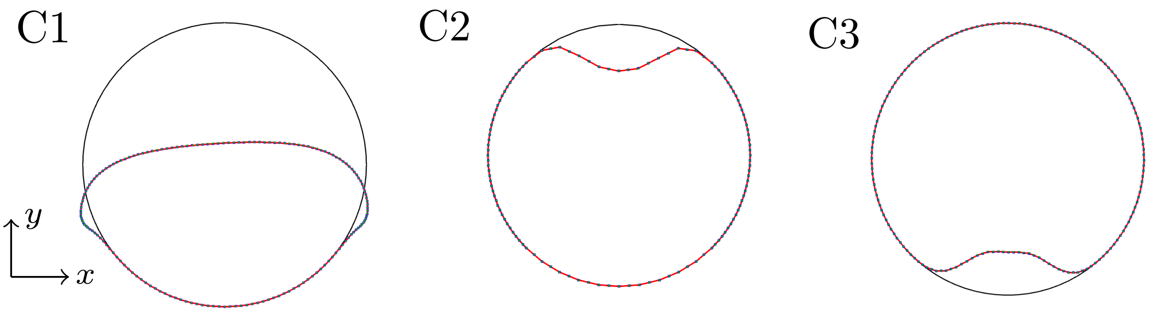

Figure 5.6: Initial cylinder shapes (black lines) and optimized shapes for $(w_1,\ w_2) = (1,\ 0)$ – optimization of the mean – using the FOSM method (red lines), SGD method (green points) and SGD-B method (blue points). Note that the three optimized shapes are almost exactly identical, thus hindering the clarity of the visualization.

5.4.2 Optimization of Standard Deviation

Due to the low (mean) Reynolds number of the flow, the perturbation of the inlet velocity profile is rapidly diffused in the domain. This results to a standard deviation two orders of magnitude smaller than the mean value. Therefore, most combinations of (w_1, w_2) would ultimately result to a dominant descent direction stemming from the mean. To this extent, this section targets exclusively the minimization of σ_F by setting $(w_1, w_2) = (0, 1)$. The same convergence criterion is employed for the FOSM-based optimization while the SGD-based ones employ $l^{\mathrm{RM}} = 25$ and are terminated after 60 iterations.

Figure 5.7 shows the estimated mean and standard deviation changes w.r.t. the initial shape as well as the corresponding MC-predicted results. As shown therein, the FOSM and

SGD-B methods result in an increase of μ_F, which can be expected since it is not explicitly considered in the optimization problem, while SGD reduces the mean by approximately 2.5%. As before all methods adequately predict the estimated change of the mean in comparison to the MC results. As regards σ_F, the FOSM-based method predicts a monotonic decrease of approximately −70% while the SGD and SGD-B show a very similar behaviour to the standard deviation results obtained from optimization of the mean. The MC results reveal that both SGD and FOSM-based methods actually fail to predict the change of σ_F, with the true value of all methods fluctuating around 0%. This mismatch, also noticed in the case of the mean optimization, can be attributed for the FOSM-based method to the non-linear relation between the uncertain variables and the QoI (note that velocity is squared in the formula of the power-loss) and to the low sample size for the SGD method. On the other hand, the SGD-B, with the same sample size as SGD, accurately estimates the change of the standard deviation of the QoI. Overall, none of the methods managed to truly decrease σ_F w.r.t. the initial configuration. Nevertheless, it is interesting to study the shape change trends exhibited by each method.

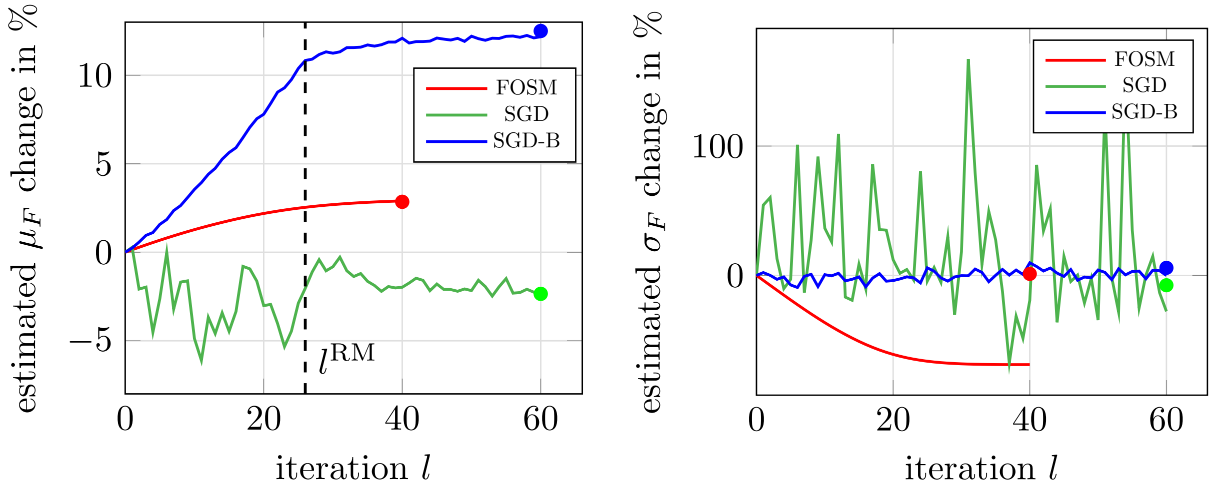

Figure 5.7: Optimization cases for $(w_1, w_2) = (0, 1)$. Left: Estimated change of the mean value of the QoI in continuous line. Right: Estimated change of the standard deviation of the QoI in continuous line. Filled circles denote the estimated decrease from the initial to the final shapes based on MC simulations.

Figure 5.8 shows the shapes resulting from the application of each method w.r.t. the initial. The SGD-B and FOSM-based methods exhibit a similar trend, where all cylinders are deformed in such a way so that they close the channel. While the deformed C1 cylinder is very similar between the two methods, only the SGD-B method reports significant deformations on C2 and C3. On the other hand, the result reported by the application of the SGD method exhibits a similar tendency as the one reported by the optimization of the mean. These observations are further validated by the increase of the mean value for the SGD-B and FOSM methods and the decrease for the SGD method, as shown in Fig. 5.7. At a first glance, the results reported by the SGD-B and FOSM methods might seem unintuitive when one targets the optimization of power-loss. However, in the context of exclusively optimizing for the minimization of the standard deviation, the direction followed by the optimizer might lead to worse results in terms of the QoI as long as all results are equally worse. Therefore, a shape update direction targeting to occlude the flow might lead to higher values of the QoI, insensitive however to the uncertainties of the inlet.

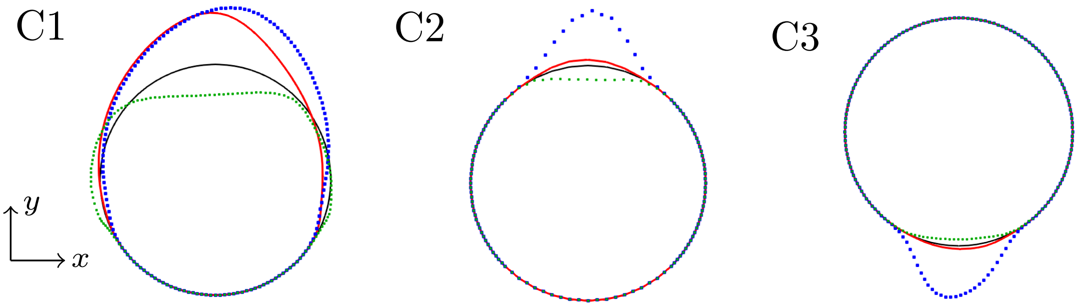

Figure 5.8: Initial cylinder shapes (black lines) and optimized shapes for $(w_1, w_2) = (0, 1)$ using the FOSM method (red lines), SGD method (green points) and SGD-B method (blue points).

5.4.3 Discussion

The investigated 2D example case serves to highlight the characteristics of the three proposed robust shape optimization methods. It is shown that all methods can be successfully coupled to the tools presented in the previous chapters. The changes that need to be made to incorporate robustness in the optimization process almost exclusively relate to the optimizer and require minimal changes in the fluid solver.

In terms of the required computational effort, the FOSM-based method requires the least amount of resources since one shape update calls for the solution of 6 CFD problems, out of which some can be warm-started from a previous solution. On the other hand, the SGD-based methods require $2N$ CFD solutions per shape update. Depending on the size of N, the application of the method can become unfeasible for CFD-based applications. However, every primal or adjoint stage can be trivially parallelized thus highlighting the potential of the methods in the context of high performance computing facilities.

Another issue that must be addressed is the choice of the step size. In all investigated cases in this section, the initial step size is computed based on the maximum displacement approach of Eq. (3.15). Employing this approach, the FOSM-based method always gives the same initial step size, depending only on $\bar{\omega}_i$. For the SGD-based methods the initial step size depends on the initial sample. This can become a crucial issue, especially for the original SGD method when the sample size is too small, since the step size remains constant until the application of the “Robbins-Monro” rule. Therefore, the speed, with which the optimization process is to progress, highly depends on the initial sample. On the other hand, the SGD-B results in a more robust choice of the step size since the complete sample space is scanned.

Furthermore, as shown by the results of this section, the FOSM-based method leads to an estimated monotonic decrease of the objective functional while the other two show fluctuations to their estimations. However, in both examined optimization cases, the SGD-B method stabilized the estimations significantly in conjunction with moderate (feasible) sample sizes in comparison to the SGD method which exhibited significant fluctuations, especially for the standard deviation.

Finally, another important topic is the accuracy of the estimation on the fly. Even though the necessary computational resources required by the SGD-based methods might be significant, they are trivial in comparison to those required for a complete MC simulation. Therefore, an accurate estimation of the relative change of the statistical moments on the fly, without the need of additional MC evaluations, is highly appreciated. To this extent, the FOSM method depends on the underlying nature of the problem. As discussed in Section 5.3, the FOSM approximation becomes accurate when the relation between the QoI and the uncertain variables is linear. In this example, in which by construction the relation is quadratic, the FOSM-based estimation of the relative change of the mean was sufficiently accurate but inaccurate for the standard deviation. Therefore, it is advised that the FOSM-based method is applied for cases in which the designer has an a priori estimate of the relation between the QoI and the uncertain variables. On the other hand, while both SGD and SGD-B methods adequately estimate the change of the mean value, only the latter accurately estimates the change of standard deviation. This constitutes a significant benefit of the proposed variant, since in addition to minimizing the fluctuating behaviour of the SGD method it is also shown herein to deliver accurate predictions on the fly with a relatively small sample size.

6 Biomedical Applications

This chapter applies the previously presented methodologies to two blood-related three-dimensional cases. Specifically, Section 6.1 presents the deterministic shape optimization of a benchmark model for the minimization of hemolysis. This model was designed by a technical committee to include flow phenomena related to blood damage in medical devices, such as hemodialysis sets, catheters, cannulas, and syringes (Steward et al. [2012]). All studies presented in Section 6.1 consider rigid walls due to the conceptual nature of the applications related to the model.

Section 6.2 studies an idealized bypass-graft. Initially, the model is thoroughly investigated by means of an FSI study. Focus is given to the influence of four relevant biomedical aspects on hemodynamic quantities of interest. The biomedical aspects are 1) the size of the anastomosis, 2) the upstream flow paths, 3) rest vs. exercise conditions and 4) relevance of FSI. The section then proceeds with several steady-state robust shape optimization studies of an idealized bypass-graft for the minimization of its hemolysis potential. The optimization studies are conducted under the rigid wall assumption. Uncertainty considerations relate to the hemolysis parameters and the non-Newtonian parameters. Select optimized shapes are then assessed by means of FSI simulations under unsteady conditions.

6.1 Idealized Medical Device

The geometry considered in this section shares characteristics of many blood-carrying medical devices. It includes sections where the flow is accelerating or decelerating, where re-circulation and significant variations in shear stress occur. All of these phenomena are believed to be related to blood damage in medical devices (Steward et al. [2012]). Due to the broad range of blood-related flow phenomena that the model captures, it is referred to as an idealized medical device.

A two-dimensional side view of the model, annotated with necessary geometrical details, is presented in Fig. 6.1. In view of the optimization study to follow, the figure distinguishes the wall segments to those free for design and those fixed to their initial configuration. The fixed inlet and outlet diameter is set to $D = 12\,\mathrm{mm}$. Upon its insertion in the domain, the flow meets a converging nozzle leading to a smaller pipe, referred to as the throat, with a diameter of $D^{\mathrm{T}} = D/3$. The throat ends at a sudden expansion and after a distance of $6.7\,D$ the flow exits the domain.

The geometry is discretized with approximately 750k CVs on a butterfly-like structured grid arrangement. The grid is gradually refined near the walls and in areas of anticipated high velocity gradients, to adequately resolve relevant flow phenomena that can lead to hemolysis. Figure 6.2 shows two cross-sectional views of the employed spatial discretization near the inlet and outlet. As shown, the domain downstream the sudden expansion consists of two highly refined regions. The first one is near the walls of the domain while the second one is at a radius equal to the radius of the throat. The latter serves to sufficiently capture

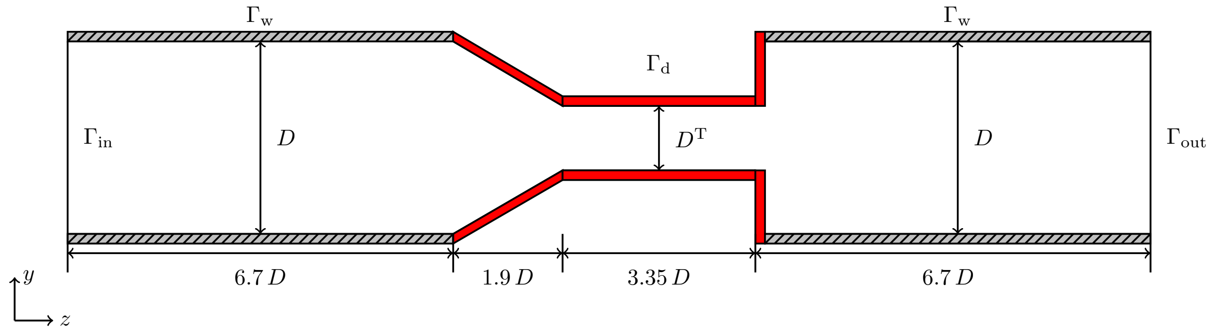

Figure 6.1: Sketch of the idealized medical device. Sections of the wall free for design are illustrated in red.

the free shear flow, occurring by the jet exiting the throat. Figure 6.3 shows a longitudinal view of the spatial discretization. As illustrated there, the mesh is further refined in the z-direction when a non-design wall (Γ_w) meets a design wall (Γ_d). This is done to ensure an accurate computation of the sensitivity.

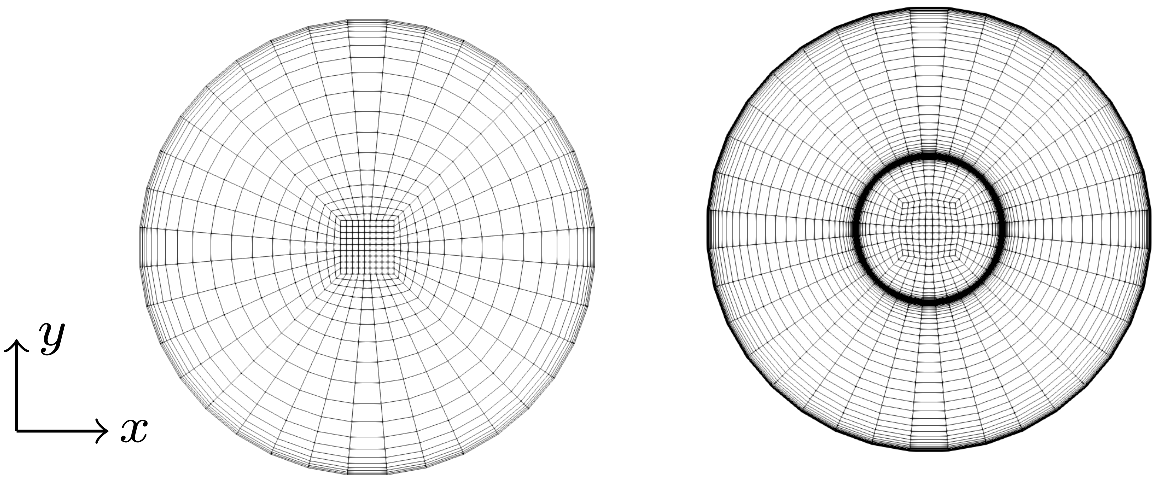

Figure 6.2: Cross-sectional views of the employed spatial discretization for the idealized medical device. Left: Mesh near the inlet. Right: Mesh near the outlet.

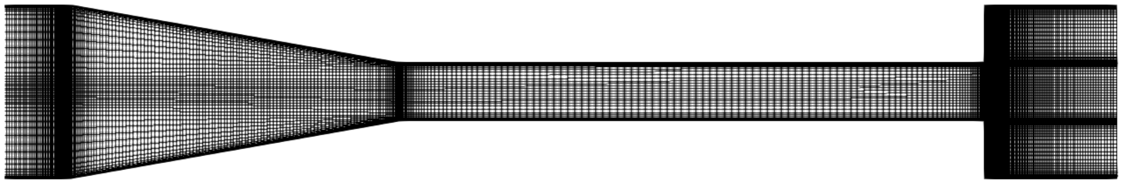

Figure 6.3: Detail of the computational grid on a longitudinal section of the geometry near the design sections.

In all studies that follow, a fully developed laminar axial velocity profile is prescribed at the inlet, viz.

$$v_z = 2v^{\mathrm{R}} \left(1 - \left(\frac{r}{R} \right)^2 \right), \tag{6.1}$$

where $R = D/2$ and v^{R} is set so that a desired Reynolds number is achieved. The fluid's density is set to $\rho = 1056\,\mathrm{kg/m^3}$ while the dynamic viscosity is set to $\mu = 3.5$ mPa·s to represent blood under physiological conditions. All investigated cases assume steady-state conditions. As regards the hemolysis model, the utilized set of parameters corresponds to GW, as denoted in Table 2.1. Furthermore, the computation of the scalar representative of shear stress employs $k = 1$, cf. Eq. (2.60). The primal equations employ the QUICK scheme for the discretization of their convective terms while the corresponding dual equations employ a downwind analogy to QUICK (Stück and Rung [2013]).

6.1.1 Primal Flow Validation

The primal flow prediction of the employed CFD model is validated against experimental data. The experimental data are extracted from a multilaboratory study conducted as part of an FDA-sponsored project for the evaluation of CFD in assessing blood flow parameters related to medical device safety (Hariharan et al. [2011]). Measurements of mean velocity and turbulent flow quantities were performed over a range of throat Reynolds number based on a particle image velocimetry (PIV) analysis. Details about the experimental studies can be found in the original paper of Hariharan et al. [2011]. The experiments were performed at three independent laboratories, one of which reported results of three trials thus amounting to a total of five experimental data sets (available at https://fdacfd.nci.nih.gov). This thesis studies exclusively laminar conditions and therefore a validating computational study is conducted for a throat Reynolds number of 500. As reported in Steward et al. [2012] and Hariharan et al. [2011], blood is considered as Newtonian in these conditions and therefore the CFD simulations conducted herein employ a fixed $\mu = 3.5\,\mathrm{mPa \cdot s}$. The reported experimental data sets are averaged, from which an average volume flux of $Q = 5.21 \cdot 10^{-6}\,\mathrm{m^3/s}$ is estimated. A fully developed parabolic profile with $v^{\mathrm{R}} = 0.046\,\mathrm{m/s}$ is thus prescribed at the inlet of the computational domain amounting to a Reynolds number at the throat of $\mathrm{Re}^{\mathrm{T}} = \rho v^{\mathrm{T}} D^{\mathrm{T}}/\mu = 500$, with v^{T} denoting the mean estimated velocity at the throat. Based on the prescribed velocity and employed discretization, an average dimensionless near-wall spacing from the walls is estimated at $y^+ \approx \mathcal{O}(10^{-2})$.

In the computational model, the coordinate origin is located at the center of the inlet boundary. Figure 6.4 presents the computed axial velocity component at the centerline of the model $(x, y = 0)$ against the experimental results. Figure 6.5 shows the computational and experimental axial velocity profile at two distinct longitudinal positions (left: $z = 11.25\,D$, right: $z = 11.83\,D$) in the vicinity of the sudden expansion. Both figures show a very good agreement of the computed velocity fields w.r.t. the averaged experimental results.

In view of the one-way coupling of the employed hemolysis models with the flow equations and due to the exclusive dependence of the former to shear stress, i.e., velocity gradients, the satisfying velocity agreements implicitly serve to verify the computationally estimated hemolysis. Naturally, the hemolysis estimation is as good as the underlying model employed for its prediction. However, as discussed in previous chapters, the employed model has been shown to adequately perform in terms of relative predictions and

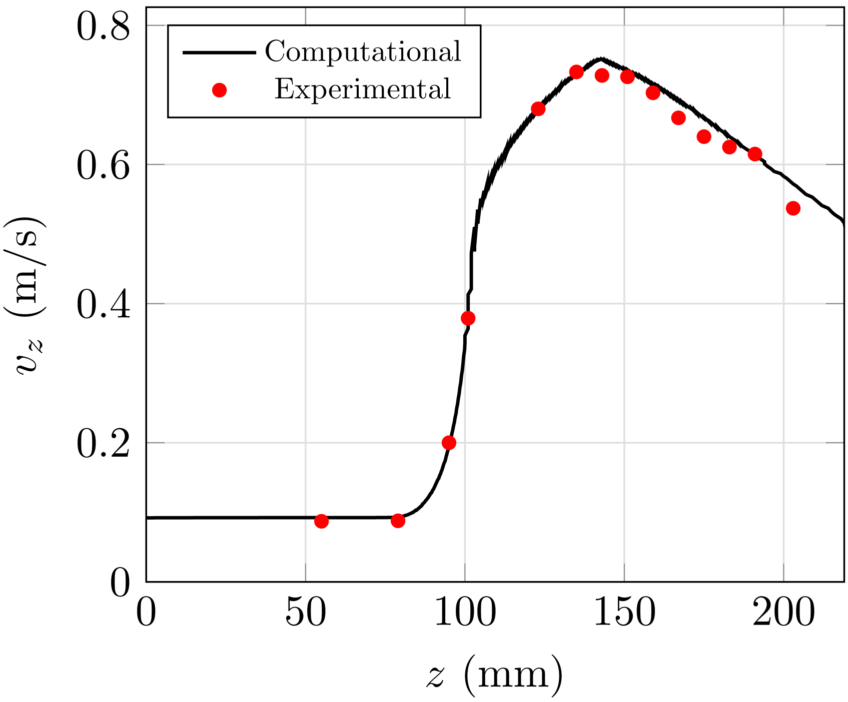

Figure 6.4: Comparison of axial centerline velocities $(x, y = 0)$ obtained from computations conducted in this thesis (black solid line) and the averaged experimental data (red points). The latter are extracted from Hariharan et al. [2011].

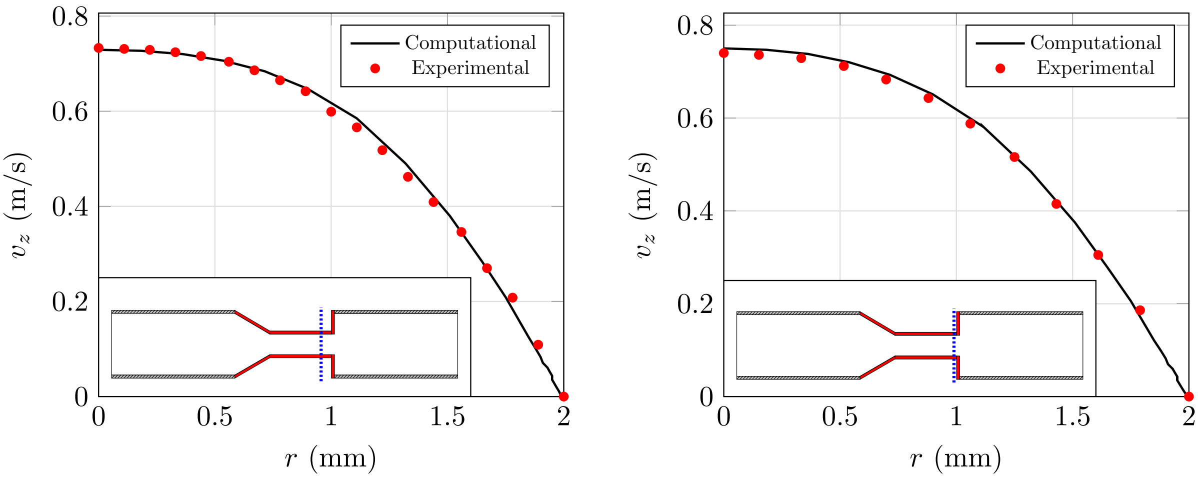

Figure 6.5: Comparison of axial velocity profiles at (left) $z = 11.25\,D$ and (right) $z = 11.83\,D$ obtained from computations conducted in this thesis (black solid line) and the averaged experimental data (red points). The latter are extracted from Hariharan et al. [2011]. Sketches at bottom left serve to approximately indicate the longitudinal position of the two profiles.

can thus provide insightful information in the context of an optimization procedure.

6.1.2 Shape Optimization Study

The idealized medical device is optimized for the minimization of its hemolysis potential for $\mathrm{Re}^{\mathrm{T}} = 500$. The objective functional is the numerator of HI, see Eq. (2.69), and the adjoint system employed for the efficient computation of the sensitivity is the one presented in Section 4.3. The descent direction is computed based on the Steklov-Poincaré method described in Section 3.2.2. The step size is updated in each optimization iteration based on Eq. (3.16) with $\theta^{\max} = D/240$. In contrast to previously presented optimization studies where the step size was kept constant, an iterative step size rule is employed here to accelerate the computationally more expensive three dimensional shape optimization. To avoid optimization instabilities due to the ever-growing step sizes, the Armijo-backtracking rule with $c \approx 0$ and $\tau = 0.5$ is additionally employed. A criterion of $(J_i - J_{i-1}) \cdot 100\% / J_{i-1} \leq 0.001$ is set to monitor convergence. Furthermore, as shown in Fig. 6.6 the shape sensitivity and corresponding displacement field is accumulated on the inlet of the throat and thus a filter aiming to smoothen the transition from Γ_{d} to $\Gamma_{\mathrm{w}} \setminus \Gamma_{\mathrm{d}}$, as described in Section 3.3.2, is not necessary.

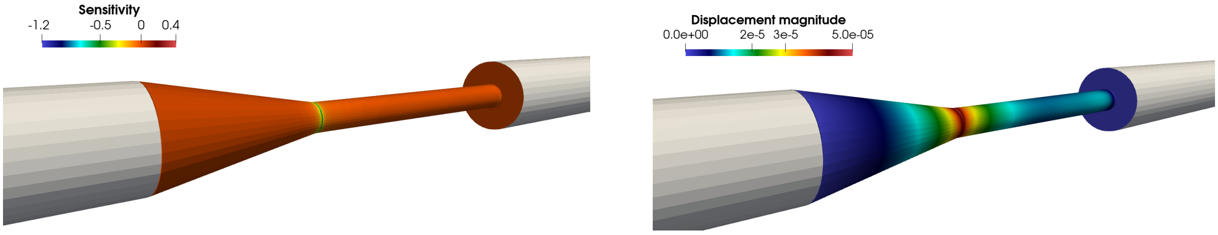

Figure 6.6: Idealized medical device. Left: Shape sensitivity of the initial shape. Right: Displacement magnitude (in m) imposed on the initial shape based on the Steklov-Poincaré method.

The optimization process resulted in 15 shape updates, as shown in Fig. 6.7 (left), after which the convergence criterion was met. The Armijo condition was activated at iteration 7 and 9, thus reducing the step size and arriving at a smooth convergence of the objective functional. The optimized solution reduces HI by approximately 19%. The optimizer, as suggested also by Fig. 6.6, proceeded at widening and smoothing the transition from the nozzle to throat. Specifically, the cross-sectional area of the throat inlet is increased by approximately 32% in the optimized case.

The change on the transition area from nozzle to throat results in a decrease of the scalar stress field, as shown in Fig. 6.8. The reduction in stress levels in turn leads to the reduction of hemolysis.

In addition to the initial and optimized shapes produced by employing the GW hemolysis parameters, the initial and optimized shape are assessed for the other two set of parameters presented in Table 2.1, namely HO and ZT. The reported HI reduction with the use of HO is approximately 14% and 16% for ZT. It is evident therefore, that the most significant improvement is achieved from the employed set of parameters (GW) during the optimization, while however the optimal shape always outperforms the initial one in terms of flow-induced hemolysis.

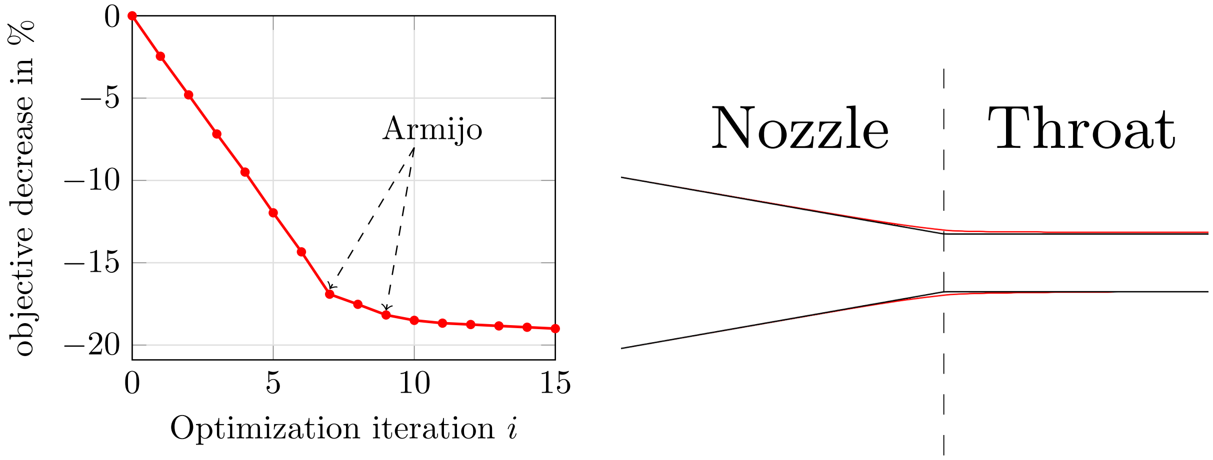

Figure 6.7: Idealized medical device. Left: Optimization convergence history. The two points highlighted by arrows denote the optimization iterations in which Armijo condition was activated. Right: Outlines of the optimized (in red) and initial (in black) shapes in the vicinity of the most pronounced deformation.

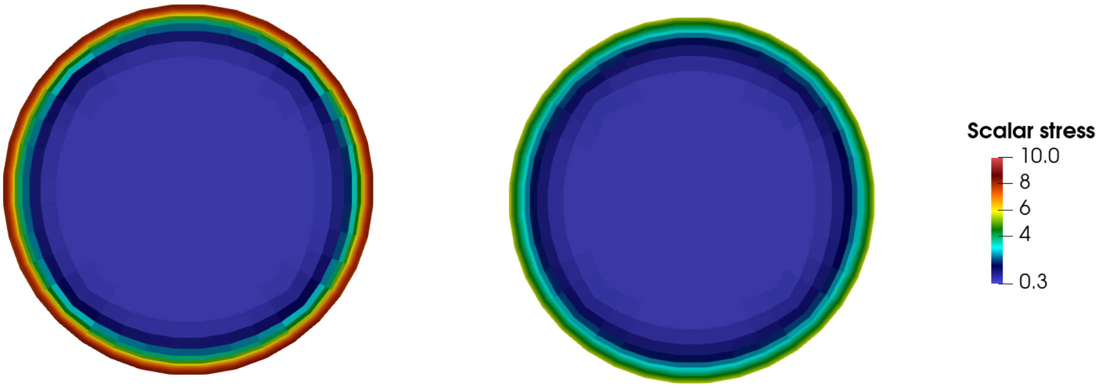

Figure 6.8: Idealized medical device. Scalar stress contours obtained from Eq. (2.60) in the cross-section of the throat inlet for the (left) initial and (right) optimized shapes.

6.2 Idealized Bypass-Graft

Cardiovascular diseases (CVDs) are the predominant cause of death worldwide, amounting to an estimated 17.9 million deaths in 2019, which corresponded to 32% of all global deaths (World Health Organization (WHO) [2023]). The most frequent CVD is considered to be *atherosclerosis*. It can lead to artery failure due to the build-up of plaque inside the arteries. An extensive plaque formation can lead to completely occluded vessels or narrowed regions (stenoses), where blood flow is restricted. Depending on the severity and location of the stenotic vessel, treatment is preferably done conservatively using medications or for more severe cases using minimal invasive techniques such as stent placement (Lanzino et al. [2009]). For the most acute cases, however, in which the functionality of distal organs is at risk, an open surgery may be advised in order to implant an *arterial bypass-graft*. An arterial bypass-graft is a segment of a healthy (biological or artificial) blood vessel that is used to divert blood around narrowed or occluded parts of an impaired artery. The connection (*anastomosis*) between the artery and the graft is prone to the development of a secondary disease called *intimal hyperplasia*. It manifests itself by an abnormal growth of the innermost layer of the arterial wall (the *intima*) and may cause a renewed occlusion (*restenosis*) of the vessel in the anastomosis region (Ghista and Kabinejadian [2013], Chiu and Chien [2011]). The risk of such a condition has been shown to strongly depend on the resulting flow conditions (*hemodynamics*) in the anastomosis region (Chatzizisis et al. [2007], Haruguchi and Teraoka [2003]). In specific, a strong correlation between wall shear stresses (WSS) and the development of intimal hyperplasia has been found (Malek et al. [1999]). The correlation is not only restricted to the magnitude of the WSS but exists also for the extent to which the WSS change their direction over the cardiac cycle. The latter is quantified by the so-called *oscillatory shear index* (OSI) (Ku et al. [1985]). While studies of the hemodynamics in arterial bypass-graft anastomoses usually focus on wall shear stress related quantities, the unnatural flow patterns in the anastomosis region may also lead to high shear stresses inside the lumen, which may damage the blood itself. While hemolysis has been extensively studied in the context of external cardiovascular devices (Yu et al. [2017], Thamsen et al. [2015], Taskin et al. [2012]), it is usually not considered in studies of implants. Nevertheless, there have been some studies on arterial bypass-grafts implicitly studying hemolysis by metrics related to shear stress, see e.g., Abraham et al. [2005a,b].

Furthermore, research has been conducted to propose remedies against unnatural hemodynamics and the resulting problem of restenosis. Studies such as those in van der Slegt et al. [2014] have turned their focus on the impact of the shape of the anastomosis while others investigate the influence of the flow path upstream the implanted graft (Wen et al. [2011]). Concurrently, focus has also been given to the effect of the graft material (Roll et al. [2008]). It has been shown that artificial graft materials are more prone to the development of a restenosis in comparison to biological tissues, which are used whenever possible (Suggs et al. [1988], Kissin et al. [2000]).

Due to the complex nature of the problem, numerical models that can predict and optimize the aforementioned factors in silico are of great interest. To this end, CFD simulations have been employed to investigate the formation of stenosis (Zhang et al. [2012]), optimal graft paths (Kyung et al. [2011]) and anastomosis shapes (Loth et al. [2008]). However, the rigid wall assumption of a classical CFD simulation has frequently proven to be inadequate, see e.g., Hsu et al. [2014], Torii et al. [2007], Bazilevs et al. [2010].

To resolve this shortcoming, extensive focus has recently been given to FSI simulations that consider the fluid flow and the displacement of the vessel wall in a coupled manner, see e.g., the recent publication (Girfoglio et al. [2021]).

The remainder of this section is structured in three main subsections. Subsection 6.2.1 employs three-dimensional FSI simulations of idealized bypass-grafts. Therein, focus is given to the influence of relevant biomedical aspects to WSS, OSI and hemolysis. Based on the results of the FSI investigations, Subsection 6.2.2 proceeds to apply several steady-state CFD-based robust shape optimization studies for the minimization of hemolysis. Finally, Subsection 6.2.3 proceeds to assess the most prominent optimized solutions under the more physiological unsteady conditions.

6.2.1 FSI Simulations before Optimization

Geometry modeling and meshing

The flow phenomena transpiring in a bypass-graft can significantly alter from patient to patient as well as from location to location in the body where the bypass is implanted. However, the goal of this thesis is not to present patient-specific optimal solutions but rather to study general trends of the problem and how an optimization of such a general configuration can prove beneficial to the underlying hemodynamics. To this end, the geometrical model employed for the studies at hand relate to idealized bypass-grafts that can be created in a reproducible manner. The meshing process begins with an initial coarse quadrilateral grid. The position of the nodes and their connectivity completely defines the geometry of the lumen surface. The coarse surface mesh is subsequently refined using a Catmull-Clark subdivision scheme (Catmull and Clark [1978]). This iterative process, schematically presented in Fig. 6.9, results in a smooth, fine surface mesh.

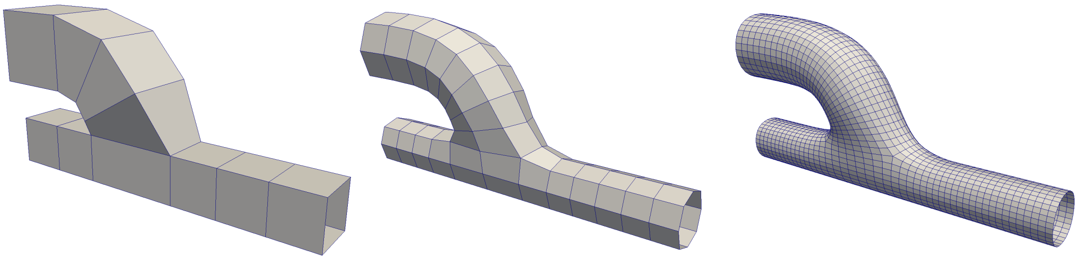

Figure 6.9: Schematic representation of the Catmull-Clark subdivision process for the production of a smooth, fine surface mesh.

An automated extrusion based on the prescribed thickness, which can spatially vary, is used to define the outer boundary of the elastic wall geometry of the surrounding arterial tissue. Based on the inner and outer boundary of the wall, the computational mesh for the structure subproblem is created. For high-order finite elements with curved surfaces, the converged surface mesh is used to define the element geometry, while the topology is taken from a previous coarser mesh in the Catmull-Clark iterative process. This approach results in the finite element discretization of the arterial wall.

The fluid mesh, that is used to discretize the lumen of the bypass section, is constructed in a block-structured hexahedral manner. The initial coarse mesh is extruded inwards by a suitable distance (approximately one quarter of the local diameter). A core of coarse hexahedrals is formed by connecting the extruded inner faces. Finally, all hexahedrals are refined such that the number of cells matches the number of surface faces in the fine surface mesh. Further details on the meshing procedure can be found in Radtke [2020].

Simulation setup

Upon creation of the computational mesh, a suitable set of BCs, able to capture as much as possible the physiological conditions of the problem, is defined. Note that the employed setup considers only the distal segment of the idealized bypass-graft, in which most hemodynamic-related problems occur. The boundary of the fluid domain is split into four sections, as shown in Fig. 6.10. These are, the inlet boundary (Γ_{in}), the outlet (Γ_{out}), the upstream proximal end (Γ_{up}) and the wall (Γ_t^{w}). At the inlet, the velocity is prescribed based on a volume flux $Q^{\text{in}}(t)$ and the assumption of a velocity profile. All studies conducted in this thesis consider a complete occlusion of the impaired artery and Γ_{up} is thus modeled as a rigid wall (Γ_{w}). The wall boundary Γ_t^{w} reduces to a simple rigid wall (Γ_{w}) for CFD simulations while it corresponds to the FSI interface (Γ_t^{FSI}) for FSI simulations. The outlet of the domain corresponds to a pressure boundary. While the absolute value of pressure is irrelevant in CFD simulations due to the assumption of blood incompressibility, it becomes significant in FSI simulations since it ultimately drives the deformation of the elastic wall. In this context, it is also worth noting that while the flow through the inlet neutralizes the flow through the outlet for a CFD simulation, this does not necessarily hold for an FSI simulation. In fact, the difference between the two corresponds to the instantaneous volume change of the fluid domain, see SCL in Eq. (2.112).

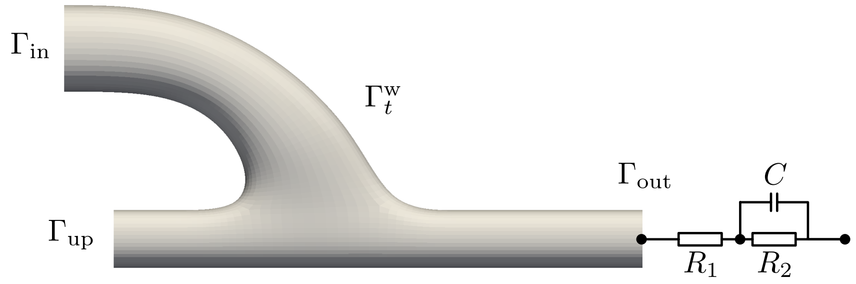

Figure 6.10: Fluid domain boundary definition.

In cardiovascular applications, the computation of the pressure at the outlet of the fluid domain is a delicate issue and is usually performed using a reduced model of the downstream vessel networks. The FSI simulations presented in this section employ a three-element Windkessel model (Bazilevs et al. [2010], Torii et al. [2001]). The model relates the flow at the outlet $Q^{\text{out}}(t)$ and the pressure $p^{\text{out}}(t)$ to be prescribed at the outlet boundary in an analogy to an electric circuit as illustrated in Fig. 6.10. This yields the ODE

$$\left(1+\frac{R_2}{R_1}\right)Q^{\text{out}}+CR_2\dot{Q}^{\text{out}}=\frac{p^{\text{out}}}{R_1}+C\dot{p}^{\text{out}}. \tag{6.2}$$

The volume flux $Q^{\text{out}}(t)$ is computed based on the velocity values of the previous fluid iteration while the parameters R_1, R_2 and C are identified such that a physiological pressure pulse is obtained.

The studies are initially conducted for three anastomoses of different cuff sizes as shown in Fig. 6.11. This distinction is made so that to preliminary investigate the impact of the shape on the hemodynamics of interest. The inner diameters of the bypass-graft and the artery are set to $D^{\text{graft}} = 14\,\text{mm}$ and $D^{\text{artery}} = 9\,\text{mm}$, respectively. The size of the impaired artery is chosen so that it approximately matches a common iliac or femoral artery (Wazzan et al. [2022], Sandgren et al. [1999]). The lengths from Γ_{in} to Γ_{out} are $L_{\text{s}} \approx 9.5\,D^{\text{artery}}$, $L_{\text{m}} \approx 10\,D^{\text{artery}}$ and $L_{\text{l}} \approx 10.5\,D^{\text{artery}}$ for the anastomosis with small, medium and large cuff, respectively. The characteristic lengths of the cuff are $l_{\text{s}} \approx 1.64\,D^{\text{graft}}$, $l_{\text{m}} \approx 2\,D^{\text{graft}}$ and $l_{\text{l}} \approx 2.35\,D^{\text{graft}}$.

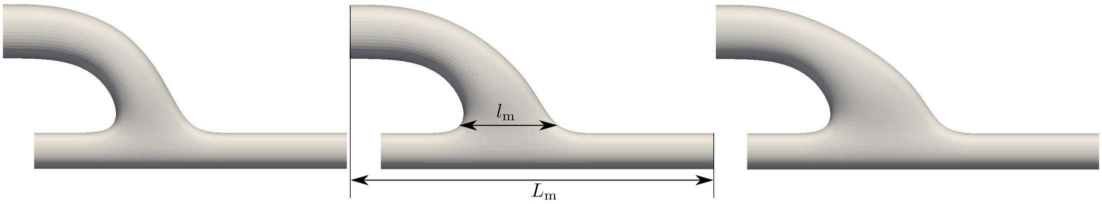

Figure 6.11: Anastomosis models with different cuff sizes. From left to right: small, medium, large.

Interest is also given to the upstream flow paths, as shown in Fig. 6.12. This is done to implicitly investigate the robustness of the estimated metrics w.r.t. potential uncertainties of the inlet. The colored sections of Fig. 6.12 are not actually included into the FSI simulations. Instead, preliminary CFD simulations are performed, in which the colored sections are exclusively considered. A parabolic Poiseuille velocity profile stemming from a desired volume flux is prescribed at the inlet of each domain. The corresponding velocity profiles at the outlet of the colored segments are then used as an inlet BC for the bypass-graft. Figure 6.13 illustrates the difference of the resulting velocity profiles for two snapshots in time.

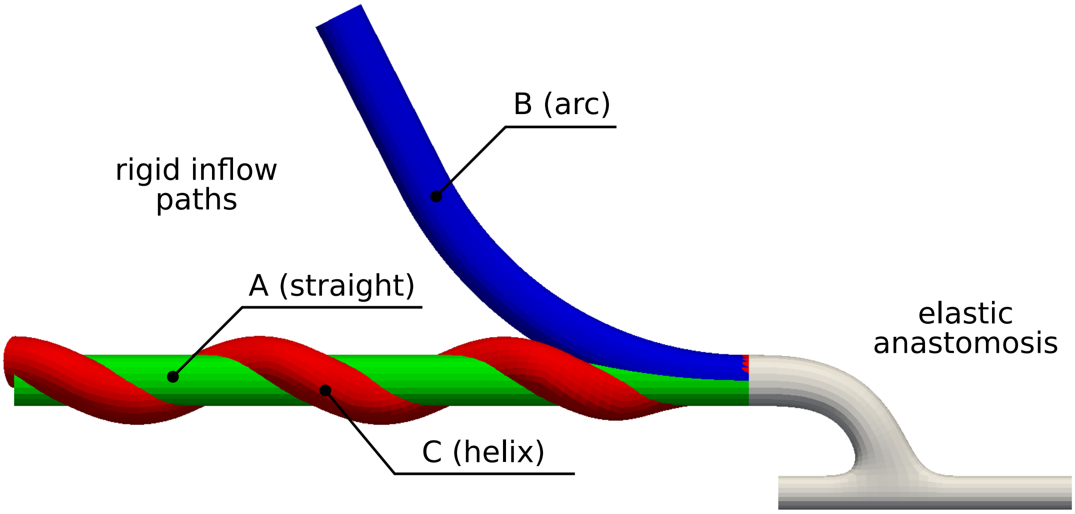

Figure 6.12: Inflow paths *straight*, *arc* and *helix* used to determine the velocity profiles at the inlet boundary of the bypass-graft.

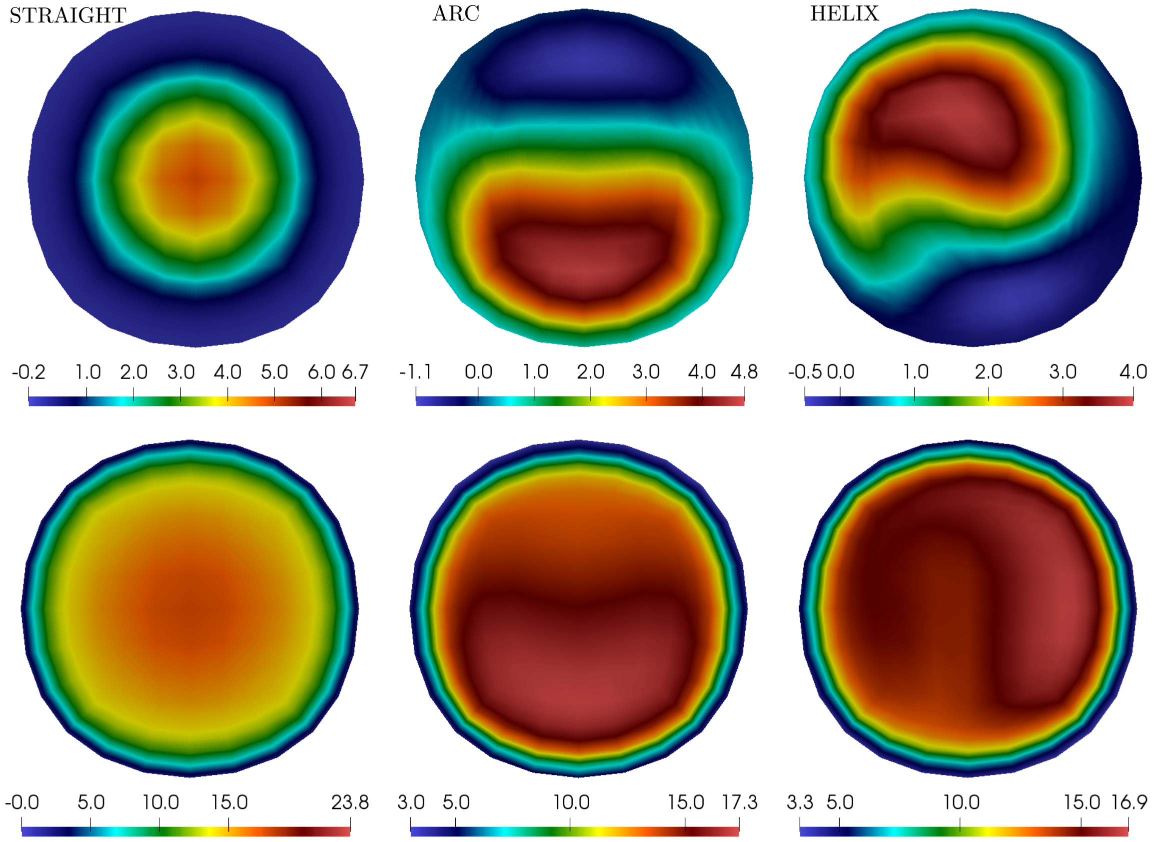

Figure 6.13: Velocity component in main flow direction (cm/s) obtained as a result of the rigid wall simulations performed for the paths *straight*, *arc*, and *helix* (left to right) in rest conditions. Top: Result for $t = 0\,\text{s}{+}n\,T$, where T is the duration of a simulated heartbeat. Bottom: Result for time instant of maximum velocity $t = 1.77\,\text{s}{+}n\,T$.

A third aspect that is investigated to study its influence on the underlying problem is the condition of the patient. Specifically, a scenario in which the patient is resting and one in which the patient is exercising are simulated. The distinction between the two is made based on the prescribed flow pulse, as shown in Fig. 6.14. The flow pulse, for both conditions, is extracted from Wilson et al. [2005] and scaled such that physiological flow velocities are obtained for the vessel sizes considered in this thesis. The rest conditions correspond to a heartbeat of $T = 0.8\,\text{s}$ while the exercise conditions are simulated by a decrease in the cardiac cycle duration to $T^{\text{e}} = 0.55\,\text{s}$. In specific, the exercise waveform was generated by shortening the diastolic portion of the rest waveform and scaling the mean volumetric flow rate, see Wilson et al. [2005]. A critical Reynolds number is estimated based on

$$\text{Re} = \frac{\rho^{\text{f}}\, v^{\text{p}}\, D^{\text{graft}}}{\mu^{\text{f}}} \quad \text{with} \quad v^{\text{p}} = \frac{4\, Q^{\text{in,p}}}{\pi (D^{\text{graft}})^2}, \tag{6.3}$$

where $Q^{\text{in,p}}$ refers to the peak volume flux during a cardiac cycle. For the rest and exercise flow conditions, the Reynolds number is 455 and 728, respectively. While it can be argued that the latter indicates initiation of weakly turbulent effects, these are not taken into account in the simulations conducted herein. As discussed in Loth et al. [2008], arterial

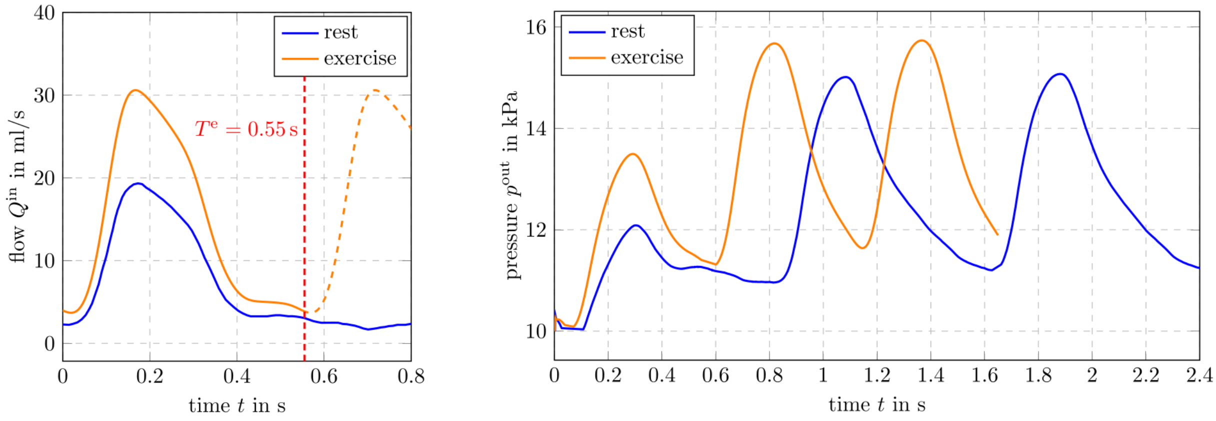

Figure 6.14: Left: Prescribed flow for rest and exercise conditions. Dashed orange line denotes part of the prescribed flow on the second simulated exercise period. Vertical dashed red line is used to illustrate the shorter exercise cardiac cycle duration. Right: Resulting outlet pressure for *straight* inflow path and medium cuff size.

bypass-grafts with an end-to-side distal anastomosis, as the ones studied in this thesis, result in typically laminar flows with turbulence being most prominent in arteriovenous grafts.

Finally, the fourth aspect that is studied is the influence of elastic walls in the simulation setup. This study serves as an initial estimate of the importance of FSI in the context of shape optimization. As outlined in Chapter 2, FSI simulations significantly increase the cost of the primal problem solution due to a) their inherent unsteady nature and b) due to the necessary coupling between the fluid and structure problems. To this extent and bearing in mind the increased number of required simulations per shape update in the context of robust shape optimization, it is deemed beneficial to preliminary examine whether FSI can be neglected for the optimization studies to follow. This study is realized by performing accompanying unsteady CFD simulations to a select few FSI ones.

Quantities of interest

The main focus of this thesis is on hemolysis. However, in the context of the application at hand, it is considered necessary to monitor additional hemodynamic quantities of interest. Specifically, quantities related to the development of intimal hyperplasia are computed. These are based on the WSS,

$$\tau_i^{\text{w}} = \tau_{ij} n_j, \tag{6.4}$$

where τ_{ij} is the shear stress fluid tensor and n_j is the normal to the surface vector. In particular, small values are regarded as critical since they promote the abnormal growth of the vessel wall. Therefore, a metric of interest relates to the spatial minimum of the temporal maximum wall shear stress L2-norm, viz.

$$\tau_{\text{min}}^{\text{w}} = \min_{x_j \in \Gamma_t^{\text{o}}} \max_{t \in T_{\text{o}}} \|\tau_i^{\text{w}}\|_2. \tag{6.5}$$

Therein, $\Gamma_t^{\mathrm{o}} \subset \Gamma_t^{\mathrm{w}}$ denotes part of the vessel wall selected as an observation region and T_{o} denotes the time interval of the observation, which corresponds to the last simulated cardiac cycle. In addition, the spatial maximum WSS,

$$\tau_{\max}^{\mathrm{w}} = \max_{x_j \in \Gamma_t^{\mathrm{o}}} \max_{t \in T_{\mathrm{o}}} \|\tau_i^{\mathrm{w}}\|_2, \tag{6.6}$$

is investigated. Extensively large values of $\tau_{\max}^{\mathrm{w}}$ are regarded as critical since they may lead to detachments or ruptures of atherosclerotic plaques and emboli that can cause occlusions of smaller downstream vessels. The existence of mechanisms that render low and high values of WSS critical has led to the hypothesis of a safe bandwidth. More details on this topic can be found in Ghista and Kabinejadian [2013].

Another metric related to the development of intimal hyperplasia is the so-called oscillatory shear index, cf. Kabinejadian and Ghista [2012], defined as

$$\mathrm{OSI} = \frac{1}{2}\left(1 - \frac{\| \int_{T_{\mathrm{o}}} \tau_i^{\mathrm{w}} \, \mathrm{d}t \|_2}{\int_{T_{\mathrm{o}}} \|\tau_i^{\mathrm{w}}\|_2 \, \mathrm{d}t}\right). \tag{6.7}$$

This quantity measures changes in the WSS direction and takes values between 0 and 0.5, with the larger values being considered as critical. The quantity represents a spatial scalar field defined over the walls of the model. In order to characterize the complete domain based on an index related to the OSI, the mean OSI over the observation region is further evaluated as

$$\text{mean OSI} = \frac{1}{A^{\mathrm{o}}} \int_{\Gamma^{\mathrm{o}}} \mathrm{OSI} \, \mathrm{d}\Gamma^{\mathrm{o}}, \tag{6.8}$$

where A^{o} denotes the area of the observation section. The observation section, in which the mean OSI and the WSS metrics are evaluated, is shown in Fig. 6.15.

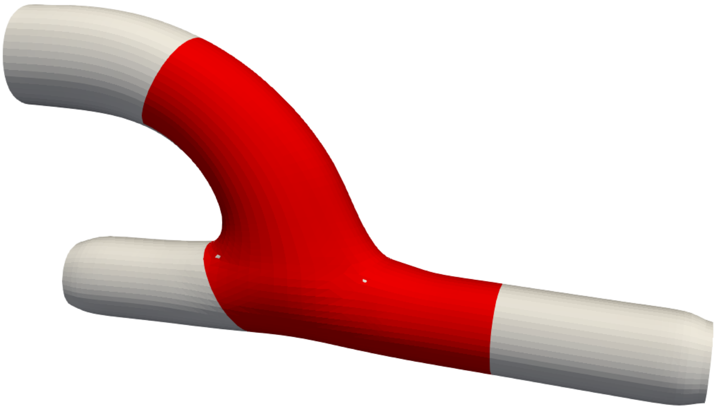

Figure 6.15: Observation region (red) in which mean OSI and WSS metrics are evaluated.

As regards the quantification of hemolysis in the context of an unsteady simulation, the hemolysis index of Eq. (2.69) is computed in each time iteration and then the complete simulation is assessed based on a time-averaged metric that reads

$$\mathrm{TAHI} = \frac{1}{T_{\mathrm{o}}} \int_{T_{\mathrm{o}}} \mathrm{HI} \, \mathrm{d}T_{\mathrm{o}}. \tag{6.9}$$

Finally, it is worth mentioning that the wall shear stress gradient is yet another quantity of interest in similar applications as it has been correlated with the risk of plaque rupture (Thondapu et al. [2020]) and intimal hyperplasia (Lei et al. [1997]). However, this metric is not monitored in this work.

Fluid and structure properties

In the pre-optimization studies, blood is assumed to be a Newtonian fluid with a constant molecular viscosity of $\mu^{\mathrm{f}} = 4\,\mathrm{mPa}\cdot\mathrm{s}$ and a density of $\rho^{\mathrm{f}} = 10^3\,\mathrm{kg/m^3}$. The simplifying assumption of a Newtonian fluid is employed at this part of the work, to enable direct comparison of the primal FSI simulations with similar setups reported in literature as the ones of Radtke [2020]. Hemolysis is estimated based on the GW set of parameters (cf., Table 2.1) and $k = 1$ for the computation of the scalar shear stress representative.

For the arterial wall, the constitutive model corresponds to the nearly incompressible Fung material as proposed in Radtke [2020]. The SEDF reads

$$
\begin{aligned}
W &= \frac{c^{\mathrm{F}}}{2}\left(e^{\overline{Q}} - 1\right) + W^{\mathrm{vol}}, \qquad \text{with} \\
\overline{Q} &= \frac{1}{c^{\mathrm{F}}}\left(\lambda^{\mathrm{F}}\,\mathrm{tr}\left(\overline{E}_{ij}\right)^2 + 2\,\mu^{\mathrm{F}}\,\mathrm{tr}\left(\overline{E}_{ij}^2\right)\right).
\end{aligned}
\tag{6.10}
$$

Therein, $\overline{E}_{ij} = \frac{1}{2}(\overline{F}_{ki}\overline{F}_{kj} - \delta_{ij})$ stands for the isochoric Green-Lagrange strain tensor, which is based on the isochoric deformation gradient $\overline{F}_{ij} = J^{-\frac{1}{3}}F_{ij}$. The volumetric term in the SEDF is chosen as $W^{\mathrm{vol}} = \frac{\kappa}{50}(J^5 + J^{-5} - 2)$. The material parameters c^{F}, λ^{F} and μ^{F} are identified by fitting the results to a reference solution. These are $c^{\mathrm{F}} = 4.37 \cdot 10^3\,\mathrm{Pa}$, $\lambda^{\mathrm{F}} = 9.98 \cdot 10^4\,\mathrm{Pa}$ and $\mu^{\mathrm{F}} = 3.15 \cdot 10^4\,\mathrm{Pa}$. Furthermore, the compression-modulus in the volumetric term is set to $\kappa = 10^6\,\mathrm{Pa}$ and the density of the arterial wall to $\rho^{\mathrm{s,artery}} = 10^3\,\mathrm{kg/m^3}$.

The constitutive model for the bypass-graft is a compressible Neo-Hooke model, see e.g., Bonet and Wood [2008], and reads

$$
W = \frac{\mu^{\mathrm{s}}}{2}\left(\mathrm{tr}(C_{ij}) - 3\right) - \mu^{\mathrm{s}}\ln(J) + \frac{\lambda^{\mathrm{s}}}{2}\left(\ln(J)\right)^2, \tag{6.11}
$$

where $C_{ij} = F_{ki}F_{kj}$ denotes the right Cauchy-Green deformation tensor. The material parameters $\lambda^{\mathrm{s}} = 1.64 \cdot 10^8\,\mathrm{Pa}$ and $\mu^{\mathrm{s}} = 3.36 \cdot 10^6\,\mathrm{Pa}$ are determined such that the compliance of the graft approximately matches that obtained from measurements in Körner [2007]. The density of the graft is set to $\rho^{\mathrm{s,graft}} = 10^3\,\mathrm{kg/m^3}$.

Numerical discretization

The structure domain is discretized using 172 hexahedral finite elements of high order employing an anisotropic ansatz space. To this end, shape functions with a polynomial order of $p = 4$ are used in the in-plane direction while $p = 2$ is used in the thickness direction. The geometry of the elements is described using the blending function method based on the same polynomial orders such that a subparametric element formulation is obtained. For details on this discretization the reader is referred to Düster et al. [2001].

A grid convergence study is performed for pure CFD simulations to arrive at the fluid domain discretization. To assess the discretization, the mean OSI of the unperturbed medium cuffed anastomosis with the inflow path *straight* is monitored. Since all quantities of interest relate, implicitly or explicitly, to shear stresses, it is assumed that a similar trend as the one monitored for mean OSI w.r.t. the discretization should appear for all quantities of interest. The employed fluid discretization consists of approximately 93k CVs since a further refinement results in changes of OSI less than 1%. The temporal terms of the fluid subproblem is discretized based on the first-order (in time) backward Euler method. The convective terms of the momentum and hemolysis equations are discretized by the TVD scheme based upon a QUICK method. The total simulation time corresponds to 3 cardiac cycles. The same time step is employed for the fluid and structure subproblem and is set to $\Delta t = 0.001\,\mathrm{s}$. Based on the prescribed settings, an average of approximately 4 FSI coupling iterations is monitored. No time iteration exceeds 12 FSI coupling iterations.

Table 6.1: Results of grid convergence study for the fluid mesh. The third column denotes the percentage change from the previous refinement level.

number of CVs	mean OSI	mean OSI change (%)
11664	0.1188	-
93312	0.1148	-3.36
314928	0.1137	-0.96

Results

In order to provide an overview of the simulation, Fig. 6.16 shows several time snapshots of the flow field obtained for a medium cuff anastomosis design. A vortex forms and collapses during the cardiac cycle, leading to the anticipation of high OSI values in the anastomosis bed, i.e., bottom part of the artery at the vicinity of the connection with the graft. This feature of the pulsating flow strongly depends on the geometry and therefore on the anastomosis design. Furthermore, Fig. 6.17 shows the maximum displacement observed for different anastomosis designs. As expected, the displacement increases with increasing cuff size. Interestingly, the differences between rest and exercise conditions are very small, in terms of the magnitude of the resulting waveforms. This can be explained by the inertial effects (of the structure and the fluid), which dampen this difference. The stiffening at large displacements inherent to the Fung material model is yet another possible reason for this.

Figure 6.19 shows the monitored hemodynamics quantities of interest for the 18 FSI simulations. The results are discussed for each quantity of interest separately and the main overall findings in terms of the optimization studies to follow are summarized below.

Oscillatory shear index (OSI). A first observation that can be made from the simulated results is that exercise conditions reduce the overall mean OSI. From a fluid dynamics point of view, larger flow rates stabilize the flow and are less prone to oscillatory velocities and from a medical point of view, physical exercise is beneficial in the prevention of CVDs. Furthermore, the results conform with the observations in Wen et al. [2011] which show that an inflow path *helix* can reduce OSI. However, it is also noted that the frequently employed assumption of a *straight* inflow path results in a lower mean OSI than the *arc* one in rest conditions. Interestingly enough, this behaviour seems to be reversed in exercise

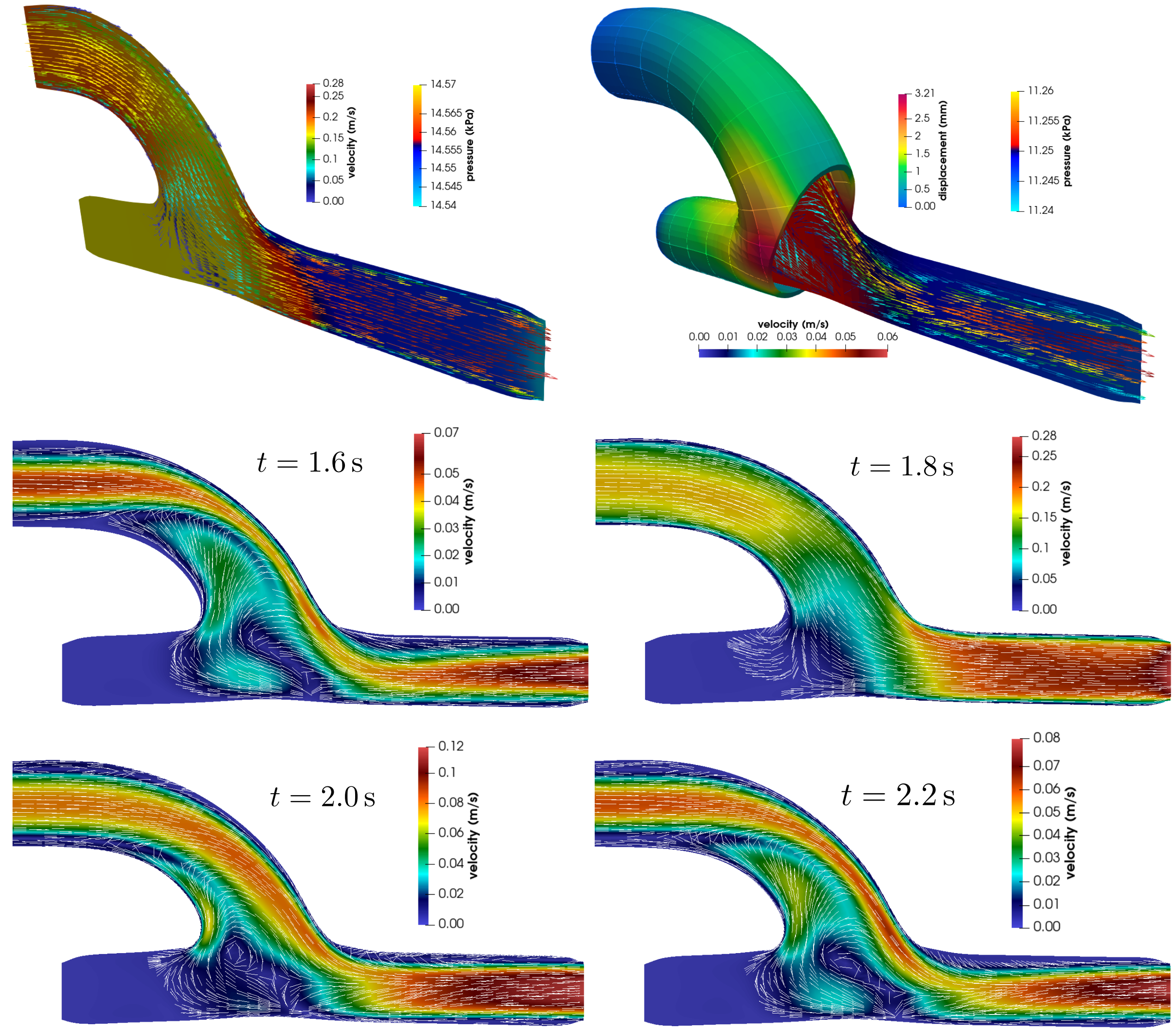

Figure 6.16: Overview of the results for the anastomosis with medium cuff size and inflow path *straight* at rest conditions. Top: Displacement magnitude (only right), velocity magnitude and pressure at peak systole ($t = 1.8\,\mathrm{s}$) (left) and diastole ($t = 2.4\,\mathrm{s}$) (right). Bottom: Velocity magnitude at different time instances during the cardiac cycle.

conditions for the larger cuffed anastomosis. Overall, the influence of the inflow path on OSI can be associated with the vortex that is developed and the overall area that this recirculatory flow occupies. This observation additionally suggests that potential uncertainties on the inlet might indeed influence the biomedical quantities of interest. However, mathematically describing these uncertainties in a general framework is oftentimes difficult due to the inherent stochastic nature of the heart and the correlation to the patient. As regards the influence of the shape on OSI, it is observed that the larger the employed cuff is, the larger the predicted mean OSI. Figure 6.18 shows the OSI distribution for the same inflow configuration and different cuff sizes. As shown, the location of the critical OSI regions is the same among all cuff sizes. A ring of high OSI values is observed in the center region of the anastomosis. With increasing cuff size, the critical OSI ring thickens. This

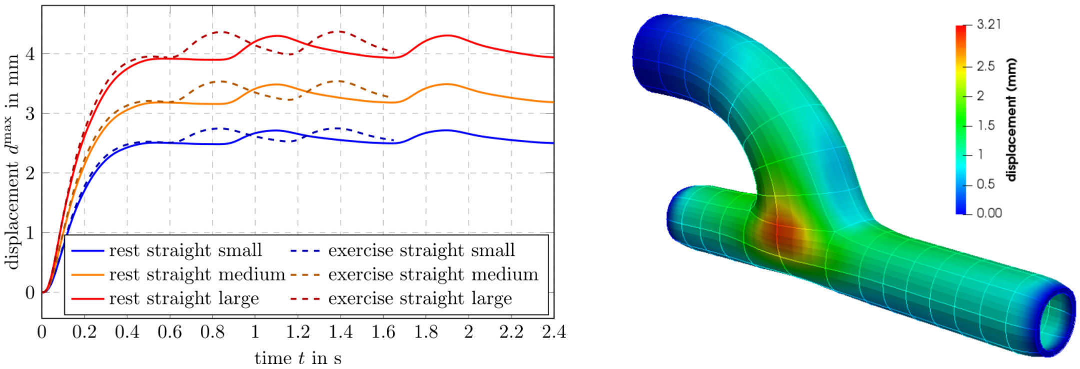

Figure 6.17: Left: Maximum displacement over time for inflow path *straight*. Right: Displacement magnitude field at $t = 2.4\,\mathrm{s}$ for the anastomosis with a medium size cuff.

does not only affect the connection between the prosthetic graft and the impaired artery but also the bed of the anastomosis, which is shown to attain more critical values as the size increases. On the other hand, the OSI field decreases in the downstream region as the cuff size increases. However, this section of the geometry is not fully monitored by the observation region (cf., Fig. 6.15) and thus this beneficial attribute is not entirely reflected in the computed mean OSI.

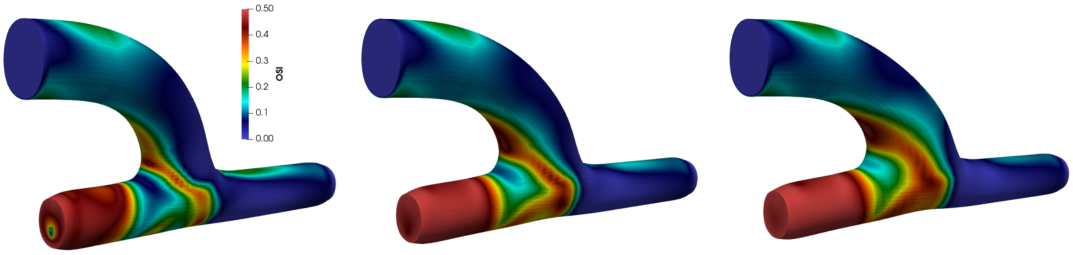

Figure 6.18: OSI field for the inflow path *helix* and rest conditions. From left to right: small, medium, large cuff size.

Wall shear stresses (WSS). As regards $\tau^{\mathrm{w}}_{\max}$, it is observed that a change from rest to exercise conditions can even double the predicted value. This is expected, as the flow through the graft increases so are the stresses on the walls. As regards $\tau^{\mathrm{w}}_{\min}$, it is shown that exercise can, in large, play a beneficial role as it increases the monitored value. Furthermore, it is interesting to note that some trends change between rest and exercise conditions. For instance, while the small cuffed anastomosis shows an upside down U-shaped pattern of $\tau^{\mathrm{w}}_{\min}$ in rest conditions, a decreasing trend is reported for the exercise conditions. The overall effect of inflow paths on the WSS is rather trivial for rest conditions based on the reported results. Significant changes are only reported in terms of $\tau^{\mathrm{w}}_{\min}$ in exercise conditions, in which the inflow path *arc* yields significantly more medically beneficial predictions in comparison to the others for a medium and a large cuffed anastomosis. The size of the cuff is also shown to be of low significance in terms of $\tau^{\mathrm{w}}_{\max}$ for rest conditions. However, the effect of the size can become more important in exercise conditions. It is also shown that in terms of $\tau^{\mathrm{w}}_{\mathrm{min}}$, the smaller the employed cuff the more favorable the result.

Time-averaged hemolysis index (TAHI). First of all, it must be noted that the reported levels of hemolysis in the considered configurations are approximately two orders of magnitude smaller than the ones reported for extravascular machinery using similar hemolysis modeling techniques, e.g., application considered in Section 6.1. Nevertheless, since hemolysis induction is closely related to shear stresses, which might drastically change when the physiological conditions of the investigated geometry change, focus should still be devoted to this matter. Similar to the discussions related to hemolysis throughout this thesis, the results presented herein are analyzed in a qualitative manner. Initially, it is observed that the trends are almost completely reversed w.r.t. the ones reported for OSI. Exercise conditions can approximately triple the levels of hemolysis induction as compared to rest conditions. Furthermore, it is shown that the inflow path *arc* produces more hemolysis in rest conditions. However, the influence of the inflow path is yet again less significant as compared to the effect of the cuff size. Contrary to the OSI observations, an increasing cuff size results in decreasing hemolysis induction. This can be associated with lower overall fluid stresses as a consequence of the increased volume in the cuff region. These results indicate that a detailed optimization of the shape of the graft could actually drastically change the hemolysis induction potential and should thus be further investigated.

Rigid wall assumption (CFD). To provide a reference on the impact of FSI on the monitored quantities of interest, 6 accompanying pure CFD simulations are realized. In order to perform a fair comparison, the CFD simulations are realized in a deformed fluid domain corresponding to an intermediate pressure of the last simulated cardiac cycle, i.e., $t = 2.04\,\mathrm{s}$ for the rest conditions and $t = 1.5\,\mathrm{s}$ for the exercise conditions. The CFD simulations are only realized for the medium cuff anastomosis since the main focus here is the effect of the rigid wall. The corresponding fluid domain for the CFD simulations at rest conditions is shown at Fig. 6.20. A comparison between the CFD results and the FSI ones is presented in Fig. 6.21. It is shown that, in large, the assumption of rigid walls leads to an overprediction of all quantities. This conforms with the initial expectations since stresses produced by the fluid flow are partially converted into structural displacement in the FSI framework. However, the overprediction is most prominent for the WSS metrics and becomes less important for mean OSI and TAHI.

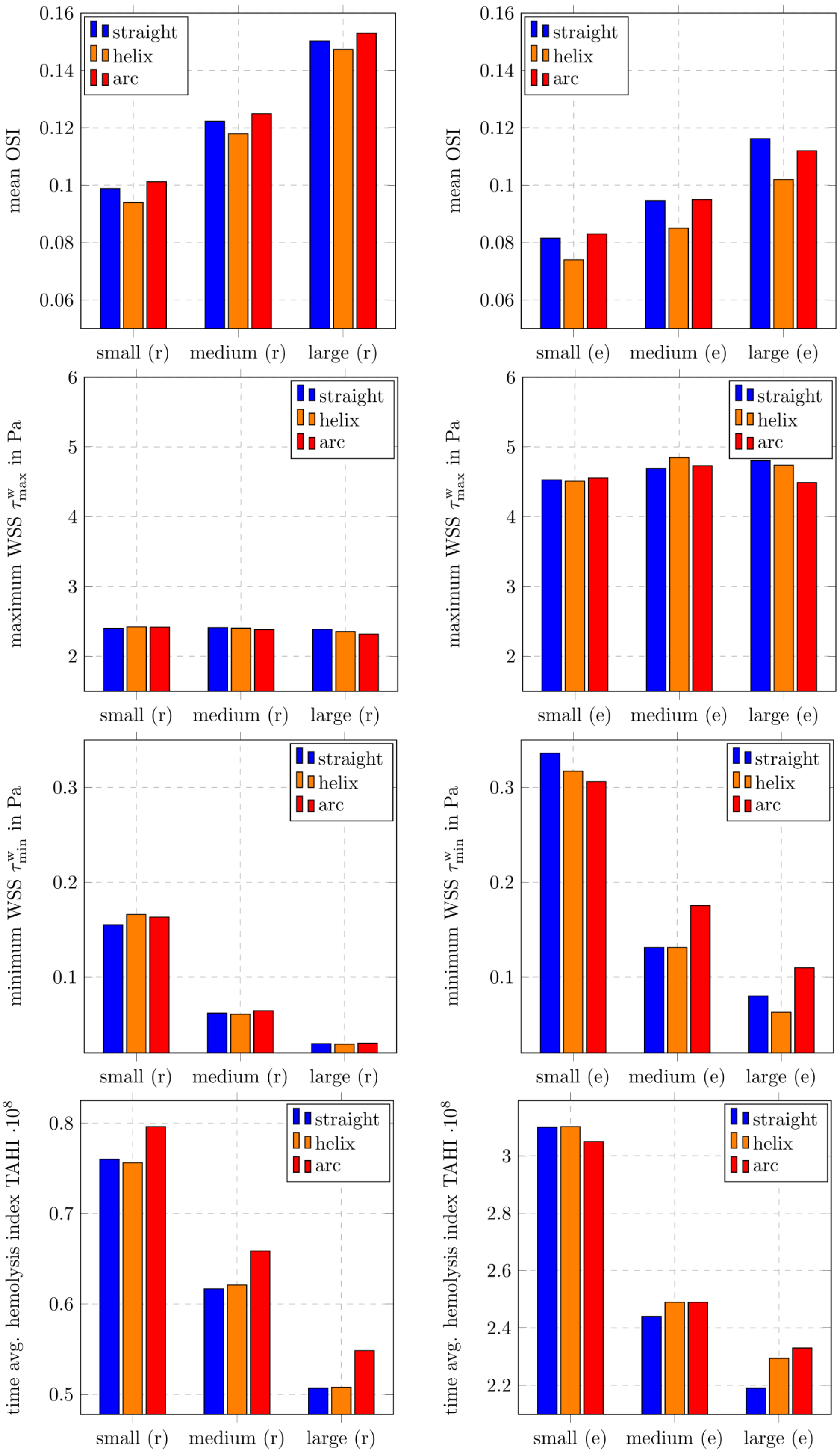

Figure 6.19: Hemodynamic quantities for rest (left) and exercise (right) obtained for the different anastomosis models (small, medium, large) with different inflow paths (*straight*, *helix*, *arc*).

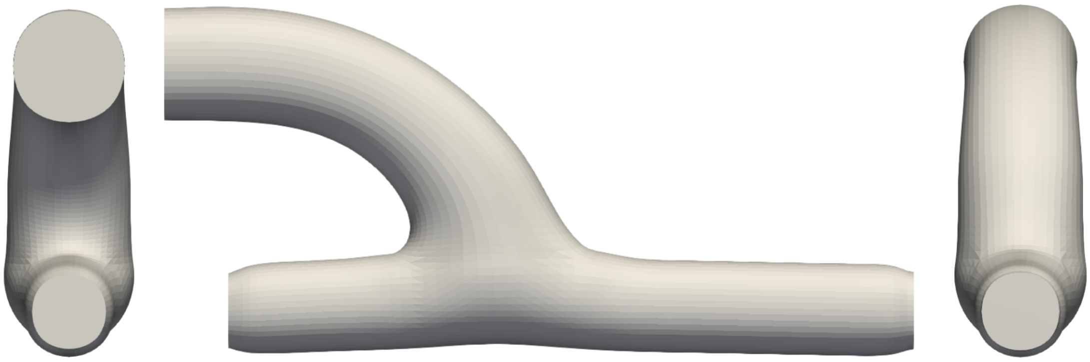

Figure 6.20: Pre-pressurized geometry of the fluid domain used for the CFD simulations at rest conditions with a rigid wall assumption.

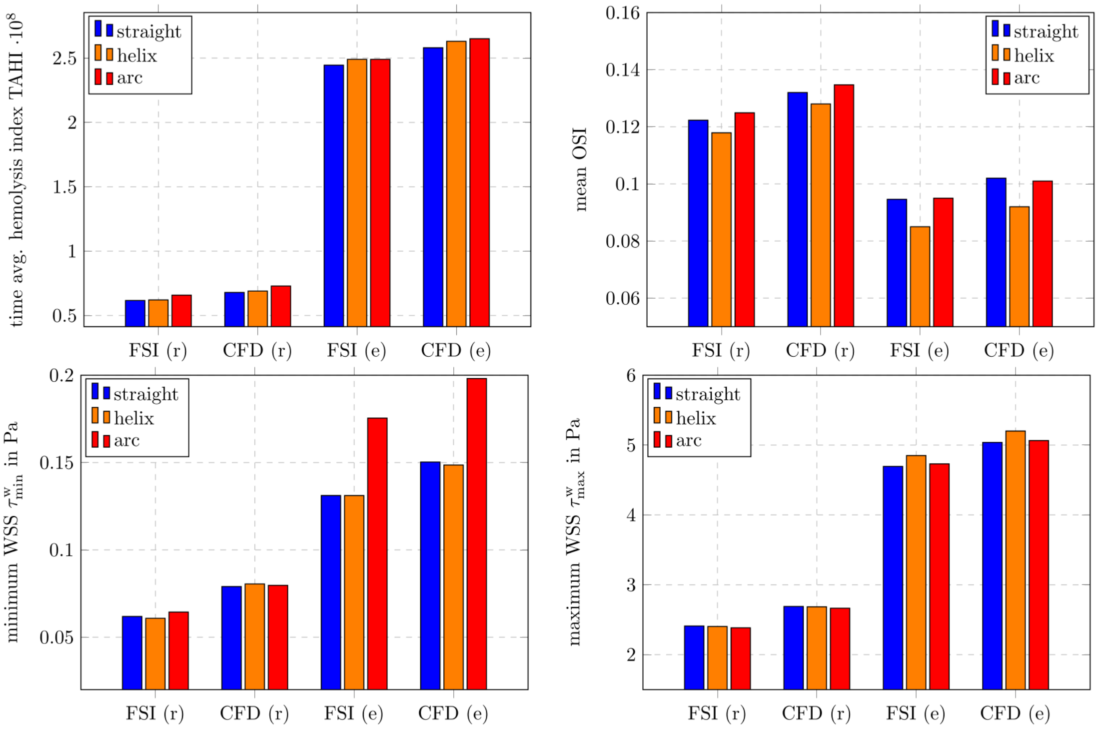

Figure 6.21: Comparison of the results obtained for the anastomosis with medium cuff size with FSI and CFD simulations for rest (r) and exercise (e) conditions.

Discussion

The considered flow scenarios capture a clinically relevant situation and the results serve well in contributing to the understanding of different aspects that influence the underlying hemodynamics, despite the fictive, idealized geometries considered. The results are evaluated in a qualitative manner to allow a preliminary classification of the importance of the investigated aspects. They suggest that, in large, the most important aspects relate to the conditions (rest or exercise) of the patient as well as the shape of the anastomosis. The inflow paths are found to be significant only for the estimation of OSI and $\tau^{\mathrm{w}}_{\mathrm{min}}$.

In particular, it is shown that a simple change of the cuff from small to large can lead to approximately 32% reduction of TAHI for almost all configurations in rest conditions. The inflow paths result in a maximum difference of the TAHI estimation of approximately 8% from *straight* to *arc* in the large cuffed anastomosis in rest conditions. The change becomes most significant from rest to exercise conditions with an increase of approximately 300%. Finally, the TAHI is overpredicted in CFD evaluations by less than 10% in all investigated configurations. In view of these findings and by considering that one cannot directly act on the physical activity of the patient, a mathematical shape optimization procedure for the minimization of hemolysis is well-justified. Furthermore, the rigid wall assumption is found to be adequate for the optimizations to follow, taking into account the extensive increase of computational resources that would otherwise be required to perform the optimization under FSI conditions.

6.2.2 Robust Shape Optimization Studies

Based on the findings of Subsection 6.2.1, the optimization problem is significantly reduced to allow a computationally feasible robust shape optimization process. To this extent, the studies presented herein employ an initial unperturbed, idealized bypass-graft, simulated under steady-state conditions and using the rigid wall assumption. The initial geometry refers to the medium cuff anastomosis. The optimization targets the minimization of the statistical moments of the (steady-state) hemolysis index HI, computed based on Eq. (2.70). As discussed in Chapter 4, the denominator of HI is kept fixed for an incompressible fluid under steady-state conditions and therefore the QoI is defined as the numerator of HI.

Primal simulation setup

The primal simulation setup is as described in Subsection 6.2.1 and Fig. 6.10, with $\Gamma^{\mathrm{w}}_{t} := \Gamma_{\mathrm{d}}$ corresponding to a rigid design wall. Due to the incompressible nature of blood and in the absence of FSI considerations, a zero pressure is set at Γ_{out}. At the inlet, a parabolic Poiseuille velocity profile is set based on the peak volume flux of the rest conditions waveform, as shown in Fig. 6.22. The prescribed flux is $Q^{\mathrm{in}} \approx 18\,\mathrm{ml/s}$ and amounts to a Reynolds number of $\mathrm{Re} = 455$ based on the Newtonian properties of Subsection 6.2.1 and D^{graft}. The flow is thus simulated under laminar conditions.

The optimization studies consider non-Newtonian blood properties. Specifically, the Carreau model is employed with the parameters presented in Table 2.4. Hemolysis is modeled similarly to the FSI studies, by employing the GW set of parameters (cf., Table 2.1) and $k = 1$ for the computation of the scalar shear stress quantity. The optimization process is considered uncertain by means of the hemolysis or non-Newtonian parameters.

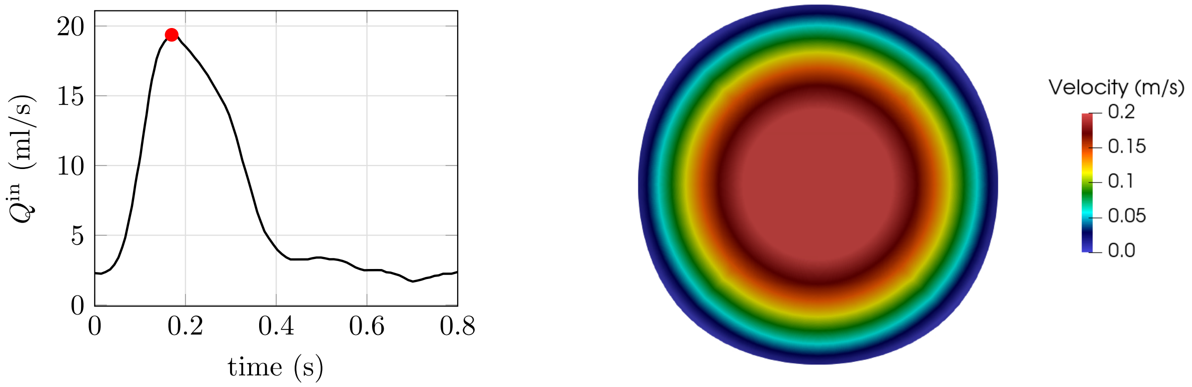

Figure 6.22: Left: Volume flux for rest conditions marked by a red point at the time instant in which the steady-state optimization studies are performed. Right: Velocity profile at the inlet based on the prescribed volume flux.

The employed computational grid corresponds to one level of refinement higher than the one employed for the FSI studies and consists of approximately 315k CVs, see Table 6.1. The average dimensionless near-wall spacing from the walls is estimated at $y^+ \approx \mathcal{O}(10^{-2})$. Even though the increase of the number of discrete CVs increases the computational requirements of the optimization studies, it guarantees a higher accuracy on the estimation of the shape sensitivities. The convective terms of the momentum and hemolysis equations are discretized using the QUICK scheme.

Optimization setup

The optimization studies consider the hemolysis or non-Newtonian parameters to be uncertain. In this context and in view of the computational requirements of each of the robust shape optimization methods, presented in Chapter 5, the FOSM method is employed for UQ as it corresponds to the lowest computational requirements. For the application of the FOSM method, each uncertain variable should be associated with a mean value and a standard deviation. A decision upon an underlying PDF is not required for the optimization, it is however necessary for a validating MC study. To this end, a normal distribution is assumed for all uncertain quantities.

Uncertain hemolysis parameters. In this case, the non-Newtonian parameters are fixed to the Carreau parameters (Table 2.4). The vector of uncertain parameters is then defined as

$$\omega_i = (C, \alpha, \beta), \tag{6.12}$$

resulting in $M = 3$ total uncertain variables. The mean value and standard deviation vectors are prescribed as

$$\bar{\omega}_i = (C_{\mathrm{GW}}, \alpha_{\mathrm{GW}}, \beta_{\mathrm{GW}}) \quad \text{and} \quad \sigma_i = (0.3C_{\mathrm{GW}}, 0.2\alpha_{\mathrm{GW}}, 0.09\beta_{\mathrm{GW}}), \tag{6.13}$$

where $(C_{\mathrm{GW}}, \alpha_{\mathrm{GW}}, \beta_{\mathrm{GW}})$ stands for the GW parameter set (Table 2.1). The choice of $\bar{\omega}_i$ is made based on the frequency that this set of parameters is used in literature, see e.g., Yu et al. [2017], Thamsen et al. [2015]. The standard deviations are chosen so that other set of parameters proposed in literature, e.g., HO or ZT, can be represented within a range of one to two standard deviations. Additionally, the probable space $[-3\sigma,\, 3\sigma]$ (99.73 % percentage of accuracy for a normal distribution) should not include unphysical solutions such as $\beta > 1$ (see Section 2.2).

Uncertain non-Newtonian parameters. In this case, the hemolysis parameters are set to GW. The vector of uncertain variables is then defined as

$$\omega_i = (\lambda, n, \mu_0, \mu_\infty), \tag{6.14}$$

resulting in $M = 4$ total uncertain variables. The mean value and standard deviation vectors are prescribed as

$$\bar{\omega}_i = (\lambda_\mathrm{C}, n_\mathrm{C}, \mu_{0,\mathrm{C}}, \mu_{\infty,\mathrm{C}}) \quad \text{and} \quad \sigma_i = (0.15\lambda_\mathrm{C}, 0.2n_\mathrm{C}, 0.25\mu_{0,\mathrm{C}}, 0.02\mu_{\infty,\mathrm{C}}), \tag{6.15}$$

where $(\lambda_\mathrm{C}, n_\mathrm{C}, \mu_{0,\mathrm{C}}, \mu_{\infty,\mathrm{C}})$ stands for the Carreau parameter set (Table 2.4). Based on the employed mean and standard deviation vectors and by assuming underlying normal distributions for each uncertain variable, Fig. 6.23 shows the probable (within 95.4% of each uncertain variable probability) space in which viscosity might take values from. As shown by Fig. 6.23, the choice of $\bar{\omega}_i$ and σ_i doesn't allow for unphysical solutions, e.g., negative viscosities, and sustains necessary characteristics of a blood non-Newtonian model, such as converging to a constant viscosity at high shear rates.

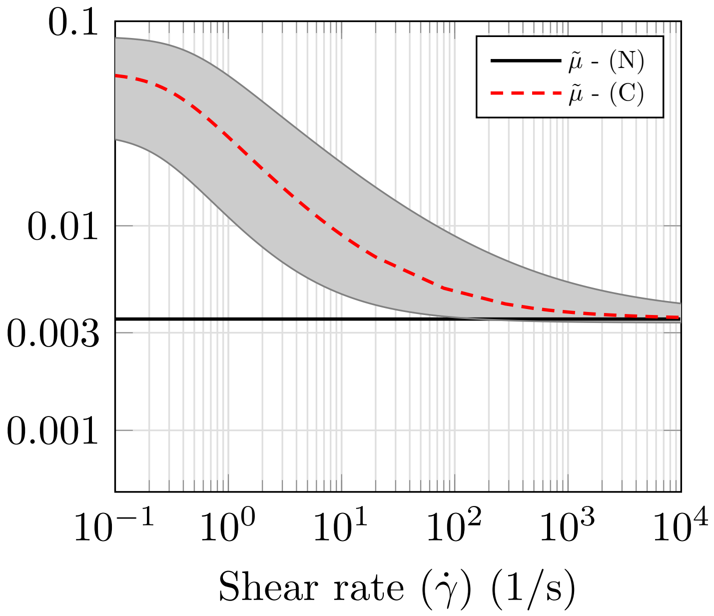

Figure 6.23: Newtonian (N) and non-Newtonian viscosity (C), based on the Carreau model. Gray area denotes the range in which viscosity is most likely (95.4% percentage of accuracy) to take values from based on the employed $\bar{\omega}_i$ and σ_i.

Each case considers three different sets of parameters (w_1, w_2), see related discussion in Chapter 5. Specifically, robust shape optimizations are performed for $(w_1, w_2) = (1, 0)$, corresponding to a minimization exclusively of the mean value of HI, for $(w_1, w_2) = (0.5, 0.5)$, corresponding to an even weighting of the mean and standard deviation and for $(w_1, w_2) = (0, 1)$, corresponding to a minimization exclusively of the standard deviation. Note that based on the current setup, the optimization for $(w_1, w_2) = (1, 0)$ is identical for both uncertain hemolysis parameters and uncertain non-Newtonian parameters. Furthermore, based on the FOSM-based optimization method, this case reduces to a "deterministic" optimization, in the sense that in the absence of uncertain considerations, the set of parameters would correspond to the employed $\bar{\omega}_i$. To simplify the notation, the cases corresponding to $(w_1, w_2) = (1, 0)$ are denoted as "DET", those with $(w_1, w_2) = (0.5, 0.5)$ are denoted as "MIXED" and $(w_1, w_2) = (0, 1)$ are denoted as "STD".

The employed optimization algorithm corresponds to Algorithm 4. However, the first-order derivatives in the direction of the uncertain variables are computed based on a first-order accurate FD method, since the number of uncertain variables M is relatively small for both investigated cases. The FD employs a perturbation size approximately 3 orders of magnitude smaller than each uncertain variable. A study has been preliminary conducted to evaluate the appropriate size of the perturbation. The adjoint system, solved for the determination of the first-order derivative in the direction of the shape and the second-order mixed derivative, corresponds to the one presented in Section 4.5. All necessary assumptions made therein for the derivation of the shape derivative hold in the investigated cases. The adjoint momentum and adjoint hemolysis equations employ the downwind analogy of QUICK to discretize the convective term.

An appropriate descent direction from the shape sensitivities is computed based on the Steklov-Poincaré method (Section 3.2.2). A constant step size is employed for all cases based on the maximum displacement rule of Eq. (3.15) with $\theta^{\max} = D^{\text{graft}}/140$. The simulations are terminated after a convergence criterion of $(J_l - J_{l-1}) \cdot 100\%/J_{l-1} \leq 0.001$ is reached or after a maximum number of iterations $l^{\max} = 230$, with l denoting the optimization iteration index.

Results

Uncertain hemolysis parameters. Figure 6.24 shows the resulting shape sensitivities and displacements for the first shape update of the three optimization cases, i.e., DET, MIXED and STD, considering uncertain hemolysis parameters. As shown there, the shape sensitivity exhibits a similar trend for all three cases with differences noted only w.r.t. the absolute values. Specifically, as the weight of the mean value of HI decreases and the weight of the standard deviation increases, the absolute values of the shape sensitivities decrease. Naturally, minor differences on the shape sensitivity fields exist. However, based on the Steklov-Poincaré method and the employed step size rule, which scales the displacement field based on a maximum desired displacement $\theta^{\max}$, the resulting displacement field is almost identical between the three cases. Note, however, that for the remaining optimization iterations the step size remains constant. Therefore, the DET optimization employs the smallest absolute step size which increases for the MIXED and STD cases, respectively. In all cases, the optimizer identifies the toe region of the anastomosis, i.e., the downstream connection of the graft with the artery, as the most influential area in the minimization of HI. This is reasonable, since this is the area in which the maximum shear stresses appear.

Figure 6.25 (left) shows the FOSM-estimated decrease of the mean value of HI for the three optimization cases. As shown therein, all three cases manage to minimize the mean by more that 35%, even though the STD case doesn't explicitly involve the optimization of the mean. As expected, the DET case leads to the biggest estimated decrease, approximately 52%, even though it employs the smallest step size. Figure 6.26 (left) shows the

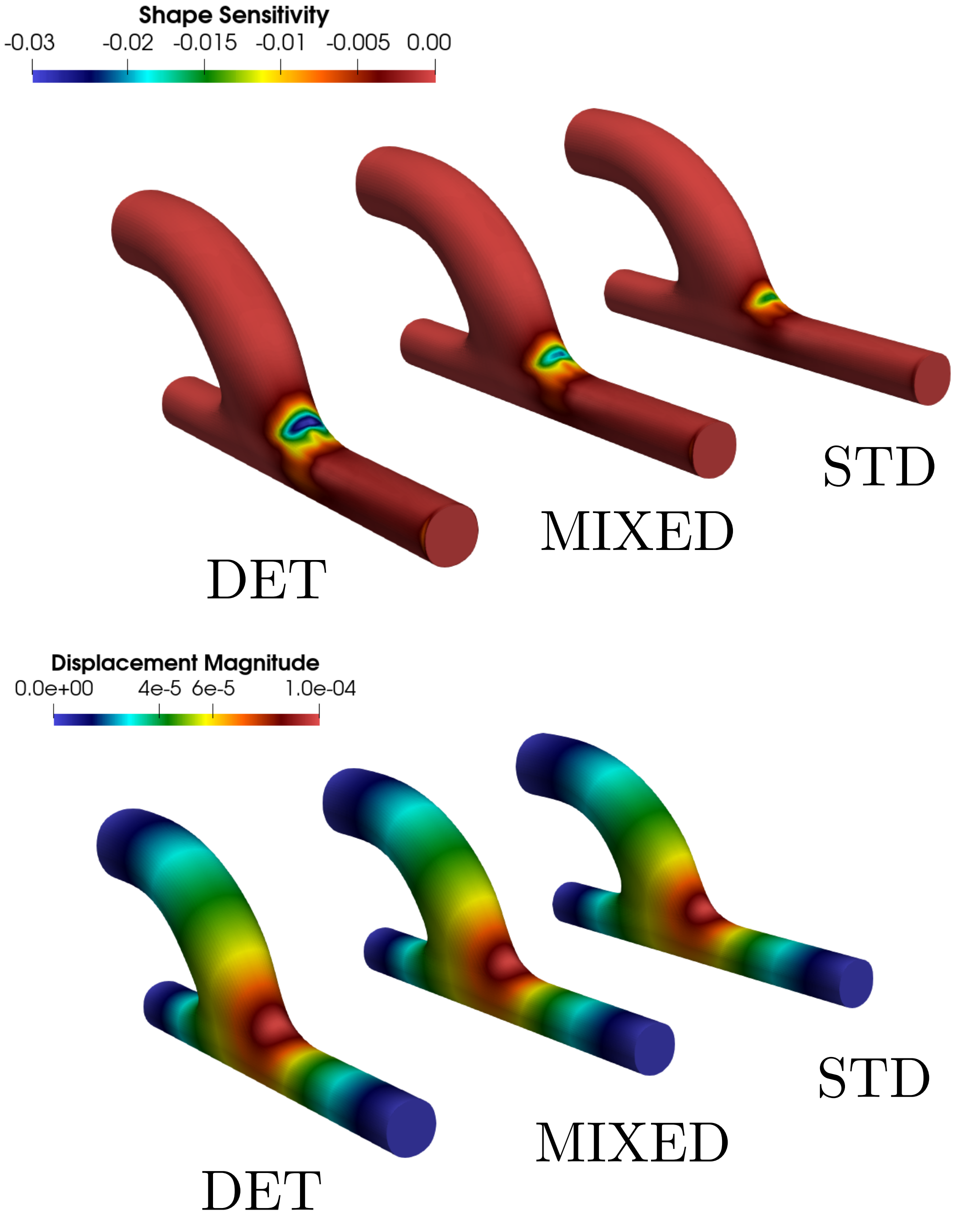

Figure 6.24: Perspective view of the initial bypass-graft with contours of shape sensitivity (top) and displacement magnitude in meters (bottom) for optimizations DET, MIXED and STD (from left to right) with uncertain hemolysis parameters.

respective FOSM-estimated decrease of the standard deviation of HI. Interestingly, the DET optimization case outperforms the other two that explicitly account for standard deviation in the formulation of the problem. This result indicates an inherent robustness of the case w.r.t. the hemolysis parameters. In view of the FOSM-predicted optimization results, the shape produced by the DET procedure is deemed as the universal optimal solution out of the three. To this end, it is further scrutinized w.r.t. the statistical moments of the QoI. MC simulations with a total sample size of $N = 1000$ are realized for the initial and optimized shapes. The samples are randomly selected using a normal distribution, for each uncertain variable, with a mean value and standard deviation as the one employed in the FOSM case. The results of the MC studies are shown in Figs. 6.25 (right) and 6.26 (right). As shown therein, the FOSM-predicted mean values of the initial and final shapes differ from the MC prediction by less than 6% . The standard deviation predictions differ by approximately 14%. Nevertheless, the underprediction of the statistical moments by the FOSM method is consistent for both initial and final shapes, thus resulting to a precise prediction of the relative decrease of the statistical moments during the optimization process.

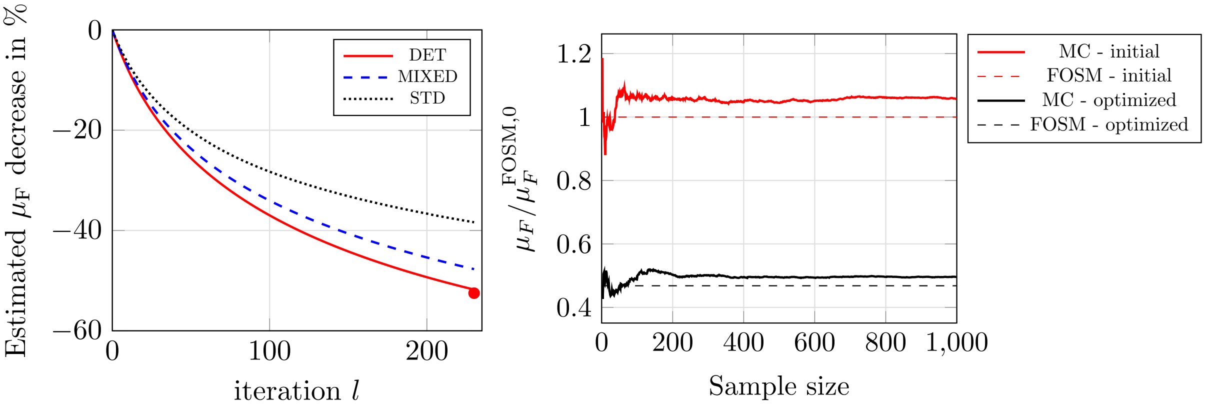

Figure 6.25: Optimizations for uncertain hemolysis parameters. Left: FOSM-predicted decrease of the mean value of the QoI. Filled circle denotes the MC-predicted mean value decrease for DET. Right: Running mean value of the QoI for the initial shape (red continuous line) and the optimized shape produced by DET (black line) computed by a MC procedure. Values are normalized by the FOSM-predicted mean value of the initial shape. Sample size of the MC simulations is $N = 1000$.

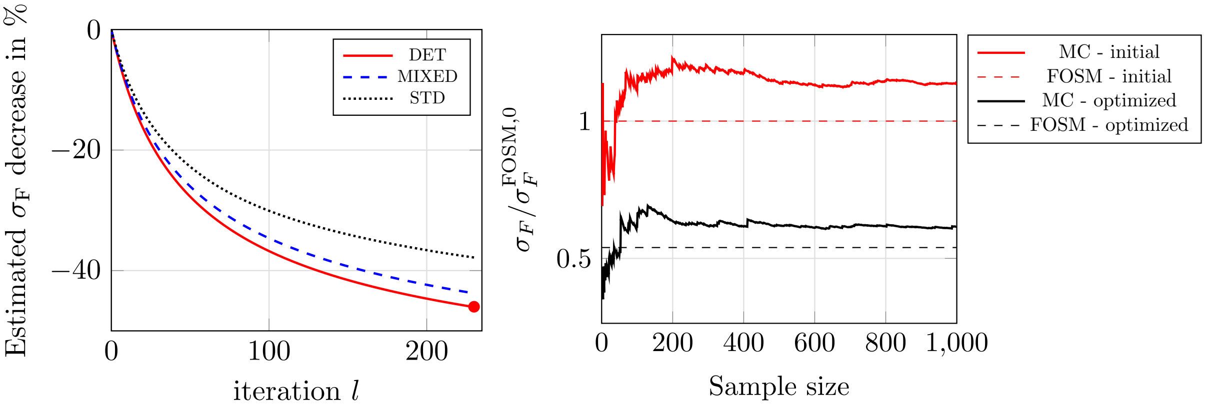

Figure 6.26: Caption as in Fig. 6.25 for standard deviation of the QoI instead of mean value.

Uncertain non-Newtonian parameters. Figure 6.27 shows the resulting shape sensitivities and displacements for the first shape update of the three optimization cases, i.e., DET, MIXED and STD, considering uncertain non-Newtonian parameters. Similar to the observations made in the case of uncertain hemolysis parameters, the lower the weight of the mean value the lower the absolute values of the shape sensitivities. The employed descent direction approach once again results to a very similar displacement field for all three cases.

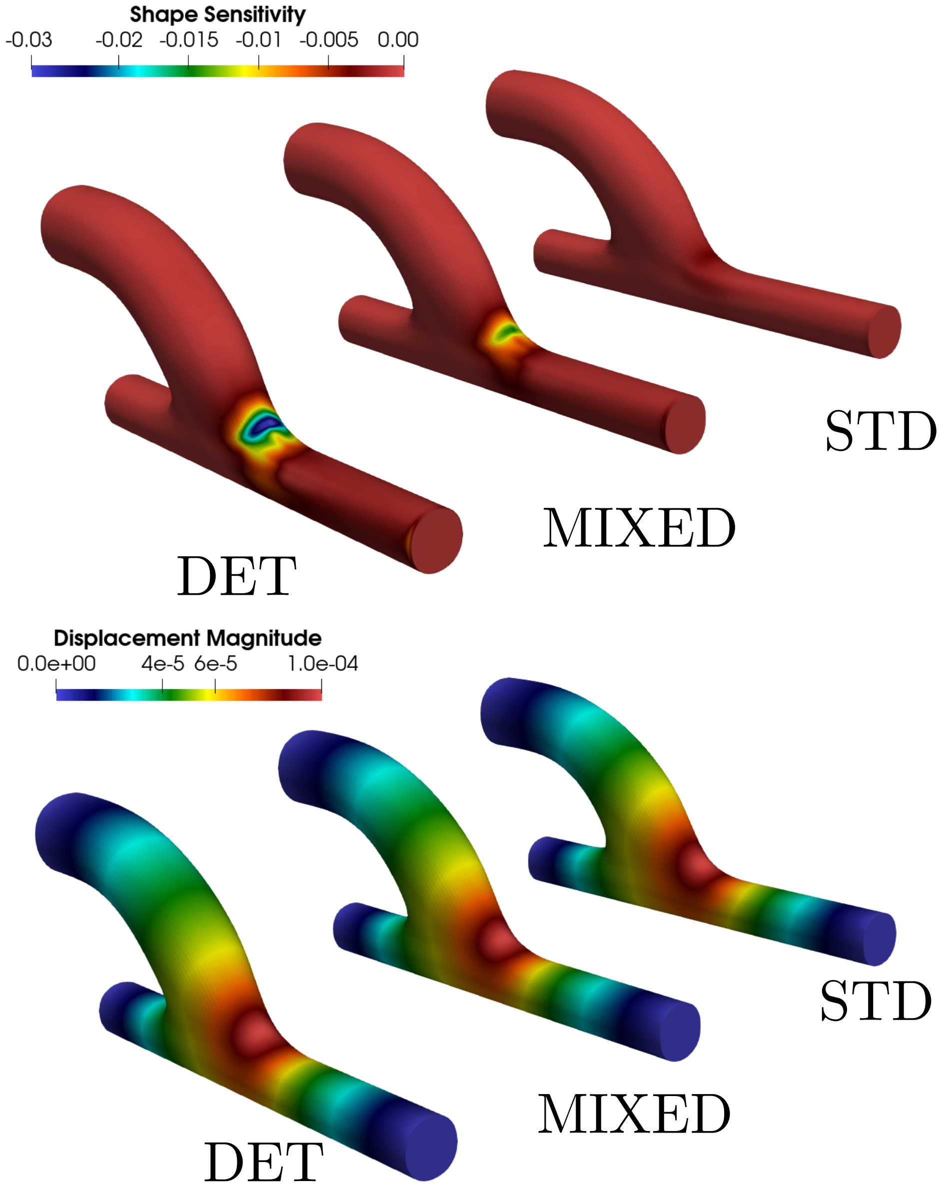

Figure 6.27: Perspective view of the initial bypass-graft with contours of shape sensitivity (top) and displacement magnitude in meters (bottom) for optimizations DET, MIXED and STD (from left to right) with uncertain non-Newtonian parameters.

Figure 6.28 (left) shows the FOSM-estimated decrease of the mean value of HI for the three optimization cases with uncertain non-Newtonian parameters. Two observations of interest can be made for these results. Firstly, it is shown that all three cases lead to a very similar optimization history w.r.t. the mean value of HI. Secondly, the MIXED optimization procedure stopped before reaching one of the termination criteria set in the optimization setup. This is attributed to mesh deformations that heavily deteriorated the grid quality thus leading to the divergence of the primal or adjoint solver. Overall, the STD procedure managed to reach approximately the same mean value decrease of 52% as the one reported by the DET procedure. As regards the FOSM-predicted standard deviation decrease, the STD procedure shows the most prominent decrease of approximately 43% while the DET procedure terminates at a decrease of approximately 40%, cf. Fig. 6.29. Based on these results, the shape produced by the STD procedure is deemed as the universal optimal solution for the case of uncertain non-Newtonian parameters. Similar to the case of uncertain hemolysis parameters, two MC simulations are conducted for the initial and optimized shape, produced by the STD procedure. The results of the MC studies are shown in Figs. 6.28 (right) and 6.29 (right). Once again the FOSM and MC-predicted mean values differ by less than 6% for both the initial and final shape. The FOSM underprediction is consistent for both shapes and the estimated decrease is thus accurately predicted during the optimization process. On the other hand, the standard deviation is significantly underpredicted by the FOSM approach with differences from the MC-estimations more than 35% for both initial and optimized shape. However, in terms of the relative decrease, the FOSM-prediction falls short by less than 5%, as shown in Fig. 6.29 (left).

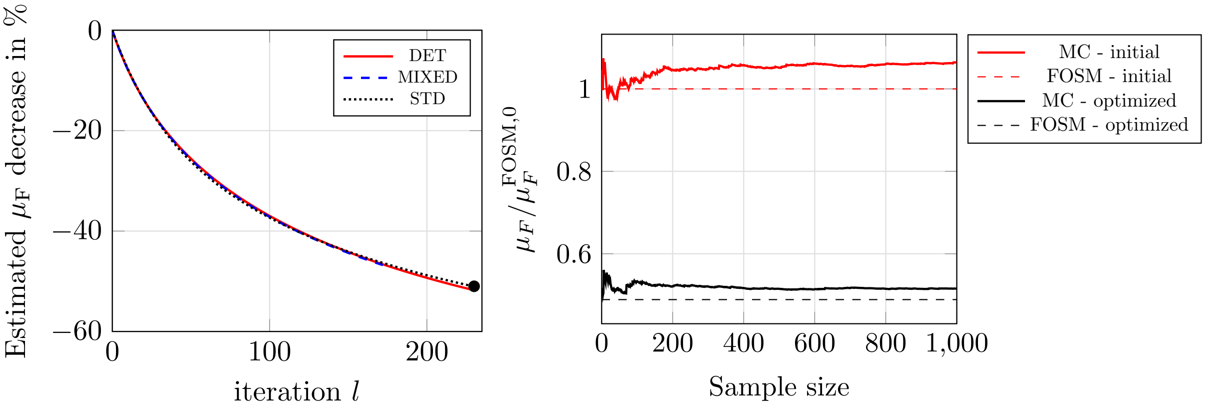

Figure 6.28: Optimizations for uncertain non-Newtonian parameters. Left: FOSM-predicted decrease of the mean value of the QoI. Filled circle denotes the MC-predicted mean value decrease for STD. Right: Running mean value of the QoI for the initial shape (red continuous line) and the optimized shape produced by STD (black line) computed by a MC procedure. Values are normalized by the FOSM-predicted mean value of the initial shape. Sample size of the MC simulations is $N = 1000$.

Figure 6.30 shows the outlines of the selected optimized shapes from the two uncertain optimization cases against the initial shape. Both optimized shapes correspond to very similar designs with minor differences, most prominent in the downstream region. As expected from the pre-optimization FSI study, which showed that the large cuff anastomosis corresponds to the lowest time-averaged hemolysis index, the optimizer proceeds to widen the cuff region. Specifically, the characteristic length of the optimized cuff is increased by approximately 37%. In addition, the optimized shape suggests that the bed of the anastomosis should be raised by a maximum of approximately $0.15l_m$. While the latter

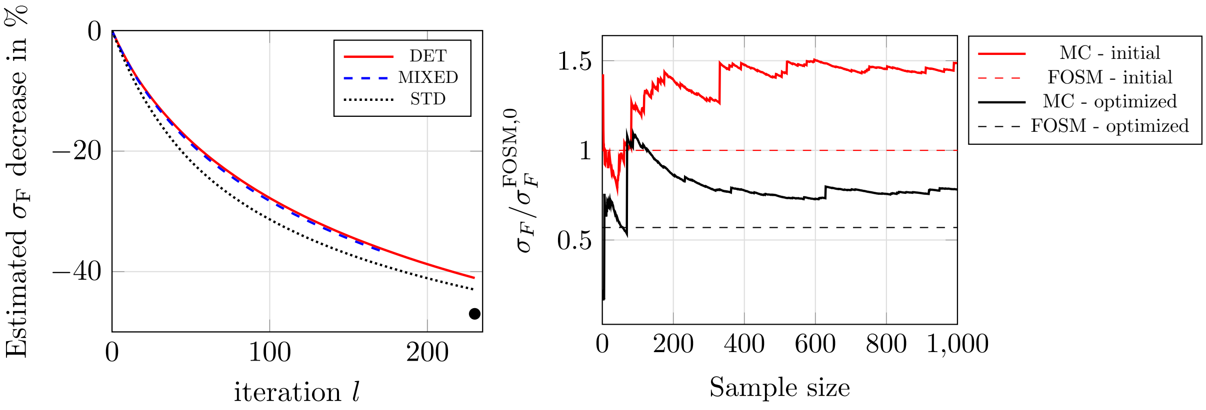

Figure 6.29: Caption as in Fig. 6.28 for standard deviation of the QoI instead of mean value.

raises questions as regards its practical implementation on a surgical procedure, there has already been biomedical interest in this direction as shown by the work of Rückert [2001].

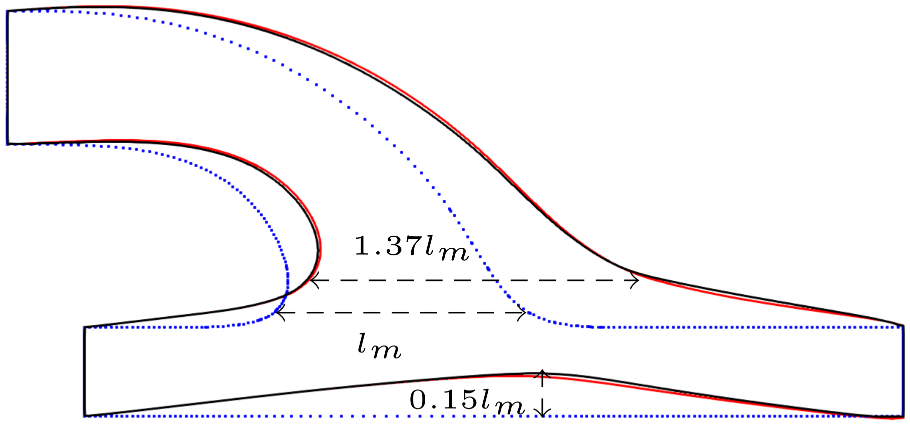

Figure 6.30: Outlines of the initial shape (blue dots), optimized for uncertain hemolysis parameters and the DET procedure (red continuous line) and optimized for uncertain non-Newtonian parameters and the STD procedure (black continuous lines).

As shown in Fig. 6.31, the optimized shapes result in a smoother transition of the blood flow from the bypass-graft to the artery. This results in a decrease of the flow shear stresses, as monitored by the scalar shear stress representative (see, Eq. (2.60)), which in turn results to the overall decrease of the potential induction of blood damage. The above observations justify the minimization of the mean value of HI. As shown by the optimization results and then validated by the MC studies, the reduction of the mean value is also accompanied by a reduction of the standard deviation. This suggests that in the optimized shapes, a simulation employing an inconsistent set of parameters poses less risk of returning an inaccurate prediction. While this might be medically irrelevant, it is significant in the ever-growing field of computational biomedical studies, especially in the context of model parameters that are hard to estimate in vivo applications. However, as shown in the studies presented herein, the minimization of the mean value might often prove sufficient to also minimize uncertainties induced by the modeling process without the need of explicitly accounting for robust shape optimization procedures.

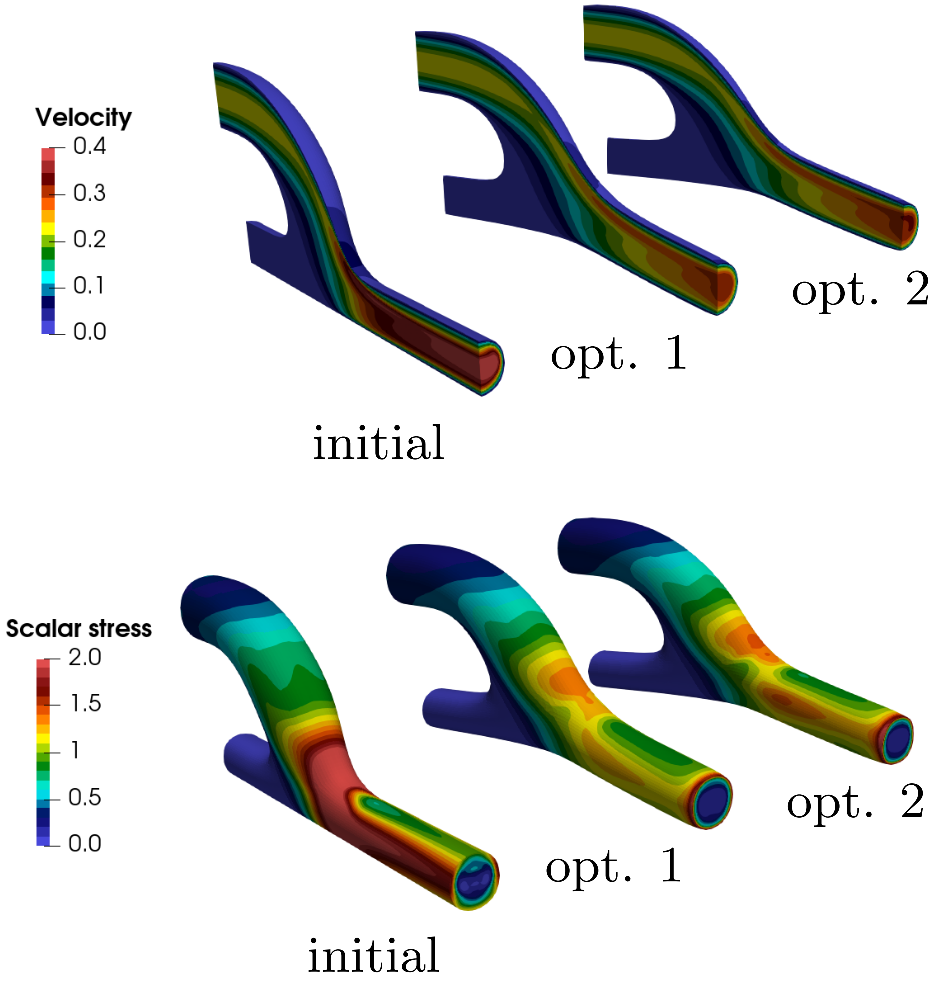

Figure 6.31: Perspective view of the initial bypass-graft and optimized for uncertain hemolysis parameters and the DET procedure (opt. 1) and uncertain non-Newtonian parameters and the STD procedure (opt. 2). Top: Velocity magnitude contours in m/s. Bottom: Scalar stress contours in Pa.

6.2.3 FSI Simulations after Optimization

The initial bypass-graft shape was optimized under simplifying assumptions, such as steady-state conditions and rigid walls. To this extent, it is interesting to investigate the performance of the optimized shape under more realistic conditions, i.e., elastic walls and periodic inflow.

The optimized shapes, denoted in Subsection 6.2.2 as opt. 1 (optimization for uncertain hemolysis parameters and $(w_1, w_2) = (1, 0)$) and opt. 2 (optimization for uncertain non-Newtonian parameters and $(w_1, w_2) = (0, 1)$), and the corresponding deformed grids are directly extracted from the optimization processes. Based on the surface meshes, new structure domains are developed based on the process described in Subsection 6.2.1. The discretization of the structure is the same as in the pre-optimization FSI studies.

One FSI simulation is realized for each optimized shape based on the setup described in Subsection 6.2.1. Even though the optimization process accounted for non-Newtonian properties, the fluid properties are now set to $\mu^{\mathrm{f}} = 4\,\mathrm{mPa \cdot s}$ and $\rho^{\mathrm{f}} = 10^3\,\mathrm{kg/m^3}$ to enable a direct comparison between the pre- and post-optimized shapes. The *straight* inflow path is employed, as it corresponds to the frequently applied Womersley velocity profile (Womersley [1955]). An exercise flow pulse, see Fig. 6.14 (left), is employed since it was found to result to the most critical time-averaged hemolysis index. All quantities of interest presented in the pre-optimization FSI study are assessed on the optimized shapes and compared to the results of the initial shape, i.e., medium cuff anastomosis of Fig. 6.11, under the same conditions. The observation region remains topologically the same as it is found to include the most critical local quantities even on the optimized shapes.

Results

Figure 6.32 collectively presents the investigated quantities of interest for the initial and optimized shapes. The time-averaged hemolysis index is decreased by approximately 41% and 37% for the opt. 1 and opt. 2 shapes, respectively, in comparison to the initial. The decrease of the index, while smaller in comparison to the steady-state optimization, is consistent with the results of the optimization, in the sense that the opt. 1 shape resulted in a slightly larger decrease of the mean value of the hemolysis index in comparison to opt. 2. Furthermore, it is shown that while a decrease of approximately 9% was reported for the investigated case when moving from the medium cuff to the large cuff in the pre-optimization FSI studies, a formal optimization procedure can result in a decrease of up to 41%. Interestingly, as shown in Fig. 6.33, the time-averaged decrease of the hemolysis index also holds for each time step individually. These results suggest that a reduced formulation of the optimization problem can serve as an efficient tool for the shape optimization of bypass-grafts without the need of explicitly accounting for the computationally intensive FSI.

As regards the metrics which the optimization process didn't explicitly account for, the observations are consistent with those made in Subsection 6.2.1. Specifically, the competitive nature between hemolysis and OSI is once again observed. The decrease of TAHI is accompanied by an increase of the mean OSI by approximately 44% for the opt. 1 shape and 41% for the opt. 2 shape. This shows a consistent trend as regards hemolysis and OSI, which necessitates the inclusion of the latter in the optimization problem, either by means of a constraint or by means of a weighted average of the two quantities in a single objective. Figure 6.34 presents a top and bottom view of the initial and optimized OSI contours. The OSI ring, initially observed in the pre-optimization studies, attains higher values of OSI on the optimized shapes. At the same time, the toe region of the anastomosis exhibits a wider area of more critical OSI values in comparison to the initial.

The WSS metrics, $\tau^{\mathrm{w}}_{\mathrm{min}}$ and $\tau^{\mathrm{w}}_{\mathrm{max}}$, are overall decreased in the optimized cases. While the reduction of $\tau^{\mathrm{w}}_{\mathrm{max}}$ is biomedically beneficial, the accompanying reduction of $\tau^{\mathrm{w}}_{\mathrm{min}}$ can become critical, see e.g., discussion in Subsection 6.2.1.

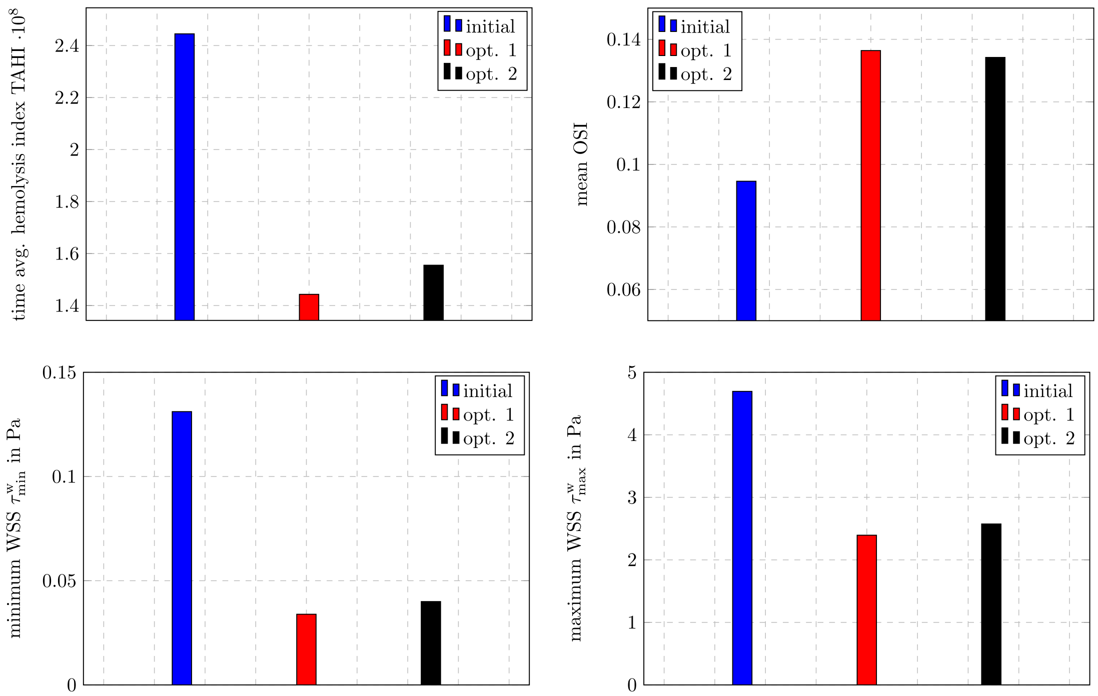

Figure 6.32: Comparison of the quantities of interest on the initial medium cuff bypass-graft and on the optimized shapes using FSI simulations for exercise conditions and *straight* inflow path.

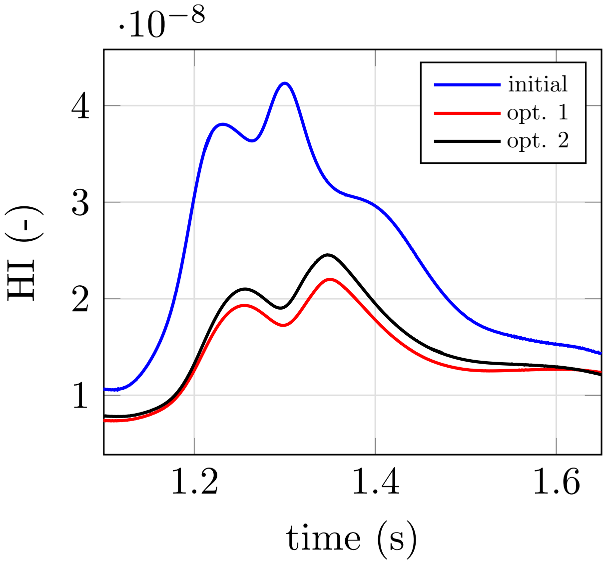

Figure 6.33: Comparison of hemolysis index over the last simulated heartbeat for initial and optimized shapes.

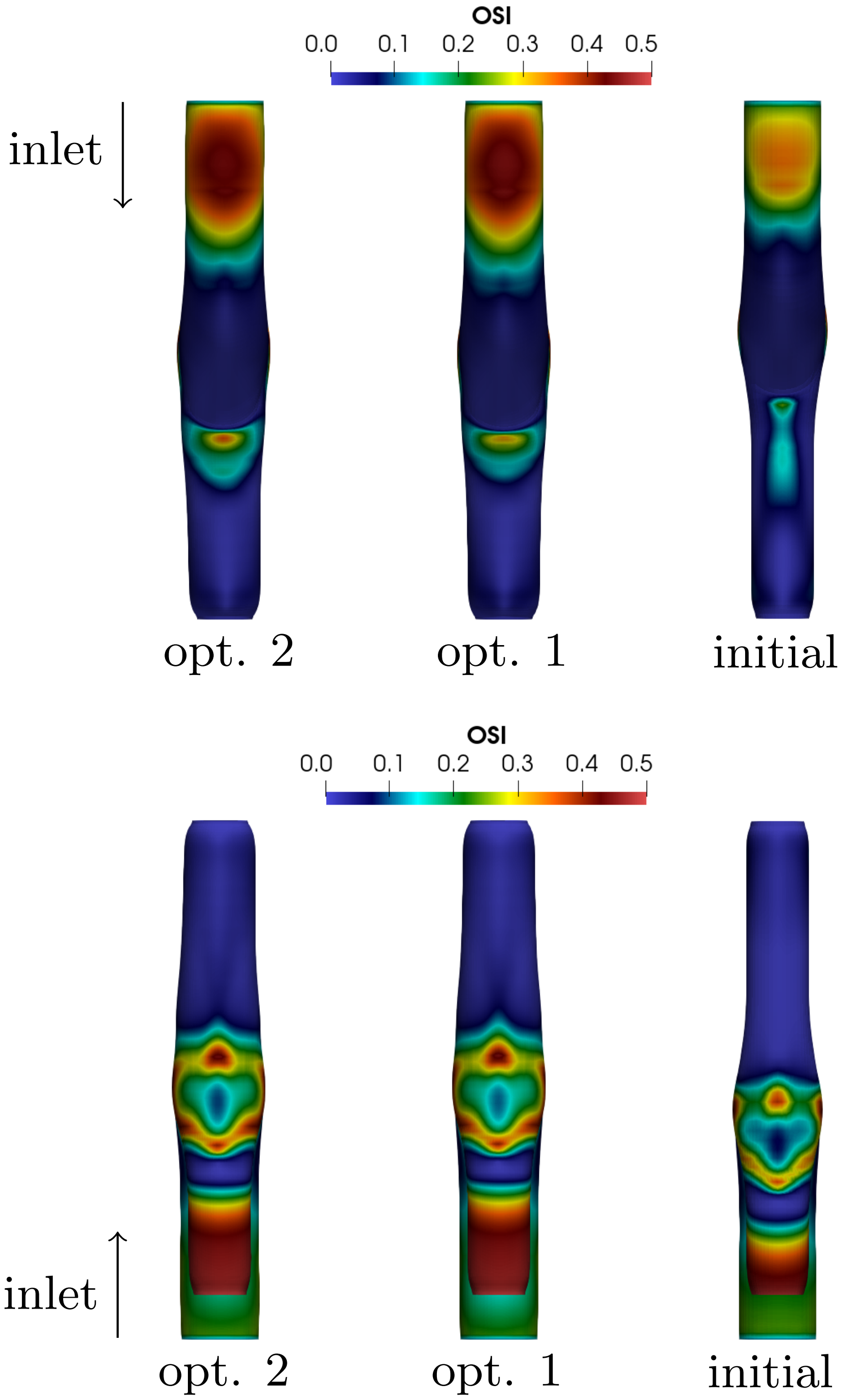

Figure 6.34: Comparison of OSI fields on initial and optimized shapes. Top: Top view of the bypass-grafts. Bottom: Bottom view of the bypass-grafts.

6.2.4 Conclusions

This section initially presented a thorough investigation of the hemodynamics in an idealized bypass-graft by employing FSI and CFD simulations. It was identified therein that the shape of the anastomosis is one of the most critical parameters in which one can intervene. Based on this finding, two robust FOSM-based shape optimization problems, considering uncertain hemolysis and non-Newtonian parameters, were constructed and applied for the minimization of the statistical moments of the hemolysis index. The optimization processes were simplified by considering steady-state conditions and rigid walls of the geometry. Additional MC investigations were conducted to investigate the accuracy with which the FOSM method predicted the statistical moments of interest. The optimization studies suggested two designs as optimal candidates, able to decrease the mean value of the hemolysis index by approximately 50%. Due to the simplifying assumptions employed in the optimization process, the optimized shapes were subsequently assessed under the more physiological unsteady FSI conditions. It was found that the steady-state optimized shapes result in significant decreases of up to 41% for hemolysis even on the unsteady, elastic walls setting. The key findings of this section are summarized as follows:

- A competitive relation between OSI and hemolysis induction w.r.t. the shape was found. Specifically, it was found that a bypass-graft that reduces the risk of hemolysis, increases, in large, OSI. This observation was consistent both at the pre- and post-optimization studies.

- Potential uncertainties on the hemolysis and non-Newtonian properties are found to be trivial in the context of the shape optimization studies conducted herein. In specific, it is shown that a deterministic optimization also decreases the standard deviation of the hemolysis index. However, it was found that in the case of uncertain non-Newtonian parameters, an optimization exclusively of the standard deviation can actually further increase the robustness of the case.

- The FOSM-based predictions of the statistical moments of hemolysis are found to be fairly accurate in the context of relative evaluations while fall short on absolute evaluations, as shown by the accompanying MC simulations.

- The optimized shapes suggest widening the anastomosis cuff and lifting the impaired artery so that to smoothen the transition of the blood flow from the graft to the artery.

- Even under the more physiologically relevant unsteady conditions with elastic graft and artery walls, the optimized shapes are found to outperform the initial shape. This finding suggests that a reduced optimization formulation, considering rigid walls and steady-state conditions can provide significant clinically relevant results at the cost of less computational effort.

7 Summary and Outlook

Adjoint-based shape optimization techniques have been extensively developed and applied in fields of conventional engineering applications. However, their application still lags behind in the field of biomedical sciences related to blood. This thesis presented advances in computational methods for modeling and optimization of blood flows. The topics that were studied in this work relate to (a) the computational modeling of blood flows, (b) the application of gradient-based parameter-free shape optimization, (c) the efficient estimation of shape sensitivities using the adjoint method and (d) the incorporation of uncertainties in the optimization problem.

(a) Computational modeling. Chapter 2 presented key aspects of CFD and FSI related to classical simulations of blood flows. These methods act as the backbone for the solution of what is referred to in this thesis as the primal problem. The state-of-the-art computational methods have been augmented by aspects of biomedical interest, such as the prediction of hemolysis and the non-Newtonian properties of blood. As regards the former, an Eulerian and Arbitraty-Lagrangian-Eulerian formulation has been employed for its seamless incorporation in the existing CFD and FSI frameworks, respectively. The employed model is one-way coupled to the flow equations, i.e., it receives information from the numerical solution of the flow equations with no retro-action on the employed fluid properties. Analytical solutions have been presented and derived for simple flow scenarios to verify the numerical implementation of the model. As regards the non-Newtonian properties of blood, three prominent shear-thinning, non-linear, algebraic viscosity models have been integrated into the computational environment. Their implementation has also been verified against analytical solutions. Finally, this thesis employs a partitioned FSI method to simulate scenarios of biomedical interest, especially in vivo conditions, in which the mechanical interdependence between the blood flow and the surrounding structure is considerable. To this end, a fluid solver and a structure solver are coupled. The novel coupling of the well-established individual solvers is verified against literature-reported results of a benchmark problem.

(b) Parameter-free shape optimization. Chapter 3 presented the shape optimization problems as considered in this thesis. The strategy refers to a CAD-free, i.e., parameter-free shape optimization approach in which the control is set as the shape itself. The optimization is performed by means of a gradient-based technique. While a common practice is the direct identification of the shape sensitivity as the necessary gradient, this thesis discussed the potential, practical drawbacks of such an approach and highlighted alternatives for the identification of a suitable descent direction given a shape sensitivity field. To this extent, most of the methods described in Chapter 3 require the solution of an additional problem, mostly in the form of PDEs, to arrive at a descent direction smoother than the shape sensitivity. The proposed alternatives were categorized as either "one-step methods" or "two-step methods". The former require the solution of a single problem to arrive at the sought descent direction field throughout the computational domain, while the latter initially compute the descent direction on the design surface and subsequently propagate the field to the interior domain. Furthermore, auxiliary aspects related to the optimization, such as the choice of a step size and the filtering of the displacement field near segments connecting design and non-design sections of the walls, were discussed. The proposed methodologies were scrutinized on a 2D CFD-based illustrative example.

(c) The adjoint method. Chapter 4 presented the continuous adjoint method for the efficient identification of shape sensitivities of internal steady-state flows. A general formulation of the adjoint steady NS equations for incompressible fluids was initially presented. Therein, the derivations considered a set of assumptions frequently holding in blood flow applications. The main focus of this thesis was on the minimization of hemolysis, i.e., blood damage, by intervening on the shape confining the blood flow. To this extent, a consistent continuous adjoint system to the flow equations augmented by the hemolysis model was derived and developed. The objective functional corresponds to a hemolysis index defined on the outlet of the computational domain. Subsequently, this thesis presented a consistent derivation of the adjoint system to the NS equations of a non-Newtonian fluid. The derivations were specified for the three shear-thinning models presented in Chapter 2. The novel adjoint systems were verified for their accuracy in estimating the sought shape sensitivity against FD results. An analytical solution was additionally constructed for the adjoint hemolysis equation on a simple flow scenario. Finally, the blood-related aspects of hemolysis and non-Newtonian viscosity properties were combined to arrive at a consistent adjoint system able to simultaneously account for both.

(d) Robust optimization. Chapter 5 dealt with the incorporation of potential uncertainties of the primal equation system in the optimization process. To this end, the objective functional was considered as a statistical quantity and the goal was the minimization of its first two statistical moments combined in a weighted average. While the employed optimization approach is based on the methodologies presented in (b) and (c), the thesis discussed two main approaches for the necessary quantification of the underlying uncertainties. In the context of the optimization, the first approach refers to the SGDM. The foundation of the method is on the evaluation of a sample of random realizations. The computational limitations of the method were discussed and a variant able to overcome some of the limitations, was proposed. The second approach that was investigated refers to the FOSM method. Based on this approach, the optimization reduces to the evaluation of pre-defined realizations and the statistical moments are evaluated based on mathematical expressions involving derivatives. Algorithms were given for the realization of each presented robust parameter-free shape optimization approach. Finally, the investigated approaches were applied in a 2D CFD-based example to illustrate their key characteristics.

Biomedical applications. The above-described topics were put to the test in Chapter 6, where two biomedical 3D applications were presented. The first application is the CFD-based deterministic optimization of an FDA-suggested idealized medical device for the minimization of its hemolysis potential. The computational primal solver was initially validated against experimental results. The optimization of the geometry led to small changes w.r.t. the initial one, able however to reduce the hemolysis index by approximately 18% in just 15 optimization iterations. Additional studies on the optimal solution showed that the result is inherently fairly robust to the employed hemolysis parameters. The second application refers to an idealized bypass-graft. A thorough investigation employing both CFD and FSI simulations was initially conducted to identify the most critical parameters affecting the hemodynamic quantities of interest. It was found that the shape of the graft is the most critical parameter in which one can externally intervene. Based on this, the idealized geometry model was optimized under simplified steady-state, rigid wall conditions for the minimization of hemolysis. The optimization study considered non-Newtonian and hemolysis parameters to be uncertain. Two designs able to decrease the mean value of the hemolysis index by approximately 50% were found. It was also shown that this problem is fairly robust against uncertainties of the non-Newtonian and hemolysis parameters. The optimized designs were subsequently evaluated using FSI simulations. It was found that the benefits of the simplified optimization studies also held, in large, under the more realistic unsteady conditions.

Future Studies

This thesis presented optimization problems based on temporally steady conditions of the primal and corresponding adjoint. While it was shown that this simplification can still provide significantly optimized results even when evaluated in unsteady flows, future studies should examine the extension of the presented adjoint methods in unsteady conditions. The development of efficient and accurate reduced-order models can benefit this research direction, due to the reversed time-propagation of the unsteady adjoint problems. In the same direction, future studies should also target the consistent development of FSI adjoint systems in the context of biomedical applications. Furthermore, as regards the topic of uncertainties, future studies could consider the shape itself to be uncertain and investigate the implications this might have on the formulation of the robust shape optimization problem. Finally, the studies conducted throughout this thesis referred to predominately academic scenarios or idealized geometries and the results were discussed with a qualitative view. To this extent, it is interesting to apply the hemolysis optimization process to extravascular machinery such as blood pumps that can later be experimentally validated or to investigate patient-specific intravascular geometries that could be extracted from CT scans.

A Additional Mathematical Aspects

A.1 Gauss Divergence Theorem for Gradient Fields

Consider the proposition

$$\int\limits_{\mathrm{CV}} \frac{\partial \phi}{\partial x_j}\,\mathrm{d}V = \int\limits_{O(\mathrm{CV})} \phi n_j \,\mathrm{d}S, \tag{A.1}$$

where ϕ is a scalar field and n_j the normal vector to the boundaries of the CV. For an arbitrary constant vector $\alpha_j \in \mathbb{R}^N$ one can write

$$\begin{aligned}\alpha_j \int\limits_{O(\mathrm{CV})} \phi n_j \,\mathrm{d}S &= \int\limits_{O(\mathrm{CV})} \phi \alpha_j n_j \,\mathrm{d}S = \int\limits_{\mathrm{CV}} \frac{\partial(\phi\alpha_j)}{\partial x_j}\,\mathrm{d}V \\ &= \int\limits_{\mathrm{CV}} \alpha_j \frac{\partial \phi}{\partial x_j}\,\mathrm{d}V + \int\limits_{\mathrm{CV}} \phi \cancelto{0}{\frac{\partial \alpha_j}{\partial x_j}}\,\mathrm{d}V = \alpha_j \int\limits_{\mathrm{CV}} \frac{\partial \phi}{\partial x_j}\,\mathrm{d}V. \end{aligned} \tag{A.2}$$

By considering that two vectors $p_j, q_j \in \mathbb{R}^N$ are equal to each other if and only if for all vectors $r_j \in \mathbb{R}^N$, $r_j p_j = r_j q_j$, proposition (A.1) is true in view of Eq. (A.2).

A.2 Derivation of Equation (2.76)

This appendix refers to a Hagen-Poiseuille fully-developed pipe flow and targets to derive an analytical expression to the hemolysis-oriented objective functional defined in Section 2.2. In this case, Eq. (2.69) can be written as

$$\mathrm{HI} = \frac{\int\limits_{\Gamma_{\mathrm{out}}} H_L^{\beta} v_i n_i \,\mathrm{d}S}{\int\limits_{\Gamma_{\mathrm{out}}} v_i n_i \,\mathrm{d}S} = \frac{\int\limits_{\Gamma_{\mathrm{out}}} H v_z(r) \,\mathrm{d}S}{\int\limits_{\Gamma_{\mathrm{out}}} v_z(r) \,\mathrm{d}S} = \frac{\mathrm{I}_1}{\mathrm{I}_2}. \tag{A.3}$$

By making use of the analytical solutions (2.71) and (2.75), the integrals I_1 and I_2 can be further expanded. Starting from the latter,

$$\begin{aligned}\mathrm{I}_2 = \int\limits_{\Gamma_{\mathrm{out}}} v_z(r)\,\mathrm{d}S &= \int\limits_0^{2\pi}\int\limits_0^{R} v_z(r) r \,\mathrm{d}r\,\mathrm{d}\phi = 2\pi V_{\max} \int\limits_0^{R} \left(r - \frac{r^3}{R^2}\right)\mathrm{d}r \\ &= 2\pi V_{\max} \left[\frac{r^2}{2} - \frac{r^4}{4R^2}\right]_0^R = \frac{1}{2}\pi V_{\max} R^2, \end{aligned} \tag{A.4}$$

and for I_1

$$\begin{aligned}\mathrm{I}_1 &= \int\limits_{\Gamma_{\text{out}}} H(r)\Big|_{z=L} v_z(r)\,\mathrm{d}S = CL^\beta \int\limits_{\Gamma_{\text{out}}} \left[2\mu V_{\max}\frac{r}{R^2}\right]^\alpha \left[V_{\max}\left(1-\left(\frac{r}{R}\right)^2\right)\right]^{(1-\beta)} \mathrm{d}S \\ &= \underbrace{CL^\beta V_{\max}^{(1+\alpha-\beta)}\left(\frac{2\mu}{R^2}\right)^\alpha}_{K} \int\limits_{\Gamma_{\text{out}}} r^\alpha \left[\left(1-\left(\frac{r}{R}\right)^2\right)\right]^{(1-\beta)} \mathrm{d}S \\ &= K\int\limits_0^{2\pi}\int\limits_0^R r^{(a+1)}\left[\left(1-\left(\frac{r}{R}\right)^2\right)\right]^{(1-\beta)} \mathrm{d}r\,\mathrm{d}\phi = 2\pi K\int\limits_0^R r^{(a+1)}\left[\left(1-\left(\frac{r}{R}\right)^2\right)\right]^{(1-\beta)} \mathrm{d}r.\end{aligned} \tag{A.5}$$

Consider $X(r) = -(\frac{r}{R})^2$, then $|X| < 1$ and by use of the generalized binomial expansion for non-integer exponents, one can write

$$\begin{aligned}\mathrm{I}_1 &= 2\pi K\int\limits_0^R r^{(a+1)}\left[(1+X(r))\right]^{(1-\beta)} \mathrm{d}r = 2\pi K\int\limits_0^R r^{(a+1)}\sum_{k=0}^{\infty}\binom{1-\beta}{k}X^k(r)\,\mathrm{d}r \\ &= 2\pi K\sum_{k=0}^{\infty}\binom{1-\beta}{k}\left(-\frac{1}{R^2}\right)^k\int\limits_0^R r^{(a+1+2k)}\,\mathrm{d}r \\ &= 2\pi K\sum_{k=0}^{\infty}\binom{1-\beta}{k}\left(-\frac{1}{R^2}\right)^k\frac{1}{a+2+2k}R^{(a+2+2k)} \\ &= 2\pi KR^{(a+2)}\sum_{k=0}^{\infty}\frac{\Gamma(2-\beta)}{\Gamma(k+1)\Gamma(2-\beta-k)}\frac{(-1)^k}{(\alpha+2+2k)}.\end{aligned} \tag{A.6}$$

By substitution of Eqs. (A.4), (A.6) in Eq. (A.3) and by expansion of K, one arrives at Eq. (2.76).

A.3 Derivation of Equation (4.112)

The variation of the sub-integral I_5' in the direction of the velocity components can be formally written as

$$\delta_{v_i}I_5'\cdot\delta v_i = \int\limits_\Omega \left(\delta_{v_i}\left[\hat{\mu}\left(\tilde{\mu}-f(\dot{\gamma})\right)\right]\cdot\delta v_i\right)\mathrm{d}\Omega = -\int\limits_\Omega \hat{\mu}\left(\delta_{v_i}f(\dot{\gamma})\cdot\delta v_i\right)\mathrm{d}\Omega. \tag{A.7}$$

To continue with the derivation, one must consider the expression of $f(\dot{\gamma})$ depending on the respective viscosity model (cf., Table 2.4).

A.3.1 Newtonian Model (N)

For a Newtonian fluid, the effective viscosity is constant and thus $\delta_{v_i} f(\dot{\gamma}) \cdot \delta v_i = 0$ leading to $\delta_{v_i} I_5' \cdot \delta v_i = 0$.

A.3.2 Power-law Model (PL)

In the case of a Power-law fluid, Eq. (A.7) can be written as

$$\begin{aligned}
\delta_{v_i} I_5' \cdot \delta v_i &= -\int\limits_{\Omega} \hat{\mu} k \Big(\delta_{v_i} \dot{\gamma}^{(n-1)} \cdot \delta v_i \Big) \, \mathrm{d}\Omega = -\int\limits_{\Omega} \hat{\mu} k \Big(\delta_{v_i} (2 S_{ij} S_{ij})^{\frac{(n-1)}{2}} \cdot \delta v_i \Big) \, \mathrm{d}\Omega \\
&= -\int\limits_{\Omega} \hat{\mu} 2k \frac{(n-1)}{2} (2 S_{ij} S_{ij})^{\frac{(n-3)}{2}} \Big(2 S_{ij} \delta S_{ij} + \underbrace{\delta S_{ij} \delta S_{ij}}_{\text{HoT}} \Big) \, \mathrm{d}\Omega \\
&= -\int\limits_{\Omega} \hat{\mu} 2k (n-1) \dot{\gamma}^{(n-3)} S_{ij} \delta S_{ij} \, \mathrm{d}\Omega. \qquad \text{(A.8)}
\end{aligned}$$

Here $\delta S_{ij} = 0.5(\partial \delta v_i / \partial x_j + \partial \delta u_j / \partial x_i)$ and higher order terms (HoT) are neglected. It is defined that $X_{ij} = 2k(n-1)\dot{\gamma}^{(n-3)} S_{ij}$, on which it holds $X_{ij} \sim S_{ij} \rightarrow X_{ij} = X_{ji}$. Equation (A.8) is further expanded as

$$\begin{aligned}
\delta_{v_i} I_5' \cdot \delta v_i &= -\int\limits_{\Omega} \hat{\mu} X_{ij} \frac{1}{2} \Big(\frac{\partial \delta v_i}{\partial x_j} + \frac{\partial \delta u_j}{\partial x_i} \Big) \, \mathrm{d}\Omega \\
&= -\int\limits_{\Omega} \hat{\mu} X_{ij} \frac{1}{2} \frac{\partial \delta v_i}{\partial x_j} \, \mathrm{d}\Omega - \int\limits_{\Omega} \hat{\mu} X_{ij} \frac{1}{2} \frac{\partial \delta u_j}{\partial x_i} \, \mathrm{d}\Omega \\
&= -\int\limits_{\Omega} \hat{\mu} X_{ij} \frac{1}{2} \frac{\partial \delta v_i}{\partial x_j} \, \mathrm{d}\Omega - \int\limits_{\Omega} \hat{\mu} X_{ji} \frac{1}{2} \frac{\partial \delta v_i}{\partial x_j} \, \mathrm{d}\Omega \\
&= -\int\limits_{\Omega} \hat{\mu} X_{ij} \frac{\partial \delta v_i}{\partial x_j} \, \mathrm{d}\Omega = -\int\limits_{\Gamma} (\delta v_i) \hat{\mu} X_{ij} n_j \, \mathrm{d}\Gamma + \int\limits_{\Omega} (\delta v_i) \frac{\partial}{\partial x_j} \Big[\hat{\mu} X_{ij} \Big] \, \mathrm{d}\Omega. \qquad \text{(A.9)}
\end{aligned}$$

This is very similar to the treatment of the tensor B_{ij} in the case of adjoint hemolysis. Additionally note that in Section 2.3, the Power-law viscosity model is formulated based on threshold considerations of $\dot{\gamma}$. These considerations are omitted on the derivation process described above.

A.3.3 Modified-Casson Model (MC)

In the case of a Modified-Casson fluid Eq. (A.7) can be written as

$$
\begin{aligned}
\delta_{v_i} I_5' \cdot \delta v_i &= -\int\limits_{\Omega} \hat{\mu}\Big(\delta_{v_i}\Big[\overbrace{\sqrt{\tau_0}(\sqrt{\lambda}+\sqrt{\dot{\gamma}})^{-1}+\sqrt{\mu_c}}^{f^*(\dot{\gamma})}\Big]^2 \cdot \delta v_i\Big)\,\mathrm{d}\Omega \\
&= -\int\limits_{\Omega} \hat{\mu}\left[2f^*(\dot{\gamma})(-\sqrt{\tau_0}(\sqrt{\lambda}+\sqrt{\dot{\gamma}})^{-2}\Big(\delta_{v_i}\left[(2S_{ij}S_{ij})^{\frac{1}{4}}\right]\cdot\delta v_i\Big)\right]\mathrm{d}\Omega \\
&= -\int\limits_{\Omega} \hat{\mu}\left[2f^*(\dot{\gamma})(-\sqrt{\tau_0}(\sqrt{\lambda}+\sqrt{\dot{\gamma}})^{-2}\dot{\gamma}^{-\frac{3}{2}}\Big(S_{ij}\delta S_{ij}+\underbrace{\delta S_{ij}\delta S_{ij}}_{\text{HoT}}\Big)\right]\mathrm{d}\Omega \\
&= -\int\limits_{\Omega} \hat{\mu}\left[-2\Big[\frac{\sqrt{\tau_0}}{\sqrt{\lambda}+\sqrt{\dot{\gamma}}}+\sqrt{\mu_c}\Big]\Big[\frac{\sqrt{\tau_0}}{(\sqrt{\lambda}+\sqrt{\dot{\gamma}})^2}\Big]\frac{1}{\dot{\gamma}^{\frac{3}{2}}}S_{ij}\right]\delta S_{ij}\,\mathrm{d}\Omega. \qquad \text{(A.10)}
\end{aligned}
$$

If $X_{ij} = -2\Big[\frac{\sqrt{\tau_0}}{\sqrt{\lambda}+\sqrt{\dot{\gamma}}}+\sqrt{\mu_c}\Big]\Big[\frac{\sqrt{\tau_0}}{(\sqrt{\lambda}+\sqrt{\dot{\gamma}})^2}\Big]\frac{1}{\dot{\gamma}^{\frac{3}{2}}}S_{ij}$ and the same methodology as described in A.3.2 is followed, then Eq. (4.112) is reached.

A.3.4 Carreau Model (C)

In the case of a Carreau fluid Eq. (A.7) can be written as

$$
\begin{aligned}
\delta_{v_i} I_5' \cdot \delta v_i &= -\int\limits_{\Omega} \hat{\mu}\Big(\delta_{v_i}\Big[\Big(1+(\lambda\dot{\gamma})^2\Big)^{\frac{n-1}{2}}(\mu_0-\mu_\infty)+\mu_\infty\Big]\cdot\delta v_i\Big)\,\mathrm{d}\Omega \\
&= -\int\limits_{\Omega} \hat{\mu}\left[\frac{n-1}{2}(\mu_0-\mu_\infty)\Big(1+(\lambda\dot{\gamma})^2\Big)^{\frac{n-3}{2}}\lambda^2\Big(\delta_{v_i}(2S_{ij}S_{ij})\cdot\delta v_i\Big)\right]\mathrm{d}\Omega \\
&= -\int\limits_{\Omega} \hat{\mu}\left[2(n-1)(\mu_0-\mu_\infty)\Big(1+(\lambda\dot{\gamma})^2\Big)^{\frac{n-3}{2}}\lambda^2\Big(S_{ij}\delta S_{ij}+\underbrace{\delta S_{ij}\delta S_{ij}}_{\text{HoT}}\Big)\right]\mathrm{d}\Omega \\
&= -\int\limits_{\Omega} \hat{\mu}\left[2(n-1)(\mu_0-\mu_\infty)\Big(1+(\lambda\dot{\gamma})^2\Big)^{\frac{n-3}{2}}\lambda^2 S_{ij}\right]\delta S_{ij}\,\mathrm{d}\Omega. \qquad \text{(A.11)}
\end{aligned}
$$

If $X_{ij} = 2(n-1)(\mu_0-\mu_\infty)\Big(1+(\lambda\dot{\gamma})^2\Big)^{\frac{n-3}{2}}\lambda^2 S_{ij}$ and the same methodology as described in A.3.2 is followed, then Eq. (4.112) is reached.

Bibliography

F. Abraham, M. Behr, and M. Heinkenschloss. Shape optimization in steady blood flow: A numerical study of non-Newtonian effects. Computer Methods in Biomechanics and Biomedical Engineering, 8(2):127–137, 2005a.

F. Abraham, M. Behr, and M. Heinkenschloss. Shape optimization in unsteady blood flow: a numerical study of non-Newtonian effects. Computer Methods in Biomechanics and Biomedical Engineering, 8(3), 2005b.

AIAA. AIAA: Guide for the Verification and Validation of Computational Fluid Dynamics Simulations (AIAA G-077-1998(2002)). 1998.

A. A. Ali, E. Ullmann, and M. Hinze. Multilevel monte carlo analysis for optimal control of elliptic pdes with random coefficients. SIAM/ASA Journal on Uncertainty Quantification, 5(1):466–492, 2017.

G. Allaire, C. Dapogny, and F. Jouve. Shape and topology optimization. In Geometric partial differential equations, part II, volume 22 of Handbook of Numerical Analysis. 2021.

L. A. N. Amaral, A. L. Goldberger, P. Ch. Ivanov, and H. E. Stanley. Modeling heart rate variability by stochastic feedback. Computer Physics Communications, 121-122: 126–128, 1999. Proceedings of the Europhysics Conference on Computational Physics CCP 1998.

I. Antonau, M. Hojjat, and K.-U. Bletzinger. Relaxed gradient projection algorithm for constrained node-based shape optimization. Structural and Multidisciplinary Optimization, 63(4):1633–1651, 2021.

H. Azegami and Z.-C. Wu. Domain Optimization Analysis in Linear Elastic Problems : Approach Using Traction Method. JSME international journal. Ser. A, Mechanics and material engineering, 39(2):272–278, 1996.

T. Bäck. Evolutionary Algorithms in Theory and Practice. Evolution Strategies, Evolutionary Programming, Genetic Algorithms. Oxford University Press, 1996.

O. Baskurt, B. Neu, and H. J. Meiselman. Red Blood Cell Aggregation. Routledge, 2011.

Y. Bazilevs, M. C. Hsu, Y. Zhang, W. Wang, T. Kvamsdal, S. Hentschel, and J. G. Isaksen. Computational vascular fluid-structure interaction: methodology and application to cerebral aneurysms. Biomechanics and Modeling in Mechanobiology, 9(4):481–498, 2010.

Y. Bazilevs, K. Takizawa, and T. E Tezduyar. Computational Fluid-Structure Interaction: Methods and Applications, chapter 8, pages 191–258. Wiley Series in Computational Mechanics. John Wiley & Sons, 2013.

Y. Bazilevs, A. Korobenko, X. Deng, and J. Yan. Novel structural modeling and mesh moving techniques for advanced fluid–structure interaction simulation of wind turbines. International Journal for Numerical Methods in Engineering, 102(3-4):766–783, 2015.

P. Benner, S. Dolgov, A. Onwunta, and M. Stoll. Low-rank solution of an optimal control problem constrained by random navier-stokes equations. International Journal for Numerical Methods in Fluids, 92(11):1653–1678, 2020.

S. A. Berger and L-D. Jou. Flows in stenotic vessels. Annual Review of Fluid Mechanics, 32(1):347–382, 2000.

R. B. Bird, W. E. Stewart, and E. L. Lightfoot. Transport Phenomena. John Wiley & Sons, Inc., New York, 2nd edition, 2006.

P. L. Jr. Blackshear, F. D. Dorman, and J. H Steinbach. Some mechanical effects that influence hemolysis. Transactions - American Society for Artificial Internal Organs, 11 (1):112–117, 1965.

G. W. S. Blair. An Equation for the Flow of Blood, Plasma and Serum through Glass Capillaries. Nature, 183(4661):613–614, 1959.

G. Bletsos, N. Kühl, and T. Rung. Adjoint-based shape optimization for the minimization of flow-induced hemolysis in biomedical applications. Engineering Applications of Computational Fluid Mechanics, 15(1):1095–1112, 2021.

G. Bletsos, N. Kühl, and T. Rung. Adjoint shape sensitivities of blood flows considering non-Newtonian properties. International Journal for Numerical Methods in Fluids, 95 (11):1791–1819, 2023.

G. Bletsos, T. Rung, and L. Radtke. Hemodynamics in arterial bypass graft anastomoses with varying cuff sizes and proximal flow paths: a fluid-structure interaction study. Computer Methods in Biomechanics and Biomedical Engineering, 28(7):1066–1085, 2024.

G. Bletsos, L. Radtke, and T. Rung. Adjoint-assisted robust shape optimization of an idealized arterial bypass graft using the FOSM method. Structural and Multidisciplinary Optimization, 2025. In press.

K.-U. Bletzinger. A consistent frame for sensitivity filtering and the vertex assigned morphing of optimal shape. Structural and Multidisciplinary Optimization, 49:873–895, 2014.

K.-U. Bletzinger, M. Firl, J. Linhard, and R. Wüchner. Optimal shapes of mechanically motivated surfaces. Computer Methods in Applied Mechanics and Engineering, 199(5): 324–333, 2010.

J. Bonet and R. D. Wood. Nonlinear Continuum Mechanics for Finite Element Analysis. Cambridge University Press, New York, 2008.

J. Broniszewski and J. Piechna. A fully coupled analysis of unsteady aerodynamics impact on vehicle dynamics during braking. Engineering Applications of Computational Fluid Mechanics, 13(1):623–641, 2019.

D. E. Brooks, J. W. Goodwin, and G. V. Seaman. Interactions among erythrocytes under shear. Journal of Applied Physiology, 28(2):172–177, 1970.

L. S. Caretto, A. D. Gosman, S. V. Patankar, and D. B. Spalding. Two calculation procedures for steady, three-dimensional flows with recirculation. In H. Cabannes and R. Temam, editors, Proceedings of the Third International Conference on Numerical Methods in Fluid Mechanics, pages 60–68, Berlin, Heidelberg, 1973. Springer Berlin Heidelberg.

A. Carnarius, F. Thiele, E. Oezkaya, and N. R. Gauger. Adjoint Approaches For Optimal Flow Control. 2010.

E. Catmull and J. Clark. Recursively generated b-spline surfaces on arbitrary topological meshes. Computer-Aided Design, 10(6):350–355, 1978.

L. Cavagna, G. Quaranta, and P. Mantegazza. Application of navier–stokes simulations for aeroelastic stability assessment in transonic regime. Computers & Structures, 85(11): 818–832, 2007.

T. Chatterjee, S. Chakraborty, and R. Chowdhury. A Critical Review of Surrogate Assisted Robust Design Optimization. Archives of Computational Methods in Engineering, 26 (1):245–274, 2019.

Y. S. Chatzizisis, A. U. Coskun, M. Jonas, E. R. Edelman, C. L. Feldman, and P. H. Stone. Role of endothelial shear stress in the natural history of coronary atherosclerosis and vascular remodeling: Molecular, cellular, and vascular behavior. Journal of the American College of Cardiology, 49(25):2379–2393, 2007.

S. Chien, S. Usami, H. M. Taylor, J. L. Lundberg, and M. I. Gregersen. Effects of hematocrit and plasma proteins on human blood rheology at low shear rates. Journal of Applied Physiology, 21(1):81–87, 1966.

J. J. Chiu and S. Chien. Effects of disturbed flow on vascular endothelium: Pathophysiological basis and clinical perspectives. Physiological Reviews, 91(1):327–387, 2011.

Y. I. Cho. Effects of the non-newtonian viscosity of blood on flows in a diseased arterial vessel. part 1: Steady flows. Biorheology, 28:241–262, 1991.

G. R. Cokelet. The rheology of human blood. Phd thesis, Massachusetts Institute of Technology, 1963.

J. Degroote, K. J. Bathe, and J. Vierendeels. Performance of a new partitioned procedure versus a monolithic procedure in fluid-structure interaction. Computers & Structures, 87(11):793–801, 2009.

J. Degroote, R. Haelterman, S. Annerel, P. Bruggeman, and J. Vierendeels. Performance of partitioned procedures in fluid-structure interaction. Computers & Structures, 88 (7-8):446–457, 2010.

I. Demirdžić and M. Perić. Space conservation law in finite volume calculations of fluid flow. International Journal for Numerical Methods in Fluids, 8:1037–1050, 1988.

A. Der Kiureghian and O. Ditlevsen. Aleatory or epistemic? Does it matter? Structural Safety, 31(2):105–112, 2009.

T. Dick, N. R. Gauger, and S. Schmidt. Combining Sobolev smoothing with parameterized shape optimization. Computers & Fluids, 244:105568, 2022.

J. Donea, A. Huerta, J. P. Ponthot, and A. Rodríguez-Ferran. Arbitrary Lagrangian-Eulerian Methods, chapter 14. John Wiley & Sons, Ltd, 2004.

A. Düster and S. Kollmannsberger. AdhoC^4 – User's Guide. Lehrstuhl für Computation in Engineering, TU München, Numerische Strukturanalyse mit Anwendungen in der Schiffstechnik, TU Hamburg-Harburg, 2010.

A. Düster, H. Bröker, and E. Rank. The p-version of the finite element method for three-dimensional curved thin walled structures. International Journal for Numerical Methods in Engineering, 52(7):673–703, 2001.

A. Düster, E. Rank, and B. Szabó. The p-Version of the Finite Element and Finite Cell Methods, pages 1–35. John Wiley & Sons, Ltd, 2017.

K. Effenberger-Neidnicht and M. Hartmann. Mechanisms of Hemolysis During Sepsis. Inflammation, 41:1569–1581, 2018.

Y. Fan, W. Jiang, Y. Zou, J. Li, J. Chen, and X. Deng. Numerical simulation of pulsatile non-Newtonian flow in the carotid artery bifurcation. Acta Mechanica Sinica, 25: 249–255, 2009.

C. Farhat, K.G. van der Zee, and P. Geuzaine. Provably second-order time-accurate loosely-coupled solution algorithms for transient nonlinear computational aeroelasticity. Computer Methods in Applied Mechanics and Engineering, 195(17):1973–2001, 2006.

M. E. Farhikhteh, E. M. Papoutsis-Kiachagias, and K. C. Giannakoglou. Aerodynamic shape optimization of wind turbine rotor blades using the continuous adjoint method. Optimization and Engineering, 2023.

J. H. Ferziger, M. Peric, and R. L. Street. Computational Methods for Fluid Dynamics. Springer Nature, 4th edition, 2020.

F. Fontan and E. Baudet. Surgical repair of tricuspid atresia. Thorax, 26(3):240–248, 1971.

K. B. Fragkos, E. M. Papoutsis-Kiachagias, and K. C. Giannakoglou. pfosm: An efficient algorithm for aerodynamic robust design based on continuous adjoint and matrix-vector products. Computers & Fluids, 181:57–66, 2019.

Y.-C. Fung. Biomechanics: Mechanical Properties of Living Tissues, chapter 3, pages 66–108. Springer New York, New York, NY, 1993.

D. Garcia, P. Pibarot, JG. Dumesnil, F. Sakr, and LG. Durand. Assessment of aortic valve stenosis severity: A new index based on the energy loss concept. Circulation, 101(7): 765–771, 2000.

A. Garon and MI. Farinas. Fast three-dimensional numerical hemolysis approximation. Artificial Organs, 28(11):1016–1025, 2004.

C. Geiersbach and W. Wollner. A stochastic gradient method with mesh refinement for pde-constrained optimization under uncertainty. SIAM Journal on Scientific Computing, 42(5):A2750–A2772, 2020.

C. Geiersbach, E. Loayza-Romero, and K. Welker. Stochastic approximation for optimization in shape spaces. SIAM Journal on Optimization, 31(1):348–376, 2021.

C. Geiersbach, E. Loayza-Romero, and K. Welker. Pde-constrained shape optimization: Toward product shape spaces and stochastic models. In K. Chen, C.-B. Schönlieb, X.-C. Tai, and L. Younes, editors, Handbook of Mathematical Models and Algorithms in Computer Vision and Imaging: Mathematical Imaging and Vision, pages 1585–1630. Springer International Publishing, Cham, 2023.

D. N. Ghista and F. Kabinejadian. Coronary artery bypass grafting hemodynamics and anastomosis design: a biomedical engineering review. BioMedical Engineering OnLine, 12(1):1–28, 2013.

K. C. Giannakoglou, D. I. Papadimitriou, and I. C. Kampolis. Aerodynamic shape design using evolutionary algorithms and new gradient-assisted metamodels. Computer Methods in Applied Mechanics and Engineering, 195(44):6312–6329, 2006.

M. Giersiepen, L. J. Wurzinger, R. Opitz, and H. Reul. Estimation of shear stress-related blood damage in heart valve prostheses - in vitro comparison of 25 aortic valves. The International Journal of Artificial Organs, 13(5):300–306, 1990.

M. B. Giles and N. A. Pierce. An Introduction to the Adjoint Approach to Design. Flow, Turbulence and Combustion, 65(3):395–415, 2000.

M. Girfoglio, A. Quaini, and G. Rozza. Fluid-structure interaction simulations with a LES filtering approach in *solids4Foam*. Communications in Applied and Industrial Mathematics, 12(1):13–28, 2021.

H. A. González and N. O. Moraga. On predicting unsteady non-Newtonian blood flow. Applied Mathematics and Computation, 170(2):909–923, 2005.

L. Goubergrits and K. Affeld. Numerical estimation of blood damage in artificial organs. Artificial Organs, 28(5):499–507, 2004.

L. Goubergrits, U. Kertzscher, and M. Lommel. Past and Future of Blood Damage Modelling in a View of Translational Research. The International Journal of Artificial Organs, 42(3):125–132, 2018.

M. Grigioni, D'A. Giuseppe, A. Amodeo, and R. M. Di Donato. Power dissipation associated with surgical operations' hemodynamics: Critical issues and application to the total cavopulmonary connection. Journal of Biomechanics, 39(9):1583–1594, 2006.

P. Hariharan, M. Giarra, V. Reddy, S. W. Day, K. B. Manning, S. Deutsch, S. F. C. Stewart, M. R. Myers, M. R. Berman, G. W. Burgreen, E. G. Paterson, and R. A. Malinauskas. Multilaboratory Particle Image Velocimetry Analysis of the FDA Benchmark Nozzle Model to Support Validation of Computational Fluid Dynamics Simulations. Journal of Biomechanical Engineering, 133(4):041002, 2011.

P. Hariharan, G. D'Souza, M. Horner, R. A. Malinauskas, and M. R. Myers. Verification Benchmarks to Assess the Implementation of Computational Fluid Dynamics Based Hemolysis Prediction Models. Journal of Biomechanical Engineering, 137(9), 2015.

A. Harten. High resolution schemes for hyperbolic conservation laws. Journal of Computational Physics, 49(3):357–393, 1983.

H. Haruguchi and S. Teraoka. Intimal hyperplasia and hemodynamic factors in arterial bypass and arteriovenous grafts: a review. Journal of Artificial Organs, 6(4):227–235, 2003.

J. He and X. Yao. Drift analysis and average time complexity of evolutionary algorithms. Artificial Intelligence, 127(1):57–85, 2001.

J. P. Heners, L. Radtke, M. Hinze, and A. Düster. Adjoint shape optimization for fluid-structure interaction of ducted flows. Computational Mechanics, 61:259–276, 2018.

G. Heuser and R. Opitz. A couette viscometer for short time shearing of blood. Biorheology, 17:17–24, 1980.

M. Hinze, R. Pinnau, M. Ulbrich, and S. Ulbrich. Optimization with PDE Constraints, volume 23. Springer Science & Business Media, 2008.

M.-C. Hsu and Y. Bazilevs. Fluid–structure interaction modeling of wind turbines: simulating the full machine. Computational Mechanics, 50(6):821–833, 2012.

M. C. Hsu, D. Kamensky, Y. Bazilevs, M. S. Sacks, and T. J. R. Hughes. Fluid-structure interaction analysis of bioprosthetic heart valves: significance of arterial wall deformation. Computational Mechanics, 54(4):1055–1071, 2014.

F. Irgens. Rheology and Non-Newtonian Fluids. Springer, 2014.

A. Jahangirian and A. Shahrokhi. Aerodynamic shape optimization using efficient evolutionary algorithms and unstructured cfd solver. Computers & Fluids, 46(1):270–276, 2011. 10th ICFD Conference Series on Numerical Methods for Fluid Dynamics (ICFD 2010).

A. Jameson. Aerodynamic design via control theory. Journal of Scientific Computing, 3: 233–260, 1988.

H. Janssen. Monte-carlo based uncertainty analysis: Sampling efficiency and sampling convergence. Reliability Engineering & System Safety, 109:123–132, 2013.

H. Jasak. Error analysis and estimation for the finite volume method with applications to fluid flows. Phd thesis, Imperial College London, 1996.

W. W. Jeong and K. Rhee. Effects of surface geometry and non-newtonian viscosity on the flow field in arterial stenoses. Journal of Mechanical Science and Technology, 23: 2424–2433, 2009.

Y. Jin. Surrogate-assisted evolutionary computation: Recent advances and future challenges. Swarm and Evolutionary Computation, 1(2):61–70, 2011.

B. M. Johnston, P. R. Johnston, S. Corney, and D. Kilpatrick. Non-Newtonian blood flow in human right coronary arteries: steady state simulations. Journal of Biomechanics, 37 (5):709–720, 2004.

F. Kabinejadian and D. N. Ghista. Compliant model of a coupled sequential coronary arterial bypass graft: Effects of vessel wall elasticity and non-Newtonian rheology on blood flow regime and hemodynamic parameters distribution. Medical Engineering & Physics, 34(7):860–872, 2012.

P. Katsapoxaki, R. Hottois, T.-S. Tran, C. Schram, G. Coussement, and T. Verstraete. Adjoint-Based Aeroacoustic Optimization of NASA Rotor37. volume 13C: Turbomachinery — Deposition, Erosion, Fouling, and Icing; Design Methods and CFD Modeling for Turbomachinery; Ducts, Noise, and Component Interactions of Turbo Expo: Power for Land, Sea, and Air, page V13CT33A010, 2023.

I. S. Kavvadias, E. M. Papoutsis-Kiachagias, and K. C. Giannakoglou. On the proper treatment of grid sensitivities in continuous adjoint methods for shape optimization. Journal of Computational Physics, 301:1–18, 2015.

S. Kishimoto, T. Maruhashi, M. Kajikawa, S. Matsui, H. Hashimoto, Y. Takaeko, T. Harada, T. Yamaji, Y. Han, Y. Kihara, K. Chayama, C. Goto, F.M. Yusoff, A. Nakashima, and Y. Higashi. Hematocrit, hemoglobin and red blood cells are associated with vascular function and vascular structure in men. Scientific Reports, 10(1), 2020.

M. Kissin, N. Kansal, P. J. Pappas, D. O. DeFouw, W. N. Durán, and R. W. Hobson. Vein interposition cuffs decrease the intimal hyperplastic response of polytetrafluoroethylene bypass grafts. Journal of Vascular Surgery, 31(1):69–83, 2000.

M. König, L. Radtke, and A. Düster. A Flexible C++ Framework for the Partitioned Solution of Strongly Coupled Multifield Problems. Computers & Mathematics with Applications, 72(7):1764–1789, 2016.

C. Körner. Die Silikon-beschichtete Polyesterprothese: Konzept, physikalische und biologische Eigenschaften. Phd thesis, Bayerische Julius-Maximilians-Universität Würzburg, 2007.

M. Kranz, J. K. Lüdeker, and B. Kriegesmann. A generalized approach for robust topology optimization using the first-order second-moment method for arbitrary response functions. Structural and Multidisciplinary Optimization, 66(5), 2023.

J. Kröger and T. Rung. CAD-Free Hydrodynamic Optimisation Using Consistent Kernel-Based Sensitivity Filtering. Ship Technology Research, 62(3):111–130, 2015.

J. Kröger, N. Kühl, and T. Rung. Adjoint volume-of-fluid approaches for the hydrodynamic optimisation of ships. Ship Technology Research, 65(1):47–68, 2018.

J. C. Krüger, M. Kranz, T. Schmidt, R. Seifried, and B. Kriegesmann. An efficient and non-intrusive approach for robust design optimization with the first-order second-moment method. Computer Methods in Applied Mechanics and Engineering, 414:116136, 2023.

D. N. Ku, D. P. Giddens, C. K. Zarins, and S. Glagov. Pulsatile flow and atherosclerosis in the human carotid bifurcation. positive correlation between plaque location and low oscillating shear stress. Arteriosclerosis, Thrombosis, and Vascular Biology, 5(3):293–302, 1985.

N. Kühl. Adjoint-Based Shape Optimization Constraint by Turbulent Two-Phase Navier-STokes Systems. Phd thesis, Technische Universität Hamburg, 2021.

T. Kuusela, T. Shepherd, and J. Hietarinta. Stochastic model for heart-rate fluctuations. Physical Review E, 67, 2003.

E. L. Kyung, S. L. Jeong, and Y. Y. Jung. A numerical study on steady flow in helically sinuous vascular prostheses. Medical Engineering & Physics, 33(1):38–46, 2011.

N. Kühl, P. M. Müller, A. Stück, M. Hinze, and T. Rung. Decoupling of control and force objective in adjoint-based fluid dynamic shape optimization. AIAA Journal, 57 (9):4110–4114, 2019.

N. Kühl, J. Kröger, M. Siebenborn, M. Hinze, and T. Rung. Adjoint complement to the volume-of-fluid method for immiscible flows. Journal of Computational Physics, 440, 2021.

N. Kühl, T. T. Nguyen, M. Palm, D. Jürgens, and T. Rung. Adjoint node-based shape optimization of free-floating vessels. Structural and Multidisciplinary Optimization, 65, 2022.

D. Lacasse, A. Garon, and D. Pelletier. Mechanical hemolysis in blood flow: user-independent predictions with the solution of a partial differential equation. Computer Methods in Biomechanics and Biomedical Engineering, 10(1):1–12, 2007.

G. Lanzino, A. A. Rabinstein, and R. D. Jr. Brown. Treatment of carotid artery stenosis: medical therapy, surgery, or stenting? Mayo Clinic Proceedings, 84(4):362–387, 2009.

H. Lee, M.-C. Song, J.-C. Suh, and B.-J. Chang. Hydro-elastic analysis of marine propellers based on a bem-fem coupled fsi algorithm. International Journal of Naval Architecture and Ocean Engineering, 6(3):562–577, 2014.

M. Lei, J. P. Archie, and C. Kleinstreuer. Computational design of a bypass graft that minimizes wall shear stress gradients in the region of the distal anastomosis. Journal of Vascular Surgery, 25(4):637–646, 1997.

L. B. Leverett, J. D. Hellums, C. P. Alfrey, and E. C. Lynch. Red Blood Cell Damage by Shear Stress. Biophysical Journal, 12(3):257–273, 1972.

F. S. Lien and M. A. Leschziner. Upstream monotonic interpolation for scalar transport with application to complex turbulent flows. International Journal for Numerical Methods in Fluids, 19(6):527–548, 1994.

R. Löhner. Applied Computational Fluid Dynamics Techniques: An Introduction Based on Finite Element Methods. John Wiley & Sons, Ltd, 2008.

F. Loth, P. F. Fischer, and H. S. Bassiouny. Blood flow in end-to-side anastomoses. Annual Review of Fluid Mechanics, 40(1):367–393, 2008.

J. N. Lyness and C. B. Moler. Numerical differentiation of analytic functions. SIAM Journal on Numerical Analysis, 4(2):202–210, 1967.

A. Malek, S. Alpher, and S. Izumo. Hemodynamic shear stress and its role in atherosclerosis. Journal of American Medical Association, 282(21):2035–2042, 1999.

A. L. Marsden. Optimization in cardiovascular modeling. Annual Review of Fluid Mechanics, 46(1):519–546, 2014.

D. P. Mok. Partitionierte Lösungsansätze in der Strukturdynamik und der Fluid-Struktur-Interaktion. Phd thesis, University of Stuttgart, 2001.

W. J. Morokoff and R. E. Caflisch. Quasi-Monte Carlo Integration. Journal of Computational Physics, 122(2):218–230, 1995.

P. M. Müller. CAD-free adjoint shape optimization of floating vessels. Phd thesis, Technische Universität Hamburg, 2023.

P. M. Müller, N. Kühl, M. Sieberborn, K. Deckelnick, M. Hinze, and T. Rung. A novel p-harmonic descent approach applied to fluid dynamic shape optimization. Structural and Multidisciplinary Optimization, 64(6):3489–3503, 2021.

P. M. Müller, G. Bletsos, and T. Rung. Shape Transformation Approaches for Fluid Dynamic Optimization. Aerospace, 10(6), 2023.

J. Nocedal and S. J. Wright. Numerical Optimization. Springer, New York, NY, USA, 2e edition, 2006.

C. Othmer. A continuous adjoint formulation for the computation of topological and surface sensitivities of ducted flows. International Journal for Numerical Methods in Fluids, 58:861–877, 2008.

D. I. Papadimitriou and K. C. Giannakoglou. A continuous adjoint method with objective function derivatives based on boundary integrals, for inviscid and viscous flows. Computers & Fluids, 36(2):325–341, 2007.

D. I. Papadimitriou and K. C. Giannakoglou. Third-order sensitivity analysis for robust aerodynamic design using continuous adjoint. International Journal for Numerical Methods in Fluids, 71(5):652–670, 2013.

E. M. Papoutsis-Kiachagias and K. C. Giannakoglou. Continuous Adjoint Methods for Turbulent Flows, Applied to Shape and Topology Optimization: Industrial Applications. Archives of Computational Methods in Engineering, 23:255–299, 2016.

E. M. Papoutsis-Kiachagias, V. G. Asouti, K. C. Giannakoglou, K. Gkagkas, S. Shimokawa, and E. Itakura. Multi-point aerodynamic shape optimization of cars based on continuous adjoint. Structural and Multidisciplinary Optimization, 59:675–694, 2019.

S. V. Patankar and D. B. Spalding. A calculation procedure for heat, mass and momentum transfer in three-dimensional parabolic flows. International Journal of Heat and Mass Transfer, 15(10):1787–1806, 1972.

T. J. Pedley. The Fluid Mechanics of Large Blood Vessels. Cambridge University Press, 1980.

K. Perktold, M. Resch, and H. Florian. Pulsatile Non-Newtonian Flow Characteristics in a Three-Dimensional Human Carotid Bifurcation Model. Journal of Biomechanical Engineering, 113(4):464–475, 1991.

J. E. V. Peter and R. P. Dwight. Numerical sensitivity analysis for aerodynamic optimization: A survey of approaches. Computers & Fluids, 39(3):373–391, 2010.

O. Pironneau. On optimum design in fluid mechanics. Journal of Fluid Mechanics, 64(1): 97–110, 1974.

O. Pirronneau. Optimal Shape Design for Elliptic Systems. Springer, New York, 1984.

M. M. Putko, A. C. Taylor, P. A. Newman, and L. L. Green. Approach for Input Uncertainty Propagation and Robust Design in CFD Using Sensitivity Derivatives. Journal of Fluids Engineering, 124(1):60–69, 2001.

A. Quarteroni, M. Tuveri, and A. Veneziani. Computational vascular fluid dynamics: problems, models and methods. Computing and Visualization in Science, 2:163–197, 2000.

J. R. R. A. Martins and J. T. Hwang. Review and Unification of Methods for Computing Derivatives of Multidisciplinary Computational Models. AIAA Journal, 51(11), 2013.

L. Radtke. A partitioned solution approach for fluid-structure interaction problems in the arterial system. Phd thesis, Technische Universität Hamburg, 2020.

L. Radtke, L.-A. Axel, E. S. Debus, and A. Düster. Convergence acceleration for partitioned simulations of the fluid-structure interaction in arteries. Computational Mechanics, 57 (6):901–920, 2016.

L. Radtke, T. Lampe, M. Abdel-Maksoud, and A. Düster. Partitioned simulation of the acoustic behavior of flexible marine propellers using finite and boundary elements. PAMM, 20(1):e202000315, 2021.

L. Radtke, G. Bletsos, N. Kühl, T. Suchan, T. Rung, A. Düster, and K. Welker. Parameter-Free Shape Optimization: Various Shape Updates for Engineering Applications. Aerospace, 10(9), 2023.

G. D. Raithby and G. E. Schneider. Numerical solution of problems in incompressible fluid flow: Treatment of the velocity-pressure coupling. Numerical Heat Transfer, 2(4): 417–440, 1979.

R. P. Rand and A. C. Burton. Area and volume changes in hemolysis of single erythrocytes. Journal of Cellular and Comparative Physiology, 61(3):245–253, 1963.

G. Rappitsch and K. Perktold. Pulsatile Albumin Transport in Large Arteries: A Numerical Simulation Study. Journal of Biomechanical Engineering, 118(4):511–519, 1996.

H. Robbins and S. Monro. A stochastic approximation method. The Annals of Mathematical Statistics, 22(3):400–407, 1951.

S. Roll, J. Müller-Nordhorn, T. Keil, H. Scholz, D. Eidt, W. Greiner, and S. N. Willich. Dacron™vs. ptfe as bypass materials in peripheral vascular surgery – systematic review and meta-analysis. BMC Surgery, 8(1):22, 2008.

R. I. Rückert. Experimentelle und klinische Untersuchungen zur Optimierung der Hämodynamik in termino-lateral Prothesenbypass-Anastomosen. Postdoctoral thesis, Medizinischen Fakultät Charié, Humboldt-Universität zu Berlin, 2001.

T. Rung, K. Wöckner, M. Manzke, J. Brunswig, C. Ulrich, and A. Stück. Challenges and Perspectives for Maritime CFD Applications. Jahrbuch der Schiffbautechnischen Gesellschaft, 103:127–139, 2009.

T. Sandgren, B. Sonesson, A.R. Ahlgren, and T. Länne. The diameter of the common femoral artery in healthy human: Influence of sex, age, and body size. Journal of Vascular Surgery, 29(3):503–510, 1999.

W.-B. Shangguan and Z.-H. Zhen-Hua Lu. Modelling of a hydraulic engine mount with fluid–structure interaction finite element analysis. Journal of Sound and Vibration, 275 (1):193–221, 2004.

M. K. Sharp and S. F. Mohammad. Scaling of Hemolysis in Needles and Catheters. Annals of Biomedical Engineering, 26(5):788–797, 1998.

D. Shepard. A two-dimensional interpolation function for irregularly-spaced data. In Proceedings of the 1968 23rd ACM National Conference, pages 517–524, New York, 1968. Advancing Computing as a Science & Profession.

S. S. Shibeshi and W. E. Collins. The Rheology of Blood Flow in a Branched Arterial System. Applied Rheology, 15(6):398–405, 2005.

J. Sokolowski and J.-P. Zolesio. Introduction to shape optimization, volume 16 of Springer Series in Computational Mathematics. Springer Berlin Heidelberg, Berlin, Heidelberg, 1992.

O. Soto and R. Löhner. On the Computation of Flow Sensitivities from Boundary Integrals. AIAA-04-0112, 2004.

W. Squire and G. Trapp. Using complex variables to estimate derivatives of real functions. SIAM Review, 40(1):110–112, 1998.

E. Stavropoulou, M. Hojjat, and K.-U. Bletzinger. In-plane mesh regularization for node-based shape optimization problems. Computer Methods in Applied Mechanics and Engineering, 275:39–54, 2014.

S. F. C. Steward, E. G. Paterson, G. W. Burgreen, P. Hariharan, M. Giarra, V. Reddy, S. W. Day, K. B. Manning, S. Deutsch, M. R. Berman, M. R. Myers, and R. A. Malinauskas. Assessment of cfd performance in simulations of an idealized medical device: Results of fda's first computational interlaboratory study. Cardiovascular Engineering and Technology, 3(2):139–160, 2012.

A. Stück. Adjoint Navier-Stokes methods for hydrodynamic shape optimisation. Phd thesis, Technische Universität Hamburg, 2012.

A. Stück and T. Rung. Adjoint Complement to Viscous Finite-Volume Pressure-Correction Methods. Journal of Computational Physics, 248:402–419, 2013.

W. D. Suggs, H. F. Henriques, and R. G. DePalma. Vein cuff interposition prevents juxta-anastomotic neointimal hyperplasia. Annals of Surgery, 207(6):717–723, 1988.

B. Szabo and I. Babuska. Finite Element Analysis. John Wiley & Sons, 1991.

M. E. Taskin, K. H. Fraser, T. Zhang, C. Wu, B. P. Griffith, and Z. Wu. Evaluation of Eulerian and Lagrangian models for hemolysis estimation. ASAIO Journal, 58(4): 363–372, 2012.

B. Thamsen, B. Blümel, J. Schaller, C. O. Paschereit, K. Affeld, L. Goubergrits, and U. Kertzscher. Numerical Analysis of Blood Damage Potential of the HeartMate II and HeartWare HVAD Rotary Blood Pumps. Artificial Organs, 39(8):651–659, 2015.

V. Thondapu, C. Mamon, E. K. W. Poon, O. Kurihara, H. O. Kim, M. Russo, M. Araki, H. Shinohara, E. Yamamoto, J. Dijkstra, M. Tacey, H. Lee, A. Ooi, P. Barlis, and I.-K. Jang. High spatial endothelial shear stress gradient independently predicts site of acute coronary plaque rupture and erosion. Cardiovascular Research, 117(8):1974–1985, 2020.

R. Torii, M. Oshima, T. Kobayashi, and K. Takagi. The hemodynamic study of the cerebral artery using numerical simulations based on medical imaging data. Journal of Visualization, 4:277–284, 2001.

R. Torii, M. Oshima, T. Kobayashi, K. Takagi, and T. E. Tezduyar. Influence of wall elasticity in patient-specific hemodynamic simulations. Computers & Fluids, 36(1):160–168, 2007.

X. S. Trompoukis, K. T. Tsiakas, V. G. Asouti, and K. C. Giannakoglou. Continuous adjoint-based shape optimization of a turbomachinery stage using a 3d volumetric parameterization. International Journal for Numerical Methods in Fluids, 95(7):1054–1075, 2023.

B. D. Upadhyay, S. S. Sonigra, and S. D. Daxini. Numerical analysis perspective in structural shape optimization: A review post 2000. Advances in Engineering Software, 155:102992, 2021.

J. G. Valdés Vázquez. Nonlinear Analysis of Orthotropic Membrane and Shell Structures Including Fluid-Structure Interaction. Phd thesis, Universitat Politècnica de Catalunya, 2007.

J. van der Slegt, S. L. Steunenberg, J. M. W. Donker, E. J. Veen, G. H. Ho, H. G. W. de Groot, and L. van der Laan. The current position of precuffed expanded polytetrafluoroethylene bypass grafts in peripheral vascular surgery. Journal of Vascular Surgery, 60(1):120–128, 2014.

B. van Leer. Towards the ultimate conservative difference scheme. II. Monotonicity and conservation combined in a second-order scheme. Journal of Computational Physics, 14 (4):361–370, 1974.

J. Vassberg and A. Jameson. Aerodynamic shape optimization part 1: theoretical background. Introduction to optimization and multidisciplinary design, pages 1–30, 2006.

R. W. Walters and L. Huyse. Uncertainty analysis for fluid mechanics with applications. ICASE, NASA Langley Research Center, 2002.

M. Wazzan, A. Abduljabbar, A. Ajlan, R. Ahmad, T. Alhazmi, A. Eskandar, K. Khashoggi, F. Alasadi, S. Howladar, and Y. Alshareef. Reference for normal diameters of the abdominal aorta and common iliac arteries in the saudi population. Cureus, 14(10), 2022.

K. Welker. Efficient PDE Constrained Shape Optimization in Shape Spaces. Phd thesis, Universität Trier,, 2016.

J. Wen, T. Zheng, W. Jiang, X. Deng, and Y. Fan. A comparative study of helical-type and traditional-type artery bypass grafts: numerical simulation. American Society for Artificial Internal Organs Journal, 57(2):399–406, 2011.

N. M. Wilson, F. R. Arko, and C. A. Taylor. Predicting changes in blood flow in patient-specific operative plans for treating aortoiliac occlusive disease. Computer Aided Surgery, 10(4):257–277, 2005.

J. R. Womersley. Method for the calculation of velocity, rate of flow and viscous drag in arteries when the pressure gradient is known. The Journal of Physiology, 127(3): 553–563, 1955.

World Health Organization (WHO). Fact sheet: Cardiovascular diseases, 2023. URL `https://www.who.int/news-room/fact-sheets/detail/cardiovascular-diseases-(cvds)`.

L. J. Wurzinger, R. Opitz, P. Blasberg, and H. Schmid-Schönbein. Platelet and coagulation parameters following millisecond exposure to laminar shear stress. Thrombosis and haemostasis, 54(2):381–386, 1985.

D. Xiu and G.E. Karniadakis. Modeling uncertainty in flow simulations via generalized polynomial chaos. Journal of Computational Physics, 187(1):137–167, 2003.

S. Xu, W. Jahn, and J.-D. Müller. CAD-based shape optimisation with CFD using a discrete adjoint. International Journal for Numerical Methods in Fluids, 74(3):153–168, 2014.

S. Yakubov, B. Cankurt, M. Abdel-Maksoud, and T. Rung. Hybrid MPI/openMP Parallelization of an Euler-Lagrange Approach to Cavitation Modelling. Computers & Fluids, 80:365–371, 2013.

S. Yakubov, T. Maquil, and T. Rung. Experience Using Pressure-Based CFD Methods for Euler-Euler Simulations of Cavitating Flows. Computers & Fluids, 111:91–104, 2015.

T. Yamaguchi, T. Ishikawa, Y. Imai, N. Matsuki, M. Xenos, Y. Deng, and D. Bluestein. Particle-Based Methods for Multiscale Modeling of Blood Flow in the Circulation and in Devices: Challenges and Future Directions. Annals of Biomedical Engineering, 38(3): 1225–1235, 2010.

K. Yeleswarapu. Evaluation of Continuum Models for Characterizing the Constitutive Behavior of Blood. Phd thesis, University of Pittsburg, 1996.

H. Yu, G. Janiga, and D. Thévenin. Computational Fluid Dynamics-Based Design Optimization Method for Archimedes Screw Blood Pumps. Artificial Organs, 40(4):341–352, 2016.

H. Yu, S. Engel, G. Janiga, and D. Thévenin. A Review of Hemolysis Prediction Models for Computational Fluid Dynamics. Artificial Organs, 41(7):603–621, 2017.

C. Zhang, S. Xie, S. Li, F. Pu, X. Deng, Y. Fan, and D. Li. Flow patterns and wall shear stress distribution in human internal carotid arteries: The geometric effect on the risk for stenoses. Journal of Biomechanics, 45(1):83–89, 2012.

T. Zhang, M. E. Taskin, H.-B. Fang, A. Pampori, R. Jarvik, B. P. Griffith, and Z. J. Wu. Study of flow-induced hemolysis using novel couette-type blood-shearing devices. Artificial Organs, 35(12):1180–1186, 2011.